



LUND UNIVERSITY

From understanding to realizing novel III-Sb materials via nanowires

Namazi, Luna

2018

Document Version:

Publisher's PDF, also known as Version of record

[Link to publication](#)

Citation for published version (APA):

Namazi, L. (2018). *From understanding to realizing novel III-Sb materials via nanowires*. [Doctoral Thesis (compilation), Lund University]. Solid State Physics, Lund University.

Total number of authors:

1

General rights

Unless other specific re-use rights are stated the following general rights apply:

Copyright and moral rights for the publications made accessible in the public portal are retained by the authors and/or other copyright owners and it is a condition of accessing publications that users recognise and abide by the legal requirements associated with these rights.

- Users may download and print one copy of any publication from the public portal for the purpose of private study or research.
- You may not further distribute the material or use it for any profit-making activity or commercial gain
- You may freely distribute the URL identifying the publication in the public portal

Read more about Creative commons licenses: <https://creativecommons.org/licenses/>

Take down policy

If you believe that this document breaches copyright please contact us providing details, and we will remove access to the work immediately and investigate your claim.

LUND UNIVERSITY

PO Box 117
221 00 Lund
+46 46-222 00 00

From understanding to realizing novel III-Sb materials via nanowires

From understanding to realizing novel III-Sb materials via nanowires

Luna Namazi



LUND
UNIVERSITY

DOCTORAL DISSERTATION

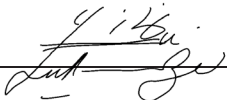
by due permission of the Faculty of Engineering, Lund University, Sweden.
To be defended on Friday, the 23rd of March, 2018, at 9:15 in the Rydberg Lecture
Hall at the Department of Physics, Lund.

Faculty opponent
Dr. Hannah Joyce

University of Cambridge

| | | | | |
|--|--|----------|--|--|
| Organization LUND UNIVERSITY | Document name DOCTORAL DISSERTATION | | | |
| | Date of issue | | | |
| Author(s) LUNA NAMAZI | Sponsoring organization | | | |
| | | | | |
| Title and subtitle | | | | |
| <p>Abstract</p> <p>Due to their unique physical and material properties, III-Sb nanowires are considered good candidates for future devices, and test beds for understanding fundamental physics. Synthesizing these nanowires however is associated with certain challenging aspects, which are generally not present for other III-V nanowires, demanding the need for in depth investigations. For instance, growing Au-seeded III-Sb nanowires directly from substrates is difficult, and considered a limitation when attempting to grow complex Sb-based structures. The crystal structure of III-Sb nanowires, in contrast to their other III-V counterparts, has been limited to zinc blende to date, with no reproducible reports on wurtzite antimonides. As the crystal structure of material has a large impact on the properties it exhibits, it can be beneficial to have access to wurtzite antimonides. To further the capacity antimonide nanowires can offer, these struggles need to be investigated and addressed through suitable methods. This thesis explores these limitations, and by providing a deeper insight, tackles the mentioned issues of Au-seeded III-Sb nanowire growth.</p> <p>Initially direct nucleation of Au-seeded $\text{InAs}_{1-x}\text{Sb}_x$ nanowires with a large range of material compositions is explored. Direct growth of nanowires with compositions on the higher end of Sb is made available through semi In-seeded growth. By changing the particle composition the contact angle is improved, and vertical nanowire growth is facilitated.</p> <p>Thereafter, through template assisted growth, complex multi-segmented selective core-shell structures of InAs-GaSb nanowires are realized. The antimonide shell will exclusively grow on the zinc blende segments of the underlying InAs core, as a result of the higher surface energy of zinc blende sidewalls.</p> <p>Finally, the thesis successfully examines various templating methods for realizing radial (GaSb), branched ($\text{InAs}_{1-x}\text{Sb}_x$), and axial (1D) (GaSb) wurtzite antimonides for the first time. The mechanisms leading to surmounting wurtzite antimonide formation barriers are explained in detail for each of the specific cases, leading to a thorough comprehension of the field. These methods, in combination with the possibility to now realize antimonide nanowires directly on substrates, opens doors towards design and synthesis of complex crystal structure engineered nanowires of pure antimonides.</p> | | | | |
| <p>Key words Nanowire growth, Antimonide material, Crystal structure engineering, Template nanowires, Wurtzite antimonide</p> | | | | |
| Classification system and/or index terms (if any) | | | | |
| Supplementary bibliographical information | | Language | | |
| ISSN and key title | | ISBN | | |
| Recipient's notes | Number of pages 201 | Price | | |
| | Security classification | | | |

I, the undersigned, being the copyright owner of the abstract of the above-mentioned dissertation, hereby grant to all reference sources permission to publish and disseminate the abstract of the above-mentioned dissertation.

Signature  Date 2018-02-12

From understanding to realizing novel III-Sb materials via nanowires

Luna Namazi



LUND
UNIVERSITY

Coverphoto: Four-segmented selective core-shell InAs-GaSb nanowires

Back coverphoto: GaSb branches on zinc blende GaSb trunk nanowire

Coverphoto by: Luna Namazi

Copyright (Luna Namazi)

Paper I © 2017, IOP Science, DOI: 10.1088/1361-6528/aa6518

Paper II © 2015, Royal society of chemistry, DOI: 10.1039/c5nr01165e

Paper III © 2018, by the authors

Paper IV © 2018, Wiley, DOI: 10.1002/sml.201703785


Solid state physics
Department of physics
Lund university
SE-22100 Lund
Sweden

ISBN 978-91-7753-585-0 (print)

ISBN 978-91-7753-586-7 (pdf)

Printed in Sweden by Media-Tryck, Lund University
Lund 2018



MADE IN SWEDEN 



Media-Tryck is an environmental-
ly certified and ISO 14001 certified
provider of printed material.
Read more about our environmental
work at www.mediatryck.lu.se

To all those who made this possible ...

Table of Contents

| | |
|--|----|
| Acknowledgements | 11 |
| Abstract | 13 |
| Popular scientific description | 15 |
| List of papers | 17 |
| 1. Introduction | 19 |
| 2. Epitaxy of III-V nanowires..... | 23 |
| 2.1. Nucleation and growth | 23 |
| 2.1.1. Thermodynamics of nucleation | 23 |
| 2.1.2. Kinetics of nucleation | 29 |
| 2.1.3. Growth modes in vapor-solid mechanism | 31 |
| 2.1.4. Surfactants | 32 |
| 2.1.5. Vapor-liquid-solid (VLS) growth mechanism..... | 33 |
| 2.2. Crystal structure | 42 |
| 2.2.1. Crystal symmetry in III-V materials..... | 42 |
| 2.2.2. Surface energies of zinc blende and wurtzite nanowire side facets..... | 50 |
| 2.2.3. Wurtzite formation in nanowires | 50 |
| 2.2.4. Crystal structure engineering..... | 52 |
| 3. Experimental Methods..... | 55 |
| 3.1. MOVPE..... | 55 |
| 3.2. Electron Microscopy | 57 |
| 3.2.1. Scanning Electron Microscopy..... | 59 |
| 3.2.2. Transmission Electron Microscopy | 60 |
| 3.2.3. X-ray Energy Dispersive Spectroscopy..... | 60 |
| 4. III-Sb nanowire growth | 63 |
| 4.1. A general overview on III-Sb material..... | 63 |
| 4.2. Au-seeded antimonide nanowire growth and associated challenges..... | 64 |
| 4.2.1. Direct nucleation of Au-seeded III-Sb nanowires from substrate | 68 |
| 4.2.2. Template assisted growth of III-Sbs | 72 |
| 5. Concluding remarks and outlook..... | 89 |

| | |
|---------------------|----|
| 6. References | 93 |
|---------------------|----|

Acknowledgements

My Deepest appreciations to my supervisor, Kimberly Thelander, for the immense support and guidance she showed me throughout these five years. This work would not have been possible without your help, patience, and encouragements. I also owe sincere thankfulness to my co-supervisor Sebastian Lehmann for the full-time contribution, constructive discussions, advice, and constant support. I would also like to sincerely thank Claes Thelander for teaching me what I know about electrical characterizations.

Jonas Johansson, words are not enough for expressing my gratitude towards your endless support. Whenever I have needed to talk, you have welcomed me with open doors, and given me valuable tips. It has been heartwarming to know you sit an office away, always there to reach out to.

I would like to thank present and past members of our group; Rong Sun, Robert Hallberg, Marcus Tornberg, Erik Mårtensson, Karl Winkler, Hanna Kindlund, Carina Babu Maliakkal, Daniel Jakobsson, Reza Zamani, Sepideh Gorji, Martin Ek, and Maria De la Mata for the fruitful discussions, and support system, you have provided throughout the passed five years (not to forget the yummy cakes!!). I would also like to thank the ex-master students of our group, specifically Loiuse Gren for the wonderful TEM work on the wurtzite GaSb nanowires, and of course Magnus Dahl; it was a pleasure to work with you on the InAsSb branches project.

My gratitude goes to the administrative and technical support staff of FTF; Dan Hessman, Anneli Löfgren, Anders Gustavsson, Heiner Linke, Line Lundfald, Abdul-Rehman Hakim, Charlotte Solberg, Gerda Rentschler, Mia Hedin, Loiuse Baldetorp, Johanna and Janne, your continuous efforts make everything run smoothly. There are many more names and I'd hate to miss any! So, a big thanks to all of you!

I would also like to extend my gratitude towards all the NanoLund staff members; Ivan Maximov, Maria Huffman, George Rydnemalm, Håkan Lapovski, Anders Kvinnefors, Mariusz Graczyk, Sara Attaran, Peter Blomqvist, Dmitry Suyatin, Søren Jeppsen, Bengt Muller, for their time, assistance and patience and for making it a better place to be.

I would also like to appreciate the time and assistance Reine Wallenberg and Gunnel Karlsson offered when I was working with the SEM-XEDS at Kemicentrum.

My gratitude goes towards all participants of the CGMS meetings and co-users of the MOVPE machines, for the discussions and sharing their knowledge.

I would also like to thank my past and present officemates; David Lindgren, and Mahtab Aghaeipour. It's been a great pleasure sharing an office with you. I appreciate the company, chitchats, and all the considerations you have shown.

I would like to express my appreciations to many more of the people in FTF. Sometimes a friendly "Hej" is enough to put a smile on the face.

Life these years would not have been the same without the presence of the amazing friends and (passed or present) co-PhD students: Malin, Kushagr, Rong, Vishal, Fangfang, Neimantas, Chunlin, Ali, Bekmurat, Gaute, David, Karl, Zhen, Frida, Sara, Regina, Damino, Bahar, Reza, Linus, Robert, Artis, Amin, Florinda, I-Ju, Olof, Laura, Martin, Mercy, ... the list goes on and on! Thank you for the trips, time, support and fun! Babak, the weekly lunches, have been something to look forward to! You are a true friend.

My dear Najmeh, having you in my life has been an experience! Every time, no matter when or how, you have been there. Needless to say all the crazy we have stirred, all the limits we have explored, and much more! You are truly one of a kind.

Reza, for all the support and understanding, for all the inspirations and patience, I thank you.

Last but not least, comes my family. I am especially indebted and truly thankful to my father, who has encouraged me tirelessly throughout the years. I would have not been standing where I am today without his constant support. And to my mother whose love, determination, and strength has always been my inspiration. Hosna, what a dull life would it have been without you!

Abstract

Due to their unique physical and material properties, III-Sb nanowires are considered good candidates for future devices, and test beds for understanding fundamental physics. Synthesizing these nanowires however is associated with certain challenging aspects, which are generally not present for other III-V nanowires, demanding the need for in depth investigations. For instance, growing Au-seeded III-Sb nanowires directly from substrates is difficult, and considered a limitation when attempting to grow complex Sb-based structures. The crystal structure of III-Sb nanowires, in contrast to their other III-V counterparts, has been limited to zinc blende to date, with no reproducible reports on wurtzite antimonides. As the crystal structure of material has a large impact on the properties it exhibits, it can be beneficial to have access to wurtzite antimonides. To further the capacity antimonide nanowires can offer, these struggles need to be investigated and addressed through suitable methods. This thesis explores these limitations, and by providing a deeper insight, tackles the mentioned issues of Au-seeded III-Sb nanowire growth.

Initially direct nucleation of Au-seeded $\text{InAs}_{1-x}\text{Sb}_x$ nanowires with a large range of material compositions is explored. Direct growth of nanowires with compositions on the higher end of Sb is made available through semi In-seeded growth. By changing the particle composition the contact angle is improved, and vertical nanowire growth is facilitated.

Thereafter, through template assisted growth, complex multi-segmented selective core-shell structures of InAs-GaSb nanowires are realized. The antimonide shell will exclusively grow on the zinc blende segments of the underlying InAs core, as a result of the higher surface energy of zinc blende sidewalls.

Finally, the thesis successfully examines various templating methods for realizing radial (GaSb), branched ($\text{InAs}_{1-x}\text{Sb}_x$), and axial (1D) (GaSb) wurtzite antimonides for the first time. The mechanisms leading to surmounting wurtzite antimonide formation barriers are explained in detail for each of the specific cases, leading to a thorough comprehension of the field. These methods, in combination with the possibility to now realize antimonide nanowires directly on substrates, opens doors towards design and synthesis of complex crystal structure engineered nanowires of pure antimonides.

Popular scientific description

For sure we have all walked out on brisk winter mornings to find frost covering everything. What is this magnificent white layer of tiny crystals sitting everywhere really? It turns out that at cold temperatures, and very high humidity, the air becomes “saturated” with water vapor. The water vapor then undergoes a “phase change” from its gaseous form, to solid ice crystals condensing on the exposed surfaces. Frost has different types, but they are all composed of branched patterns of ice crystals, forming in fractal structures. But have you ever encountered frosted surfaces where the little needle-like frost crystals are magically standing up on the surface? I’m sure I have! Let’s take a look at the figure below. The ice crystals are aligned vertically on the exterior surface of a car. This type of frost, known as *hoar frost*, forms under extreme conditions, where the vapor phase supersaturation is significantly high.



Figure 1. Frost ice crystals formed vertically in needle-like structures on the exterior of a car.

Water of course is not the only material that can crystallize. If given ample time, most material form crystals upon solidification. And depending on their inherit properties, they can crystallize in a vast number of structures. The crystal structure simply defines the arrangement of atoms; the building blocks of material, in a solid crystal with respect to one another. Ice can crystallize in two different variants; namely hexagonal ice, and cubic ice.

In fact, the crystallization process of material is carefully controlled in research and industry, to ensure suitable shapes, dimensions, material composition, and structures with high qualities to fit a vast variety of applications in technology. Needle-like crystals, similar to the frost needles in the image, are artificially “grown” in highly controlled environments. These crystals are referred to as *Nanowires*; wires with dimensions on the order of one billionth of a meter. Just to put it in perspective, the diameter of a strand of hair is 1000 times larger than the diameter of a typical nanowire. Nanowire growth is usually conducted from a highly saturated vapor phase- similar to the ice needles- onto a surface, referred to as the substrate. An intermediate liquid phase can be also introduced on the substrate to facilitate and localize the anisotropic growth. Anisotropy in this context is referred to difference in measured length in different directions. This liquid phase is referred to as the *seed particle*; analogous to seeding plant growth.

A group of material referred to as III-Vs, when grown as nanowires, similar to ice also crystalize in a hexagonal or cubic structure. Each of the crystal structures may offer different properties for the same material. Therefore it is interesting to have access to both. However, a subgroup of them known as *antimonides*, on the one hand prove to be specially challenging to grow in the hexagonal structure. As a result, their potential properties remain unexplored. On the other hand, gold-seeded nanowires of these materials typically do not grow directly on the substrate (unlike the case shown for ice needles in the image).

In the past five years, I have focused on exploring and utilizing methods for addressing the challenges associated with gold-seeded antimonide nanowire growth. The direct growth of antimonide nanowires is facilitated by changing the seeding material from gold to predominantly indium particles. In addition, various template structures are developed where the antimonide material transfers and maintains the crystal structure of the template. Through the templating method, hexagonal antimonide material is realized for the first time, opening doors to characterizing them, and potentially using their properties in future applications.

List of papers

I. Direct nucleation, morphology and compositional tuning of $\text{InAs}_{1-x}\text{Sb}_x$ nanowires on InAs (111) B substrates

L. Namazi, S. Gorji Ghalamestani, S. Lehmann, R. R. Zamani, and K. A. Dick

Nanotechnology, 28, 16, 165601 (2017)

I initiated the project together with the second author, planned the project, performed the growth, analysis and interpretation, and had the main role in writing the paper.

II. Selective GaSb radial growth on crystal phase engineered InAs nanowires

L. Namazi, M. Nilsson, S. Lehmann, C. Thelander, and K. A. Dick

Nanoscale, 7, 23, 10472 (2015)

I performed the growth and data analysis, and was actively involved in writing the paper.

III. Realization of wurtzite GaSb using InAs nanowire templates

L. Namazi, L. Gren, M. Nilsson, M. Garbrecht, C. Thelander, R. R. Zamani, and K. A. Dick

Submitted to *Advanced functional materials*

I initiated and planned the project, developed the growth, and analyzed and interpreted the data. I had the main role in writing the bulk of the paper.

IV. Sb incorporation in wurtzite and zinc blende $\text{InAs}_{1-x}\text{Sb}_x$ branches on InAs template nanowires

M. Dahl*, L. Namazi*, R. R. Zamani, K. A. Dick

Small, 1703785 (2018)

I initiated the project, and supervised the first author both in planning and developing the growth, and also in data interpretation. I had the main role in writing the paper.

1. Introduction

Nanotechnology, a field in which objects with dimensions on the order of a few nanometers are synthesized, characterized, optimized, and ultimately applied within the existing industry, has found its way into numerous fields of research and science. As examples of these areas electronics [1], optics [2], fundamental physics [3], chemistry [4], and biology [5][6] could be mentioned. For instance in the semiconductor industry, there is ongoing demand for scaling down the dimensions of transistors in order to fit a larger number on a certain chip size, which in turn would increase the computational ability of devices.

Nanoscale objects can have various shapes and sizes, as well as material compositions depending on the desired applications. III-V semiconductors, material compounds from group III and V elements of the table of elements, have proven to be very suitable for electronics and optics [7][8][9]. This is due to the significantly high carrier mobilities they possess, which is a requirement for high-speed devices in electronics. Also, a large fraction of these materials have direct band gaps, which is beneficial in optics and optoelectronics.

“Nanofabrication” referred to techniques utilized for synthesizing and constructing nano-sized objects, can be carried out by different methods. The two categories for synthesizing nanomaterial are namely the “top-down” and the “bottom-up” techniques. The former is referred to techniques where bulk material is patterned or etched by various processing steps into nano-sized structures, while the latter involves methods through which atoms and molecules are manipulated to self-assemble in desired shapes, constructing nano-dimensioned structures into existence.

Nanowires are defined as nanostructures constrained in two dimensions to a diameter of few tens of nm, while in the third dimension –usually referred to as the nanowire length- have typical values ranging from few hundreds of nm to a few μm , or even mm. Due to their unique geometry, nanowires have attracted considerable attention, making them suitable candidates for many applications in various fields [10]. To state a few examples, their small size and unique geometry allows them to be considered as good candidates for further downscaling electronic devices [11], and for realizing quantum confinement [12][13]. Also, they provide strain relaxation in the radial direction when materials with different lattice constants are assembled on one another [14][15][16][17]. Strain in material

in this context is referred to the deformation when atoms in a crystal are displaced relative to their reference lattice constants. Therefore, in contrast to bulk, the nanowire geometry can prevent complications arising from lattice mismatch in heterostructure synthesis. Nanowires can be realized by both the bottom-up and top-down nanofabrication techniques, and can possess a large variety of material compositions [18]. As a few examples of single elemental and compound nanowires the following can be mentioned: II-VI nanowires: ZnTe, CdS, group IV nanowires: Si, Ge, and III-V nanowires: InAs, GaSb. The majority of the given examples are binaries; material constructed of two elements. However, two binary materials can be combined to form a ternary, which could in turn share some of the properties of both its constituting binaries, while demonstrating properties unique to itself. As an III-V example for ternaries one can mention $\text{InAs}_{1-x}\text{Sb}_x$. This material system can have a band gap smaller than both InAs and InSb at an Sb composition of $x = 0.63$ [19]. Thus, ternaries allow the possibility of precise modulation of physical and material properties such as band gap, through material composition.

III-V nanowires combine the unique geometrical properties of nanowires with the desirable material properties of III-V semiconductors. They open doors to understanding fundamental physics [3][20] including quantum phenomena (such as tunneling), realizing high-speed low-power transistors [21][22], and applying fundamental physics to device configurations; for example tunneling field effect transistors (TFETs) [23][24][25]. For various reasons they also prove to be suitable candidates for optical applications [26][27][28]; for instance, because of their geometry they can couple in light and act as good waveguides [29].

Of the III-V material systems, Sb-based materials offer the highest electron (InSb: $7.7 \times 10^4 \text{ cm}^2\text{V}^{-1}\text{s}^{-1}$) and hole (GaSb: $850 \text{ cm}^2\text{V}^{-1}\text{s}^{-1}$) mobilities. These are excellent electronic properties, leading to faster operating devices. Therefore, when coupled with the unique nanowire geometry, realizing binary and ternary antimonides can be beneficial for the future of electronic and optoelectronic industry [30][31][32][33]. Therefore, it is necessary to not only synthesize, but to also understand the fundamentals of their growth, leading to tailored Sb-based material grown as nanowires, which can then be characterized and optimized to desire. However, growing antimonide nanowires are associated with a number of challenges, such as the existence of a barrier when growing them directly from substrates, and in the wurtzite crystal structure. The mentioned challenges are required to be addressed before attempting to grow them fit for applications.

Crystal structure, known as the atomic ordering in crystals, plays an important role on the properties material exhibit. Therefore, it is important to gain control and modulate it as desired. III-V nanowires mainly grow in zinc blende or wurtzite

crystal structures. Discussions regarding this topic will be given in length further on in the thesis (chapter 2.2).

This thesis extensively studies the fundamentals of nucleation and growth of Sb-based material systems with an end goal of realizing complex structures and novel materials. Through Au-seeded nanowires grown by Metal-organic vapor phase epitaxy (MOVPE), step by step, existing challenges of Sb-based material synthesis are tackled, leading to a comprehensive understanding of the field. These understandings are then utilized in the direction of accessing Sb-based material in wurtzite crystal structure. A major fraction of this work develops and tailors suitable templates through crystal structure control and design.

As a starting point, the limitation imposed on Au-seeded nanowire growth, and the nucleation barrier of direct growth from substrates is addressed. Subsequently, by exploiting a combination of known material properties of antimonides, together with manipulation of surface energy along the length of single nanowires through crystal structure, complex core/shell heterostructures are achieved. From there, the thesis progresses towards understanding and overcoming the nucleation barrier of wurtzite antimonides. As wurtzite III-Sbs are novel material never existing before, realizing them allows systematic studies on their physical and material properties (such as band gap and surface energies respectively), and opens doors towards potential applications.

The content of the thesis discusses the epitaxy of III-V nanowires in chapter 2, providing fundamentals of nucleation and parameters affecting it in chapter 2.1, epitaxial growth mechanisms central to nanowire epitaxy; namely vapor-solid (VS) and vapor-liquid-solid (VLS), finally arriving on crystal structure, surface energies and template design in chapter 2.2. The experimental methodology utilized for synthesizing and characterizing the nanowires is explained in chapter 3. In chapter 4, an overview of results from III-Sb growth is provided, together with addressing the challenges of Au-seeded antimonide nanowire growth. In Chapter 5, the thesis arrives on concluding remarks regarding the covered work, together with an out scope of the possible continuation direction(s) of this research line.

2. Epitaxy of III-V nanowires

In brief, Epitaxy refers to crystalline growth where the *crystal orientation*; the atomic ordering of the constituting atoms in a crystal, of the underlying material is transferred to and maintained within the new growing crystal.

Epitaxy is governed by two main factors; Thermodynamics, which defines the related energies and driving forces of the growth processes, and kinetics, which determines at what rates these processes take place. For epitaxial growth to occur, an initial stage is required; namely nucleation. Nucleation in this context is referred to small clusters of particles from the initial phase- typically gaseous or liquid- forming nuclei in the final phase (solid in this work). Once stable nuclei form, epitaxial growth of crystalline structures will continue accordingly.

In this chapter the key aspects of nucleation thermodynamics, and kinetics of nucleation and growth will be covered classically. The vapor-solid growth mechanism, and material parameters such as surfactant effects that have a significant impact on nucleation will follow. From there, more specific discussions related to nanowire nucleation and main growth mechanisms of Au-seeded nanowires will be covered. More specifically, particle assisted nucleation, particle size impact, nucleation positioning, and particle contact angle will be elaborately discussed. In the final subchapter crystal structure will be introduced, and crystal structure engineering will be discussed.

2.1. Nucleation and growth

2.1.1. Thermodynamics of nucleation

In thermodynamics, depending on the constituting particles, systems can be single or multi-component (one or more different species that are independent from one another). Independent of the number of components, systems are homogeneous; consisting of a single phase, or heterogeneous; where separate phases within the system coexist. The thermodynamic state of a system is defined by the sum of the *chemical potentials* of all components in all phases. Chemical potential of a component can be defined as the partial derivative of Gibbs free energy; a

thermodynamic potential of the system, at given temperature and pressure as stated below:

$$\mu_i = (\partial G / \partial n_i)_{T,P} \quad 2.1$$

The total chemical potential of the system will then be:

$$\mu = G/n \quad 2.2$$

If a system is left undisturbed from surrounding influences (temperature, pressure, and exchange of material) it will move towards the lowest possible energy state called *equilibrium*. With regard to the minimum of Gibbs free energy, the system is said to be in thermodynamic equilibrium when the chemical potential (μ_i) of all components (N_c) are equal among each other in each of the N_P phases ($\sigma_j, j = 1, \dots, N_P$) of the system [34]:

$$\mu_i(\sigma_1) = \mu_i(\sigma_2) = \dots = \mu_i(\sigma_{N_P}) \quad i = 1, \dots, N_C \quad 2.3$$

In a single component system where a fraction of material undergo a phase transition from phase α to phase β , the equality above can be written as:

$$\mu_\alpha - \mu_\beta = 0 \quad 2.4$$

For growth to happen, a transition from an initial phase to a stable target phase must be induced. For this, a deviation from equilibrium is required such that the chemical potential of the target phase be smaller than that of the initial phase. This will lead to material passing the phase boundary from the initial phase towards the target phase in order to reach a new equilibrium. During crystal growth processes, a grower controls the difference in chemical potential through parameters such as temperature and pressure. The introduced difference of chemical potential of the system is usually referred to as *supersaturation*. Supersaturation can be written as the ratio between actual partial pressure and the equilibrium partial pressure when the difference in chemical potential is induced by changes in pressure at constant temperature, or the ratio between actual concentration and the concentration in equilibrium:

$$\Delta\mu \equiv \mu_\beta - \mu_\alpha = k_B T \ln(p_\alpha/p_\beta); \Delta\mu = k_B T \ln(C_\alpha/C_\beta) \quad 2.5$$

In phase transitions where the target phase is solid, $\Delta\mu$ is also regarded as the *growth affinity* or the *driving force for crystallization*. The larger supersaturation is, the further the rate of phase transition will be enhanced.

If the initial system is entirely in one phase (gaseous for instance), the phase transition to solid does not occur spontaneously when the equilibrium is shifted. Instead, the system initially remains in a metastable phase of supersaturation (vapor with partial pressure above the condensation point) before undergoing phase transition. The reason for the unlikely existence of the species in the form of the metastable phase is the energy cost for creating an interface between the old and new phases. The energy required for forming this interface may vary depending on the *surface energy* of each phase. The new phase is only formed when the supersaturation is sufficiently large.

Surface energy (γ) is defined as reversible work needed to form one unit area of surface (or interface) at equilibrium under constant conditions of the system. In a solid, surface energy can be regarded as half the melting heat per atom. This concept arises from the fact that at the surface of the solid only half of the atomic bonds are formed; therefore to melt the solid only half the bonds need to be broken. To simplify, the surface energy of any solid is proportional to its number of *dangling bonds*. Dangling bonds or *unsaturated bonds* refer to atomic bonds of the surface atoms that do not chemically bind the atom to others, but instead extend in the direction of the exterior of the solid bulk. Note that, in isotropic surfaces, the surface energy remains constant independent of the direction. However, this is not the case in crystalline solids; depending on the crystallographic direction on the surface, the surface energy will be different.

In general, two classes of nucleation exist, which will be briefly covered in the following subchapters. If the new phase spontaneously forms in a homogeneous initial phase, *Homogeneous* nucleation has occurred. Any inhomogeneity introduced into the metastable system such as substrate, or small particles, may reduce the required deviation from equilibrium, therefore facilitate nucleation. These cases are referred to as *Heterogeneous* nucleation, where by destructing the pre-existing interface some energy is released, leading to a total reduction of the energy barrier.

Homogeneous nucleation

Upon nucleation, an amount of energy is released through formation of the volume of the nuclei. If the size of a nucleus is too small, the released energy will not be large enough to overcome the energy barrier of surface (interface) formation, and consequently, nucleation will not proceed. Hence, the creation of a nucleus can be described through the change in Gibbs energy (ΔG_N). This quantity is composed of two contributions in unstrained nuclei: a) an amount of substance with volume V enters the new phase, releasing energy proportional to its volume (negative value), b) the energy cost of creating the interface between the metastable phase and the new phase, which is proportional to the surface area of the interface (S) (positive

value). Therefore, the change in Gibbs energy should be negative for nucleation to proceed. The change in Gibbs energy can be written as:

$$\Delta G_N = \Delta G_V + \Delta G_S \quad 2.6$$

Through a simplified case, in which the nucleus is assumed to be a sphere with radius r (for instance: liquid in a bulk of vapor (condensation), or solid in a bulk of liquid (freezing), or solid in a bulk of vapor (sublimation)) and unstrained, the components can be described as: $\Delta G_V = (\Delta g/v)(4/3)\pi r^3$, and $\Delta G_S = \gamma 4\pi r^2$. Where Δg is the molar change of Gibbs energy for transitioning to the new phase, and a negative value. From this:

$$\Delta G_N = 4\pi[\gamma r^2 + (\Delta g/v)r^3]/3 \quad 2.7$$

With increasing nucleus size, Gibbs energy initially increases as a result of unfavourable interface (r^2 dependence), until gradually favourable volume formation counterbalances the energy cost (r^3 dependence), and nucleation proceeds. This is depicted in the graph of figure 2.1. The maximum of the Gibbs energy gives the *critical nucleus size* required for stable nuclei to form:

$$r^* = -2v\gamma/\Delta g \quad 2.8$$

Where v is the molar volume in the new phase. The activation energy required to create a stable nucleus with this size will then be equal to:

$$\Delta G_{N\ Homo}^* = (16/3)\pi\gamma^3(v/\Delta g)^2 \quad 2.9$$

At the critical point, The chemical potential of the nucleus and the metastable ambient are equal, and Gibbs free energy decreases for both a decrease and increase in r ; if the nucleus size is smaller, it will not be stable and will decompose, if the size is bigger than the critical value the energy cost of adding material to the nucleus decreases and the nucleus can thus grow. Growth will no longer be limited by nucleation and, thermodynamically forming the new phase will be more favourable until a new equilibrium is reached. Moreover, the critical nucleus size is inversely proportional to supersaturation ($\Delta\mu \propto 1/r^*$); the higher the supersaturation is, the smaller the critical size will become. Kinetic parameters such as adatom diffusion may limit growth however, which will be covered further in the thesis.

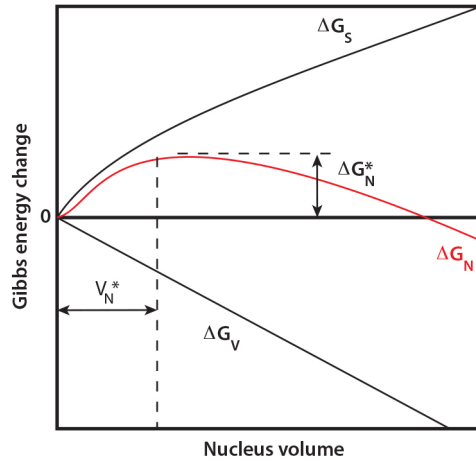


Figure 2.1. Change of Gibbs energy for creating a spherical nucleus of volume V_N^* in homogeneous nucleation. The volume (ΔG_V) and surface (ΔG_S) terms, and their sum (ΔG_N) is shown. At critical nucleus size (V_N^*), the nucleus will be stable and continue to grow.

Homogeneous nucleation induces spontaneous nucleus formation within the initial phase. In epitaxy it is desired to avoid such situations in order to have control over growth, so that instead of spontaneous phase transitions within the ambient phase, nucleation and growth will happen on the solid substrate, where desired. Epitaxial growth is therefore performed below the critical supersaturation necessary for homogeneous nucleation.

Heterogeneous nucleation

In epitaxy, nuclei form in the presence of a crystalline substrate. The pre-existing solid surface reduces the interface area with the metastable ambient phase. Therefore, the nucleation energy barrier is significantly smaller than homogeneous nucleation. However, a new interface will be created between the substrate and the nucleus, which must be taken into consideration.

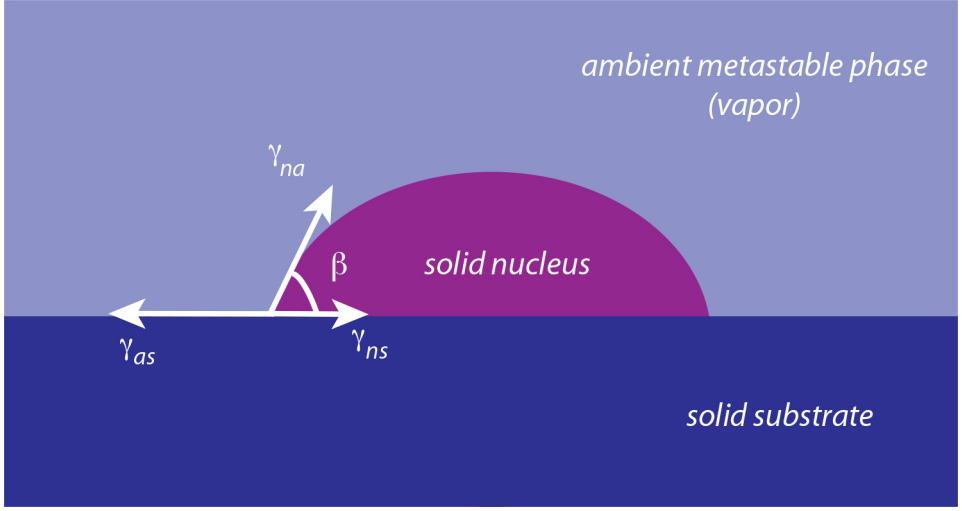


Figure 2.2. Schematic illustration of the surface energies in heterogeneous nucleation.

As schematically illustrated in figure 2.2, due to the existence of the substrate, the nucleus shape can be considered as a spherical cap with a wetting angle of β , instead of a full sphere. Depending on the affinity of the solid substrate and nucleus material, the wetting angle can vary between 0 and 180°. The interfacial energies are related to each other through *Young's equation* as:

$$\cos \beta = (\gamma_{as} - \gamma_{ns}) / \gamma_{an} \quad 2.10$$

These interfacial energies represent the amount of energy required to create a unit area of each of the interfaces. The volume of this spherical cap is related to the wetting angle through a geometrical shape factor defined as:

$$f = (2 - 3 \cos \beta + \cos^3 \beta) / 4 \quad 2.11$$

Upon heterogeneous nucleation a new ambient-nucleus interface is created, while at the same time the existing ambient-solid interface is converted into nucleus-solid interface. The nucleation energy will thus have two surface terms related to the nucleus-ambient metastable phase and nucleus-solid interface, and one volume term:

$$\Delta G_N = (\Delta G_S)_{na} + (\Delta G_S)_{ns} + f \times \Delta G_V^{Homo} \quad 2.12$$

From the expressions above (with $r^*_{Hetero} = r^*_{Homo}$) the critical heterogeneous nucleation barrier will be reduced with respect to the homogeneous nucleation barrier by the geometrical factor f :

$$\Delta G^*_{N\ Hetero} = (16/3)\pi\gamma_{na}^3(v/\Delta g)^2 \times f \quad 2.13$$

The reduction of the energy barrier can be clearly observed in figure 2.3 where the change in Gibbs free energy is compared between hetero and homogeneous nucleation.

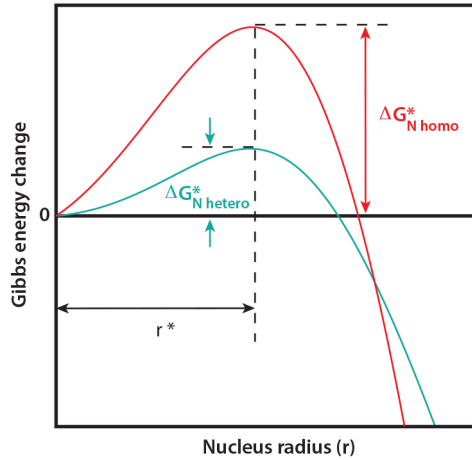


Figure 2.3. Change in Gibbs free energy when creating unstrained spherical nucleus in heterogeneous and homogeneous nucleation.

Depending of the wetting angle, heterogeneous nucleation can be 2 or 3 dimensional. If β is close to zero, then the nucleus is completely wetting the surface. In this case 2D nucleation occurs. In case $0 < \beta \leq \pi$, then incomplete wetting happens, and consequently nucleation will become 3D.

2.1.2. Kinetics of nucleation

As mentioned previously, crystal growth usually occurs away from equilibrium. Under these conditions growth is governed by a combination of thermodynamic and kinetic processes. At the nanometer regime, atomic-level control and effects such as adatom diffusion are more pronounced. Kinetics of epitaxial growth describes atomistic rate processes, which are strongly dependent on the location of an atom on the surface.

Due to unsaturated bonds, the atomistic structure of the surface is typically different from that of the bulk. This is more pronounced for semiconducting material, which unlike metals, have directional bonds. A simplified model for addressing atomistic processes in epitaxy was given by Kossel for the first time [35]. In this model, the adsorbed atoms known as *adatoms*, arriving from the vapor phase are viewed as cubic building blocks that can move around on the solid surface (*diffuse*) until they are either incorporated into growth, or desorbed back into vapor. Depending on the location of an adatom, it can have different number of first-neighbouring atoms (atoms with which bonds are shared). As a result, depending on the number of unsaturated bonds, they are bound differently to the surface.

From a Kossel crystal point of view, when considering rows of atoms in their *close-packed direction* (direction in which the atoms are most densely packed), a crystal surface may be *flat* (F), *stepped* (S) or *rough (kinked)* (K). The flat surfaces usually have the highest surface density of atoms (In a Kossel crystal, the {100} surfaces). Each atom on such a surface possesses one dangling bond. Growth on this surface usually requires a 2D heterogeneous nucleation. The step facet- being the {110} facets in the Kossel crystal- offers two dangling bonds per atom. The roughest surface in the low-index planes of a Kossel crystal is the kinked facet. This corresponds to the {111} planes, and each atom of this surface has three unsaturated atomic bonds. For growing on this facet, no nucleation is in fact needed and the arriving atoms may get directly incorporated at the kink sites without any energy barriers to overcome. Growth rate is simply expected to increase with increasing supersaturation on these surfaces.

As mentioned, adatoms arriving on the surface of the solid are adsorbed, and diffuse until one of the following occurs: desorption (re-evaporation into the vapor), nucleation on an atomically flat surface (either 2D or 3D nucleation), or incorporation at atomic kinks or steps. The average length that a specific adatom may diffuse on the surface before it gets incorporated in the crystal, or desorbs from the surface is referred to as the *diffusion length*. The diffusion length of the growth species on the substrate is a critical parameter when discussing the kinetics of crystal growth. For a given component, it is largely dependent on temperature, and surface structure as follows [36]:

$$\lambda = a(k_D/k_{des})^{1/2} \exp[(E_{des} - E_D)/2k_B T] \quad 2.14$$

Where a determines the distance between the adsorption and desorption sites, k_D and k_{des} are pre exponential factors for surface diffusion and desorption respectively, and E_D and E_{des} are the activation energies for diffusion and desorption respectively. k_B is the Boltzmann constant and T represents temperature. The energy barrier for desorption (E_{des}) is usually much larger than

the diffusion barrier (E_D), and also much larger than the thermal energy ($k_B T$) at typical growth temperatures, therefore the adatoms will migrate for quite a distance before they can re-evaporate ($\lambda \gg a$). In the high temperature range, referred to as the *desorption regime*, the diffusion length decreases exponentially with T . The residence time on the surface is short, and the adatoms are likely to re-evaporate before getting incorporated in growth. On the contrary, the residence time of the adatoms is long for the low temperature range, and adatoms are more likely to get incorporated. Best epitaxial growth however, is obtained at large diffusion lengths. Therefore, epitaxy is usually conducted right below the temperature range where significant desorption commences.

2.1.3. Growth modes in vapor-solid mechanism

In epitaxy, usually heterogeneous nucleation takes place from a supersaturated vapor phase to a solid crystalline phase. Therefore this growth mechanism is known as the *vapor-solid (VS)* mechanism.

The surface energies involved in heterogeneous nucleation have a significant role in the early layers of growth on a substrate with different material. Depending on this, growth can be categorized into different growth modes. In the following the four most relevant growth modes are briefly introduced. Note that, since the ambient phase is specifically vapor in VS growth, the notation “vapor” will replace “ambient” in the following discussions.

In thin film growth, depositing layers with smooth growth surfaces are usually desired. In terms of Young’s equation, this can be expressed through a wetting angle of 0. If the solid-vapor interfacial energy is $\gamma_{sv} \geq \gamma_{ns} + \gamma_{nv}$, a complete wetting of the substrate surface by the newly growing layer will take place. This condition occurs when the depositing adatoms are more attracted to the substrate surface than to themselves. Under these conditions growth proceeds in a layer-by-layer atomically flat fashion. This growth mode is referred to as the *Frank-Van der Merwe* growth mode. In this mode, nucleation usually proceeds by the formation of 2D nuclei.

If the adatoms have a large bond-strength (are more attracted to themselves than the substrate surface), then instead of flat surfaces 3D island formation occurs. This condition is fulfilled when γ_{sv} is small compared to γ_{nv} , leading to a wetting angle of approximately π in Young’s equation. This will result in the following relation between the surface energies involved in nucleation: $\gamma_{ns} \geq \gamma_{sv} + \gamma_{nv}$. Under this condition, the growing layer will not wet the substrate. In this growth mode known as the *Volmer-Weber* mode, the total energy of the system (nucleus and substrate) is minimum when a larger fraction of the substrate is left exposed to the metastable vapor phase. Here nucleation proceeds by forming 3D nuclei.

An intermediate situation may occur during epitaxy. In this case the first few atomic layers wet the substrate surface completely, and atomically flat growth happens similar to the Frank-Van der Merwe mode ($\gamma_{sv} \geq \gamma_{ns} + \gamma_{nv}$). Eventually, after reaching a critical thickness, as strain is accumulated in the epitaxial layer $\gamma'_{ns} \geq \gamma_{sv} + \gamma_{nv}$ applies. From this point onwards growth continues as 3D islands, with a thin wetting 2D layer underneath. This mode is known as the *Stranski-Krastanov* or *layer-plus-island* growth mode. Note that γ'_{ns} is the interfacial energy between the nucleus and the already grown monolayer(s) of the same material, and hence is not the same as γ_{ns} , where the solid surface is that of the initial substrate.

Another mode, that is of significant importance is known as the *Step-flow* growth mode. Step-flow growth can in fact be regarded as a special case of Frank-Van der Merwe growth. At a given supersaturation, when the solid-vapor surface energy is low, due to the higher nucleation barrier, nucleation happens less frequently. Under these conditions, adatom attachment to existing kinks and steps is more likely to occur instead of new nuclei formation. Therefore, the degree of supersaturation at the growth front is determined by kinetic factors such as adatom arrival and desorption rates, adatom diffusion, and adatom attachment to the existing steps. This type of growth is indeed observable in some epitaxial growths, such as the wurtzite shell growth of GaSb on InAs discussed in paper III of this thesis. In order to surpass this mode and move towards Frank-Van der Merwe layer growth, supersaturation of the vapor is required be sufficiently increased so that 2D layer growth can occur.

2.1.4. Surfactants

Surfactants (short for surface active agents) are generally referred to atoms or molecules that change the thermodynamic and/or kinetic properties of a surface upon adsorption. These species remain on the surface without being incorporated; hence affect the nucleation and overall growth mechanism.

Surfactants can change the direction of a thermodynamic process by changing (usually lowering) the surface (or interfacial) energy between the solid and the vapor (liquid) phase [37]. This will lead to a change in the wetting angle of the nucleus, a reduction of the critical supersaturation, and hence critical nucleus radius. The mentioned is observable in the schematic graph of figure 2.4.

From a kinetics point of view, surfactant species can affect the diffusivity of the arriving adatoms on the surface, which will consequently modify nucleation and growth. At relatively high temperatures, the diffusion length of the arriving species is longer than the distance between step and kink sites, leading to a step-flow growth mode (adatom attachment to kink sites more frequent than nucleation

events). On the contrary at low temperatures, as the diffusivity decreases, adatoms are more likely to encounter one another, before reaching kink sites, and so, will form new nuclei. At the presence of surfactant species the energetics of incorporation of the arriving adatoms at steps and kinks will be affected, meanwhile the adatoms need to exchange positions with the surfactant atoms in order to get incorporated in the crystal lattice [38]. In both cases the diffusion of the adatoms is affected. As the diffusivity is altered in the presence of surfactants, step flow or 2D nucleation can be favoured, possibly being in contrast with the nucleation and growth mode expected when surfactants are absent.

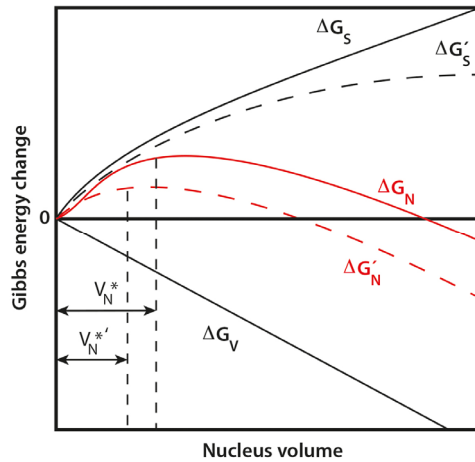


Figure 2.4. Effect of surfactant on lowering the critical nucleus size. The Gibbs energy in the presence of surfactants ($\Delta G'_S$) is smaller than ΔG_S , leading to a reduction of the total Gibbs energy ($\Delta G'_N < \Delta G_N$). This in turn causes the critical nucleus size to be smaller in the presence of surfactants ($V_N^{*'} < V_N^*$).

In the present context, surfactants are mainly referred to elemental adatoms that tend to be relatively heavy (large atomic number) having longer covalent bonds, hence tend to stay on the surface instead of getting incorporated within the crystal lattice during growth. As examples of elemental surfactants Sb ($Z = 51$) and Bi ($Z = 83$) could be named. There have been many reports in literature on thin layer growth where Sb (and/or Bi) changes 3D nucleation to 2D, enhances anisotropic growth in certain crystallographic direction, or even alters the atomic ordering of the layers [39][40][41].

2.1.5. Vapor-liquid-solid (VLS) growth mechanism

As an alternative growth mechanism to VS, an intermediate liquid particle can be introduced to facilitate nucleation from the supersaturated vapor phase to solid. In this case, nucleation and growth takes place under the liquid particle within a

confined area determined by the particle diameter via the extension of a 2D nucleus. This results in nucleation driven vertical growth of cylindrical columns with dimensions defined by the particle diameter, which, if small enough, are usually referred to as *nanowires*. Material will go through two phase transitions, hence two supersaturated phases will play roles in nucleation: Material from a supersaturated vapor phase will condense into the liquid particle with a lower supersaturation compared to vapor, and solid nuclei will form at the liquid-solid interface from the supersaturated liquid. For this reason this mechanism is mainly referred to as the *vapor-liquid-solid (VLS)* mechanism. In the following the key parameters for nucleation such as supersaturation, adatom diffusion, impact of particle size, position of nucleus formation, and contact angle will be covered.

Particle-assisted nucleation: thermodynamic and kinetic aspects

The particle chosen for VLS is usually a metal particle. In III-V nanowire growth, either a foreign metal such as Au, or the group III metal of the crystal components, such as In, for InAs is chosen. At temperatures above the eutectic temperature of the metal-material alloy (semiconducting material in the case of semiconductor nanowire growth), the alloy is liquid [41]. And since most liquid metals do not wet semiconducting surfaces, it agglomerates into liquid particles sitting on the substrate. The liquid particle wetting will be elaborated further in chapter 2.1.5, under the subheading: “particle contact angle”. But initially the thesis will discuss how/why introducing an intermediate liquid phase will facilitate nucleation and growth.

The liquid alloy becomes supersaturated by vapor influx to a concentration above the equilibrium concentration of that temperature. Crystallization occurs through this intermediate particle only if [42]:

1. The vapor-solid supersaturation ($\Delta\mu_{VS} = \mu_V - \mu_S$) is larger than the liquid-solid supersaturation ($\Delta\mu_{LS} = \mu_L - \mu_S$): $\Delta\mu_{VS} > \Delta\mu_{LS}$. Equivalently, the chemical potential of the vapor be larger than that of liquid ($\mu_V > \mu_L$). This is the necessary condition for positive vapor-liquid influx.
2. The liquid-solid supersaturation is positive: $\Delta\mu_{LS} > 0$. Or in other words, the chemical potential of liquid be larger than that of the solid ($\mu_L > \mu_S$). This condition is necessary for liquid-solid flux. The equilibrium concentration of the liquid particle at a given temperature can be regarded equal to the chemical potential of the solid.

The effective supersaturations of the vapor and liquid phase (Φ and ζ respectively) with regard to that of the solid can be defined as:

$$\Phi = \exp(\Delta\mu_{VS}/k_B T) - 1 ; \zeta = \exp(\Delta\mu_{LS}/k_B T) - 1$$

2.15

According to the conditions set above, growth via the VLS mechanism can only happen when:

$$\Phi > \zeta > 1$$

2.16

Interestingly, if solely supersaturation is considered, the existence of a liquid particle should not promote VLS over VS on the substrate since: $\Delta\mu_{VS} > \Delta\mu_{LS}$. However, it happens that the particle also reduces the critical nucleus size as a result of $\gamma_{LS} < \gamma_{VS}$. This statement can be explained as follows. Assuming that the nucleation rate follows an Arrhenius expression:

$$k_{nuc} = v_{nuc} e^{-\Delta G^*/k_B T}$$

2.17

Where v_{nuc} ; the Zeldovich factor [43] is the rate at which the adatoms attach to the nucleus. If v_{nuc} is assumed to be similar for nucleation at the substrate surface from vapor, and at the liquid-solid interface of the particle nanowire, then for VLS to be promoted: $\Delta G_{LS}^* < \Delta G_{VS}^*$. This can only be achieved through the difference in the interfacial energies of the two nuclei.

VLS is typically carried out at low nucleation and growth temperatures compared to VS growth (usually around 400-500 °C for III-V semiconductors). These temperatures are usually well below the evaporation temperature (at least one) of the growth species, therefore, supersaturation of the liquid particle does not solely happen via direct impingement from vapor. In addition, at these temperatures the adatoms possess long diffusion lengths, therefore they can diffuse on the substrate and on the nanowire sidewalls until they reach the liquid droplet. Consequently, for explaining VLS, the surface diffusion effects and diffusion-induced supersaturation of the liquid particle need to come into consideration. In VLS the metallic particle acts not only as a chemical catalyst (adsorption of adatoms from vapor, and enhancing precursor decomposition in CVD techniques), but also more importantly, as a collector for material, where it redirects adatom diffusion to the top of the growing nanowire. To have adatom diffusion (sidewall adatoms and/or substrate adatoms) to the top it is required that the liquid chemical potential be smaller than the chemical potential of the adatoms far from the top (μ_A). In other words for at least one of the two adatom types (sidewall or substrate) $\Delta\mu_{LS} < \Delta\mu_{AS}$, where $\Delta\mu_{AS} = \mu_A - \mu_S$. The effective adatom supersaturation is described as [42]:

$$\eta = \exp(\Delta\mu_{AS}/k_B T) - 1$$

2.18

Therefore the condition for attaining adatom diffusion to the top of the nanowire would be:

$$\eta > \zeta$$

2.19

Note that the supersaturation for the two different adatom systems may likely be different from one another. Moreover, the adatom supersaturation can be affected by desorption from the surface or incorporation into surface growth (VS). When adatoms have a lower chemical potential than the vapor, surface growth occurs. VLS growth happens under conditions where vapor and diffusion fluxes to the particle are positive:

$$\Phi > \eta > \zeta$$

2.20

Furthermore, VLS is usually conducted under *steady-state* conditions; meaning that the supersaturation of the liquid particle is treated as constant by a dynamic balance between two non-equilibrium processes: constant nucleation of 2D islands at the liquid-solid interface, and replenishment of supplies into the particle. Figure 2.5 schematically illustrates the key kinetic processes contributing to steady-state VLS growth [42].

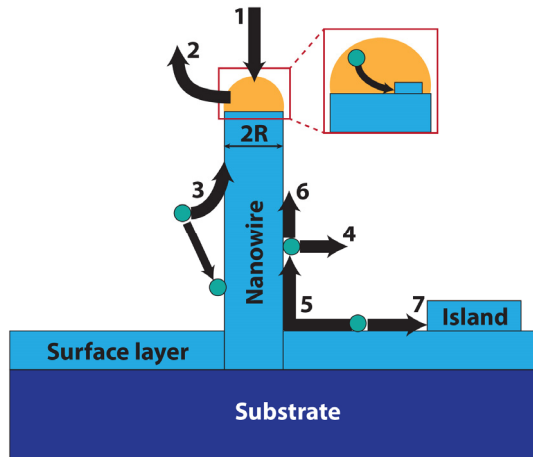


Figure 2.5. Main kinetic processes contributing to steady-state VLS growth.

The following paragraph summarizes all the possible scenarios in VLS with respect to figure 2.5:

Pathways 1 and 2 show material impingement and desorption directly to and from the particle respectively. At high temperatures, as the diffusion length of the adatoms decreases (desorption increases), the liquid particle acts solely as a chemical catalyst. Under these conditions VLS proceeds in an adsorption-induced

mode; vapor influx leads to particle supersaturation, which in turn leads to nucleation of 2D islands that extend laterally to cover the entire liquid-solid interface. However, typical VLS temperatures are well below this range where as explained above, adatom diffusion plays a significant role. Adatoms directly impinged to the sidewall (pathway 3) can diffuse toward the liquid particle. The diffusion process may be hindered by desorption or surface incorporation. In addition, with high enough surface diffusivity, adatoms impinged to the substrate may diffuse onto the sidewalls (pathway 5) and toward the liquid particle (pathway 6). However, these adatoms can get incorporated in surface growth on the substrate as shown in pathway 7, desorbed from the substrate or the sidewalls (pathway 4). The adatoms reaching the liquid particle will contribute to supersaturating the particle, enabling 2D nucleation and growth.

When the particle diameters are small, as in the case of nanowires, the dimensions of the growing crystals are small in comparison to the total area of the substrate. Thus, in order to be incorporated in nanowire growth, the substrate adatoms must diffuse a significant distance on the substrate surface to reach the growth site. Therefore in nanowire growth, a definition known as *collection area* is encountered, which depicts the circular area around the nanowire from which material can be collected and incorporated into growth. If the collection area of adjacent nanowires have an overlap, the average amount of material reaching each growth front will be reduced, and *competition for material* will happen [44].

Of the pathways adatoms follow, getting incorporated into surface growth on the sidewalls will lead to an increase of the nanowire diameter. This is usually referred to as *radial growth*, and depending on the composition of the sidewall and the later growing layer, can be accounted as a *shell layer*. This VS growth may happen through 2D and also 3D nucleation on the sidewalls (as discussed in chapters 2.1.2 and 2.1.3), extending to cover the sidewall surface of the nanowire entirely (or partially). Radial growth typically happens when the diffusion length is not long enough to reach the top, and adatoms meet each other before desorption [45]. It can also happen that, surface growth on the sidewalls proceeds via step-flow mode. In this case, the arrival of adatoms diffusing from the substrate, along with other kinetic phenomena locally determine the supersaturation on the sidewall, and layer growth happens bottom to top (in one direction) on the sidewalls, opposed to extension of 2D nucleation event(s) laterally on the sidewalls.

It is noteworthy to add that the surface energetics of the sidewalls is of utmost importance for shell growth as it affects the supersaturation and consequently nucleation free energy. This fact is exploited in the work of paper II, where selective shell growth along lengths of single nanowires is accomplished through alternative segments of wurtzite and zinc blende, which possess different surface energies. Following the same discussion, as mentioned in chapter 2.1.4,

introducing surfactants into the system will undoubtedly affect radial growth of the nanowires. It may lead to an enhancement of radial growth, or change the growth mode from 2D layer to island growth [46][47][48]. Further in the thesis, examples of such phenomena will be discussed in length.

Particle size impact

In the case of a liquid particle sitting on top and bound to a cylindrical rod with radius R , the chemical potential of the particle will be defined as [49]:

$$\Delta\mu \propto (2\gamma_{VL} \sin \beta / R) \quad 2.21$$

Where γ_{VL} is the droplet surface energy, and β is the contact angle. The effects of contact angle will be covered in more detail later in the thesis, under the heading “Particle contact angle”. From the relation above it can be understood that for small enough particle diameters, the chemical potential will be relatively low (as a result of high pressure within the particle). In other words, at given vapor pressures, smaller particles will have more adatom desorption through their surface, which will in turn hinder nanowire growth from particles smaller than a certain critical size. This is known as the *Gibbs-Thomson* effect.

Nucleation positioning

In general, VLS proceeds in a *mononuclear mode* in nanowires: a single 2D nucleation event occurs at the liquid-solid interface and laterally spreads over the entire interface very fast, creating one monolayer of crystalline material. In this mode, the waiting time between each nucleation event, during which the particle accumulates material, is longer than the time it takes for a nucleated island to spread across the interface. As a result, growth rate is limited by waiting time between consecutive nucleation events. Upon each nucleation event (followed by a monolayer growth), by instantaneously removing material from the particle, the particle volume changes, hence the surface area of the particle decreases by ΔS_L . Since in such small dimensions the metastable phase (liquid particle) cannot be assumed infinitely large, the Gibbs free energy of island formation ($\Delta G_{isl} = G_{V\ isl} + G_{S\ isl}$) must have a correctional term accounting for this change in liquid surface area [49]:

$$\Delta G = \Delta G_{isl} + \gamma_{LV} \Delta S_L \quad 2.22$$

This correction term is on the same order of the other surface terms within ΔG_{isl} , and therefore has a large impact on nucleation formation and cannot be omitted.

The surface term of the nucleation barrier will now be position dependent: The change in surface area will be different if nucleation happens at the center of the

liquid-solid interface; completely surrounded by liquid, or at the *triple phase line* (TPL); on the periphery of the liquid droplet, where some part of the nucleus will be exposed to vapor. The volume energy for the two cases though, will indeed be similar.

This position dependency of the nucleation free energy has a significant role on the final crystal structure of the nanowire; hence it will be revisited in chapter 2.2.3; wurtzite formation in nanowires.

Particle contact angle

In the following the discussion takes one step back in order to explore the importance of contact angle of the liquid particle with the substrate or nanowire top facet.

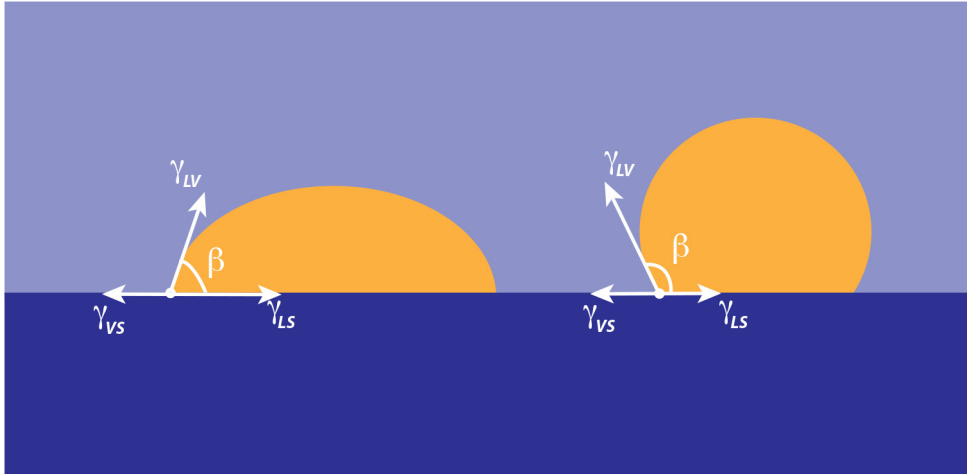


Figure 2.6. Schematic illustration of different scenarios of a liquid particle sitting on a solid substrate with different contact angles surrounded by vapor.

Assume a scenario shown in figure 2.6 where, a liquid particle with a given volume is sitting on top of a solid substrate within an ambient vapor. The surface term of the Gibbs energy of this three-phase system can be written as [49]:

$$G_S = \gamma_{LV} 2\pi R^2 / (1 + \cos \beta) + \gamma_{SL} \pi R^2 + \gamma_{SV} (S_0 - \pi R^2) \quad 2.23$$

Where R is the radius of the liquid-solid interface, and S_0 is the surface area of the solid. The system will go towards equilibrium by minimizing the surface energy. Hence, the system will reach minimum energy only if the contact angle satisfies Young's equation:

$$\gamma_{SV} = \gamma_{SL} + \gamma_{LV} \cos \beta \quad 2.24$$

For the liquid particle to agglomerate on the surface opposed to wetting it (revisit section 2.2.3); $\gamma_{SV} < \gamma_{SL} + \gamma_{LV}$. The following situations can then arise:

- 1) For $\gamma_{SV} > \gamma_{SL}$: the contact angle must be below $\pi/2$ to fulfil equation 2.24 ($\beta < \pi/2$)
- 2) For $\gamma_{SV} < \gamma_{SL}$: the contact angle should be above $\pi/2$ ($\beta > \pi/2$), where for the extreme case at $\beta = \pi$: $\gamma_{SV} = \gamma_{SL} - \gamma_{LV}$

From the above in order to have an agglomerated liquid particle sitting on the substrate surface, the surface energies must meet the following condition:

$$\gamma_{SV} \leq \gamma_{SL} + \gamma_{LV} \quad 2.25$$

If this condition is not met, the particle will wet the substrate surface (remember that in the current case the particle diameter is not constant as it is not pinned to any boundaries) and consequently, the required supersaturation-which is related to the surface/volume ratio- will not be met to avail 2D nucleation at the liquid-solid interface. Noteworthy is that, introducing species such as surfactants will drive the system away from the latter mentioned inequality; by changing γ_{SV} , γ_{LV} and γ_{SL} relative to each other, it will alter the contact angle, potentially causing the particle to wet the substrate. This is indeed an issue when intending to grow Au-seeded III-Sb nanowires directly from substrates. The presence of the surfactant Sb will cause the mentioned change in contact angle, and hinder nanowire growth. Therefore, surfactants not only affect the VS growth (of nanowires or surfaces alike), but also have a significant impact on growth in the VLS mode. One can of course, by changing other parameters of the system such as the liquid particle composition, or deposition of a monolayer on the substrate surface, counteract the surfactant footprint, causing de-wetting of the particle, and hence facilitating particle-assisted growth. In Paper I this challenge is addressed and tackled for a large compositional range in $\text{InAs}_{1-x}\text{Sb}_x$ nanowires. For higher Sb compositions, the particle composition changes dramatically from mainly Au, to mainly In, counteracting Au-particle wetting.

Now, assume another scenario where a liquid particle with volume V is sitting on top of a cylindrical rod with radius R . For the particle to stay pinned to the top facet periphery (not wetting the sidewall(s)) as shown in figure 2.7a, there must be a balance between both horizontal (F_h) and vertical forces (F_v) interacting at the TPL (unbalanced scenarios shown in figures 2.7 b and c respectively). The surface energies related to these forces will be of the following surfaces:

γ_{LS} : Liquid-solid top facet, γ_{VS} : Vapor-solid sidewall, γ_{SV} : Vapor-solid top facet, γ_{LV} : Liquid-vapor, γ'_{LS} : Liquid-solid sidewall

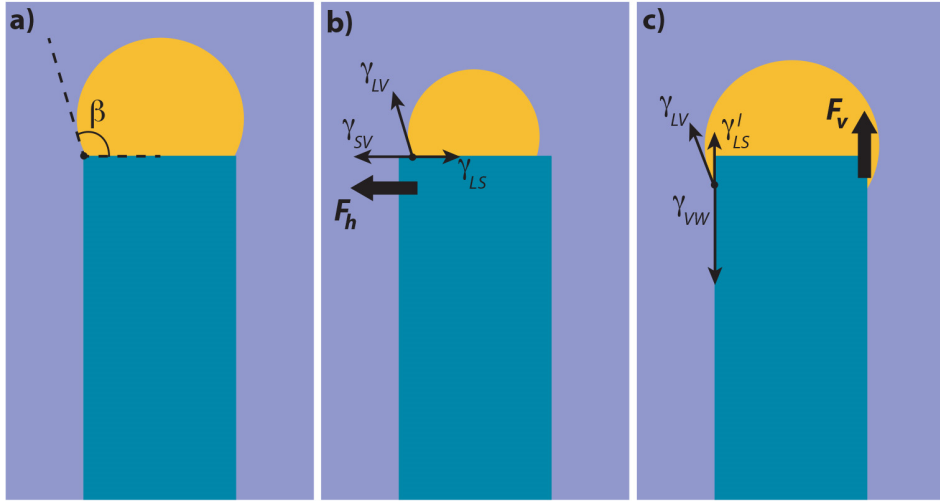


Figure 2.7. a) Liquid particle pinned to the top of cylindrical rod with contact angle $\beta > 90^\circ$. Unstable particle for axial nanowire growth under unbalanced b) horizontal, and c) vertical forces at the TPL.

This stability will guarantee vertical growth of the cylinder so long as the necessary growth conditions are maintained. In addition, based on the Nebo'sin-Shchetin criterion for stable nanowire growth, the contact angle of the particle positioned on the top facet should be larger than $\pi/2$ [50]. If by any chance the particle stability is meddled with (by altering the surface energetics or contact angle through changing the volume of the particle), the particle will no longer prefer the top facet and will either partially or completely wet one or more of the sidewalls. This matter will be revisited in chapter 4.2.2. Template assisted growth of III-Sbs; Side-by-side wurtzite InAs-GaSb nanowires.

All the discussions above are central to synthesizing nanowires from liquid particles. The work in this thesis is focused on III-V nanowire growth from Au seed particles on (111) B oriented substrates, therefore in the discussions above, the terms “liquid particles” will be replaced by Au particles (foreign-metal seeded), “solid substrate” with III-V (111) B substrates, and “cylindrical rods” with III-V nanowires. Noteworthy to mention that, the cylindrical geometry of the nanowire is merely an approximation, and in reality the nanowires are faceted, up taking a hexagonal geometry grown along the (111) direction.

2.2. Crystal structure

III-V nanowires predominantly grow in the cubic *zinc blende* or hexagonal *wurtzite* crystal structures. This is in contrast to their bulk form, where wurtzite is usually not a stable structure. In the following chapter these structures, along with basic crystallographic concepts central to key topics of this thesis will be introduced and discussed. Origins of wurtzite formation in the nanowire configuration will be explored, and methods used for controlling the crystal structure of a growing nanowire will be covered. Antimonides are an exception to this polytypism, as they do not grow in wurtzite. Since overcoming this deviation is the specific focus of this work, this topic will also be briefly addressed.

2.2.1. Crystal symmetry in III-V materials

When atoms of a solid are ordered in a periodic manner in all three dimensions, the solid is said to be a *crystal*. The smallest block of this periodicity from which the entire crystal lattice can be constructed is known as the *unit cell* of the crystal. The physical dimensions of the unit cell of a crystal are known as the *lattice parameters*. These parameters are an intrinsic property of the material, which depend on the atomic bond strength of the constituting atoms of the crystal. Therefore, materials composed of different atoms that share the same crystal structure will typically have different lattice parameters.

The simplest crystal lattices are the cubic lattices- shown in figures 2.8a-c, and they can be described as follows: *simple cubic structure*, where an atom sits at each of the eight corners of the cubic unit cell (figure 2.8a), the *body-centered cubic structure (BCC)*, which has an extra atom sitting in the center of the simple cubic, (figure 2.8b), and the *face-centered cubic structure (FCC)*, in which one atom is positioned in the center of each face of the simple cubic structure (figure 2.8c). If the unit cell is cubic, all three dimensions are of equal length, with an angle of 90° between them, meaning that they are represented by only one lattice parameter; a_0 . For other types of unit cells, more lattice constants are necessary to define the size of their unit cell. The vast majority of metallic elemental crystals are BCC or FCC, while the only elemental crystal believed to have a simple cubic structure is Po.

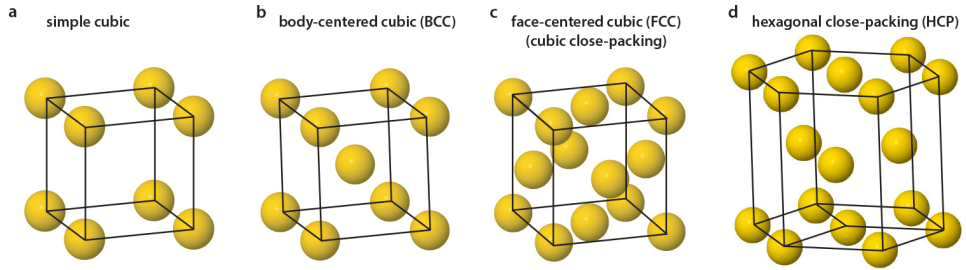


Figure 2.8. Cubic crystal structures demonstrated in: a) simple cubic, b) body-centered cubic, and c) face-centered cubic structures. d) Demonstrates the hexagonal close-packed (HCP) crystal structure. (3D atomic models created using Rhodius software tool [51]).

Crystal faceting

Any given crystal is terminated by a number of surfaces. As mentioned in the previous chapter, different surfaces demonstrate different energies depending on the number of dangling bonds they possess, and in general, surfaces are not energetically favourable over the bulk volume of a crystal. Otherwise, the solid crystal would undergo *sublimation* to reduce its bulk volume. Therefore, the system will move towards reducing its total energy by minimizing the total surface energy of the crystal. For this to happen, the surfaces with the highest energies will grow with the highest rate, leaving the lower energy surfaces larger in size. These lower energy surfaces are what will define the final shape of a crystal in equilibrium. As demonstrated in figure 2.9, based on *Wulff's construction theorem*, in equilibrium the following relation is established between the formed facets, and their surface energies [52][53]:

$$r_j/\gamma_j = \text{constant}$$

2.26

Where r_j is the vector drawn from the center of the crystal cross section, perpendicular to facet j , and γ_j is the corresponding surface energy of that facet. In figure 2.9a, the surface energies of all twelve facets are considered equal, hence their equal length. Now if facet b has a higher surface energy compared to a and c , based on Wulff's theorem r_b must increase proportionally.

Assuming that the surface energy of six alternating facets out of the total twelve of the crystal in figure 2.9 have a higher surface energy similar to facet b (figure 2.9b), then due to a smaller nucleation barrier, these facets will have a higher growth rate and grow smaller, while leaving the six other facets with lower surface energies with a larger length. If the difference in surface energies of these two facet types is high enough, in a given time, the “ b ” type facets will grow out, eventually leading to a six-faceted final shape of the crystal.

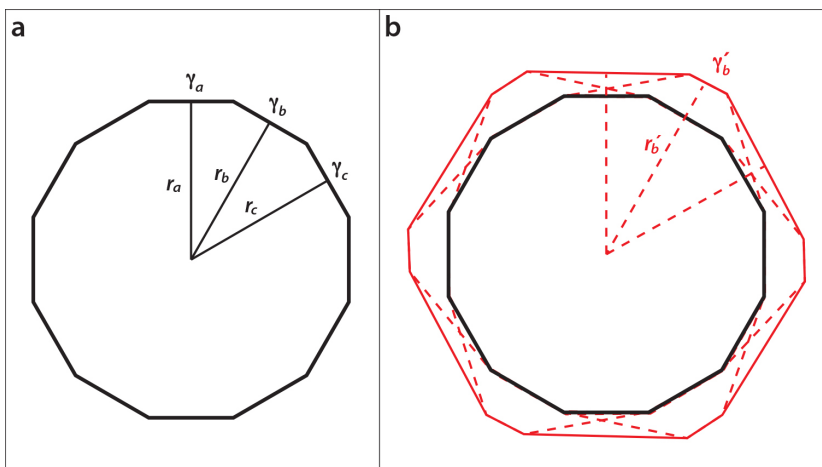


Figure 2.9. Shape of a crystal with twelve side facets that have a) equal surface energies, hence equal lengths in equilibrium. b) based on Wulff's construction theorem if facet b, and all other five alternative facets have a higher surface energy, they will grow at a higher rate, reducing their surface length, and therefore changing the equilibrium shape of the crystal.

It is worth the reminder that, in this work crystal growth happens away from equilibrium, and kinetic factors will also play a role in the final shape of the crystal. However, the discussions on crystal shape formation at equilibrium are still of relevance, as kinetics will promote faster growth of surfaces with higher energy, over surfaces with lower energy.

More over, in anisotropic growth, as it is the case with nanowires, the side facets defined by lower surface energy facets are not always the only facets that form. Usually *truncation* happens; some small, higher indexed facets also form to “close” the shape of the crystal. In order to connect the side facets to the facet in the anisotropic growth direction (top or bottom facet in nanowire growth), higher indexed facets, which can also close the crystal with minimum surface area, are created. These facets will be those with the lowest surface energies formable under the given growth conditions. In other words, those higher indexed facets, where the product of surface energy and surface area is minimized, will form to close the crystal shape.

Close-packing

Going back to the topic of crystal structure, for simplicity, in the following discussion, the atoms will be approximated by spherical balls. Imagine one-dimensional chains of atoms in which the atoms are in close-proximity similar to the schematic in figure 2.10a. If these 1D chains are positioned beside one another such that each atom of the second chain falls in the void created by two adjacent atoms of the first chain, *close-packed* 2D planes of atoms are formed. This is

shown in figure 2.10b. Each atom in this ordering, is surrounded by six other atoms; in a *hexagonal* fashion.

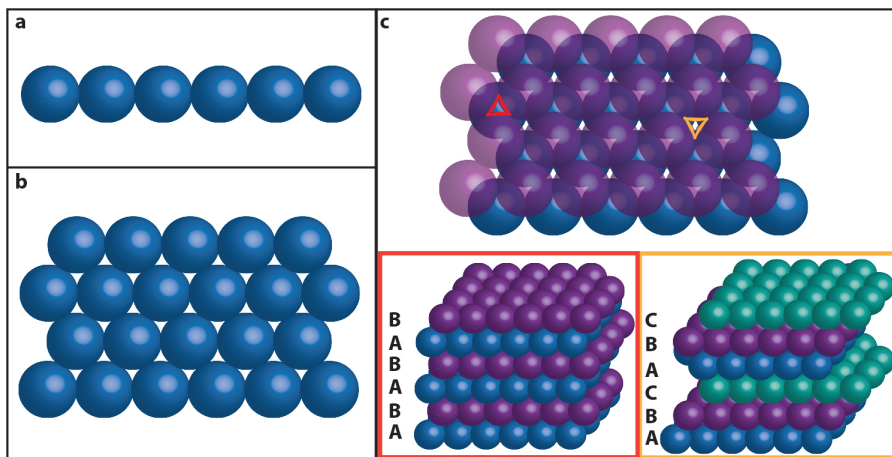


Figure 2.10. Schematic demonstration of crystal atoms in a) 1D b) 2D and c) 3D close packed configuration.

For constructing 3D close-packed structures, two 2D close-packed planes are positioned on top of one another such that each spherical atom of plane 2 falls into the valley created by three adjacent atoms of plane 1. Figure 2.10c schematically demonstrates this, where blue spheres represent the first, and purple spheres the second close-packed plane. Two types of voids are then created in the 3D structure, namely the *tetrahedral void*; shown with the red triangle in figure 2.10c, and the *octahedral void*; indicated with the yellow triangle. The tetrahedral voids fall exactly on top of atoms in plane 1, therefore if atoms of a third plane were to sit in these voids, they would be exactly aligned with the atoms of the first plane. In this situation, every third plane in the 3D close-packed structure would repeat itself, resulting in an *ABAB...* stacking sequence. The red inset in figure 2.10c demonstrates this stacking. This is called the *hexagonal close-packed (HCP)* structure. The HCP structure is schematically demonstrated in figure 2.8d. On the other hand, if the atoms of the third plane are stacked such that they fall into the octahedral voids, the position of these atoms will be completely unique. This new layer position will then be called “C”, and if the three layers repeat the same ordering as shown in the yellow inset of figure 2.10c, an *ABCABC...* stacking will be created, with every fourth layer repeating itself. The schematic represents the FCC crystal structure.

Common crystal structures in III-Vs

The two most common crystal structures in III-Vs are the *zinc blende (ZB)*, a cubic structure, and the *wurtzite (WZ)*; an HCP structure. The zinc blende structure

consists of two FCC unit cells interlaid with a translation of $a_0/4$ along the three axes with respect to one another. If the constructing atoms are all from the same material, such as Si, zinc blende represents a *diamond* structure. Compound materials such as III-Vs however, are constituted of two types of atoms. Therefore, the constructing atoms of each of the FCC structures are of a different elemental atom for compounds. For III-V material, one of the FCC sublattices consists of group III atoms while the other of group V. The unit cell of zinc blende III-V material therefore consists of an FCC unit, where all the atom sites are occupied by group III atoms, interlaid with four group V atoms, positioned such that they form symmetric tetrahedral bonds with the group III atoms.

Similarly in the wurtzite structure the group III and V atoms form an hcp sublattice. The unit cell is hexagonal, meaning that it is not symmetric in all three directions. It consists of a rhombus base, which is defined by three equal-length (a_0) vectors with 120° between them and a vertical axis with length c , defining the height of the unit cell. Figure 2.11 shows the unit cells of zinc blende and wurtzite schematically.

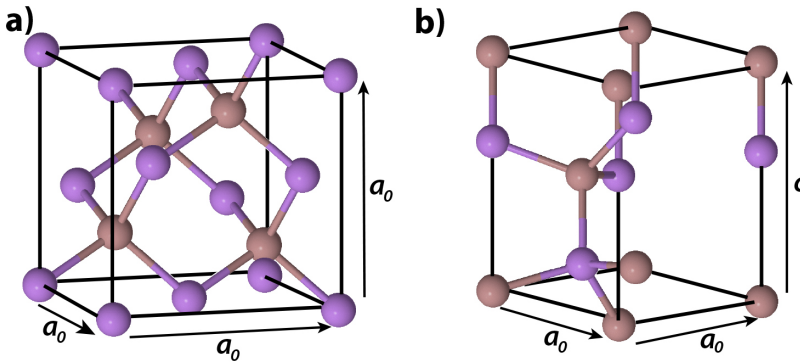


Figure 2.11. Schematic representations of a) zinc blende and b) wurtzite unit cells. (3D atomic models created using Rhodius software tool [51]).

In general, the directions and planes in crystals are defined through specific indices based on their unit cell geometry. For cubic cells, notations called *Miller indices* are usually used. If the unit cell axes are defined using three orthogonal vectors with equal lengths (a_1, a_2, a_3), (h, k, ℓ) will denote a plane that intercepts these axes at three points of: a_1/h , a_2/k , and a_3/ℓ . In better words, the Miller indices are defined as the inverses of the intercepts of said plane in the basis of the lattice axes. For instance a plane defined as (100), will not intersect the a_2 and a_3 axes (will intersect them at infinity), but will intersect and is orthogonal to a_1 . All planes equivalent to (hkl) due to the symmetry of the crystal lattice will be defined as the $\{hkl\}$ plane family. Direction $[hkl]$ is the direction of a vector connecting point hkl in the lattice to the origin of the real coordinate system, and all directions

equivalent to $[hkl]$ are noted as the $\langle hkl \rangle$ family. In cubic systems $[hkl]$ is the direction perpendicular to plane (hkl) . In the case where any of the intercepts are at negative values on the axes, then the negative sign is demonstrated with a *minus* sign or a *bar* in the Miller indices.

For a hexagonal lattice, the *Miller-Bravais* indices are used. These indices have four digits; the first three are related to the rhombus base of the unit cell, and the fourth digit is related to the c-axis of the unit cell. These indices are denoted as $(hkil)$, where $i=-(h+k)$. As an example plane (0001) is parallel to the base plane. In figure 2.12 the technologically most relevant planes of the zinc blende (figure 2.12a), and wurtzite (figure 2.12b) are demonstrated.

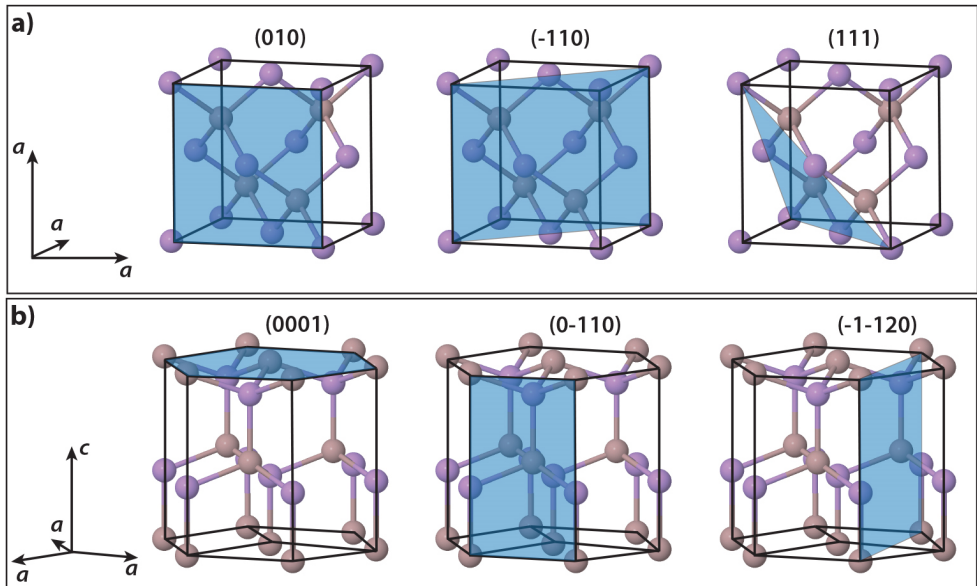


Figure 2.12. a) zincblende unit cell with (100), (110), and (111) planes, and b) wurtzite unit cell with (0001), (0-110), and (1-120) planes defined in blue. (3D atomic models created using Rhodius software tool [51]).

In compound materials such as III-V semiconductors, due to the two types of atoms, a concept known as *polarity* will occur. In III-V material, polarity can be defined as the internal electric field of the crystal caused by the asymmetry in the charge distribution of a III-V bond. The terminating atoms on a non-reconstructed surface define the surface polarity; depending on which type of atoms (or what ratio between the two types) is present on the surface, the planes are said to be *polar* (or *semi-polar*). If the numbers of the two atom types are equal on a given plane, then that surface is said to be *non-polar*. For instance, the $\{111\}$ planes of a zinc blende structure may be terminated by either group III or group V atoms. These types of surfaces are then denoted as: $\{111\}$ A or $\{111\}$ if group III

terminated, and $\{111\}$ B or $\{-1-1-1\}$ planes if group V terminated. Polarity will affect the properties of the planes, such as their surface energies [54][55].

In relation to previous discussions on surface energy, the crystals will grow faster in the directions with the highest surface energy, and the determining side facets of the crystals will be those with the lowest surface energies, along with possible facets that allow for a closed surface of the crystal.

Zinc blende and wurtzite structures are demonstrated in figure 2.13a and b, along the $\langle 110 \rangle$ and $\langle 11-20 \rangle$ directions respectively, where group III atoms are displayed with green, and group V atoms with pink spheres. Each stacking position (A for instance) represents a III-V atomic bond. The close-packed directions of zinc blende; $\langle 111 \rangle$, and wurtzite; $\langle 0001 \rangle$ are equivalent, and as observed, in this direction, the overall stacking of zinc blende and wurtzite is similar to FCC and HCP, with the only crystallographic difference between these two being the stacking sequence. If every one of the C planes in the zinc blende structure are rotated by 60° however, the ABAB... stacking sequence of wurtzite can be obtained. Noteworthy is that, the group III and V atoms form strong covalent bonds that are slightly ionic (depending on the electronegativity) with one another, which are arranged in a tetrahedron fashion for both crystal structures. The energetic difference between the two structures is related to the bond length of the third-nearest-neighbour, which is shorter for wurtzite compared to zinc blende. Ionic bonds lead to a contraction of the c-axis, hence favouring wurtzite, while covalent bonds lead to an elongation of the c-axis, stabilizing zinc blende structures [56]. Therefore, the higher the ionicity of a material, the more it is prone to wurtzite structures.

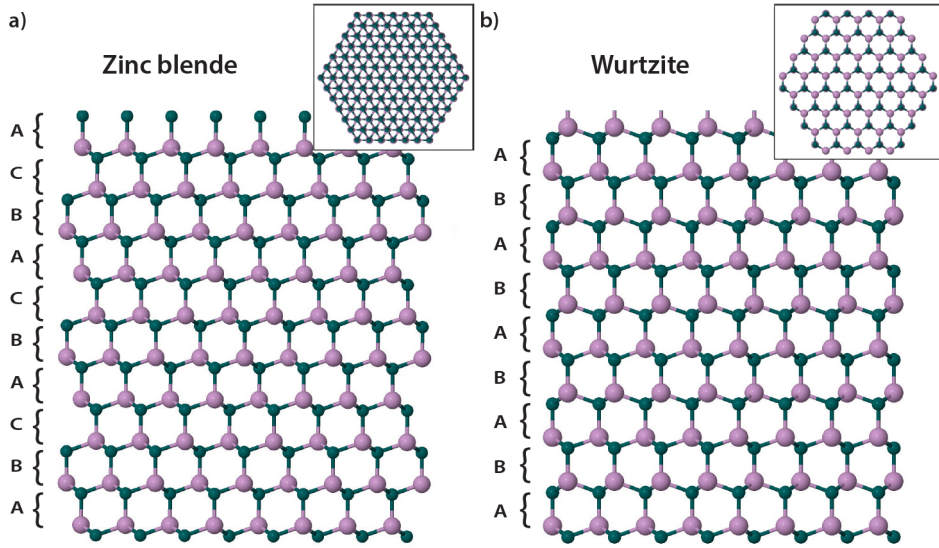


Figure 2.13. a) Zinc blende crystal structure viewed along the $\langle 110 \rangle$ direction. The inset image depicts the top view of the ZB crystal structure along the $[111]$ direction. b) Wurtzite crystal structure from the $\langle 11-20 \rangle$ direction. The inset in the figure depicts the top view of the WZ crystal structure along the $[0001]$ direction. (3D atomic models created using Rhodius software tool [51]).

In the bulk form, most III-Vs take up the zinc blende structure. Nitrides, which are very ionic, are an exception, as they form in the wurtzite structure. This dissimilarity is rooted in the difference of the bulk cohesive energies of wurtzite and zinc blende of these materials; $\psi = E_{WZ} - E_{ZB}$. Bulk cohesive energy is defined as the thermodynamic energy gain of bringing atoms together to form a crystal (wurtzite or zinc blende), and so is a negative value. Material with small ionic bonds such as Nitrides, where the difference in bulk cohesive energy is negative, tend to form wurtzite in bulk. Other III-Vs; namely phosphides, arsenides, and antimonides, have positive cohesive energy differences, and form zinc blende. The smaller the difference in bulk cohesive energies of a material, the more prone a material will be to stacking fluctuations [57].

In the nanowire configuration though, III-V material with bulk zinc blende crystal structure, can form wurtzite. This stems from an interplay between the volume and surface energies coupled with the position of nucleation of wurtzite and zinc blende nanowires, and liquid supersaturation. More explanation will be provided in chapter 2.2.3.

The following sub chapter describes surface energies of wurtzite and zinc blende nanowire side facets, which is essential for addressing the statement in the previous paragraph on how polytypism is coupled with nucleus position, and

supersaturation. Moreover, in paper II, this difference is exploited to selectively grow shell layers on side facets with higher surface energies.

2.2.2. Surface energies of zinc blende and wurtzite nanowire side facets

Nanowires growing along the cubic $\langle 111 \rangle$ /wurtzite $[0001]$ directions have hexagonal cross sections defined by six vertical (110) or (211) planes for zinc blende, and (11-20) or (1-100) planes for wurtzite nanowires. Zinc blende can also be defined by alternating (111) A/B micro-faceted sidewalls. Based on their orientation, nanowires with side facets belonging to the (110) and (11-20) families, and (211) and (1-100) families can be categorized type I and II respectively. These two types are oriented differently with 30° rotation along their close-packed axis. As mentioned previously, surface energy can be defined as the amount of energy spent on breaking the atomic bonds to create a crystal surface, and therefore can be calculated through the energy of dangling bonds of the formed surface. Calculations show that the surface energy of wurtzite sidewalls is lower than their zinc blende counterparts [58][59]. Typically zinc blende (211) side facets have a higher surface energy than (110), and wurtzite (11-20) side facets have a higher energy than their (1-100) counterparts [60]. From calculated surface energies of different material summarized in [60][61], in general the surface energy of zinc blende sidewalls are higher than their wurtzite counterparts. It can be concluded that:

$$\gamma_{WZ}^{(1-100)} < \gamma_{WZ}^{(11-20)} < \gamma_{ZB}^{(110)} < \gamma_{ZB}^{(211)} \quad 2.27$$

It is worth noting that, there is a spread of the surface energies between different calculations [61], and that the exact values are material-dependent to a large extent. In addition, the sequence can be different depending on the growth conditions. For instance the V/III ratio has an impact on the surface energies, and is not included in the calculations mentioned above.

2.2.3. Wurtzite formation in nanowires

The crystal structure of each monolayer is determined by the orientation positioning of its 2D nucleus with respect to the underlying layer. This positioning will determine whether the stacking of the last two underlying layers are of the wurtzite (ABAB) stacking or of that of zinc blende (ABCABC). The formation energy of a 2D nucleus at the solid-liquid interface with radius r , perimeter $c_1 r$, and surface area of $c_2 r^2$, and monolayer height h , can be written as [57]:

$$\Delta G = -[\Delta\mu_{LS} - \psi] c_2 r^2 h / V_{mn} + \gamma_{eff} c_1 r h \quad 2.28$$

Where $\Delta\mu_{LS}$ is the difference in the liquid-solid chemical potential, and V_{mn} is the mononuclear elemental volume.

The effective surface energy will depend on the nucleus position. For nanowires with vertical side facets it is determined as:

$$\gamma_{eff} = (\gamma_{WV} - \gamma_{LV} \sin \beta)x + \gamma'_{SL}(1 - x) \quad 2.29$$

Where x is the length of the nucleus exposed to the TPL. If the nucleus forms at the center of the solid-liquid interface, surrounded completely by liquid ($x=0$), then γ_{eff} will only be dependent of γ'_{SL} . This value is crystal phase independent, meaning: $\gamma'_{SL}(WZ) = \gamma'_{SL}(ZB)$. Since the difference in cohesive energy is 0 for zinc blende, and a positive value for wurtzite (ψ_{WZ}), then the formation energy will be a smaller negative value for wurtzite compared to zinc blende. As a result, nucleation will always prefer zinc blende if positioned in the center of the solid-liquid interface, due to a higher energy gain.

For polytypism to occur, according to the models the nucleus must be positioned at the TPL. By this it can gain energy through the lower surface energy of wurtzite side facets compared to zinc blende; $\gamma_{WV}(WZ) < \gamma_{WV}(ZB)$, lowering the nucleation barrier for wurtzite.

The critical nucleation barriers can thus be calculated for wurtzite and zinc blende as:

$$\Delta G_{ZB}^* = C[\gamma_{eff}^2(ZB)/\Delta\mu] \quad 2.30$$

$$\Delta G_{WZ}^* = C[\gamma_{eff}^2(WZ)/(\Delta\mu - \psi_{WZ})] \quad 2.31$$

Where C is a constant pre-factor including the nucleus dimension, and volume. The wurtzite structure will be favoured when $\Delta G_{WZ}^* < \Delta G_{ZB}^*$, while the zinc blende structure will dominate when $\Delta G_{WZ}^* > \Delta G_{ZB}^*$. The critical chemical potential corresponding to $\Delta G_{WZ}^* = \Delta G_{ZB}^*$ thus will be:

$$\Delta\mu_c = [\psi_{WZ}/(1 - (\gamma_{eff}(WZ)/\gamma_{eff}(ZB))^2)] \quad 2.32$$

Wurtzite will hence be kinetically preferred only when the difference in liquid-solid chemical potential is larger than the critical chemical potential defined above; $\Delta\mu > \Delta\mu_c$.

In summary for wurtzite to occur in nanowires two conditions must be met:

- a) Nucleation of wurtzite islands occurs at the TPL, where, due to the surface energy gain, the nucleation barrier will be smaller for wurtzite than zinc blende ($\gamma_{eff}(WZ) < \gamma_{eff}(ZB)$). This difference in surface energy is of course material-dependent.
- b) The liquid supersaturation is large enough to compensate the bulk energy difference; ψ_{WZ} . The liquid supersaturation may be affected by kinetic parameters such as adatom arrival to the particle. Therefore, through growth parameters such as temperature, and V/III ratio, the kinetics of adatom arrival can be influenced in such a manner that could promote wurtzite or zinc blende growth. Kinetic control of the nanowire polytypism through V/III ratio is utilized quite frequently in the work of this thesis (papers II, III, and IV), therefore will be briefly covered in chapter 2.2.4.

Interesting is that, controlling the mentioned growth parameters in condition (b), not only affects the liquid supersaturation through adatom arrival, but also has an impact on the presence and amount of a certain adatom in the vapor. This could in turn influence the surface energies [62][63], which then ultimately will have an impact on condition (a).

Both these conditions are indeed affected by the presence of species such as surfactants. By altering the surface energy of the sidewalls, surfactants may hinder wurtzite formation. In addition, surfactant adatoms sitting on the sidewalls will affect the adatom diffusivity, hence changing the adatom arrival to the liquid particle through diffusion. If the adatom arrival is reduced, it will in turn lead to a lower supersaturation of the liquid particle, making wurtzite growth challenging.

2.2.4. Crystal structure engineering

In recent years, many efforts have been made to kinetically control the polytypism in III-V nanowires. Studies reporting crystal structure control through growth temperature, controlling the total precursor flow, the V/III ratio, and nanowire diameter all demonstrate successful results [64][65][66][67][68][69][62][70][63]. Generally in these cases, the adatom arrival to the liquid particle is meddled with, changing the supersaturation of the liquid particle and the interfacial energies. For instance, adatom diffusivity is drastically lowered at low temperatures, hence zinc blende growth can be expected. In contrast, at higher temperatures, wurtzite will be favoured. It is necessary to note that temperature also affects precursor decomposition in MOVPE, which will contribute to the amount of available adatoms. Additionally, temperature can directly effect nucleation [71]. Controlling polytypism through nanowire diameter can be explained through material supply

to the particle. For low areal density of particles, the particles with smaller diameters will have a faster arrival rate of material compared to larger diameters, since their collection area on the substrate is identical.

Polytypism control is achieved through V/III ratio in this work. At a constant temperature for both crystal types, zinc blende is grown at high V/III ratios, while for achieving wurtzite, a much lower (two orders of magnitude) V/III ratio is utilized. It is noteworthy to mention that, the change in V/III ratio is mainly obtained through changing the group V precursor flow. At high V/III ratios, less group III adatoms will reach the liquid particle, thus the liquid supersaturation will be lowered leading to the suppression of wurtzite growth. This reduction in the adatom arrival rate results from a higher radial growth rate in the presence of more group V adatoms; as a larger fraction of the existing group III adatoms on the side facets will get incorporated in radial growth, again reducing the adatom arrival to the particle.

Being able to control the crystal structure will facilitate growth of nanowires with minimal number of stacking defects along their axial length. In addition, the ability to control polytypism with high precision, allows engineering the crystal structure along the length of single nanowires, alternating between segments of wurtzite and zinc blende, with abrupt interfaces, and segment lengths down to a few nanometer. In paper II, the InAs template core is obtained through this method.

3. Experimental Methods

This chapter briefly describes the methods used for synthesizing, and also characterizing the nanowires studied in the work of this thesis.

3.1. MOVPE

Epitaxy can be realized by different methods such as Molecular beam epitaxy (MBE), Chemical beam epitaxy (CBE), and Metal organic vapor phase epitaxy (MOVPE). The epitaxial growth of the nanowires in this work has been carried out by MOVPE. Because of the high throughput and high working pressure it offers in comparison to the other methods, MOVPE is more desirable in industry [72]. In this method, the sources (mainly group III) are metal organic compounds of the elements of interest. The group V elements are usually supplied as hydride gases, which despite being ideal sources for MOVPE, as they do not contaminate the growing material, they are highly toxic. Sb is an exception from this, and will be discussed in more detail in section 4.1. Suitable hydride sources of this element are not available. Instead, metalorganic compounds of Sb are used for Sb-based material synthesis. The metal organic sources are usually in their liquid form with TMIn being an exception as it is supplied as a powdered solid source. In contrast to the other epitaxy methods mentioned above, MOVPE is a non-vacuum technique, where the source material are introduced into the reactor in their vapor phase. At elevated temperatures, these chemical compounds are physisorbed on the surface and decompose. It is worth noting that partial or complete pyrolysis can also occur in the gas phase. In general, as illustrated in the schematic image in figure 3.1, MOVPE has three main parts; the supply, the reactor, and the exhaust, which will all be briefly covered in the following.

The metal organic sources are kept in a container so called as the *bubbler* at a constant temperature that has been pre-set according to the requirements of a process. The bubbler has an *inlet* and *outlet*, from which a highly purified carrier gas; commonly H_2 , is *pushed* through the inlet into the source. The H_2 then *bubbles* in the material, gets saturated with it, and the mixture flows out from the outlet into the pipelines that connect the sources to the rest of the system. There

are generally two pipelines; the *vent* and *run* lines, connected to the outlet of the bubbler. The run line directs the vapor directly into the reactor, where growth takes place, while the vent line bypasses the reactor, directly transferring the precursors to the exhaust. This two-line configuration is for facilitating stable supply of material when commencing growth or switching precursors. The gas flow rates are controlled by *Mass Flow Controllers (MFCs)*. In contrast to the metalorganic sources, the hydride sources are provided in highly pressurized gas cylinders and so are in no need of bubblers.

The main body of an MOVPE system is the reactor where epitaxy takes place at elevated temperatures. The susceptor, where the samples are placed, is locally heated to reduce undesired growth of material on other parts as much as possible (cold wall reactor configuration). Nonetheless, parasitic growth occurs and cleaning is required when switching material systems in order to avoid cross-contamination. The susceptor is made of SiN covered graphite for these MOVPE systems, which is compatible with temperatures required for growing III-V semiconductors.

The precursor flows are introduced into the reactor, chemical pyrolysis of the precursors takes place within the reactor and the metal organic sources decompose (as do the hydrides), liberating the pure elemental atoms. Epitaxial growth ensues as the group III and V atoms form chemical bonds on the substrate. The byproducts of the pyrolysis of the precursors along with unconsumed material are purged out of the reactor through the exhaust.

A pump located in the exhaust, which is controlled by a valve, attains the rather low pressure of the system. The toxic material are either burnt, or neutralized within the exhaust segment in a component referred to as the *scrubber* of the MOVPE system before exiting.

The nanowires studied in this thesis have been grown using two slightly different MOVPE systems, both from Aixtron. In the following two paragraphs the main aspects and differences of these systems are summarized.

Aixtron (200/4) is a horizontal, cold wall, and low-pressure (100 mbar) MOVPE system, in which the gas is guided horizontally through a *liner* made of quartz glass. The total flow of the carrier gas, H_2 , is set at 13 l/min within the reactor as a standard value in the growth recipes. Susceptor heating is attained via infrared lamps up to a maximum temperature of 750 °C. The liner is easily retractable so that changing and cleaning it is facilitated. The susceptor is designed to accommodate three 2", or one 4" wafers at a time. Rotation of the susceptor is beneficial in this system, as it may further assist the homogeneity of the precursor supply to the substrate.

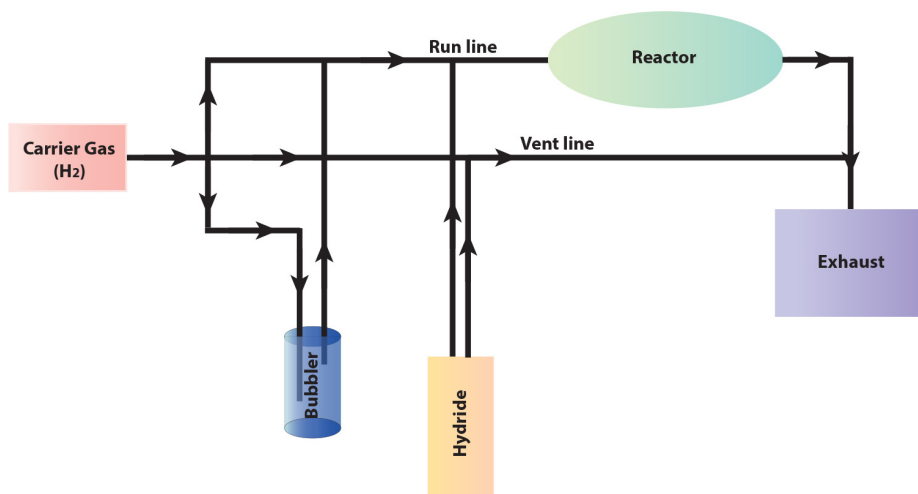


Figure 3.1. Schematic of an MOVPE system where the gas flow directions are depicted by the arrowheads. The carrier gas (H_2) transports the metal organic source materials from their bubblers to the reactor. MOVPE takes place inside the reactor, and the unwanted material is transported to the exhaust.

A 3x2" close-couple showerhead reactor (CCS) from Aixtron was also used with H_2 as the carrier gas with a total flow of 8 l/min as the standard value and a pressure of 100 mbar. As the name suggests, in this reactor the gas flow is from above the susceptor through a holey *quartz shield*, which resembles a showerhead. The quartz-shield can be easily removed and cleaned when necessary. With this reactor design, a more homogeneous precursor supply is guaranteed. A graphite coil resistively heats the susceptor, offering temperatures up to a maximum of 800 °C.

3.2. Electron Microscopy

Electron microscopy is referred to microscopy techniques that utilize a beam of electrons for illuminating the specimen. According to the Rayleigh criterion stated below, the maximum attainable resolution of the microscope is determined by the wavelength of its illumination source

$$\delta = \frac{0.61\lambda}{\mu \sin \beta}$$

3.1

Where, δ is the smallest distance that can be resolved, λ is the wavelength of the illumination source, μ the refraction index of the medium, and β the collection

angle. For the best optical microscopes the denominator of the equation above is approximated to 1, therefore the resolution is roughly half the wavelength. However, in reality the maximum resolution is not feasible, as the resolution of a microscope heavily relies and is limited by technical factors such as source stability, lens aberration, and so on.

In contrast to visible light where the highest attained resolution is about 300 nm, if the illumination source is changed to electrons the resolution can improve drastically since electrons have much smaller wavelengths than visible photons. The wavelength of an electron beam, determined by the de Broglie equation, is dependent on the energy of the electrons (E):

$$\lambda \sim 1.22/\sqrt{E}$$

3.2

Therefore, the resolution of the microscope can be tuned by controlling the energy of the incident electron beam.

Since electrons have mass and are charged, a number of interactions take place when they collide with material (figure 3.2). A fraction of the incident electrons undergo *inelastic* scattering, losing part or their entire energy. Another fraction undergo *elastic* scattering, preserving their entire energy. Therefore, in contrast to visible light where the collected signal is only the reflected (and at times the transmitted depending on the setup) beam from the sample, in electron microscopy various signals may be obtained which all can be used for gaining different information from the sample.

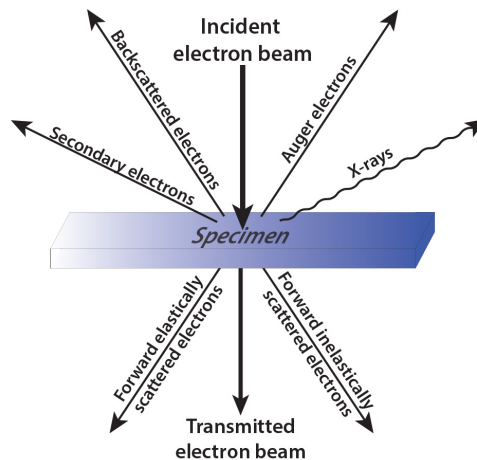


Figure 3.2. The interaction of an incident high-energy electron beam with a specimen results various electron signals (demonstrated with straight arrows), and the characteristic X-ray photon signal (wavy arrow). Note that there are other photon signals such as visible light, bremsstrahlung X-rays etc. that are not depicted here since they are out of the scope of this thesis.

Of these signals, the non-transmitted signals, which are usually collected above the surface of the specimen, e.g. *backscattered electrons (BSE)* and *secondary electrons (SE)*, are used in *Scanning electron microscopy (SEM)*, while the transmitted electrons are used for *Transmission electron microscopy (TEM)*. The mentioned microscopy techniques are briefly introduced in sections 3.2.1 and 3.2.2 respectively.

3.2.1. Scanning Electron Microscopy

The initial and therefore essential characterization method used after every growth run in the work presented here is Scanning Electron Microscopy (SEM). It is a technique where a focused beam of electrons is raster scanned over the sample. Typical energies utilized for the beam are usually a few tens of keV (commonly 5-30 keV). Since the samples investigated by SEM are *thick* (more than approximately 100 nm for most semiconductors), the beam does not traverse through the specimen (no transmitted signal). This means that all the electrons will interact either elastically or inelastically with the atoms of the sample numerous times before finally losing all their energy or backscattering out of the specimen.

If the electrons interact with the atoms of the specimen in an inelastic way losing some of their energy to the electrons of the atoms within, a number of the valence electrons of the specimen will get enough kinetic energy to escape into the vacuum. These are called *Secondary electrons (SE)*. Since these electrons usually don't possess energies exceeding 50 eV, only electrons close to the surface (5-10 nm) manage to escape the bulk while the SEs generated deeper within the specimen get reabsorbed. Since the interaction volume is small, SEs provide high spatial resolution. Therefore, topological information of the specimen surface is attainable.

When the electrons undergo elastic scattering events, i.e. the electrons encounter coulomb scattering as they are deflected by the positively charged nuclei of the atoms, they can escape the bulk of the material without any energy loss. The electrons that have basically “bounced back” from inside the specimen are called *Back Scattered Electrons (BSE)*. Since these electrons have high energies (similar to the electron beam energy), they usually emerge from a further depth in comparison to SEs. Therefore, they provide a lower spatial resolution. However since the number of BSEs heavily depends on the atomic number of the atoms (Z) they give a strong Z -contrast, in a manner that heavier elements deflect the electrons stronger hence appear brighter.

Different detectors with relevant designs and positioning are available for detecting each of these signals. In this work, SE electrons are detected to mainly gain topological information such as nanowire morphology, and faceting from the

samples. A LEO 1560, Hitachi SU1080, and a JEOL JSM-6700F have been used for this purpose. It is worth noting that the latter has been mainly used for acquiring compositional information by utilizing an installed X-ray Energy Dispersive Spectroscopy (XEDS) detector. XEDS is covered in more detail in section 3.3.

3.2.2. Transmission Electron Microscopy

If the energy of the electron beam is high enough (typically on the orders of a few hundreds of keV) and the samples prepared are thin enough (around maximum 100 nm for most semiconductors), part of the incident beam can “pass through” the sample. Since the energy of the electrons is very high, a large fraction of these transmitted electrons directly transmit through the specimen without undergoing any interaction. Meanwhile, a smaller fraction undergoes elastic and some inelastic interactions along their trajectory through the sample. Detection of these signals is achieved by a characterization technique named Transmission Electron Microscopy (TEM).

The elastically scattered electrons from the lattice planes of crystalline samples can give information on the crystal structure of the sample; i.e. the positioning of the atoms within the crystal [73].

In this work The TEM was operated in the High Resolution mode (HRTEM) to gain information about the atomic positioning of the crystal planes, hence information on the crystal structure, and possible crystal defects.

A JEOL 300F has been used to obtain crystal information in this work. Nanowires were transferred to lacey-carbon copper TEM grids by mechanically rubbing the grid on the growth substrate.

3.2.3. X-ray Energy Dispersive Spectroscopy

Of the signals generated by illuminating a specimen with an electron beam, characteristic X-rays are one of the most useful signals. These X-rays are produced as a result of inelastic interaction of the incoming electrons with the specimen atoms. When the incoming electron has enough energy and *knocks out* an electron from the inner shell of the specimen atom, it *excites* the atom. This excited atom goes back to the ground state by allowing an outer shell electron to fill the empty state in the inner shell. In this process, one of the possible paths through which the outer shell electron releases its extra energy is emitting an X-ray photon with the same energy. The electron configuration of each element is specific to itself. As a consequence, since the energy of the emitted X-ray corresponds precisely to the

difference between the electron energy levels, the X-ray is an elemental fingerprint of the emitting atom. Therefore, by detecting these X-rays compositional information of the specimen can be acquired. Each element has a set of *family peaks*, depending on through which outer shell electron the atom relaxes. There are families of K, L, and M peaks; i.e. electrons filling in the K electron layer, the L layer, and M layer respectively. In figure 3.3 a simplified schematic of the electronic structure of an atom and the corresponding X-ray families are given.

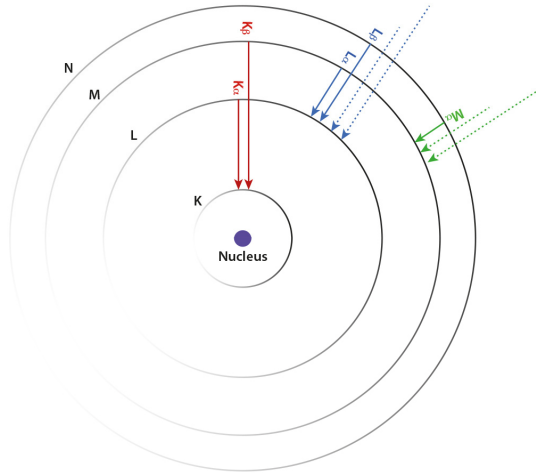


Figure 3.3. Schematic illustration of the electron configuration of an atom with the K, L, and M electron shells circling the nucleus. The main electron transitions related to the K, L, and M families are also demonstrated.

X-ray energy dispersive spectroscopy (XEDS, also known as EDS or EDX) is referred to a method where the characteristic X-ray energies emitted from the ionized atoms of the material under investigation is plotted versus the number of counts. The Energy of the useful characteristic X-rays are typically above 1 keV, and, the information is presented as intensity spectra. These X-rays interact with the detector, generating a number of electron-hole pairs depending on the energy of the incoming X-ray. The XEDS detector, which is a reversed biased p-i-n diode, separates the electrons and holes, creating a charge pulse that is amplified and measured. Unlike what seems like a continuous process due to the high speed, it is actually serial processing of single X-rays one at a time. Therefore, the XEDS not only detects the X-rays, but also separates them according to their energy (hence the name dispersive spectroscopy). The composition of the specimen can be defined by determining the concentration of each of the consisting elements in comparison to one another. The concentration of each element is related to the observed intensity of the characteristic X-ray [73].

XEDS detectors can be installed on both SEMs and TEM/Scanning Transmission Electron Microscope (STEMs). The interaction volume of the electron beam and the specimen depends on the beam diameter and the beam spreading, which in turn depend on the beam energy and the sample thickness. A small probe size is chosen when scanning the electron beam over the specimen to facilitate attaining spatially resolved elemental information. One can choose a single point or area and have counts versus energy. By doing this, “point and ID” analysis is acquired. Or, in contrast, one can choose a single energy and scan the entire area. This gives counts of that specific energy versus positions that are known as compositional maps. They can be line scans; i.e. 1D elemental maps, or area maps, where the position is in 2D.

4. III-Sb nanowire growth

4.1. A general overview on III-Sb material

Among all III-V materials, III-Sbs offer some of the most interesting properties desired for optoelectrical and electronic device applications. For instance among III-Vs, the narrowest room temperature band gap [74], smallest charge carrier effective masses, hence highest carrier mobilities are presented by this material family. To mention a few examples, due to the very small band gap $\text{InAs}_{0.37}\text{Sb}_{0.63}$ has, it is suggested as a suitable replacement for the conventional HgCdTe low wavelength infrared detector [33], which has a low thermal conductivity, is soft, and harmful for the environment. InAsSb is harder, has a higher thermal conductivity, and is slightly less harmful [75]. The InAs-GaSb heterostructure material system is also of interest due to the broken band alignment it demonstrates[76]. The broken band alignment is suitable for various device applications such as tunnelling devices [24][77]. Both these material systems will be investigated more in detail within this work. When it comes to electronic applications, InSb demonstrates the highest room temperature electron mobility among III-V material; $77000 \text{ cm}^2/\text{Vs}$, whereas GaSb has a considerably high room temperature carrier mobility of $1000 \text{ cm}^2/\text{Vs}$. Hence these materials are suitable for n- and p- type devices respectively [75][78][79][80][81].

Also, due to the very small effective masses of these material systems, and in particular InSb and $\text{InAs}_{0.37}\text{Sb}_{0.63}$ ($m_e=0.015m_0$ and $0.010m_0$ respectively), quantum confinement can be achieved at rather large dimensions; dimensions that are readily available at nanowire diameters, making nanowires of these materials interesting candidates for quantum studies [82].

However, growing III-Sb materials is more challenging when compared to other III-Vs. To name a few of these challenges one can mention the difficulty in obtaining high purity (less unintentional C incorporation or other impurities) or compositional homogeneity in the grown material. The impurity incorporation can be related to the lack of suitable hydride Sb precursors for MOVPE. As it was covered in more detail in section 3.1, typically in MOVPE the group V elements are supplied as hydride sources, such as AsH_3 , while the group III elements are supplied as metal organic compounds (the related group III metal accompanied by

alkyl ligands). When adsorbed on the growth surface, the hydrides release H atoms, which react with the alkyl ligand creating the related alkane (usually methane or ethane), which is purged away. Hence, the C atom in the alkyl group is not incorporated into the growing crystal. Since SbH_3 is very unstable, and storing or transporting it is unreliable, in MOVPE Sb is supplied as a metal organic compound. This in turn gives rise to more impurity incorporation [83].

Apart from that, antimonide-based material growth is challenging on a more fundamental level. Irregular growth on the surface may occur due to the very low vapor pressure of Sb causing it to stick to the surface [84]. Since Sb is a surfactant, it tends to stay on top of the surface of the growing material, getting less incorporated into the crystal [83][85], influencing a large number of surface-related processes such as precursor decomposition and surface diffusion during material deposition. Also, the low vapor pressure of Sb in comparison to other group V elements (2×10^{-4} torr at 450 °C) [86] leads to a phenomenon referred to as the *memory effect* inside the reactor during MOVPE. The memory effect of the reactor is related to the longer desorption time from the surface Sb requires compared to other III and V elements. As a result, Sb remains in the “memory” of the reactor longer, and is not purged away as rapidly as the other elements. This makes it difficult to grow sharp interfaces when switching from Sb-based materials to Sb-free materials.

4.2. Au-seeded antimonide nanowire growth and associated challenges

Au-seeded Sb-based III-V nanowires, similar to most other III-V materials can be grown in various combinations of group III and V elements. The composition could consist of a sole group III element such as In, Ga, or Al combined with Sb (binaries), of two group III elements and Sb such as InGaSb, or one group III element, Sb, and another group V element, such as InAsSb, and GaPSb. The two latter cases, as discussed previously, are known as ternaries. The first report on III-Sb “whiskers” dates back to 1990, where the authors report on accidental appearance of GaSb whiskers under non-optimized planar GaSb MOVPE growth conditions [87], followed by a report on InSb whiskers in 1992 [88]. The field remained rather stagnant for another decade, until interest in realizing III-Sb nanowires suddenly increased due to their promising features in areas such as quantum transport [89][90], thermoelectric generation [91], low-power electronics [78][79][81], and as a beneficial test-bed for studying fundamental physical phenomena, such as Majorana investigations [3][92]. GaSb for instance, grown as nanowires, is currently attractive for the implementation of p-type field-effect

transistors (FETs) due to its high hole mobility and band gap (0.72 eV for zinc blende GaSb). In combination with n-type InAs, this material system is considered suitable for efficient tunnelling field-effect transistors (TFETs) [24], partially owing it to their broken band alignment. It is generally accepted that a heterostructure with a broken band alignment is essential in increasing the on-current of TFETs through a reduction of the tunnel barrier [93]. In addition, attempting to synthesize certain ternary antimonide compounds such as $\text{InAs}_{1-x}\text{Sb}_x$ in the nanowire geometry, issues such as miscibility gaps that exist in the bulk form for antimonides do not impose a problem. Therefore, through material composition tunability, the entire band gap range is accessible.

Within the past few years, III-Sb nanowires have been successfully grown by various methods. Here however, for the sake of cohesiveness with the work of the thesis, the main focus will be on particle-assisted growth. Particle-assisted growth includes III-Sb growth using foreign seed particles such as Au [94], Ag [95], and Sn [96], and self-seeded growth such as In particles for InSb [97], and Ga particles for GaSb [98]. The choice of seed particle offers benefits, as well as possible drawbacks associated with that specific seed material. Regardless of the growth method, III-Sb nanowires mainly demonstrate defect-free zinc blende crystal structures [99]. Non-defective crystal structure is typically a preference in device applications, as it promotes better device performances [100]. In fact, this has been used to the benefit in a number of studies, where, by introducing small amounts of Sb, the authors change the crystal structure of III-V nanowires from mixed to zinc blende [101]. This is explained through a lower required supersaturation of the particle for a III-V-Sb ternary material compared to that of the initial III-V binary. In addition, the lower ionicity of InSb and GaSb bonds compared to other III-Vs can lead to an increased critical supersaturation for growing wurtzite antimonides. Also, the surfactant effect of Sb on the interfacial energies may result in a preference towards zinc blende.

However, synthesis of Au-seeded III-Sb has several aspects worthy of noting, some of which have proven to be challenging. In the following some of the general but important factors will be briefly introduced. Following that, discussions on specific challenges associated with antimonide nanowire growth, which are the main focus of this thesis will be mentioned, and later elaborated.

Unlike other group V elements such as As and P, although also low, Sb is significantly soluble in Au at typical nanowire growth temperatures [102]. Ex-situ particle composition measurements mostly reveal stoichiometric AuIn or AuIn_2 for InSb [30][103][104], and AuGa or AuGa_2 for GaSb [94][105], along with small traces of Sb. The ex-situ group III composition of the particle has a direct relation with the Sb molar fraction during growth. For relatively low Sb precursor flows, the AuGa_2 (AuIn_2) particle composition can be expected for GaSb (InSb), while at

relatively high Sb flows AuGa (AuIn) particles will form. The consequence of this higher group III accumulation in the seed particle will be an increase in the particle diameter. Related to this, a general property of Au-assisted III-Sb nanowires is the increase in diameter during axial heterostructure epitaxy when switching from non-Sb to Sb-containing material systems. This diameter increase can be as mentioned, related to a higher uptake of the group III element by the particle as Sb, or it can also be related to the surfactant-caused change in contact angle when introducing Sb, and/or the lattice parameter differences of the two materials. The nanowire diameter increase under discussion here is indeed solely related to VLS. In addition, antimonide growth is usually accompanied by a significant amount of radial growth. This is a direct consequence of the zinc blende crystal structure preference of antimonides, as will be discussed shortly, and the higher surface energy zinc blende possesses. Figure 4.1b illustrates an increase in diameter of the top segment of an InAs-InSb nanowire.

The *reservoir effect* occurs when the concentration of a particular atom has a gradual accumulation or decrease in the liquid seed particle. This could lead to compositional gradient when growing heterostructures. Typically this happens when switching the group III precursor. However Sb-even though low- is soluble in Au, hence for heterostructures including III-Sbs, the reservoir effect may lead to a gradient when switching group V from or to Sb. This could also lead to an initial delay in commencing growth (for binaries), and a gradual incorporation of Sb in the nanowire composition for ternaries of antimonides. Therefore in ternaries, this effect results in a gradual composition change when a sharp interface is desired [106][17].

Another important parameter worth noting is that, when attempting to axially grow Sb-based nanowires, generally the V/III ratio requires fine-tuning. Unlike As and P which have a very high vapor pressures [107][108], Sb has a relatively low vapor pressure and thus tends to stick to the surface [101]. Therefore in contrast to arsenides and phosphides where the V/III ratio range leading to successful nanowire growth is wide, for successful growth of antimonide nanowires the V/III ratio is rather narrow.

Moreover, Sb-based materials have a rather low melting point, compared to other III-Vs. For instance, InSb melts at 525 °C. Therefore the growth temperature windows of these nanowires are very limited. Since the precursors are metalorganics in MOVPE, the growth temperature should be high enough to guarantee sufficient precursor decomposition [109], and low enough to avoid melting the Sb materials. GaSb has a higher melting point of 712 °C compared to InSb, but is still considered low compared to most other III-Vs.

III-Sbs are very sensitive to oxidation [110]. Therefore even though substrates of these materials are available, annealing at high temperatures is essential for

removing the oxide layer prior to growth. This combined with the low melting temperatures of Sb-based material, leads to difficulties when attempting to utilize antimonide substrates for MOVPE. As a result, antimonide nanowires are usually grown on other III-V substrates. However, when attempted to grow from Au particles, the presence of surfactant Sb in the system will affect, and lower the contact angle of Au on the substrate, compromising direct nucleation of Sb based nanowires [50]. Consequently, the particles will move laterally on the surface and instead of vertical nanowire growth, in-plane growth will take place. This is observable in figure 4.1a. In order to overcome this issue, and facilitate epitaxial Au-seeded Sb-based nanowire synthesis, the common approach is to nucleate and grow III-Sbs heteroepitaxially upon a *stem* of a different material [111][112][113][103]. The material composition of the stem segment in most cases is of the growth substrate. As demonstrated in figure 4.1b, this stem serves as a facilitator on which the contact angle of the Au seed particle is increased. However, when performing antimonide synthesis in the absence of other group V material supplies, this stem may decompose leading to broken nanowires, hence failing in accomplishing standing nanowires. This is observable in figure 4.1c. The direct nucleation barrier of nanowires from substrates is generally an issue solely associated with Au-seeded particles. A number of studies demonstrate direct growth of epitaxial III-Sb nanowires from substrates through self-seeded [114] [115][116][117], selective area growth [118], or foreign particles other than Au [119]. Among these, the studies demonstrating ternary III-Sb nanowire growth however, report on no, or very narrow Sb compositional tuning of the nanowires.

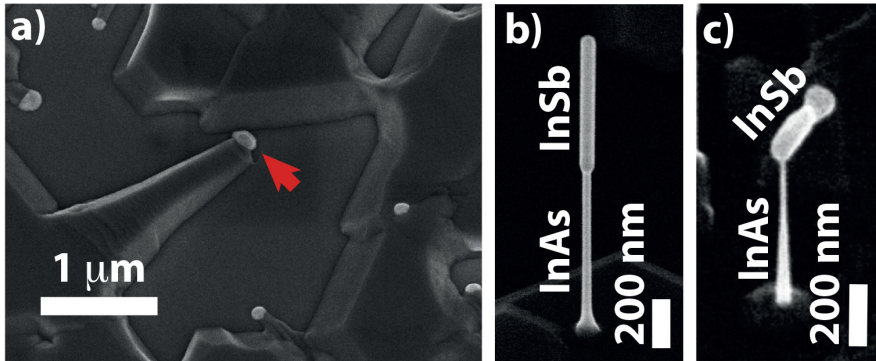


Figure 4.1. a) Traces of material grown on the substrate by the Au seed particle, caused by the presence of Sb in the system when attempting to grow directly from the substrate. The red arrow points at a seed particle. b) Successful vertical growth of InSb on an InAs stem. The stem aids in improving the contact angle, therefore vertical growth of Sb-based material is facilitated on a stem. c) Decomposition of the InAs stem especially close to the heterostructure interface in the lack of As precursor when growing.

As mentioned, antimonide nanowires mainly grow in the zinc blende crystal structure. Although this can be beneficial when crystal structure purity is desired,

it limits accessing antimonides in the wurtzite structure. This is in fact not only a characteristic of Au-seeded nanowire growth, but a very general characteristic of antimonides; wurtzite antimonides have not been grown reproducibly in any configuration. There have been studies though, reporting short segments of crystal structures other than zinc blende in III-Sb nanowires, such as wurtzite or higher hexagonal ordered crystal structures (4H) [97][120][121].

In the following chapters the issues covered in the two latter-most paragraphs; direct nucleation and growth of III-Sb nanowires from substrates, and growth of wurtzite antimonides, will be expanded, and addressed in respective order. As a tool for accessing the desired material or nanowire structures, *template nanowire growth* through crystal structure engineering will also be discussed.

4.2.1. Direct nucleation of Au-seeded III-Sb nanowires from substrate

As mentioned above, the presence of Sb imposes a limitation on direct nucleation and growth of Au-seeded III-Sb nanowires from the substrate as a result of contact angle alterations. This subject has been generally discussed already in chapters 2.1.4; Surfactants, and 2.1.5; VLS, subchapter: Particle contact angle. In the specific case of Au-seeded antimonides, [84] demonstrates a reduced contact angle of Au in the presence of Sb. The lowered contact angle can be explained as follows: Sb will preferentially stick to the Au surface, reducing the involved surface and interfacial energies (γ_{LV} , and γ_{LS}). The multiphase system will minimize its total interfacial energy by readjusting the geometry to accommodate the changes in γ_{LV} , and γ_{LS} . Basically, the equilibrium geometry of the system will ultimately be determined by the balance between the surface area of the liquid hemisphere, and the surface area of the solid-liquid interface. It can be that, Sb leads to $\gamma'_{LV} > \gamma'_{LS}$, so that the system reshapes itself to reach total energy minimum by reducing the liquid surface area, and increasing the liquid-solid surface area. By this, according to Young's equation, the particle will wet the surface, and the contact angle will reduce to lower than $\pi/2$ (recall for having a contact angle larger than $\pi/2$, $\gamma_{SL} > \gamma_{SV}$ must be satisfied). The low contact angle will in turn compromise nanowire growth, since contact angles larger than $\pi/2$ are crucial for stable nanowire growth [50]. The reason why III-Sbs are successfully grown on stems can be related to the finite size of the top (111) B surface, which prevents the particle from expanding, thus keeping the contact angle above $\pi/2$.

In the work of this thesis, this issue is addressed through Au-seeded $\text{InAs}_{1-x}\text{Sb}_x$ nanowire growth on (111) B InAs substrates. As already mentioned, previous studies show that [84] substantial differences of the contact angle can be observed when annealing Au-particles in atmospheres containing either As or Sb. Au particles annealed under As are almost hemispherical with a much higher contact

angle compared to the rather flat Au particles annealed under Sb. By introducing the third element into the material system (As), larger contact angles, and hence successful nanowire growth can be ensured under very low relative concentrations of Sb. This is because As adatoms being present in the system not only affect the supersaturation of the particle, but also affect the interface energies. From here, the Sb concentration in the vapor phase can be increased step by step for each experiment, to systematically study and understand that under given conditions, how far the presence of As can counterbalance the surfactant effect of Sb. The Sb vapor phase composition is given as the ratio of the Sb precursor; trimethyl antimony (TMSb) molar fraction to the total group V molar fraction:

$$x_v = [TMSb]/([TMSb] + [AsH_3]) \quad 4.1$$

The effects on morphology and Sb incorporation in the nanowires of several controllable growth parameters are systematically mapped out in paper I, on which full descriptions can be found in the appended paper. Importantly, from this work it is understood that with increasing Sb vapor phase composition under constant group III flow, the solid phase incorporation of Sb (x) also increases. This is observable from the blue data points in the graph shown in figure 4.2.

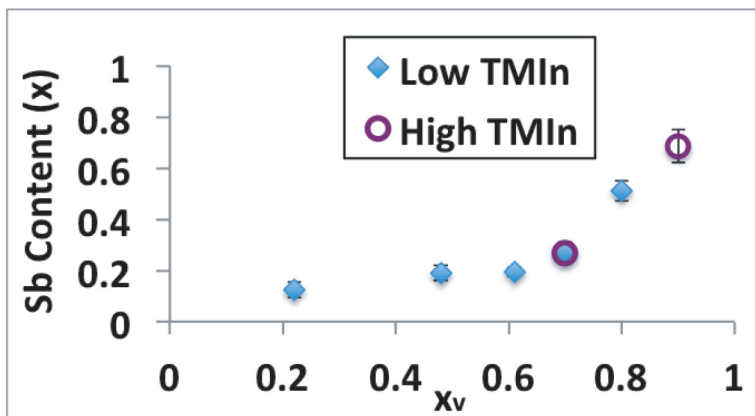


Figure 4.2. Increase in Sb content of nanowires with increasing x_v . Blue data points represent nanowires grown under lower TMIn flows compared to the purple data points. (Reprinted with permission from [122]).

Based on this finding, the solid Sb content of the nanowires can be used as a gauge qualitatively reflecting the vapor phase composition. However, passed a critical x_v (0.8 under these conditions), vertical growth will again be hindered. At this point the Sb composition in the vapor will be high enough to result in particle wetting.

Another solution to this problem is to change the seed particle composition. By increasing the TMIn flow under constant x_v (decreasing the V/III ratio), a

transition from Au seeded to semi In-seeded nanowire growth occurs as shown in the overview SEM images of figure 4.3. At the lower end of V/III ratios (shown in figure 4.3 c of the thesis) the particles are immensely larger than the particles on the tip of nanowires grown at V/III ratios above this range.

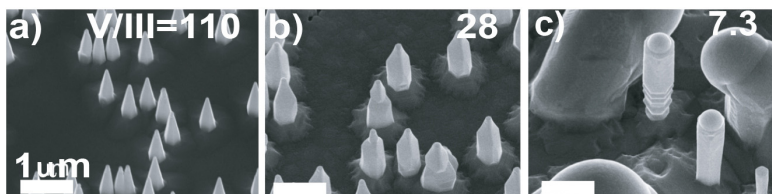


Figure 4.3. SEM overview images of nanowires grown at a constant vapor phase composition of 0.8, with V/III ratios of 110, 28, and 7.3.

Au is not detected in the particles related to the semi In-seeded grown nanowires, which indicates that, the volume of Au in the particles (if any) is well below the detection limitation of the detector. This implies that, existing Au particles act merely as a sinks for collecting In adatoms. It is also worth noting that, at such high In flows, In particle formation needs not to rely on the presence of Au particles. In fact, if a bare substrate is placed in the reactor along side the main samples, vertical nanowires grow from spontaneously formed In particles on the substrate surface. Interesting is that the morphology of these nanowires closely resembles those grown on substrates with initial Au seed particles. Figure 4.4 shows a comparison between the morphology of the nanowires growing from bare InAs substrates, and from substrates with predeposited Au-seed particles with an areal density of 0.1 and 1 particle/ μm^2 .

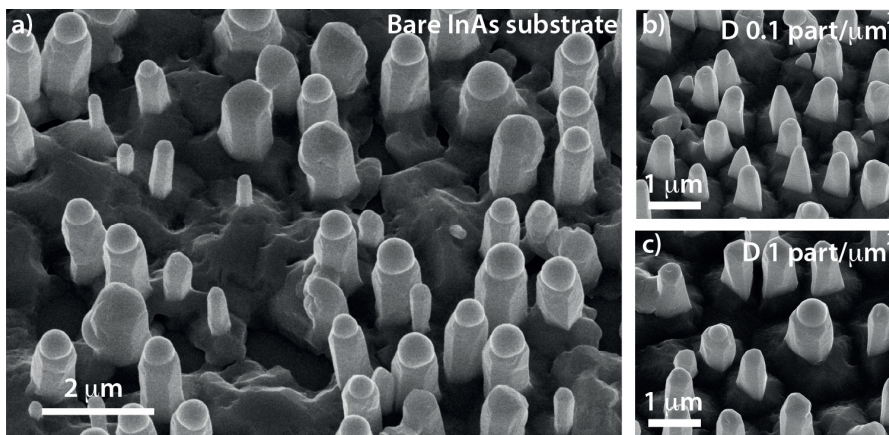


Figure 4.4. Under growth conditions of V/III ratio = 19, and $x_v = 0.8$, a) In-seeded nanowires grown on a bare InAs substrate. b) Semi-In seeded nanowires grown on a substrate containing initial Au aerosols with a surface density of 0.1 part/ μm^2 , and c) with a surface density of 1 part/ μm^2 .

The Sb composition of nanowires from all three samples demonstrated in figure 4.4 show similar values. More interesting is that, in fact the V/III ratio in general does not affect the Sb incorporation in the nanowires. Basically, over the large range of studied V/III ratios (varying In only), the Sb incorporation remains more or less constant, not changing in a cohesive manner.

The invariance of Sb incorporation to V/III ratio opens doors towards tackling the lowered contact angle of the particle at high Sb vapor phase compositions. By increasing the TMIn flow one order of magnitude (more detail can be found in paper I), the liquid particle will change from Au to mainly In. It can be that, since In and Sb practically have a high solubility, Sb does not play the same surfactant role for In as it does for Au. In addition, it is reported that the γ_{LV} of pure In is lower in comparison to Au [123], and surfactants will have a more significant impact on higher energy surfaces. Moreover, the significant increase of In in the particle will most likely affect the γ_{LS} interfacial energy relative to that of Au. Therefore the change in particle composition can lead to changes in the contact angle. Apart from that, semi-In seeded growth occurs at very low V/III ratios, where there exists an abundance of In. It could be that, under these conditions, In adatoms will be sitting on the exposed solid, shielding the surface from Sb adatoms, which will then practically compromise the effects stemming from the surfactant nature of Sb. This will clearly change the balance in the interfacial energies. In either case, the increase in contact angle of the In particles ultimately facilitates nucleation and growth of vertical nanowires. Consequently, the nanowires can be grown at even higher Sb vapor phase compositions than possible through Au-seed particles. Going back to figure 4.2, these data points are given in hollow purple circles.

For all of the nanowires grown in paper I, regardless of the morphology and seeding material, there is an extremely significant amount of radial growth. This is quantified for a typical nanowire shown in the STEM image and radial compositional analysis of figures 4.5 a and b respectively. Radial growth is also readily observable from SEM images. In figure 4.3 for example, for the Au-seeded nanowires significant tapering occurs (figure 4.3 a and b), and for the semi In-seeded nanowires enormous column-like morphologies are visible (figure 4.3 c). Worth noting is that, for increasing Sb vapor phase composition, for the Au-seeded nanowires the tapering also significantly increases. In these growth conditions, there is an abundance of both group III and V adatoms, which can lead to significant radial growth.

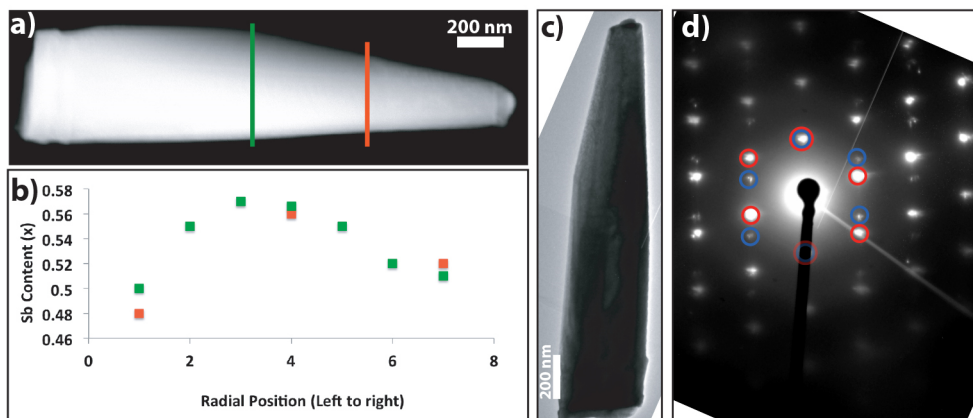


Figure 4.5. a) STEM image of an InAsSb nanowire from which the radial compositional point data shown in (b) has been acquired. b) the radial composition demonstrates the core-shell structure of the nanowire, with an Sb-poor shell in comparison to the core. c) TEM overview of the same nanowire from which the diffraction pattern in (d) is taken. d) the diffraction pattern shows a zinc blende crystal structure (red circles) with occasional twinning (blue circle).

In addition, since the nanowires are antimonides, as discussed at the beginning of this chapter, it is expected their crystal structure to be zinc blende. This is indeed the case, as demonstrated for one nanowire in figure 4.5 c and d. It has already been covered in chapter 2.2.2; Surface energies of zinc blende and wurtzite side facets, that zinc blende side facets typically have a higher surface energy compared to wurtzite. This is a reason why antimonide nanowires have large amounts of radial growth in general [124], and clearly the case for the nanowires under discussion here. Ideally, for axial nanowire growth, minimum, or better even, control over radial growth is preferred. Therefore, general measures need to be taken to gain control over the radial growth of III-Sb nanowires. One method is to control the crystal structure; with a lower surface energy, hence a higher nucleation barrier compared to zinc blende, wurtzite crystal structures may offer the required control. This will be covered within the next chapters.

4.2.2. Template assisted growth of III-Sbs

Initially in this chapter, the concept of crystal structure-template nanowires will be covered. This method is extensively used for realizing complex antimonide structures within this thesis; therefore descriptions on this topic are essential prior to continuation of the antimonide nanowire growth topic. Recalling from chapter 2.2.4; crystal structure engineering, upon full control of crystal structure, the structure of nanowires can be designed and engineered to desire. Nanowires with pure crystal structures of either wurtzite or zinc blende can be grown with minimal to no stacking defects along their entire length, or alternatively, multiple

alternating segments with desired lengths can be designed along the axial length of single nanowires. Figure 4.6 demonstrates overview SEM and high-resolution TEM (HRTEM) images of wurtzite, twinned zinc blende and multi segmented InAs nanowires respectively. The crystal structure of these nanowires is precisely controlled through the set V/III ratio; high V/III values for zinc blende, and low for wurtzite. However, the growth parameters need to be optimized precisely for the specific growth conditions and dimensions of the seed particles.

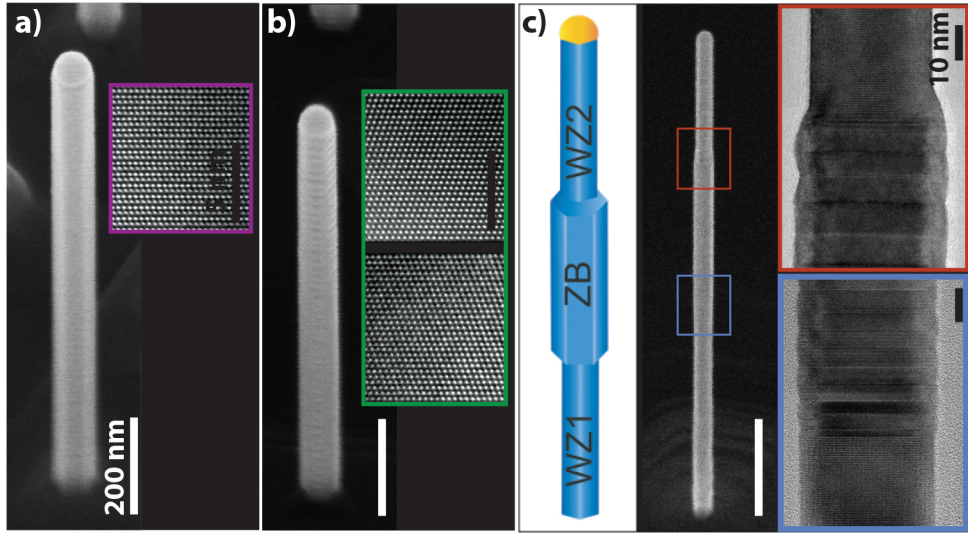


Figure 4.6. SEM images of InAs nanowires with a) pure wurtzite crystal structure, along with HRTEM inset, and b) twinned zinc blende crystal structure, along with HRTEM insets representing each of the twins. c) Schematic representation of an InAs multi segmented nanowire with alternating wurtzite (WZ1)- zinc blende (ZB)- wurtzite (WZ2) segments, together with an SEM image of said nanowire. The insets show TEM images of the interface between the crystal structures.

Since each of the wurtzite and zinc blende crystal structures has their specific material and physical characteristic, depending on the aimed application, each of the mentioned configurations may be of significant importance. For instance, for the same material, the measured and/or predicted band gap of the two crystal structures may possess different values [125][126][127], or there may exist a band offset between the conduction/valence bands of wurtzite and zinc blende [128]. Therefore alternating segments of different crystal structures of the same material can avail access to *crystal structure quantum dots* [127]. Also, recalling from chapter 2.2.2, the surface energies of the wurtzite and zinc blende crystal structures are different, with zinc blende usually having the higher value. Higher surface energy leads to higher surface growth driven by the lower nucleation barrier. By exploiting this fact, the nanowires can be designed as templates with multiple crystal structures, so that along the length of single nanowires radial

growth is hindered on some segments, while prevailed on others, leading to a selective core-shell structure. In addition to offering a platform for intriguing applications such as coupled quantum dots [129], these core-shell structures can facilitate fundamental studies of radial growth on different crystal facets [130][131].

InAs-GaSb selective core-shell

Manipulating the surface energy of the side facets of nanowires through crystal structure control is one way of controlling radial growth. Paper II, demonstrates selective GaSb shell layers on InAs nanowires with alternating wurtzite, zinc blende, and wurtzite segments. GaSb grows essentially on the zinc blende segments. The selective shell growth is clearly demonstrated in figure 4.7, through a schematic illustration, SEM overview, and XEDS elemental map of a typical selective core-shell nanowire. The InAs core of this nanowire is constructed of three consecutive segments of; from bottom to top: wurtzite (WZ1), zinc blende (ZB) and wurtzite (WZ2). Worth noting is that, as observable from the schematic and SEM images of figure 4.7, under these conditions an unintentional axial GaSb segment also grows.

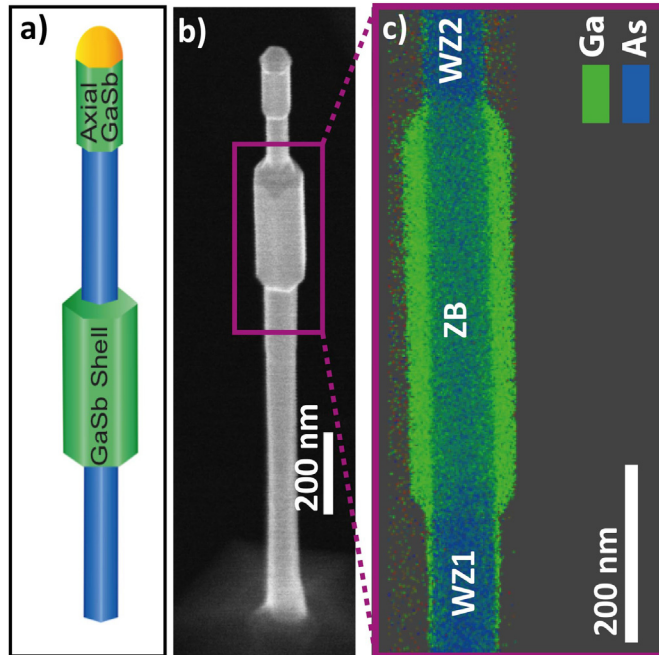


Figure 4.7. InAs-GaSb core-selective shell nanowire demonstration. a) a schematic of the core-shell structure depicting GaSb growth on the zinc blende (ZB) structure, and the axial GaSb segment. b) SEM image of a core-selective shell nanowire where all four segments are clearly distinguishable. The ZB segment and a part of the WZ1 and WZ2 segments are marked with a box, an area from which the elemental map in figure c) is attained. c) STEM-XEDS elemental map demonstrating the preference of GaSb growth mainly on the ZB segment.

The shell growth is extremely sensitive to the slightest deviations in the crystal structure. In figure 4.8 overview and HRTEM images are given for nanowires with a defect-free, and defective zinc blende segment. It is clear from the dents in the latter that, even for short stacking defects (being wurtzite in an otherwise zinc blende stacking) the shell growth is suppressed for the lower surface energy stacking. Also, from figure 4.8 (b and d specifically) it is understood that the shell layer transfers the crystal structure of its underlying core. Inheriting the crystal structure information is to be expected if the growing layer is in epitaxial relation with its underlying layer [132].

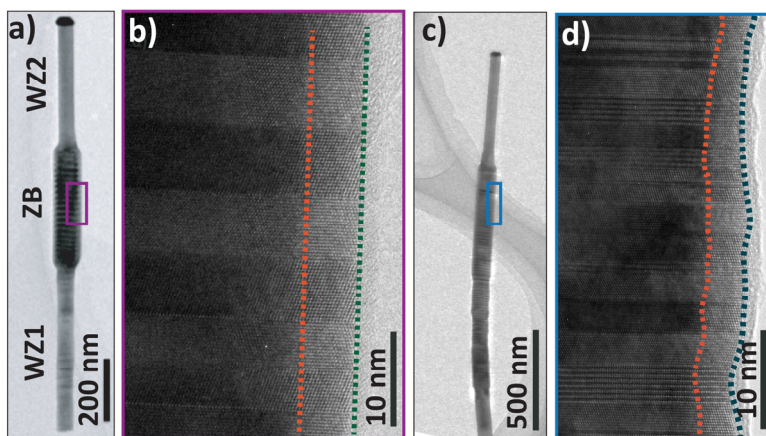


Figure 4.8. a) Overview TEM image of fine tuned InAs template core-selective GaSb shell nanowire with alternating WZ1-ZB-WZ2 segments b) HRTEM image of zinc blende core-shell segments highlighted in (a) shows a defect-free twinned zinc blende structure, together with smooth and even shell growth. c) Overview TEM image of a core-shell nanowire in which the core crystal structure has not been optimized. d) Demonstrates a HRTEM image of the highlighted core-shell segment of (c), which reveals a mixed crystal structure along with uneven shell growth. The red dashed lines show approximately where the InAs-GaSb interface is, while the green dashed lines indicate the GaSb-vacuum interface. (Reprinted with permission from [131]).

Systematically studying GaSb shell layer growth on InAs template nanowires with different segments deepens the understanding of how the directly controllable growth parameters influence the selectivity and quality of this radial growth. These parameters, namely the total precursor flow, shell growth time, growth temperature, and the V/III ratio of the growth precursors, may all have an impact on the selectivity of radial growth. For instance, studying the GaSb shell growth temperature within the range of 420 °C to 500 °C reveals that the selective radial growth cannot be efficiently tuned with temperature. The related observations concerning each of the mentioned parameters are discussed in detail in the appended paper (II). However, the study reveals that, the V/III ratio of the precursors at constant total flow values has the highest impact on controlling the selectivity of the GaSb shell, being the most effective method for controlling the thickness of the selective shell in given time.

The shell V/III ratio studies performed in paper II, reveal that the diameter of the wurtzite segment of the core InAs nanowire, and the InAs-GaSb core-shell nanowires grown under different V/III ratios remain constant, which indicates no GaSb shell growth on wurtzite segments. It is also understood that the zinc blende + GaSb diameter drops drastically as the V/III ratio increases. In contrast, the diameter and axial length of the axial GaSb segment increases with increasing V/III. This suggests that the two GaSb growth fronts; the axial GaSb segment, and the selective radial growth on the zinc blende InAs segment, are competing for material in a fashion that at low V/III ratios selective radial growth is promoted, while growth of the axial segment is suppressed. As the V/III ratio is increased to higher amounts, axial growth is favoured over selective shell growth.

Through what is understood from the selectivity of GaSb shell growth on InAs core templates, it is possible to design and grow structures with multiple segments of alternating core-shells along the length of single nanowires. This can be done with very high precision of single segment lengths and axial positions. Figure 4.13 demonstrates nanowires grown with three core-shell segments separated by short wurtzite insets in between. In figure 4.9a a schematic of the design is illustrated. The positioning and length of these segments are controlled with the set growth times of each segment. Figure 4.9b demonstrates an overview SEM image of a sample with multiple core-shell segmented nanowires. in the magnified image in the inset the three separate zinc blende (selective core-shell) segments, and the two short wurtzite insets are observed more clearly. Figure 4.9c shows an overview TEM image of an identical nanowire, from which the STEM-XEDS elemental maps are obtained. These maps clearly demonstrate the selectivity precision of the grown GaSb shell, as it is not detectable on the short wurtzite insets.

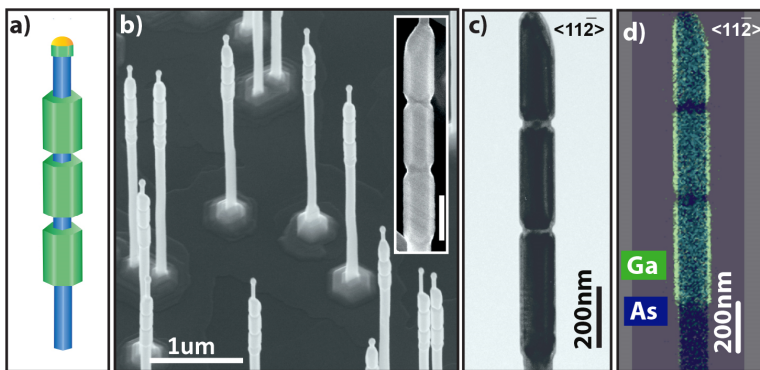


Figure 4.9. Multiple (here three) segmented core-selective shell InAs-GaSb nanowire. a) a schematic illustration of such a nanowire. b) SEM overview image of a sample with three segmented core-selective shell structures. The inset is a magnified image of a representative nanowire from the same sample. The scale bar in the inset corresponds to 200 nm. c) Overview TEM image of said nanowire. d) XEDS elemental map of the nanowire in c) where green represents the Ga atoms (hence GaSb shell) and blue As atoms (InAs core). (Reprinted with permission from [131]).

As seen from the demonstrated results, under these rather typical growth conditions, GaSb exclusively grows on zinc blende, leaving the wurtzite segments bare. In fact, the low surface energy of wurtzite side facets, and the rather high nucleation barrier of wurtzite antimonides, is the main components leading to this phenomenon. On one hand the general tendency towards lower ionicity of III-Sbs, and their positive, large difference in cohesive energy is one reason for this utterly low preference to form wurtzite. On the other hand, the presence of the surfactant Sb in the system will likely decrease the surface energy of wurtzite and zinc blende side facets alike. It could be that, it decreases the surface energy of the wurtzite side facets significantly more than zinc blende, maintaining the lower preference of wurtzite formation versus zinc blende as discussed in section 2.2.3; wurtzite formation in nanowires. Extreme conditions may alter the imbalance as will be discussed later.

Suitable templates for realizing wurtzite antimonides

In fact, wurtzite antimonides have never been systematically studied, or reproducibly realized before. It is therefore, necessary to study the possibility, and the required circumstances for surmounting the wurtzite antimonide nucleation barrier. By this, not only a fundamental challenge will be addressed, but also doors will open for synthesizing novel material, which in turn may potentially offer properties useful for various applications. Only once the material is synthesized, needed steps can be taken to characterize said properties, and verify their value to possible applications.

Since growing III-Sb nanowires in wurtzite is challenging, obtaining these structures would extremely benefit from a suitable wurtzite template to provide a foundation for the growing nanowire to adapt the wurtzite structure. As already discussed, to facilitate III-Sb nanowire nucleation typically these nanowires are grown on a stem segment of non-Sb material [84](and the references within). Although this stem segment can have a wurtzite crystal structure, typical axial growth from Au seed particles on wurtzite stems will not provide the necessary template for realizing wurtzite antimonide nanowires. In the growth direction the (111) B zinc blende planes are equivalent to (0001) wurtzite planes. Therefore on a (0001) plane of the wurtzite trunk, both planes can easily form. Hence, when introducing Sb into the system, the axially growing nanowire will not be limited by any epitaxial or directional bounds to maintain the wurtzite structure, and will simply change to zinc blende by creating a C stacking layer. This is demonstrated in the schematic illustration of figure 4.10, in the axial direction, where for both wurtzite and zinc blende segments on the wurtzite stem (*trunk*) segments, a perfect epitaxial relation is observable at the interface. Thus, it is needed to provide a template that can “lock” the crystal structure of the newly growing nanowire to that of the underlying structure. This locking mechanism stems from the energy

cost of creating structural defects to change the crystal structure from wurtzite to zinc blende. This energy cost is essentially higher than that of forming wurtzite antimonides.

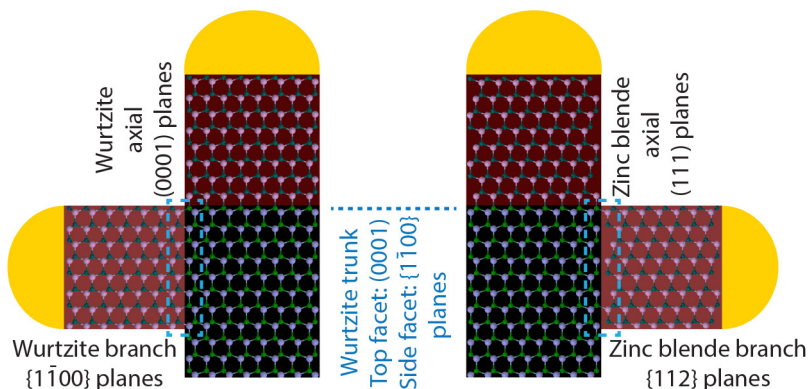


Figure 4.10. Schematic illustration of wurtzite trunk with wurtzite (left hand side) and zinc blende (right hand side) axial and branch segments. The axial segments in both cases are in complete epitaxial relation with the trunk segment. From the right hand side image it is seen that that from every 6 planes of the growing zinc blende branch, one only one matches with that of the underlying wurtzite side facet (marked with blue dashed box). This is in contrast with the wurtzite branches (left hand side). (Reprinted with permission from [133]).

Radial growth of III-Sb shell layers on wurtzite templates is one method for obtaining the required “locking” mechanism. As the growing shell layer is an extension of the already existing side facet, the growing layer must maintain the underlying structure in order to keep its epitaxial relation to the core [132][134]. Authors in [135] study this case of $\text{InAs}_{1-x}\text{Sb}_x$, where wurtzite InAs acts as a template for growing wurtzite ternary $\text{InAs}_{1-x}\text{Sb}_x$ shell layers. As discussed in this paper this method might limit the Sb composition by strain, making high Sb compositions inaccessible. However, this will not be a limiting factor when growing binary systems, as will be shortly discussed in the next subchapter.

An alternative approach for attaining wurtzite antimonide material, while accessing a 1D structure, is to grow branches from secondary Au seed particles deposited on the sidewalls of wurtzite template nanowires. Through this approach localized growth through the vapor-liquid-solid (VLS) growth mechanism is achievable, while the new forming structure is forced to maintain the stacking sequence of that section of the nanowire, which is located underneath the secondary particle. This will lead to the extension of the side facet (regardless of the crystal structure it has) into a 1D structure at a localized position as shown schematically in figure 4.10, the branch segments. In the branch direction, the crystallographic planes of wurtzite side facet ($\{1100\}$) and zinc blende ($\{112\}$) do not match. In the right hand side schematic of figure 4.14 it is clear that from

every 6 planes of the growing zinc blende branch, only one matches with that of the underlying wurtzite side facet. Another advantage of this method is the possibility to overcome the strain-induced limitation of radial growth for ternary material systems, as the 1D structure of the nanowire branches are efficient in strain relaxation in the radial direction due to their small diameter [136][137].

Wurtzite GaSb shell on InAs core templates

Wurtzite GaSb is indeed a potentially interesting novel material, as it has not been synthesized to date. The theoretical predictions on the electronic bands of wurtzite GaSb suggest differences from that of the zinc blende counterpart. For instance, all predictions point towards a positive offset in the valence band edge alignment of wurtzite compared to zinc blende [138][139][128][140][141]. In addition, there are controversies between the predicted band gap values and hence, band alignments of wurtzite and zinc blende GaSb. Some studies report a larger band gap for wurtzite compared to zinc blende, leading to a *type II (staggered)* band alignment [138], while others predict a smaller value, hence *type I (straddling)* band alignment [139][128][140][141]. In either case, the material needs to be synthesized, and characterized to settle the mentioned controversies.

Utilizing the template assisted growth method, and through knowledge gained from the studies of papers I and II about radial growth of antimonides in general, and GaSb on zinc blende InAs segments specifically, wurtzite GaSb shell layers are successfully grown on InAs wurtzite template nanowires in paper III. Figure 4.11 demonstrates the bare wurtzite InAs core, and the wurtzite InAs-GaSb core-shell nanowires. Notable is that, similar to results in paper II, an unintentional axial GaSb segment is also observable. Additionally, a tapered morphology is observed for the core-shell structure.

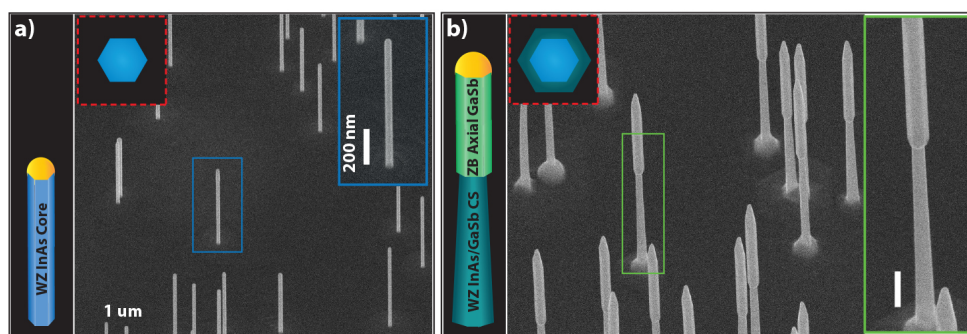


Figure 4.11. a) Schematic, overview and magnified SEM images of the wurtzite InAs core nanowires which are used as templates for growing GaSb wurtzite shells demonstrated in (b). b) schematic, overview and magnified SEM images of the wurtzite InAs-GaSb core-shell nanowires.

More specifically, from paper I it is understood that high total flows lead to more overgrowth, and from both I and II it is concluded that low V/III ratios enhance radial growth significantly. Through this understanding, shell layers of wurtzite GaSb with substantial and controllable thicknesses have been grown at similar conditions to the selective shell growth on zinc blende (similar low V/III ratio value, and slightly higher temperature), but with the significant difference being the much higher (around an order of magnitude) total flow.

Indeed, providing a suitable template for the shell growth is of essential importance. As already mentioned in the last part of the previous subchapter, epitaxial shells layers are required to transfer the crystallographic information from their underlying structure. By providing a wurtzite InAs core template with minimum defects, the growing layer is forced to form wurtzite. More information on the growth parameters can be found in paper III. Figure 4.12 demonstrates overview, and high resolution-TEM, images from the core-shell nanowires confirming their wurtzite crystal structure. The acquired XEDS elemental maps confirm the core-shell material composition to be InAs-GaSb, as expected.

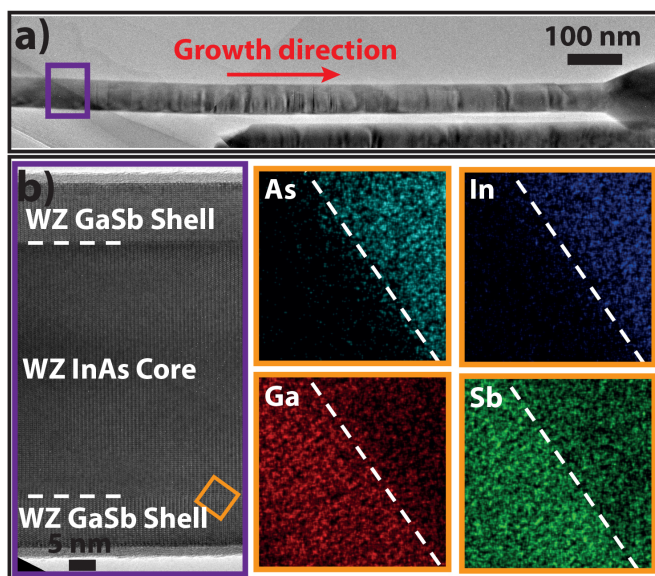


Figure 4.12. a) TEM overview of wurtzite InAs-GaSb core-shell nanowire, b) HRTEM image of highlighted area of the core-shell segment showing wurtzite crystal structure of core and shell. Insets demonstrate elemental maps of the core-shell interface, confirming the InAs-GaSb composition.

Under typical conditions, as seen in paper II, the high nucleation barrier of wurtzite GaSb hinders shell growth on a wurtzite core. This is generally the case, unless the supersaturation of vapor is increased so much that, it overcomes said barrier. This is indeed the case here; a high total flow increases the amount of

available material, hence increasing the vapor supersaturation. Also, the slightly higher growth temperature of these shell layers has an impact on the efficiency of precursor cracking, again increasing the total amount of present adatoms.

Another finding of this study is that the tapering of the shell occurs in steps, at which the thickness of the shell suddenly decreases. This is shown in figure 4.13. Interesting is that, a large number of these steps coincide with the occasional presence of stacking defects. This is an indication that the stacking defects act as a small barrier for the growing shell, hindering it temporarily. This can be the case only if the shell grows by step-flow mode along the length of the nanowires, bottom towards top along the side facets ([000-1] direction) as opposed to outward growth in the $\langle 1-100 \rangle$ direction (normal to the side facets). When the growing shell meets a stacking fault perpendicular to its growth direction, the energy barrier it needs to overcome is sufficiently large so that the existence of the stacking fault briefly blocks the step-flow growth. This leads to the stepwise tapered morphology of the wurtzite shell. This is schematically illustrated in figure 4.13c. Otherwise, the barrier-like behaviour of stacking faults would be in opposition to what would be expected from radial shell growth on stacking defects. First of all, stacking defects would act as kinks, hence as preferential nucleation sites, expected to increase radial growth of the shell. Secondly, defects in an otherwise wurtzite structure are layers with zinc blende stacking. Since zinc blende side facets have a higher surface energy compared to wurtzite, it would be expected that, existing zinc blende insertions would enhance shell growth, instead of hindering it. Worth noting is that not every defect leads to a stepping; shown by green arrows in figure 4.13b, or even more importantly, stepping occasionally occurs in the absence of stacking defects as well. A speculation explaining this could be that the step-wise tapering morphology is also a result of diffusion-limited growth. More discussions on this matter can be found in paper III.

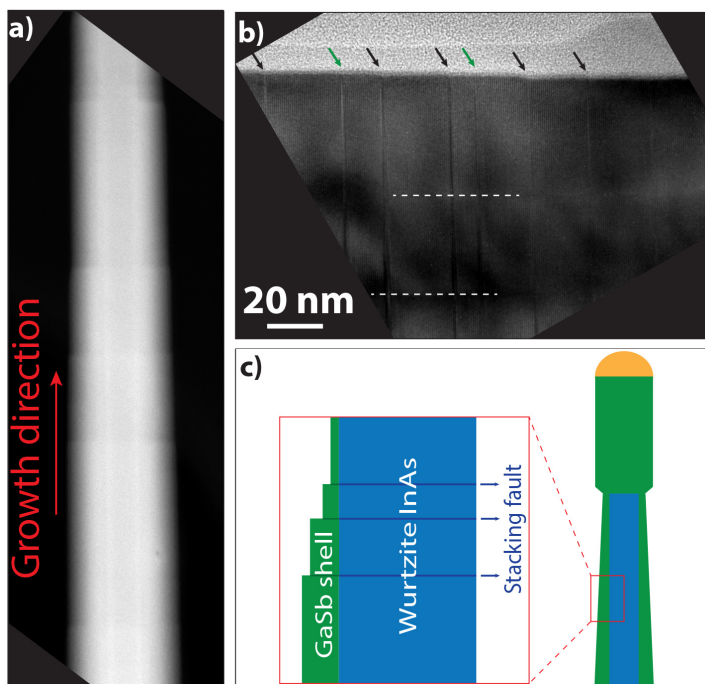


Figure 4.13. STEM-HAADF image of core-shell nanowire demonstrating the step-like morphology. b) HRTEM image showing the correlation between lateral steps and stacking defects. Black arrows indicate the steps that are associated with stacking defects, while green arrows point to the defects that have not caused stepping. (c) Schematic illustration of the correlation between stacking defects and lateral steps.

The shell thickness is controllable by set growth time. Interesting to note is that, due to the bottom-up shell growth, in order to have a full coverage on the InAs core, sufficient time must be provided. Basically, when not given the required time for a full coverage, a fraction of the core will remain bare towards the top of the nanowire. More details regarding the shell coverage and uniformity are discussed in detail in paper III.

Wurtzite $\text{InAs}_{1-x}\text{Sb}_x$ branches nanowires on wurtzite InAs templates

Radial growth of wurtzite GaSb provides a valuable insight to the associated challenges of VS growth of wurtzite antimonides. However, a fundamental understanding of synthesizing wurtzite antimonides through the VLS mechanisms still remains unaddressed. In addition, realization of crystal structure engineered multi-segments and quantum dots of the same material require growth in the axial direction. Therefore, successfully growing axial wurtzite antimonides are essential for realizing the latter mentioned structures in III-Sb materials. Even though controlled growth of very short wurtzite segments of III-Sb binary nanowires have already been demonstrated [121], there have been no reports on Sb-rich ternary

segments of InSb nanowires in the wurtzite crystal structure. This statement indeed holds for $\text{InAs}_{1-x}\text{Sb}_x$ as well, and it has been demonstrated already that, by adding a small amount of Sb to InAs, the crystal structure of the nanowire changes to zinc blende [142]. It is not fully understood however, why and how Sb causes the structure to be zinc blende, or at what Sb composition this occurs, and whether or not this critical composition is dependent on the growth conditions, or what relative roles kinetics and thermodynamics play. In other words, to what extent the antimonides are forced to adapt the unfavourable wurtzite structure. Ternary materials offer the unique opportunity to investigate possible limitations of Sb incorporation in wurtzite structures.

Even though they grow in a different direction than the typical (111) B₂ branches on nanowires have a high aspect ratio. Therefore, if isolated from the trunk, they can be considered as 1D structures. In addition, as argued before, through template-assisted growth on wurtzite trunks, the branches could be forced to adapt the wurtzite structure. In paper IV, $\text{InAs}_{1-x}\text{Sb}_x$ branches are grown on InAs wurtzite trunk nanowires a wide range of Sb vapor phase compositions up to $x_v=0.89$. For comparison, branches are grown on zinc blende InAs trunks simultaneously. The branches initially grow along the $\langle 112 \rangle$ direction, and parallel $\langle 1-100 \rangle$ for zinc blende, and wurtzite branches, respectively. The branches may ultimately change direction, for which details can be found in paper IV.

During branch growth, an axial $\text{InAs}_{1-x}\text{Sb}_x$ segment grows above the original trunk, while a shell layer also covers the trunk radially, unconditional of the trunk crystal structure. Figure 4.14 demonstrates a schematic illustration of said nanowires, along with example overview and magnified SEM images of wurtzite and zinc blende branched nanowires growing under the same Sb vapor phase composition from the studied range. SEM images of other vapor phase compositions are available in paper IV. The simultaneous trunk overgrowth provides valuable information; through studying its composition, Sb incorporation through VLS and VS can be directly compared.

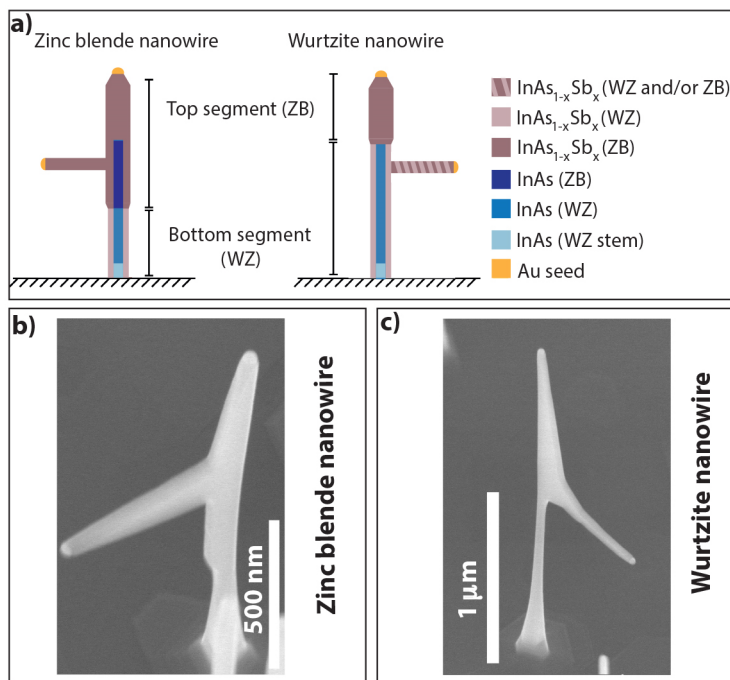


Figure 4.14. a) Schematic representation of zinc blende and wurtzite $\text{InAs}_{1-x}\text{Sb}_x$ branches grown on InAs template trunk nanowires. b) Overview and magnified SEM images of branched zinc blende nanowires. c) Overview and magnified SEM images of branched wurtzite nanowires. (Reprinted with permission from [133]).

The zinc blende branches extend the crystal structure of the underlying zinc blende trunk throughout their entire length. The wurtzite branches on the other hand, offer more interesting insights on the crystal structure they adapt. Firstly, they nearly always grow in the vicinity of trunk stacking faults. The stacking defect facilitates nucleation of wurtzite antimonide. It can be argued that, the existence of a zinc blende stacking in the otherwise wurtzite affects the solid-liquid interfacial energy between the secondary Au particle, and the underlying portion of the trunk side facet. Or alternatively, kinetic factors are in play, with the stacking defect acting as a barrier, preventing further migration of the secondary particle, and ultimately forcing the branch to grow from the stacking defect. What is of utmost interest is that, the stacking defect not only propagates into the otherwise wurtzite branch, but it is responsible for the appearance of a zinc blende structure coexisting parallel to the wurtzite structure in the branch. Figure 4.15 demonstrates a wurtzite branch growing in relation to a stacking defect at the same growth conditions as figure 4.14, where the parallel wurtzite and zinc blende segments of the branch are deducible from HRTEM analysis given in figure 4.15c.

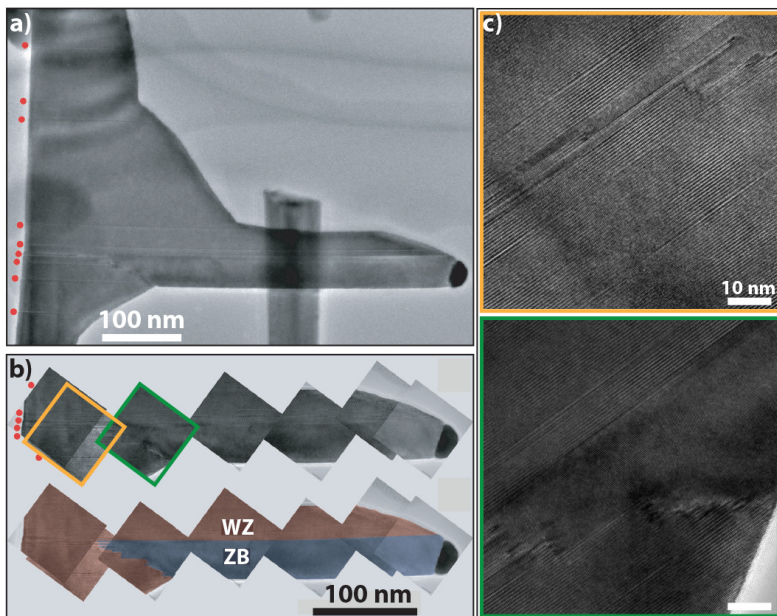


Figure 4.15. a) overview TEM wurtzite branched nanowire where parallel zinc blende and wurtzite segment coexist within the branch. The red dots mark the stacking defects. b) TEM image of the branch in which the wurtzite and zinc blende structures are color coded with red and blue respectively. c) demonstrates HRTEM images of the marked boxes of figure (b), in which the gradual change in crystal structure from wurtzite to zinc blende through grain boundaries are observable. (Reprinted with permission from [133]).

Also from the HRTEM images in figure 4.15c it can be noticed that the change in crystal structure from wurtzite to zinc blende is via grain boundaries, which is typically unfavourable due to the high formation energy. From this it can be concluded that the wurtzite antimonide formation is possibly even less favourable. The TEM image depicts the parallel zinc blende segment eventually taking over, as the Au particle moves onto the energetically more favourable zinc blende.

Rare cases of pure wurtzite branches are also reported in paper IV. These branches do not originate from a stacking defect on the trunk. Figure 4.16 demonstrates such a branch. It is observable that, two defect lines run through the branch, and partially through the trunk. This indicates that, the stacking defects are originated from the branch and propagate into the trunk. Forming wurtzite antimonide is so unfavourable that, the system gains energy by forming stacking defects running perpendicular to the growth direction, instead of pure wurtzite. It can also be speculated that, the defects observable in structurally impure wurtzite branches (such as figure 4.15), are produced by the wurtzite antimonide branch (similar to the nanowire in figure 4.16), propagating all the way into the branch, instead of the Au particles migrating on the trunk to find a favourable defective region.

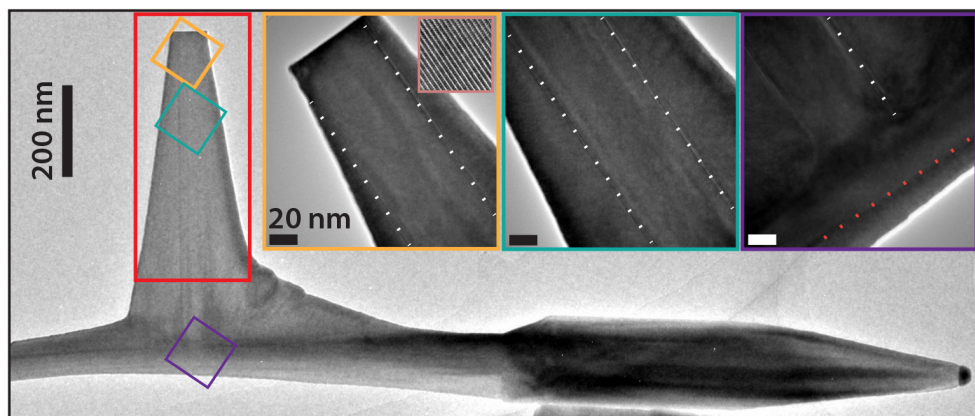


Figure 4.16. Overview and HR TEM images from a pure wurtzite branch. White dashed lines mark the defect lines propagating from the branch, partially into the trunk. The red dashed line shows the interface between the original trunk and the overgrown InAsSb shell layer. (Reprinted with permission from [133]).

The branch composition of the wurtzite and zinc blende nanowires are compared for three different Sb vapor phase compositions in table 1 of paper IV. It can be understood that, the zinc blende structure incorporates more Sb under given growth conditions. This statement holds for the parallel wurtzite-zinc blende segments within wurtzite branches as well, suggesting that Sb incorporation in wurtzite is less favourable compared to zinc blende.

The average Sb incorporation of the parallel segments in the wurtzite branch is similar to that of the zinc blende branches grown under the same conditions. This indicates that the total amount of Sb that is incorporated within the branches is determined by the vapor phase composition. This also reveals a very important fact; there simply exists a limitation to how much Sb can get incorporated into wurtzite under given conditions, and the excess amount is segregated out of wurtzite, and incorporated within the zinc blende segment instead. For pure wurtzite branches, the excessive Sb is expelled from the VLS growing branch, into a more Sb-rich shell layer grown through VS.

More detailed studies and comparisons on Sb incorporation in wurtzite and zinc blende are available within paper IV, which are all inline with the claims discussed in the previous paragraphs.

Side-by-side wurtzite InAs-GaSb nanowires

Another method for enabling 1D wurtzite antimonide growth is through particle destabilization on a wurtzite template nanowire, followed by antimonide growth. The stability of Au-In particles on InAs wurtzite nanowires have been extensively studied in [143]. With decreasing V/III, the authors report destabilization of the particle positioned on the top facet of the nanowires through In accumulation in the particle. They report a truncated facet on the top that plays an important intermediate role in the particle sliding to the side facet. They follow up their argument by recommencing growth, where they observe a number of the nanowires axially growing on the side facet, downwards, heading towards the (111) B substrate which is assumed to be energetically more favourable under typical growth conditions.

Here, after growing InAs wurtzite nanowires with the stable Au-In particle located on the top facet, the temperature is increased by 20 °C, and TMGa and TMSb precursors are provided at a low V/III ratio. At these V/III ratios, Ga starts accumulating in the particle faster than depletion through precipitation on the liquid-solid (000-1) top facet, leading to an increased particle size. As the contact angle of the particle exceeds the limit, it migrates onto the side facet, wetting more than one side facet. This is demonstrated in the schematic, overview and magnified images of figure 4.17. Growth of wurtzite GaSb then occurs, downwards covering three out of six adjacent side facets of the InAs nanowire. The XEDS elemental line-scan of figure 4.17c confirms the side-by-side configuration of the InAs-GaSb nanowires. From the images it is clear that the nanowires are significantly bent. This is due to the lattice mismatch between InAs and GaSb wurtzite [144]. GaSb has the larger lattice constant; therefore the strain causes the nanowires to bend inwards on InAs.

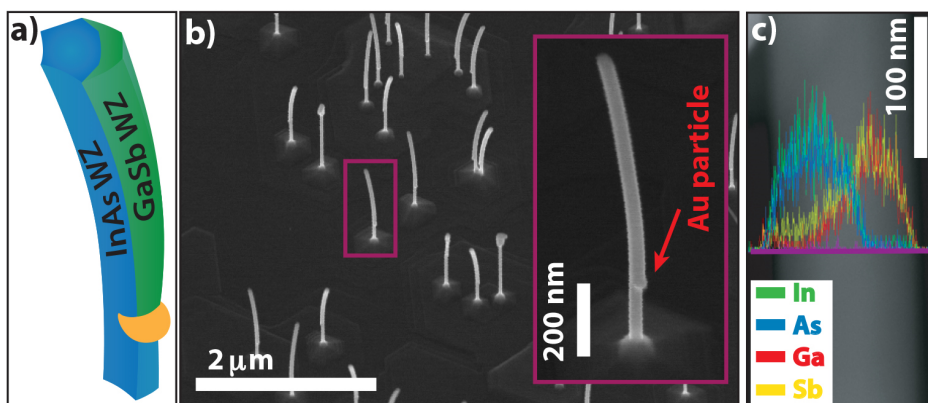


Figure 4.17. InAs-GaSb wurtzite sided-by-side nanowires: a) schematic illustration, b) SEM overview and magnified inset, and c) STEM image with elemental linescan along the radial direction of the nanowire demonstrating InAs and GaSb segments existence side-by-side.

Figure 4.18 shows overview and HRTEM images of said nanowires. It is clear that, similar to other template assisted nanowires discussed before, the GaSb segment adapts the wurtzite crystal structure of InAs. Interesting is the stepped-tapering morphology of the wurtzite GaSb observed in the top segment. This is very much inline with observations made on wurtzite GaSb shell growth discussed previously, caused by step-flow growth. Here again, steps related to occasional stacking defects (black arrow in figure 4.18b), and unrelated to them (orange arrow) are present. However, the stepping is in the opposite direction to what would be initially presumed as the growth direction; the tapering is upwards although the particle-initiated growth should be downwards.

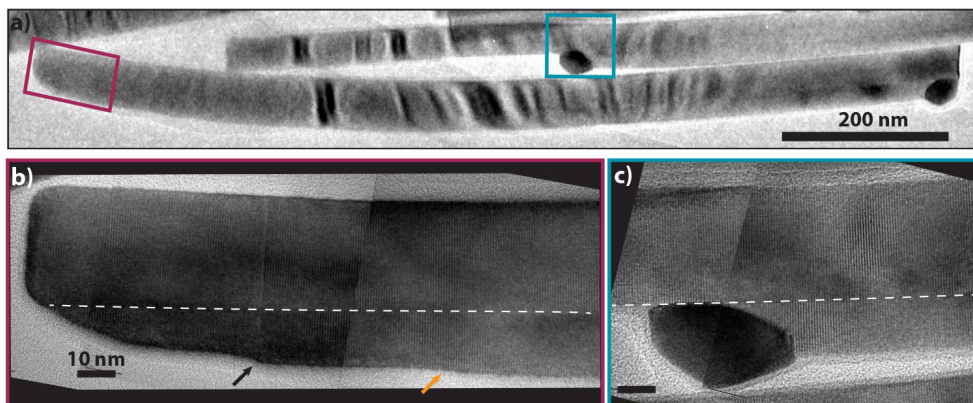


Figure 4.18. TEM overview (a) and HRTEM images (b, and c) of two side-by-side wurtzite InAs-GaSb nanowires. From b and c it is clear that both the InAs and GaSb segments have a wurtzite crystal structure. The white dashed lines represent the interface between the InAs and GaSb segments. The black arrow indicates a stepping event of the GaSb related to a stacking defect, while the orange arrow shows a stepping in the absence of any stacking defects.

This observation holds information of a very important fact: Either, in addition to the VLS grown GaSb segment on the side, a VS shell growth occurs, from particle upwards, causing this tapered morphology. Or possibly, the particle sliding is not associated with simultaneous growth of GaSb, and in fact, GaSb growth happens after particle repositioning on the side fact, along the more favourable (111) B direction, from particle towards top. This would indeed be a very special, but plausible case of template assisted VLS, in which the crystal structure is bound to that of the parallel InAs template.

Leaving the InAs template accessible, this method would indeed be best suitable for accessing 1D wurtzite antimonide. The InAs template can be removed using wet chemical etching methods, liberating the wurtzite antimonide segment. Following from this, 1D wurtzite antimonide structures will be available, which can be studied separated from influences of the InAs templates.

5. Concluding remarks and outlook

III-V nanowires in general, have been considered attractive candidates for future applications in electronics, and optoelectronics for the best part of the passed two decades. Not only does the nanowire geometry offer dimensions suitable for the miniscule future technology, but it also avails the possibility of realizing material in metastable crystal structures typically not achievable in bulk. Since the physical and material properties (band gap and surface energy values for instance) heavily rely on the crystal structure, the nanowire geometry allows access to novel material with property combinations never available before. Many attempts have been successfully made to understand the polytypism of these nanowires, and gain full control over engineering them to desire. By this, multiple alternating segments of the same material, but with different crystal structure is realizable along the length of single nanowires. Also, this control allows construction of template structures for facilitation of more complex material systems and combinations.

III-Sbs are of the most promising material systems as they offer the highest carrier mobilities and lowest band gap energies among III-V material combinations. However synthesizing III-Sb nanowires have been accompanied with certain challenges. For instance nucleating these nanowires with Sb-rich compositions directly on substrates is regarded as one of the difficulties associated with these material systems. Or, another significant challenge that synthesizing antimonides possess, is that even in the nanowire configuration they demonstrate an utterly low preference to grow in the metastable wurtzite crystal structure.

This thesis has systematically studied and addressed the mentioned challenges of III-Sb nanowire growth. Through ternary $\text{InAs}_{1-x}\text{Sb}_x$ nanowires, the direct nucleation challenge is tackled and nanowires with Sb compositions up to $x = 0.75$ are achieved. The higher end of the Sb composition spectrum is accessible through semi In-seeded as opposed to the typical Au-seeded growth, explained by the different surface energy of In and Au particles in the presence of surfactant Sb. These nanowires are immensely overgrown however, and methods for controlling the radial growth need to be devised.

In addition, through crystal structure engineering, suitable InAs template nanowires have been designed, synthesized and utilized for accessing a variety of antimonide based structures and material systems. First, selective core-shell segments of InAs-GaSb have been realized by exploiting the difference in surface

energy of alternating wurtzite and zinc blende InAs segments along the length of single nanowires. Systematic studies on the growth conditions reveal that the V/III ratio of the shell has the highest impact on the growing selective shell. This method not only is one way of controlling the overgrowth of antimonides as mentioned in the previous paragraph, but it also opens doors to unique applications such as co-axial double quantum dots where, the transport of electrons and holes can be separated.

Second, through wurtzite InAs core templates shell layers of GaSb wurtzite are realized for the first time. The wurtzite antimonide nucleation barrier is overcome at significantly higher than typical precursor total flows. The shell growth mechanism is studied in detail, where, the step-wise morphology of the shell layer suggests a step-flow growth mechanism. Realizing wurtzite GaSb opens doors towards clearing the controversy between theoretical predictions of the band gap configuration and energy of said material. The first step in this direction is already taken through electrical characterization of these wurtzite core-shell nanowires, where the higher valence band offset of wurtzite versus zinc blende GaSb is confirmed through the higher hole mobility of wurtzite. However, further studies on the band gap energy are required for clearing the controversy.

Third, using InAs wurtzite and zinc blende templates, wurtzite and zinc blende 1D branches of $\text{InAs}_{1-x}\text{Sb}_x$ are synthesized and compared. It is understood that the barrier of forming wurtzite antimonide is so large that, when growing wurtzite branches the particle likely migrates on the side facet until encountering stacking defects, then from which the branch grows. The zinc blende structure of the defect is then transferred into the branch and eventually the wurtzite branch partially transforms into zinc blende through grain boundaries, giving rise to parallel wurtzite and zinc blende segments within the branch. Or alternatively, if no trunk stacking defects are involved, the branch grows with a pure wurtzite structure. However, to partially lower the energy cost, it forms stacking defects that run through the entire branch, and well into the trunk structure. In addition, the Sb incorporation into wurtzite is systematically lower than zinc blende (pure branch or segments within the branch) at given growth conditions. The growth condition sets the limit, and the excessive Sb is segregated from wurtzite segment of wurtzite branches and incorporated within the parallel zinc blende segment instead.

These 1D wurtzite antimonide configurations require in-depth characterizations. However, since the wurtzite branches are usually accompanied by parallel zinc blende segments, and the material composition of these two segments differ from one another, interpreting the electrical characterization data performed on the branches will be challenging, as the carriers will transport through two separate channels (wurtzite and zinc blende). Isolating the wurtzite structure from the zinc

blende through chemical etching techniques will likely be difficult as well, since the material system is identical, with the only difference being the crystal structure and composition.

Another method for acquiring 1D wurtzite antimonides through InAs wurtzite templates is by growth through a delocalized particle onto the sidewall of the template. Through this fourth templating method, InAs-GaSb side-by-side nanowires are grown. This configuration will allow isolation of the electron and hole carriers from one another; something that is difficult to accomplish in coaxial core-shell configurations. In addition, through wet chemical etching techniques the GaSb wurtzite segment can be separated from its InAs template, and exclusively studied. In addition, if zinc blende segments are introduced into the wurtzite InAs template, it may lead to a multi wurtzite-zinc blende segmented GaSb structure, which can be separated by etching techniques.

Thus, this thesis overcomes the main challenges associated with III-Sb nanowire growth, opening doors towards the unique possibility of characterizing and perhaps utilizing these nanowires in the near future. If the characterizations prove promising, it will be likely necessary to take the next step and synthesize these materials template free, directly from substrates. Possibly only through template free growth intricate multi-segmented structures of antimonides will become feasible. The ground work however, of the future steps are laid within the work of this thesis, as a concrete understanding of antimonide crystal structure, radial and axial growth, and their direct nucleation from substrates is now available.

6. References

- [1] R. Waser, *Nanoelectronics and Information Technology*. 2012.
- [2] J. M. Martínez-Duart, R. J. Martín-Palma, and F. Agulló-Rueda, *Nanotechnology for Microelectronics and Optoelectronics*. 2006.
- [3] V. Mourik, K. Zuo, S. M. Frolov, S. R. Plissard, E. P. A. M. Bakkers, and L. P. Kouwenhoven, “Signatures of Majorana fermions in hybrid superconductor-semiconductor nanowire devices,” *Science*, vol. 336, no. 6084, pp. 1003–7, May 2012.
- [4] G. Whitesides, J. Mathias, and C. Seto, “Molecular self-assembly and nanochemistry: a chemical strategy for the synthesis of nanostructures,” *Science*, vol. 254, no. 5036, pp. 1312–1319, Nov. 1991.
- [5] A. K. Naik, M. S. Hanay, W. K. Hiebert, X. L. Feng, and M. L. Roukes, “Towards single-molecule nanomechanical mass spectrometry,” *Nat. Nanotechnol.*, vol. 4, no. 7, pp. 445–50, Jul. 2009.
- [6] V. K. Varadan, L. Chen, and J. Xie, *Nanomedicine: Design and Applications of Magnetic Nanomaterials, Nanosensors and Nanosystems*. 2008.
- [7] S. S. Li, Ed., *Semiconductor Physical Electronics*. New York, NY: Springer New York, 2006.
- [8] R. G. Walker, “High-speed III-V semiconductor intensity modulators,” *IEEE J. Quantum Electron.*, vol. 27, no. 3, pp. 654–667, Mar. 1991.
- [9] S. Mokkapati and C. Jagadish, “III-V compound SC for optoelectronic devices,” *Mater. Today*, vol. 12, no. 4, pp. 22–32, Apr. 2009.
- [10] Y. Li, F. Qian, J. Xiang, and C. M. Lieber, “Nanowire electronic and optoelectronic devices,” *Mater. Today*, vol. 9, no. 10, pp. 18–27, Oct. 2006.
- [11] A. Hellemans, “Nanowire Transistors Could Keep Moore’s Law Alive - IEEE Spectrum.” [Online]. Available: <http://spectrum.ieee.org/semiconductors/devices/nanowire-transistors-could-keep-moores-law-alive>. [Accessed: 25-Apr-2016].
- [12] S. N. Mohammad, “Understanding quantum confinement in nanowires: basics, applications and possible laws,” *J. Phys. Condens. Matter*, vol. 26, no. 42, p. 423202, Oct. 2014.
- [13] X. Zhao, C. M. Wei, L. Yang, and M. Y. Chou, “Quantum Confinement and Electronic Properties of Silicon Nanowires,” *Phys. Rev. Lett.*, vol. 92, no. 23, p. 236805, Jun. 2004.
- [14] J. Johansson and K. A. Dick, “Recent advances in semiconductor nanowire heterostructures,” *CrystEngComm*, 2011.

- [15] H. Chu, C. Zhou, J. Wang, and I. J. Beyerlein, "Misfit Strain Relaxation Mechanisms in Core/Shell Nanowires," *JOM*, vol. 64, no. 10, pp. 1258–1262, Sep. 2012.
- [16] O. Landré, D. Camacho, C. Bougerol, Y. M. Niquet, V. Favre-Nicolin, G. Renaud, H. Renevier, and B. Daudin, "Elastic strain relaxation in GaN/AlN nanowire superlattice," *Phys. Rev. B*, vol. 81, no. 15, p. 153306, Apr. 2010.
- [17] M. de la Mata, C. Magén, P. Caroff, and J. Arbiol, "Atomic Scale Strain Relaxation in Axial Semiconductor III-V Nanowire Heterostructures," *Nano Lett.*, vol. 14, no. 11, pp. 6614–6620, Oct. 2014.
- [18] C. N. R. Rao and A. Govindaraj, "Carbon Nanotubes," in *Nanotubes and Nanowires*, 2011.
- [19] S. P. Svensson, W. L. Sarney, H. Hier, Y. Lin, D. Wang, D. Donetsky, L. Shterengas, G. Kipshidze, and G. Belenky, "Band gap of $\text{InAs}_{1-x}\text{Sb}_x$ with native lattice constant," *Phys. Rev. B*, vol. 86, no. 24, p. 245205, Dec. 2012.
- [20] I. van Weperen, S. R. Plissard, E. P. A. M. Bakkers, S. M. Frolov, and L. P. Kouwenhoven, "Quantized conductance in an InSb nanowire," *Nano Lett.*, vol. 13, no. 2, pp. 387–91, Feb. 2013.
- [21] M. S. Gudiksen, L. J. Lauhon, J. Wang, D. C. Smith, and C. M. Lieber, "Growth of nanowire superlattice structures for nanoscale photonics and electronics," *Nature*, vol. 415, no. 6872, pp. 617–20, Feb. 2002.
- [22] B. Ganjipour, A. W. Dey, B. M. Borg, M. Ek, M.-E. Pistol, K. A. Dick, L.-E. Wernersson, and C. Thelander, "High current density Esaki tunnel diodes based on GaSb-InAsSb heterostructure nanowires," *Nano Lett.*, vol. 11, no. 10, pp. 4222–6, Oct. 2011.
- [23] A. W. Dey, E. Lind, J. Svensson, M. Ek, C. Thelander, and L.-E. Wernersson, "Design of radial nanowire tunnel field-effect transistors," in *72nd Device Research Conference*, 2014, pp. 81–82.
- [24] A. W. Dey, B. M. Borg, B. Ganjipour, M. Ek, K. A. Dick, E. Lind, C. Thelander, and L.-E. Wernersson, "High-Current GaSb/InAs(Sb) Nanowire Tunnel Field-Effect Transistors," *IEEE Electron Device Lett.*, vol. 34, no. 2, pp. 211–213, Feb. 2013.
- [25] K. Tomioka and T. Fukui, "Tunnel field-effect transistor using InAs nanowire/Si heterojunction," *Appl. Phys. Lett.*, vol. 98, no. 8, p. 83114, Feb. 2011.
- [26] M. T. Borgström, J. Wallentin, M. Heurlin, S. Fält, P. Wickert, J. Leene, M. H. Magnusson, K. Deppert, and L. Samuelson, "Nanowires With Promise for Photovoltaics," *IEEE J. Sel. Top. Quantum Electron.*, vol. 17, no. 4, pp. 1050–1061, Jul. 2011.
- [27] M. A. Zimmler, F. Capasso, S. Müller, and C. Ronning, "Optically pumped nanowire lasers: invited review," *Semicond. Sci. Technol.*, vol. 25, no. 2, p. 24001, Feb. 2010.
- [28] C. P. T. Svensson, T. Mårtensson, J. Trägårdh, C. Larsson, M. Rask, D. Hessman, L. Samuelson, and J. Ohlsson, "Monolithic GaAs/InGaP nanowire light emitting diodes on silicon," *Nanotechnology*, vol. 19, no. 30, p. 305201, Jul. 2008.
- [29] X. Guo, Y. Ying, and L. Tong, "Photonic nanowires: from subwavelength waveguides to optical sensors," *Acc. Chem. Res.*, vol. 47, no. 2, pp. 656–66, Feb. 2014.

- [30] P. Caroff, J. B. Wagner, K. a Dick, H. a Nilsson, M. Jeppsson, K. Deppert, L. Samuelson, L. R. Wallenberg, and L.-E. Wernersson, "High-quality InAs/InSb nanowire heterostructures grown by metal-organic vapor-phase epitaxy.," *Small*, vol. 4, no. 7, pp. 878–82, Jul. 2008.
- [31] Y. Wang, J. Chi, K. Banerjee, D. Grützmacher, T. Schäpers, and J. G. Lu, "Field effect transistor based on single crystalline InSb nanowire," *J. Mater. Chem.*, 2011.
- [32] Y. Zhang, L.-M. Tang, F. Ning, D. Wang, and K.-Q. Chen, "Structural stability and electronic properties of InSb nanowires: A first-principles study," *J. Appl. Phys.*, vol. 117, no. 12, p. 125707, Mar. 2015.
- [33] J. Svensson, N. Anttu, N. Vainorius, B. M. Borg, and L.-E. Wernersson, "Diameter-Dependent photocurrent in InAsSb nanowire infrared photodetectors.," *Nano Lett.*, vol. 13, no. 4, pp. 1380–5, Apr. 2013.
- [34] U. W. Pohl, "Thermodynamics of Epitaxial Layer-Growth," in *Epitaxy of Semiconductors: Introduction to Physical Principles*, Berlin, Heidelberg: Springer Berlin Heidelberg, 2013, pp. 131–170.
- [35] W. Kossel, "Zur Theorie des Kristallwachstums," *Nachrichten von der Gesellschaft der Wissenschaften zu Göttingen, Math. Klasse*, pp. 135–143, 1927.
- [36] U. W. Pohl, "Atomistic Aspects of Epitaxial Layer-Growth," in *Epitaxy of Semiconductors: Introduction to Physical Principles*, Berlin, Heidelberg: Springer Berlin Heidelberg, 2013, pp. 171–224.
- [37] I. Markov, "Surfactants in Semiconductor Heteroepitaxy: Thermodynamics and/or Kinetics?," in *Collective Diffusion on Surfaces: Correlation Effects and Adatom Interactions*, 2001, pp. 259–271.
- [38] I. Markov, "Kinetics of nucleation in surfactant-mediated epitaxy," *Phys. Rev. B*, vol. 53, no. 7, pp. 4148–4155, Feb. 1996.
- [39] R. R. Wixom, L. W. Rieth, and G. B. Stringfellow, "Sb and Bi surfactant effects on homo-epitaxy of GaAs on (001) patterned substrates," *J. Cryst. Growth*, vol. 265, no. 3–4, pp. 367–374, May 2004.
- [40] Z. X. Yang, N. Han, M. Fang, H. Lin, H. Y. Cheung, S. P. Yip, E. J. Wang, T. F. Hung, C. Y. Wong, and J. C. Ho, "Surfactant-assisted chemical vapour deposition of high-performance small-diameter GaSb nanowires," *Nat. Commun.*, 2014.
- [41] E. A. Anyebe, M. K. Rajpalke, T. D. Veal, C. J. Jin, Z. M. Wang, and Q. D. Zhuang, "Surfactant effect of antimony addition to the morphology of self-catalyzed InAs_{1-x}Sb_x nanowires," *Nano Res.*, 2015.
- [42] V. G. Dubrovskii, "Vapor-Liquid-Solid growth of nanowires," in *Nucleation theory and growth of nanostructures*, 1st ed., Springer-Verlag Berlin Heidelberg, 2014, pp. 275–395.
- [43] R. P. Sear, "Nucleation: theory and applications to protein solutions and colloidal suspensions," *J. Phys. Condens. Matter*, 2007.
- [44] M. T. Borgström, G. Immink, B. Ketelaars, R. Algra, and E. P. A. M. Bakkers, "Synergetic nanowire growth," *Nat. Nanotechnol.*, vol. 2, no. 9, pp. 541–544, Sep. 2007.

- [45] X. L. Chen, Y. C. Lan, J. Y. Li, Y. G. Cao, and M. He, "Radial growth dynamics of nanowires," *J. Cryst. Growth*, vol. 222, no. 3, pp. 586–590, 2001.
- [46] D. Kandel and E. Kaxiras, "Surfactant Mediated Crystal Growth of Semiconductors," *Phys. Rev. Lett.*, vol. 75, no. 14, pp. 2742–2745, Oct. 1995.
- [47] J. Massies, N. Grandjean, and V. H. Etgens, "Surfactant mediated epitaxial growth of $\text{In}_x\text{Ga}_{1-x}\text{As}$ on GaAs (001)," *Appl. Phys. Lett.*, 1992.
- [48] M. Copel, M. C. Reuter, M. Horn Von Hoegen, and R. M. Tromp, "Influence of surfactants in Ge and Si epitaxy on Si(001)," *Phys. Rev. B*, 1990.
- [49] V. G. Dubrovskii, "Fundamentals of nucleation theory," in *Nucleation theory and growth of nanostructures*, 1st ed., Springer-Verlag Berlin Heidelberg, 2014, pp. 1–73.
- [50] V. A. Nebol'sin and A. A. Shchetinin, "Role of Surface Energy in the Vapor–Liquid–Solid Growth of Silicon," *Inorg. Mater.*, vol. 39, no. 9, pp. 899–903.
- [51] S. Bernal, F. J. Botana, J. J. Calvino, C. López-Cartes, J. A. Pérez-Omil, and J. M. Rodríguez-Izquierdo, "The interpretation of HREM images of supported metal catalysts using image simulation: Profile view images," *Ultramicroscopy*, vol. 72, no. 3–4, pp. 135–164, 1998.
- [52] D. L. Smith, *Thin-film Deposition: Principles and Practice*. McGraw-Hill, 1995.
- [53] R. DeHoff, *Thermodynamics in Materials Science*, Second Edition. Taylor & Francis, 2006.
- [54] W. Sun, Y. Guo, H. Xu, Q. Gao, H. Hoe Tan, C. Jagadish, and J. Zou, "Polarity driven simultaneous growth of free-standing and lateral GaAsP epitaxial nanowires on GaAs (001) substrate," *Appl. Phys. Lett.*, 2013.
- [55] C. I. Oppo, J. Malindretos, R. R. Zamani, D. Broxtermann, J. Segura-Ruiz, G. Martinez-Criado, P. C. Ricci, and A. Rizzi, "Polarity dependent strongly inhomogeneous In-incorporation in GaN nanocolumns," *Nanotechnology*, 2016.
- [56] T. Ito, "Simple Criterion for Wurtzite-Zinc-Blende Polytypism in Semiconductors," *Jpn. J. Appl. Phys.*, vol. 37, no. Part 2, No. 10B, pp. L1217–L1220, Oct. 1998.
- [57] V. G. Dubrovskii, "Crystal structure of III-V nanowires," in *Nucleation theory and growth of nanostructures*, 1st ed., Springer-Verlag Berlin Heidelberg, 2014, pp. 499–571.
- [58] R. Leitsmann and F. Bechstedt, "Surface influence on stability and structure of hexagon-shaped III-V semiconductor nanorods," *J. Appl. Phys.*, 2007.
- [59] T. Akiyama, K. Sano, K. Nakamura, and T. Ito, "An empirical potential approach to wurtzite-zinc-blende polytypism in group III-V semiconductor nanowires," *Japanese J. Appl. Physics, Part 2 Lett.*, 2006.
- [60] N. V. Sibirev, M. A. Timofeeva, A. D. Bol'shakov, M. V. Nazarenko, and V. G. Dubrovskii, "Surface energy and crystal structure of nanowhiskers of III–V semiconductor compounds," *Phys. Solid State*, vol. 52, no. 7, pp. 1531–1538, Jul. 2010.
- [61] V. Pankoke, P. Kratzer, and S. Sakong, "Calculation of the diameter-dependent polytypism in GaAs nanowires from an atomic motif expansion of the formation energy," *Phys. Rev. B*, vol. 84, no. 7, p. 75455, Aug. 2011.

- [62] H. J. Joyce, J. Wong-Leung, Q. Gao, H. H. Tan, and C. Jagadish, "Phase perfection in zinc Blende and Wurtzite III-V nanowires using basic growth parameters.," *Nano Lett.*, vol. 10, no. 3, pp. 908–15, Mar. 2010.
- [63] S. Lehmann, J. Wallentin, D. Jacobsson, K. Deppert, and K. A. Dick, "A general approach for sharp crystal phase switching in InAs, GaAs, InP, and GaP nanowires using only group V flow.," *Nano Lett.*, vol. 13, no. 9, pp. 4099–105, Sep. 2013.
- [64] K. a. Dick, J. Bolinsson, M. E. Messing, S. Lehmann, J. Johansson, and P. Caroff, "Parameter space mapping of InAs nanowire crystal structure," *J. Vac. Sci. Technol. B Microelectron. Nanom. Struct.*, vol. 29, no. 4, p. 04D103, 2011.
- [65] P. Caroff, K. A. Dick, J. Johansson, M. E. Messing, K. Deppert, and L. Samuelson, "Controlled polytypic and twin-plane superlattices in iii-v nanowires.," *Nanotechnol.*, vol. 4, no. 1, pp. 50–5, Jan. 2009.
- [66] J. Bolinsson, P. Caroff, B. Mandl, and K. A. Dick, "Wurtzite-zincblende superlattices in InAs nanowires using a supply interruption method.," *Nanotechnology*, vol. 22, no. 26, p. 265606, Jul. 2011.
- [67] R. E. Algra, M. A. Verheijen, M. T. Borgström, L.-F. Feiner, G. Immink, W. J. P. van Enckevort, E. Vlieg, and E. P. A. M. Bakkers, "Twinning superlattices in indium phosphide nanowires.," *Nature*, vol. 456, no. 7220, pp. 369–72, Nov. 2008.
- [68] J. Johansson, K. A. Dick, P. Caroff, M. E. Messing, J. Bolinsson, K. Deppert, and L. Samuelson, "Diameter Dependence of the Wurtzite - Zinc Blende Transition in InAs Nanowires," pp. 3837–3842, 2010.
- [69] P. Caroff, J. Bolinsson, and J. Johansson, "Crystal Phases in III--V Nanowires: From Random Toward Engineered Polytypism," *IEEE J. Sel. Top. Quantum Electron.*, vol. 17, no. 4, pp. 829–846, Jul. 2011.
- [70] H. Huang, X. Ren, X. Ye, J. Guo, Q. Wang, X. Zhang, S. Cai, and Y. Huang, "Control of the crystal structure of InAs nanowires by tuning contributions of adatom diffusion.," *Nanotechnology*, vol. 21, no. 47, p. 475602, Nov. 2010.
- [71] J. Johansson, L. S. Karlsson, C. P. T. Svensson, T. Mrtensson, B. A. Wacaser, K. Deppert, L. Samuelson, and W. Seifert, "Structural properties of $\square 111 \square B$ -oriented III-V nanowires," *Nature Materials*. 2006.
- [72] G. B. Stringfellow, "Non-hydride group V sources for OMVPE," *J. Electron. Mater.*, vol. 17, no. 4, pp. 327–335, Jul. 1988.
- [73] D. Williams and C. Carter, *Transmission Electron Microscopy: A Textbook for Materials Science*. 2009.
- [74] I. Vurgaftman, J. R. Meyer, and L. R. Ram-Mohan, "Band parameters for III-V compound semiconductors and their alloys," *J. Appl. Phys.*, 2001.
- [75] M. Razeghi, S. Abdollahi Pour, E. Huang, G. Chen, A. Haddadi, and B. Nguyen, "Type-II InAs/GaSb photodiodes and focal plane arrays aimed at high operating temperatures," *Opto-Electronics Rev.*, vol. 19, no. 3, pp. 261–269, Jan. 2011.
- [76] V. V. R. Kishore, B. Partoens, and F. M. Peeters, "Electronic structure of InAs/GaSb core-shell nanowires," *Phys. Rev. B*, vol. 86, no. 16, p. 165439, Oct. 2012.

- [77] B. M. Borg, K. A. Dick, B. Ganjipour, M.-E. Pistol, L.-E. Wernersson, and C. Thelander, "InAs/GaSb heterostructure nanowires for tunnel field-effect transistors.," *Nano Lett.*, vol. 10, no. 10, pp. 4080–5, Oct. 2010.
- [78] B. R. Bennett, M. G. Ancona, and J. B. Boos, "Compound Semiconductors for Low-Power p-Channel Field-Effect Transistors," *MRS Bull.*, vol. 34, no. 7, pp. 530–536, Jan. 2011.
- [79] S. Datta, T. Ashley, J. Brask, L. Buckle, M. Doczy, M. Emeny, D. Hayes, K. Hilton, R. Jefferies, T. Martin, T. J. Phillips, D. Wallis, P. Wilding, and R. Chau, "85nm gate length enhancement and depletion mode InSb quantum well transistors for ultra high speed and very low power digital logic applications," in *IEEE International Electron Devices Meeting, 2005. IEDM Technical Digest., 2005*, pp. 763–766.
- [80] T. S. Low, M. W. Dvorak, M. Farhoud, R. E. Yeats, M. Iwamoto, G. K. Essilfie, T. Engel, B. Keppeler, J. S. C. Chang, J. Hadley, G. Patterson, F. Kellert, N. Moll, S. R. Bahl, C. P. Hutchinson, E. Ehlers, M. E. Adamski, M. K. Culver, D. C. D'Avanzo, and T. Shirley, "GaAsSb DHBT IC technology for RF and microwave instrumentation," in *IEEE Compound Semiconductor Integrated Circuit Symposium, 2005. CSIC '05., 2005*, p. 4 pp.
- [81] T. Ashley, L. Buckle, S. Datta, M. T. Emeny, D. G. Hayes, K. P. Hilton, R. Jefferies, T. Martin, T. J. Phillips, D. J. Wallis, P. J. Wilding, and R. Chau, "Heterogeneous InSb quantum well transistors on silicon for ultra-high speed, low power logic applications," *Electron. Lett.*, vol. 43, no. 14, p. 777, 2007.
- [82] H. A. Nilsson, M. T. Deng, P. Caroff, C. Thelander, L. Samuelson, L.-E. Wernersson, and H. Q. Xu, "InSb Nanowire Field-Effect Transistors and Quantum-Dot Devices," *IEEE J. Sel. Top. Quantum Electron.*, vol. 17, no. 4, pp. 907–914, Jul. 2011.
- [83] A. Aardvark, N. J. Mason, and P. J. Walker, "The growth of antimonides by MOVPE," *Prog. Cryst. Growth Charact. Mater.*, vol. 35, no. 2–4, pp. 207–241, Jan. 1997.
- [84] B. Mattias Borg and L.-E. Wernersson, "Synthesis and properties of antimonide nanowires.," *Nanotechnology*, vol. 24, no. 20, p. 202001, May 2013.
- [85] F. Dimroth, C. Agert, and A. . Bett, "Growth of Sb-based materials by MOVPE," *J. Cryst. Growth*, vol. 248, pp. 265–273, Feb. 2003.
- [86] G. M. Rosenblatt and C. E. Birchenall, "Vapor Pressure of Antimony by the Torsion-Effusion Method," *J. Chem. Phys.*, vol. 35, no. 3, p. 788, Jul. 1961.
- [87] F. Pascal, F. Delannoy, J. Bougnot, L. Gousskov, G. Bougnot, P. Grosse, and J. Kaoukab, "Growth and characterization of undoped and N-type (Te) doped MOVPE grown gallium antimonide," *J. Electron. Mater.*, vol. 19, no. 2, pp. 187–195, Feb. 1990.
- [88] C. H. Chen, K. T. Huang, D. L. Drobeck, and G. B. Stringfellow, "Tertiarybutyldimethylantimony for InSb growth," *J. Cryst. Growth*, 1992.
- [89] S. Gazibegovic, D. Car, H. Zhang, S. C. Balk, J. A. Logan, M. W. A. De Moor, M. C. Cassidy, R. Schmits, D. Xu, G. Wang, P. Krogstrup, R. L. M. Op Het Veld, K. Zuo, Y. Vos, J. Shen, D. Bouman, B. Shojaei, D. Pennachio, J. S. Lee, P. J. Van Veldhoven, S. Koelling, M. A. Verheijen, L. P. Kouwenhoven, C. J. Palmstrøm, and

- E. P. A. M. Bakkers, "Epitaxy of advanced nanowire quantum devices," *Nature*, 2017.
- [90] B. Ganjipour, M. Leijnse, L. Samuelson, H. Q. Xu, and C. Thelander, "Transport studies of electron-hole and spin-orbit interaction in GaSb/InAsSb core-shell nanowire quantum dots," *Phys. Rev. B*, vol. 91, no. 16, p. 161301, Apr. 2015.
- [91] S. Yazji, M. Y. Swinkels, M. De Luca, E. A. Hoffmann, D. Ercolani, S. Roddaro, G. Abstreiter, L. Sorba, E. P. A. M. Bakkers, and I. Zardo, "Assessing the thermoelectric properties of single InSb nanowires: The role of thermal contact resistance," *Semicond. Sci. Technol.*, 2016.
- [92] M. T. Deng, C. L. Yu, G. Y. Huang, M. Larsson, P. Caroff, and H. Q. Xu, "Anomalous zero-bias conductance peak in a Nb-InSb nanowire-Nb hybrid device.," *Nano Lett.*, vol. 12, no. 12, pp. 6414–9, Dec. 2012.
- [93] A. Seabaugh, "Fundamentals and current status of steep-slope tunnel field-effect transistors," in *European Solid-State Device Research Conference*, 2011.
- [94] M. Jeppsson, K. A. Dick, J. B. Wagner, P. Caroff, K. Deppert, L. Samuelson, and L.-E. Wernersson, "GaAs/GaSb nanowire heterostructures grown by MOVPE," *J. Cryst. Growth*, vol. 310, no. 18, pp. 4115–4121, Aug. 2008.
- [95] A. T. Vogel, J. de Boer, M. Becker, J. V. Wittemann, S. L. Mensah, P. Werner, and V. Schmidt, "Ag-assisted CBE growth of ordered InSb nanowire arrays," *Nanotechnology*, vol. 22, no. 1, p. 15605, Jan. 2011.
- [96] R. R. Zamani, S. Gorji Ghalamestani, J. Niu, N. Sköld, and K. A. Dick, "Polarity and growth directions in Sn-seeded GaSb nanowires," *Nanoscale*, 2017.
- [97] B. Mandl, K. a Dick, D. Kriegner, M. Keplinger, G. Bauer, J. Stangl, and K. Deppert, "Crystal structure control in Au-free self-seeded InSb wire growth.," *Nanotechnology*, vol. 22, no. 14, p. 145603, Apr. 2011.
- [98] S. Schulz, M. Schwartz, A. Kuczkowski, and W. Assenmacher, "Self-catalyzed growth of GaSb nanowires at low reaction temperatures," *J. Cryst. Growth*, 2010.
- [99] K. A. Dick, "A review of nanowire growth promoted by alloys and non-alloying elements with emphasis on Au-assisted III–V nanowires," *Prog. Cryst. Growth Charact. Mater.*, vol. 54, no. 3, pp. 138–173, 2008.
- [100] M. D. Schroer and J. R. Petta, "Correlating the nanostructure and electronic properties of InAs nanowires," *Nano Lett.*, 2010.
- [101] D. L. Dheeraj, G. Patriarche, H. Zhou, T. B. Hoang, A. F. Moses, S. Grønsberg, A. T. J. van Helvoort, B.-O. Fimland, and H. Weman, "Growth and characterization of wurtzite GaAs nanowires with defect-free zinc blende GaAsSb inserts.," *Nano Lett.*, vol. 8, no. 12, pp. 4459–63, Dec. 2008.
- [102] K. a. Dick, "A review of nanowire growth promoted by alloys and non-alloying elements with emphasis on Au-assisted III–V nanowires," *Prog. Cryst. Growth Charact. Mater.*, vol. 54, no. 3–4, pp. 138–173, Sep. 2008.
- [103] D. Ercolani, F. Rossi, A. Li, S. Roddaro, V. Grillo, G. Salvati, F. Beltram, and L. Sorba, "InAs/InSb nanowire heterostructures grown by chemical beam epitaxy.," *Nanotechnology*, vol. 20, no. 50, p. 505605, Dec. 2009.

- [104] S. R. Plissard, D. R. Slapak, M. A. Verheijen, M. Hocevar, G. W. G. Immink, I. van Weperen, S. Nadj-Perge, S. M. Frolov, L. P. Kouwenhoven, and E. P. A. M. Bakkers, "From InSb Nanowires to Nanocubes: Looking for the Sweet Spot," *Nano Lett.*, vol. 12, no. 4, pp. 1794–1798, Apr. 2012.
- [105] Y. N. Guo, J. Zou, M. Paladugu, H. Wang, Q. Gao, H. H. Tan, and C. Jagadish, "Structural characteristics of GaSb/GaAs nanowire heterostructures grown by metal-organic chemical vapor deposition," *Appl. Phys. Lett.*, vol. 89, no. 23, p. 231917, 2006.
- [106] S. G. Ghalamestani, M. Ek, and K. A. Dick, "Realization of single and double axial InSb-GaSb heterostructure nanowires," *Phys. status solidi - Rapid Res. Lett.*, vol. 8, no. 3, pp. 269–273, Mar. 2014.
- [107] H. W. Melville and S. C. Gray, "The vapour pressure of red phosphorus," *Trans. Faraday Soc.*, vol. 32, p. 1026, Jan. 1936.
- [108] A. Lisak and K. Fitzner, "Vapor pressure measurements of arsenic and arsenic trioxide over condensed phases," *J. Phase Equilibria*, vol. 15, no. 2, pp. 151–154, Apr. 1994.
- [109] "Decomposition Mechanism of Trimethylantimony and reactions with Trimethylindium."
- [110] C. W. Wilmsen, "Oxide/III-V Compound Semiconductor Interfaces," in *Physics and Chemistry of III-V Compound Semiconductor Interfaces*, C. W. Wilmsen, Ed. Boston, MA: Springer US, 1985, pp. 403–462.
- [111] B. M. Borg, K. A. Dick, J. Eymery, and L.-E. Wernersson, "Enhanced Sb incorporation in InAsSb nanowires grown by metalorganic vapor phase epitaxy," *Appl. Phys. Lett.*, vol. 98, no. 11, p. 113104, Mar. 2011.
- [112] L. Lugani, D. Ercolani, F. Beltram, and L. Sorba, "Growth mechanism of InAs–InSb heterostructured nanowires grown by chemical beam epitaxy," *J. Cryst. Growth*, vol. 323, no. 1, pp. 304–306, May 2011.
- [113] M. Jeppsson, K. A. Dick, J. B. Wagner, P. Caroff, K. Deppert, L. Samuelson, and L. E. Wernersson, "GaAs/GaSb nanowire heterostructures grown by MOVPE," *J. Cryst. Growth*, 2008.
- [114] B. Mandl, K. A. Dick, D. Kriegner, M. Keplinger, G. Bauer, J. Stangl, and K. Deppert, "Crystal structure control in Au-free self-seeded InSb wire growth," *Nanotechnology*, vol. 22, no. 14, p. 145603, Apr. 2011.
- [115] S. Conesa-Boj, D. Kriegner, X.-L. Han, S. Plissard, X. Wallart, J. Stangl, A. Fontcuberta i Morral, and P. Caroff, "Gold-free ternary III-V antimonide nanowire arrays on silicon: twin-free down to the first bilayer," *Nano Lett.*, vol. 14, no. 1, pp. 326–32, Jan. 2014.
- [116] W.-N. Du, X.-G. Yang, X.-Y. Wang, H.-Y. Pan, H.-M. Ji, S. Luo, T. Yang, and Z.-G. Wang, "The self-seeded growth of InAsSb nanowires on silicon by metal-organic vapor phase epitaxy," *J. Cryst. Growth*, vol. 396, pp. 33–37, Jun. 2014.
- [117] E. A. Anyebe and Q. Zhuang, "Self-catalysed InAs_{1-x}Sb_x nanowires grown directly on bare Si substrates," *Mater. Res. Bull.*, vol. 60, pp. 572–575, Dec. 2014.
- [118] A. C. Farrell, W.-J. Lee, P. Senanayake, M. A. Haddad, S. V. Prikhodko, and D. L. Huffaker, "High-Quality InAsSb Nanowires Grown by Catalyst-Free Selective-Area

- Metal-Organic Chemical Vapor Deposition.,” *Nano Lett.*, vol. 15, no. 10, pp. 6614–9, Oct. 2015.
- [119] A. T. Vogel, J. de Boor, M. Becker, J. V Wittemann, S. L. Mensah, P. Werner, and V. Schmidt, “Ag-assisted CBE growth of ordered InSb nanowire arrays,” *Nanotechnology*, vol. 22, no. 1, p. 15605, Jan. 2011.
- [120] M. Pozuelo, H. Zhou, S. Lin, S. A. Lipman, M. S. Goorsky, R. F. Hicks, and S. Kodambaka, “Self- catalyzed growth of InP/ InSb axial nanowire heterostructures,” *J. Cryst. Growth*, 2011.
- [121] S. Gorji Ghalamestani, S. Lehmann, and K. A. Dick, “Can antimonide-based nanowires form wurtzite crystal structure?,” *Nanoscale*, vol. 8, no. 5, pp. 2778–86, Jan. 2016.
- [122] L. Namazi, S. G. Ghalamestani, S. Lehmann, R. R. Zamani, and K. A. Dick, “Direct nucleation, morphology and compositional tuning of InAs_{1-x}Sb_x nanowires on InAs (111) B substrates,” *Nanotechnology*, vol. 28, no. 16, p. 165601, Apr. 2017.
- [123] B. J. Keene, “Review of Data for the Surface-Tension of Pure Metals,” *International Materials Reviews*. 1993.
- [124] M. Jeppsson, K. a. Dick, J. B. Wagner, P. Caroff, K. Deppert, L. Samuelson, and L.-E. Wernersson, “GaAs/GaSb nanowire heterostructures grown by MOVPE,” *J. Cryst. Growth*, vol. 310, no. 18, pp. 4115–4121, Aug. 2008.
- [125] Z. Zanolli, F. Fuchs, J. Furthmüller, U. von Barth, and F. Bechstedt, “Model GW band structure of InAs and GaAs in the wurtzite phase,” *Phys. Rev. B*, vol. 75, no. 24, p. 245121, Jun. 2007.
- [126] B. Ketterer, M. Heiss, E. Uccelli, J. Arbiol, and A. F. I. Morral, “Untangling the Electronic Band Structure of Wurtzite GaAs Nanowires by Resonant Raman Spectroscopy,” *ACS Nano*, 2011.
- [127] M. Nilsson, L. Namazi, S. Lehmann, M. Leijnse, K. A. Dick, and C. Thelander, “Single-electron transport in InAs nanowire quantum dots formed by crystal phase engineering,” p. 9, Nov. 2015.
- [128] M. Murayama and T. Nakayama, “Chemical trend of band offsets at wurtzite/zinc-blende heterocrystalline semiconductor interfaces,” *Phys. Rev. B*, 1994.
- [129] M. Nilsson, L. Namazi, S. Lehmann, M. Leijnse, K. A. Dick, and C. Thelander, “Electron-hole interactions in coupled InAs-GaSb quantum dots based on nanowire crystal phase templates,” *Phys. Rev. B*, vol. 94, no. 11, p. 115313, Sep. 2016.
- [130] T. Rieger, T. Schäpers, D. Grützmacher, and M. I. Lepsa, “Crystal Phase Selective Growth in GaAs/InAs Core–Shell Nanowires,” *Cryst. Growth Des.*, vol. 14, no. 3, pp. 1167–1174, Mar. 2014.
- [131] L. Namazi, M. Nilsson, S. Lehmann, C. Thelander, and K. A. Dick, “Selective GaSb radial growth on crystal phase engineered InAs nanowires,” *Nanoscale*, vol. 7, no. 23, pp. 10472–81, Jun. 2015.
- [132] S. G. Ghalamestani, A. M. Munshi, D. L. Dheeraj, B.-O. Fimland, H. Weman, and K. A. Dick, “Self-catalyzed MBE grown GaAs/GaAs(x)Sb(1-x) core-shell nanowires in ZB and WZ crystal structures,” *Nanotechnology*, vol. 24, no. 40, p. 405601, Oct. 2013.

- [133] M. Dahl, L. Namazi, R. R. Zamani, and K. A. Dick, "Sb Incorporation in Wurtzite and Zinc Blende $\text{InAs}_{1-x}\text{Sb}_x$ Branches on InAs Template Nanowires," *Small*, 1703785, Jan. 2018.
- [134] H. I. T. Hauge, M. A. Verheijen, S. Conesa-Boj, T. Etzelstorfer, M. Watzinger, D. Kriegner, I. Zardo, C. Fasolato, F. Capitani, P. Postorino, S. Kölling, A. Li, S. Assali, J. Stangl, and E. P. A. M. Bakkers, "Hexagonal Silicon Realized," *Nano Lett.*, 2015.
- [135] C. Thelander, P. Caroff, S. Plissard, and K. A. Dick, "Electrical properties of $\text{InAs}_{1-x}\text{Sb}_x$ and InSb nanowires grown by molecular beam epitaxy," *Appl. Phys. Lett.*, vol. 100, no. 23, p. 232105, Jun. 2012.
- [136] L. C. Chuang, M. Moewe, C. Chase, N. P. Kobayashi, C. Chang-Hasnain, and S. Crankshaw, "Critical diameter for III-V nanowires grown on lattice-mismatched substrates," *Appl. Phys. Lett.*, vol. 90, no. 4, p. 43115, Jan. 2007.
- [137] F. Glas, "Critical dimensions for the plastic relaxation of strained axial heterostructures in free-standing nanowires."
- [138] A. Belabbes, C. Panse, J. Furthmüller, and F. Bechstedt, "Electronic bands of III-V semiconductor polytypes and their alignment," *Phys. Rev. B*, vol. 86, no. 7, p. 75208, Aug. 2012.
- [139] C. Y. Yeh, S. H. Wei, and A. Zunger, "Relationships between the band gaps of the zinc-blende and wurtzite modifications of semiconductors," *Phys. Rev. B*, 1994.
- [140] A. De and C. E. Pryor, "Predicted band structures of III-V semiconductors in the wurtzite phase," *Phys. Rev. B*, vol. 81, no. 15, p. 155210, Apr. 2010.
- [141] M. Gmitra and J. Fabian, "First-principles studies of orbital and spin-orbit properties of GaAs, GaSb, InAs, and InSb zinc-blende and wurtzite semiconductors," *Phys. Rev. B*, 2016.
- [142] T. Xu, K. A. Dick, S. Plissard, T. H. Nguyen, Y. Makoudi, M. Berthe, J.-P. Nys, X. Wallart, B. Grandidier, and P. Caroff, "Faceting, composition and crystal phase evolution in III-V antimonide nanowire heterostructures revealed by combining microscopy techniques," *Nanotechnology*, vol. 23, no. 9, p. 95702, Mar. 2012.
- [143] M. U. Tornberg, K. A. Dick, and S. Lehmann, "Thermodynamic Stability of Gold-Assisted InAs Nanowire Growth," *J. Phys. Chem. C*, p. acs.jpcc.7b06138, Sep. 2017.
- [144] F. Bechstedt and A. Belabbes, "Structure, energetics, and electronic states of III-V compound polytypes," *J. Phys. Condens. Matter*, vol. 25, no. 27, p. 273201, Jul. 2013.

Paper I



Direct nucleation, morphology and compositional tuning of $\text{InAs}_{1-x}\text{Sb}_x$ nanowires on InAs (111) B substrates

Luna Namazi¹, Sepideh Gorji Ghalamestani¹, Sebastian Lehmann¹,
Reza R Zamani¹ and Kimberly A Dick^{1,2}

¹ Solid State Physics, Lund University, Box 118, SE-221 00 Lund, Sweden

² Centre for Analysis and Synthesis, Lund University, Box 124, SE-221 00 Lund, Sweden

E-mail: Luna.Namazi@ftf.lth.se

Received 7 February 2017

Accepted for publication 7 March 2017

Published 27 March 2017



Abstract

III–V ternary nanowires are interesting due to the possibility of modulating their physical and material properties by tuning their material composition. Amongst them $\text{InAs}_{1-x}\text{Sb}_x$ nanowires are good candidates for applications such as Infrared detectors. However, this material has not been grown directly from substrates, in a large range of material compositions. Since the properties of ternaries are alterable by tuning their composition, it is beneficial to gain access to a wide range of composition tunability. Here we demonstrate direct nucleation and growth of $\text{InAs}_{1-x}\text{Sb}_x$ nanowires from Au seed particles over a broad range of compositions ($x = 0.08\text{--}0.75$) for different diameters and surface densities by means of metalorganic vapor phase epitaxy. We investigate how the nucleation, morphology, solid phase Sb content, and growth rate of these nanowires depend on the particle dimensions, and on growth conditions such as the vapor phase composition, V/III ratio, and temperature. We show that the solid phase Sb content of the nanowires remains invariant towards changes of the In precursor flow. We also discuss that at relatively high In flows the growth mechanism alters from Au-seeded to what is referred to as semi In-seeded growth. This change enables growth of nanowires with a high solid phase Sb content of 0.75 that are not feasible via Au-seeded growth. Independent of the growth conditions and morphology, we report that the nanowire Sb content changes over their length, from lower Sb contents at the base, increasing to higher amounts towards the tip. We correlate the axial Sb content variations to the axial growth rate measured *in situ*. We also report spontaneous core–shell formation for Au-seeded nanowires, where the core is Sb-rich in comparison to the Sb-poor shell.

Supplementary material for this article is available [online](#)

Keywords: III–V nanowire, $\text{InAs}_{1-x}\text{Sb}_x$, ternary, antimonide, material tunability, Au-seeded, direct nucleation

(Some figures may appear in colour only in the online journal)

1. Introduction

Among binary III–V semiconductors, InAs and InSb, and consequently their ternary $\text{InAs}_{1-x}\text{Sb}_x$ compound offer some of the most interesting properties, making them suitable for many applications in electronics and optoelectronics. Of these properties for InAs one can mention a small band gap of 0.35 eV, a

low electron effective mass of $0.023m_0$, hence a high electron mobility of $33\,000\text{ cm}^2\text{ V}^{-1}\text{ s}^{-1}$ [1–3], and for InSb a band gap of 0.17 eV, and a low electron effective mass of $0.013m_0$ that results in an electron mobility of $77\,000\text{ cm}^2\text{ V}^{-1}\text{ s}^{-1}$ [4, 5]. InSb also has a hole mobility of $850\text{ cm}^2\text{ V}^{-1}\text{ s}^{-1}$. These properties are of high importance for high-speed low-power electronic devices and quantum transport studies [6]. In addition, due

to its high thermoelectric figure of merit (0.6), InSb is also considered a good candidate for thermoelectric power generation [7]. InAs_{1-x}Sb_x as a combination of these binary materials offers precise modulation of the physical and electrical properties between those of InAs and InSb as a result of compositional tunability. For instance, the band gap can be tuned through most of mid-infrared (IR) range (2–8 μm), hence InAs_{1-x}Sb_x has proven to have a high potential for future optical applications such as IR photodetectors [8] and gas sensors [9]. Also, at a composition of $x = 0.63$ the narrowest band gap among all III–V materials can be reached (around 100 meV) [10]. Similar to its constituting binary InSb, InAs_{1-x}Sb_x also has a small electron effective mass. As a result, quantum confinement happens in larger structures that are readily accessible with the nanowire geometry. Therefore, this material system is interesting for fundamental electron transport studies [11, 12].

However, as a result of the rather large lattice mismatch between InAs and InSb, a miscibility gap is reported for the bulk pseudobinary system of InAs–InSb over almost the entire compositional range at conventional growth temperatures [13–15]. Grown in the form of nanowires instead, compositions of InAs_{1-x}Sb_x within the reported miscibility gap have been achieved [16]. This opens the possibility of tuning the composition of InAs_{1-x}Sb_x nanowires to suit various applications.

In general, growing Sb-based nanowires from Au seed particles directly from the substrate has been shown challenging [17, 18]. In order to overcome some of these challenges, a stem (often the same material as the substrate) is grown to assist the nucleation of the Au particle when exposed to Sb [17, 19]. InAs_{1-x}Sb_x nanowires have not been an exception from this approach until now, where in the study reported in [16], an InAs stem is grown to facilitate InAs_{1-x}Sb_x nucleation on InAs substrates.

Since InSb has the highest lattice parameter amongst III–V materials, its ternary InAs_{1-x}Sb_x with material compositions high in the Sb content will also have large lattice parameters. Therefore growing these materials on substrates of other materials usually results in defect formation. However, due to strain relaxation realized in nanowires, different compositions of InAs_{1-x}Sb_x nanowires can be grown heteroepitaxially on InAs stems [20]. By this, vertical growth from Au particles in the presence of Sb on InAs substrates is realized [18].

There are reports on full compositional tuning of Au-seeded grown InAs_{1-x}Sb_x nanowires with stems [16, 20]. However, the presence of the stem can cause some additional challenges and limit the growth parameter space of such nanowires. For instance, since As has a high vapor pressure, As-containing segments tend to decompose when exposed to a long duration of As-free and/or Sb-containing environments [18]. Even though a few studies on directly grown InAs_{1-x}Sb_x nanowires from the substrate have been carried out, they do not demonstrate a wide composition range. For instance, InAs_{1-x}Sb_x self-seeded nanowire growth on Si substrates are reported in the literature [21–23]. Selective area growth on InAs substrates has been carried out recently [24] where a small range of tuning between $x = 0.08$ – 0.15 is reported.

Therefore, studying direct nucleation and growth of Au seeded InAs_{1-x}Sb_x nanowires from InAs substrates, can offer further understanding of the Sb incorporation within the nanowires, and clarifying if and in what manner the mentioned factors are interrelated.

We demonstrate direct nucleation and growth of InAs_{1-x}Sb_x on InAs (111) B substrates using different Au particle diameters and surface densities. We report a comprehensive study on the growth of InAs_{1-x}Sb_x nanowires covering a compositional range from very low Sb contents of $x = 0.08$ up to $x = 0.75$. We have systematically investigated the axial growth rate, and Sb content of these nanowires with respect to the particle diameter, density, and growth conditions such as temperature, total precursor flow, the group V and the group III precursor flows, and V/III ratio. We show that the aerial density of the initial seed particle, and the vapor phase composition have an impact on the Sb incorporation into the nanowires, while temperature, and group III precursor flow do not have any clear effects. The group III precursor flow however, has a significant effect on nucleation of nanowires grown directly from the substrate.

2. Experimental details

The nanowires were grown by means of metal organic vapor phase epitaxy (MOVPE) in a $3 \times 2''$ close-couple shower-head reactor (Aixtron CCS) with H₂ as the carrier gas with a total flow of 81 min^{-1} and at a pressure of 100 mbar. InAs (111) B epi-ready substrates covered with pre-deposited Au aerosol nanoparticles, with different diameters of 30, 40, 50, and 60 nm, and two different surface densities of 0.1, and $1 \mu\text{m}^{-2}$ were utilized. By this, we study the diameter and density effects on the nanowire morphology as well as the Sb incorporation. trimethylindium (TMIIn) was used as the group III precursor, while trimethylantimony (TMSb) and arsine (AsH₃) were used as the two group V precursors. The ratio between the group V precursors, namely the vapor phase composition is defined as:

$$x_v = \frac{[\text{TMSb}]}{[\text{TMSb}] + [\text{AsH}_3]}, \quad (1)$$

where [TMSb] and [AsH₃] are the molar fractions of Sb and As precursors. However, the Sb content in the solid phase composition of the nanowires is simply referred to as 'x' throughout the paper.

Prior to growth, the samples were annealed at 550 °C to remove the native oxide on the substrates. This was done under a supply of AsH₃ with a molar fraction of 2.5×10^{-3} to prevent InAs substrate decomposition at high temperatures. Afterwards the temperature was ramped down to the set growth temperature—mainly 450 °C, except for the temperature studies—and the nanowire growth was commenced by simultaneously introducing TMSb and TMIIn into the reactor, while changing the AsH₃ molar fraction to a lower value. Unless stated otherwise, the growth time was set to 50 min. For studying the temperature dependence, all growth parameters were kept constant while only the temperature was varied for each run from 435 °C to 480 °C. For the V/III ratio

series the group III precursor molar fraction (TMIn) was solely changed to a different value for each run while that of the group V precursors were kept constant; i.e. TMSb and AsH₃ at 4×10^{-4} and 1.0×10^{-4} , respectively. By doing this, x_v was kept at a constant value of 0.8; therefore this series was not performed under an identical total flow value. When studying the effects of x_v , the group V vapor phase composition, on the solid phase composition, it was varied ranging from 0.2 to 0.96, while keeping the growth time and temperature constant. To achieve this wide range of solid phase composition the V/III ratio was also varied in addition to x_v . For the total flow studies, the V/III ratio and x_v were kept constant at 19 and 0.8, respectively.

For terminating growth, all the precursors were simultaneously turned off, and the samples were cooled under a H₂ flow (see SI 1 is available online at stacks.iop.org/NANO/28/165601/mmedia).

The grown samples were investigated by means of scanning electron microscopy (SEM) (Zeiss LEO Gemini 1560) with typical accelerating voltages of 5–15 kV, under a tilting angle of 30° with respect to the substrate surface normal. For gaining compositional information a JEOL SEM (JSM-6700F) equipped with an x-ray energy dispersive spectroscopy (XEDS) detector was used. In order to achieve compositional information along the entire length of the nanowires, the as-grown samples were placed grown-side-down on sticky carbon tape to transfer the nanowires from the substrate onto a conductive carbon tape. The substrate was then removed and XEDS was performed with an acceleration voltage of 15 kV on the laying nanowires. This voltage was chosen to be able to cover the characteristic x-ray energies of the present elements ranging from the L_α lines of In at 3.28 keV as the lowest, to the K_α lines of As at 10.53 keV being the highest in value. The compositional analysis was carried out for 20–30 nanowires per sample. High resolution transmission electron microscopy (HRTEM) was performed in a JEOL 3000F TEM, equipped with a field-emission gun and operated at an acceleration voltage of 300 kV. XEDS analysis was conducted with high angle annular dark field in scanning TEM (HAADF-STEM) mode by using an Oxford Instrument XEDS and a HAADF detector for compositional investigations of one sample. For TEM characterization, the nanowires were transferred to lacey carbon in film coated copper TEM grids by mechanically breaking them off from the growth substrate. Using a Laytec optical reflectometry system the axial growth rate of nanowires on one sample was measured *in situ* [25].

3. Results and discussions

In this section we will demonstrate and discuss the results obtained on the nanowire morphology and Sb content from the different studied growth parameters. Initially, in section (3.1) the change along the axial and radial directions of the Sb content of the nanowires investigated for one selected sample is discussed. It is necessary to mention that the Sb content of all nanowires investigated by XEDS

gradually increases from the base towards a certain height, from where onwards the Sb content remains more or less constant. Therefore, the Sb content presented in the rest of the work is an average value over the Sb content of four or more points along the axial length of each nanowire. Also, in this section (3.1) the axial growth rate is correlated with Sb content along the axial direction of the nanowire.

From there onwards, we will discuss how the directly controllable growth parameters affect the direct nucleation, morphology, and Sb incorporation into the nanowires, i.e. (3.2) the Au particle diameter and density, (3.3) the growth temperature, (3.4) changes in V/III ratio by only changing TMIn, and (3.5) varying the vapor phase composition.

For each studied growth condition, samples covered with Au aerosol of two areal densities of 0.1 and 1 μm⁻², and four nominal diameters of 30, 40, 50, and 60 nm for each density were used. We will first demonstrate the effects of the areal density and initial particle diameter (section 3.2), and throughout the rest of the paper samples with an initial Au particle diameter of 40 or 50 nm will be presented in order to keep the discussion short.

3.1. Correlating the axial growth rate and composition of the nanowires

Using the *in situ* optical reflectometry system the axial growth rate of nanowires on a sample with a nominal particle diameter of 50 nm and a density of 1 μm⁻² was measured. This study was conducted in order to deduce whether or not the growth rate and the Sb incorporation along the length of the nanowires were correlated. TEM combined with XEDS was also utilized for studying the faceting of the nanowires, radial composition, and also for confirming the data obtained from SEM-XEDS regarding the axial Sb content.

Figure 1(a) is an SEM image of the grown nanowires on their original substrate, while figure 1(b) shows a low magnification TEM image of a nanowire, which reveals a dominant zinc blende structure with a few twin defects (more deducible from the diffraction pattern in the inset). From the overview SEM image of figure 1(a) we can already observe three main segments along the nanowire lengths where a change in faceting occurs. This is confirmed from the intensity profiles of a HAADF-STEM image shown in figure 1(c), where each line shows a different radial cross section. The lower part of the nanowire seems to have a hexagonal (possibly truncated, {112}-type faceted) cross section, while in the middle the cross section tends from hexagonal to triangular. This triangular shape becomes less dominant close to the tip, possibly due to emergence of more twin defects causing facet rotation. It is worth mentioning that the very short segment at the very top of the nanowire contains a twin plane that has led to the visible diffraction contrast in figure 1(c). XEDS point measurements along the length of nanowires from the same sample were carried out post growth using SEM. Figure 1(d) demonstrates the analyzed sites on a nanowire lying on a carbon tape from which compositional information has been obtained. In figure 1(e), a HAADF-STEM image of a nanowire from which axial line scans are

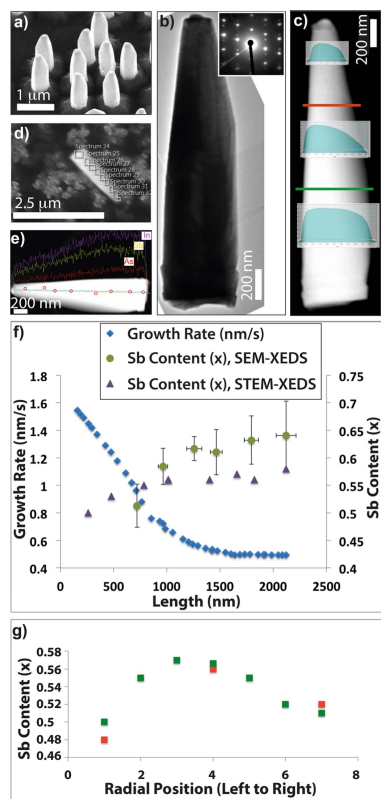


Figure 1. (a) 30° tilted SEM image showing nanowires with three segments along the length in which a facet change occurs. The growth was done with a total precursor flow of 4.6×10^{-4} , at 450 °C for 50 min. The initial Au-seed particles have a diameter of 50 nm and a surface density of $1 \mu\text{m}^{-2}$. (b) Low magnification TEM image of a similar wire as those shown in (a), from which the diffraction pattern in the inset is taken. The nanowire demonstrates a zinc blende structure with occasional twin defects. (c) STEM image with overlaid intensity profiles on the positions where the facet changes take place. The red and green lateral lines depict radial positions that the elemental mapping demonstrated in (g) are obtained from. Note, the darker contrast observed below the particle in figure (c) is merely a diffraction contrast from a twinned segment. (d) SEM image of a representative nanowire on which elemental point analyses are attained along the length by SEM-XEDS (demonstrated by green data points in (f)). The nanowire is lying laterally on a sticky carbon tape. (e) Elemental mapping along the nanowire length obtained by STEM-XEDS. The line scans demonstrate the intensity variations of the characteristic x-rays of In, As, and Sb elements axially. The red circles are related to the points from which elemental point analysis (demonstrated in graph (f)) by the purple data points) are extracted. (f) Graph plotting the growth rate (left vertical axis) and the Sb content (right vertical axis) of the nanowires gained by SEM and STEM-XEDS versus nanowire length. The growth rate and the Sb content show a correlated opposing trend. Also, it is clear that the plots related to the Sb content gain by the two different methods are in close agreement. (g) The radial Sb content of the nanowires taken from the two positions along the length marked in figure (c). The plots confirm the spontaneous core-shell formation of the ternary $\text{InAs}_{1-x}\text{Sb}_x$ nanowires with an Sb-poor shell and an Sb-rich core.

obtains is depicted. Also, point analyses along the length of this nanowire have been carried out which are marked by the red circles. The datasets obtained from SEM and STEM XEDS in figure 1(f) related to the axial Sb content of the nanowires on the right axis (green and purple data sets) are comparable. Both datasets show that the Sb content of the nanowires varies along the length: increasing from lower amounts at the base to higher amounts towards the tip. It is directly understood from this comparison that there is a very close overlap of the data obtained from the SEM and TEM, where the STEM-XEDS data sets fall close to the lower end of the error bars of the SEM-XEDS data sets. It is also worth mentioning that all the other samples investigated by SEM-XEDS throughout the paper show a similar trend of increasing Sb content along the length.

The graph in 1(f) also depicts the axial growth rate on the left axis versus the length of the nanowire as deduced from *in situ* optical reflectometry. An initial decrease in the axial growth rate can be deduced from the graph. Note that two slightly different slopes are observed, which may be correlated to the facet changings marked in figure 1(c). The drastic decrease in growth rate might be related to the migration length of the adatoms diffusing from the surface. As the diffusion length limit is reached, less material reaches the particle; hence the growth rate decreases [26]. This decline continues until a steady but low growth rate is reached. Connecting this to the increasing trend of Sb concentration along the length of the nanowires demonstrates a close correspondence of the growth rate and Sb incorporation with an opposing trend. Note the offset in length related to nanowires on which XEDS analysis using an SEM has been performed. This is related to nanowires breaking off from their as-grown substrates onto the carbon tape somewhere close to the base and not precisely at the end, leaving small studs behind. As a result not complete length nanowires are transferred to the carbon tape. Comparing the two plots of Sb content and growth rate, it can be speculated that the first regime, where the Sb content is increasing while the growth rate decreases, may be related to the time it takes for Sb adatoms to accumulate within the particle, hence a strong increase in the Sb content over the length of the nanowires over the first regime is observed. This may also affect the growth rate; as more Sb is accumulated in the particle the nanowire growth gradually shifts from InAs, which is reported to have a faster growth rate, towards InSb , with a slower growth rate in comparison. This gradual change in Sb composition along the length may also be related to change in lateral facets along the nanowire length. It must be noted however that, we do not deduce any direct causations from the correlation between the two plots, and simply report on observing them.

Moreover, radial compositional analysis was done on different positions along the length of the nanowire using STEM-XEDS. These positions are marked with the red and green lines on figure 1(c). Ternary nanowires are known to spontaneously form core-shell structures [27–31]. Since the growth mechanisms of axial and radial growths are completely different, (vapor-liquid-solid (VLS) versus vapor-solid (VS), respectively), different material compositions of

the core and the shell of the nanowires can occur as a result of different pathways of adatom incorporation in VLS and VS. In rare cases these different pathways may also lead to different crystal structures of the core and shell, but we do not observe this spontaneous crystal change. The spontaneous core-shell formation is asserted for these nanowires as well from the graph in figure 1(g) where radial point analyses of the red and green lines on figure 1(c) are demonstrated. The Sb content is plotted versus the radial position on the depicted nanowire of figure 1(c), from far most left to the far most right. From both data sets, it is clear that the Sb content is much higher in the middle compared to the side of the nanowire. This indicates that the shell has a lower Sb content in comparison to the core. Therefore, the change in the axial Sb content of figure 1(f) is also related to a more Sb-poor shell in comparison to the core. Regarding this matter, it may also be speculated that the gradual increase in Sb composition along the axial direction of the nanowire may partially be an outcome of the core-shell formation. As evident from the tapered morphology of the nanowire, the shell is thicker towards the bottom in comparison to the top. With knowledge that the shell is Sb-poor, it can be reasoned that it may lead to a lower average Sb count from the bottom compared to the top. As the shell thins down towards the tip of the nanowire, the acquired Sb signals will be mainly from the core, which is Sb-rich compared to the shell.

3.2. Au particle diameter and density

In figures 2(a)–(h), SEM images of eight samples with Au particle diameters from 30 to 60 nm and two surface densities of 0.1 and $1 \mu\text{m}^{-2}$ per diameter are shown. All these samples are grown under identical growth conditions (same growth run). Note that all the nanowires have tapered morphology. This statement holds for all of the nanowires that are seeded with Au particles throughout the paper. The dimensions of the initial Au particles affect the morphology and aspect ratio of the nanowires. From these images, it is clear that the areal density drastically affects the morphology of the grown nanowires, as the nanowires on samples with the higher areal density (density of $1 \mu\text{m}^{-2}$) are shorter and thinner, which may suggest lower average radial and axial growth rates. The graph in figure 2(i) confirms the trends observed with the length dependence on the areal density. The displayed tendency can be explained by a competition for material between the nanowires at a higher surface density, limited by the diffusion length of the adatoms and the collection area of the nanowires [32, 33].

The tapering of the nanowires grown under these specific growth conditions shows a step-like structure where the angle of the tapering changes along the length. This is more obvious from the SEM images in figures 2(a)–(d) (surface density of $0.1 \mu\text{m}^{-2}$). This may be related to the previously mentioned axial change in composition, as the precursor pyrolysis, surface energies, and many other factors that affect VS growth on the side facets are altered by composition.

It can also be speculated that the crystal structure of the nanowires is largely affected by their initial particle diameter and surface density [34], i.e. nanowires grown on samples with higher Au particle surface densities are different in their crystal structure compared to lower surface densities. An explanation to the tapering from midway to the top of the smaller diameter nanowires, may be speculated as a change in crystal structure midway along the length, from where after they grow with what seems like a mixed crystal structure. This is deduced from the contrasts observed in the SEM images; where there is a change in the crystal structure, or a facet rotation in case of twinning, one can observe the change in contrast along the nanowires. This is in contrast with the case of larger diameters, where the crystal structure appears to be mixed from the very base of the nanowires. It is worth noting though, most studies on Sb-based nanowires report zinc blende crystal structures even at very low Sb concentrations [16, 35]. However, due to the large dimensions, the majority of the nanowires were not suitable for acquiring interpretable crystal structure information using the TEM.

It is worth noting that overgrowth towards the base of the nanowires with the lower surface density is much larger in comparison to their counterparts with the higher surface density. From the graph in figure 2(i), no conclusive effect of the initial diameter of the Au particle on the length can be deduced.

Measuring the solid phase Sb content of the nanowires for different initial Au particle diameters and densities shows a trend of higher Sb content for lower surface densities in comparison with the higher density. Four data sets for the two different surface densities are illustrated in the graph in figure 2(j). Three of the data sets (marked with green circles) correspond to the same growth batch, while the other (marked purple) is grown under a different set of parameters. The latter is demonstrated only as a further proof of the concept under discussion. Even though most data points fall within the error bars, the same trend of a higher Sb content for lower surface densities is always present. This could be an indication of competition for Sb between neighboring nanowires. However, the shorter length of the nanowires of samples with higher surface densities may also be an explanation to this; as it has been mentioned already in section 3.1, the Sb content of the nanowires increases along the length. As a result, shorter nanowires (samples with a higher surface density) will have a lower average value for the solid phase Sb content in comparison to the longer (lower surface density) nanowires. Another observation is that Au diameter does not seem to have a strong effect on the Sb incorporation in the nanowires.

3.3. Growth temperature

The growth temperature was varied from 435°C to 480°C with steps of 15°C at constant precursor molar fractions and growth time of 15 min. The lower limit of this temperature range was chosen due to the lack of sufficient precursor decomposition at low temperatures [37]. Due to the obvious drop in the vertical growth rate visible in images 3 (c) and (f),

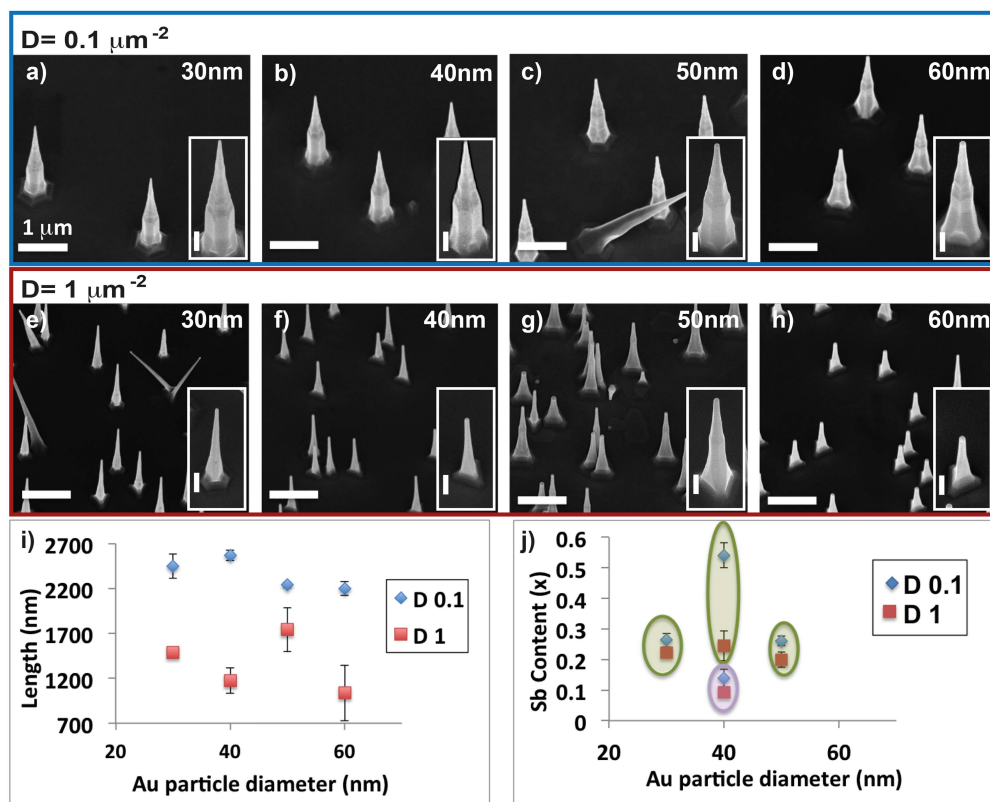


Figure 2. (a)–(h) SEM images of $\text{InSb}_{1-x}\text{Sb}_x$ nanowires grown at $T = 435^\circ\text{C}$, $x_v = 0.22$, $V/\text{III} = 140$ with a growth time of $t = 15$ min, grown from Au particles with diameters of 30–60 nm with two different surface densities of 0.1 and $1 \mu\text{m}^{-2}$. The insets in the images show a higher magnification of a representative nanowire of the related sample. The scale bars in the inset figures correspond to 200 nm. The length and morphology of the nanowires is drastically affected by the surface densities (compare figures (a) with (e) and (d) with (h)). (i) Nanowire length versus the Au seed particle diameter for two surface densities of $0.1 \mu\text{m}^{-2}$ (blue data points) and $1 \mu\text{m}^{-2}$ (red data points) which demonstrates a clear decrease in length for the higher surface density. A slight trend of decreasing length is also deducible as the diameter of the particle increases. However, this trend is not very rigid since the differences in the length of the different samples are comparable to the error bars of the data points. Note that the outlying point related to 50 nm $1 \mu\text{m}^{-2}$ may also be related to occasional spreads in aerosol particle diameter and density observed from sample to sample, however, since the observed trend is not pronounced, it does not affect the deduced conclusions. (j) Sb content of nanowires with different diameters and surface densities. The data points circled with green ovals are all grown at the same growth conditions, while the one circled with purple is related to another growth condition. It is clear that independent of the growth parameters the nanowires grown from a lower surface density have higher Sb incorporated within them.

the temperature was not increased higher than 480°C . In fact, growth at 480°C was performed solely just to confirm the decreasing growth rate with increasing temperatures under our conditions. As shown in the SEM images in figures 3(a)–(h), and the graph in figure 3(i), the growth temperature drastically affects the length; higher temperatures lead to shorter nanowires. Considering the low melting point of InSb (525°C), this reverse length dependency may be explained by a higher amount of decomposition of the nanowires at higher temperatures. Similar reverse behavior has been observed in the study reported in [36]. This may indicate that at higher temperatures the thermodynamic driving force for axial

growth decreases. Also, at higher temperatures surface growth becomes more favorable than vertical nanowire growth, leading to shorter nanowire lengths [36]. From the SEM images in figure 3; more specifically figures 3(a) and (b) where the lengths are sufficient to deduce information on the morphology of the nanowires, it is observable that the temperature also has an impact on their morphology and side facet formation. Temperature affects the surface energetics, precursor decomposition, and also the diffusion length of the present adatoms, all of which in turn can have a role on the ultimate morphology of the nanowires. However, from the XEDS data depicted in figure 3(j), it can be concluded that the

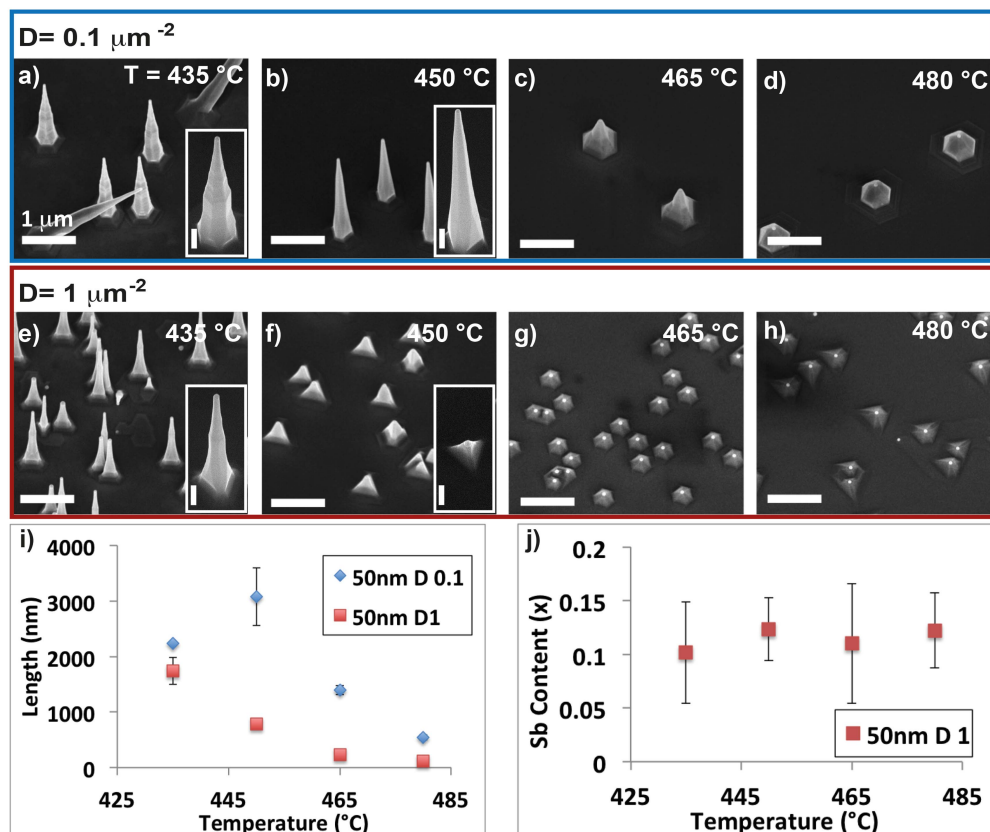


Figure 3. Nanowires grown at $x_v = 0.22$, $V/III = 140$ with a growth time of $t = 15$ min from Au particles with a diameter of 50 nm. (a)–(d) SEM images of nanowires grown at temperatures between 435 °C and 480 °C from samples with a surface density of $0.1 \mu\text{m}^{-2}$, and (e)–(h) a surface density of $1 \mu\text{m}^{-2}$. The insets in the images show a higher magnification image of a representative nanowire of the related sample. The scale bars correspond to 200 nm. (i) Nanowire length dependence on growth temperature. The graphs show a clear decrease of length for increasing temperature for both surface densities. Note that the outlying data point related to 50 nm D0.1, 450 °C is related to occasional aerosol particle density deviations between samples. (j) Sb content of the nanowires versus the growth temperature. The data points show that the Sb content is independent of the growth temperature.

temperature does not significantly affect the Sb incorporation in the nanowires within the investigated range. Therefore, the length dependency on the growth temperature is decoupled from the Sb incorporation.

It is worth noting that growth at temperatures below 435 °C was not carried out due to two main reasons: (a) in order to limit the number of variables throughout the rest of the study the temperature series were first performed to investigate which temperature lead to the highest aspect ratio. This was the case at 450 °C for the lower surface density sample although for the higher surface density, growth at 435 °C offered a much higher aspect ratio. (b) Since TMSb decomposition becomes less efficient with decreasing temperatures [38], lower temperatures than 435 °C were not

investigated, and 450 °C was chosen as the constant temperature for continuing the rest of the studies.

3.4. V/III ratio (varying only the TMIn flow)

Keeping the vapor phase composition at a constant value of $x_v = 0.8$, the V/III ratio was changed by changing the TMIn molar fraction. V/III ratios from 110 to 7.3 were studied from which SEM images are shown in figures 4(a)–(f). An interesting observation is that at high TMIn flows there is a high amount of In accumulation in the Au particles which is clear from the large change in particle morphology observed in SEM images (figures 4(e) and (f)). The nanowires on the samples grown with a high In flow are not homogeneous in their morphology. As seen in the SEM images in figure 4,

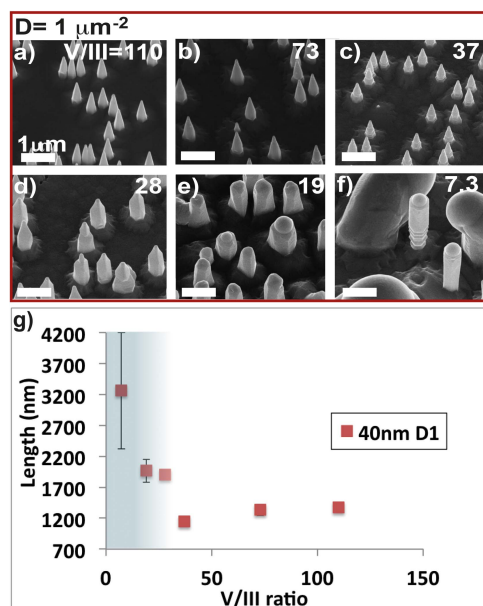


Figure 4. Nanowires grown at a constant vapor phase of $x_v = 0.8$ with a growth time of $t = 50$ min (a)–(g) 30° tilted SEM images of nanowires grown from particles with a diameter of 40 nm and a surface density of $1 \mu\text{m}^{-2}$, with V/III ratios varying between 110 and 7.3. The morphology, length and diameter of these nanowires are affected by the V/III ratio. There is an obvious change in the morphology and dimension of the nanowires grown with a higher V/III ratio than 28 (a)–(c), and 28 and below (d)–(f). This increase in length is also observable in the graph in (g) which depicts the length dependency of the nanowires on the V/III ratio. This is related to the semi In-assisted growth mechanism occurring at an excess of TMIn for the lower V/III ratios (blue-faded highlighted area in the plot). Graph (h) demonstrates a slight decrease in length for the Au-assisted grown nanowires (higher V/III) ratios. As self-assisted growth starts dominating, the length of the nanowires, and also inhomogeneity of their morphologies (demonstrated by the increasing size of the error bars) increases drastically.

especially figure 4(e), some of the nanowires do not demonstrate a seed particle on the top. This could imply that the particle is consumed during growth or cool down. It is interesting to note that in the XEDS spectra, Au signals are not obtained from any of the nanowires, not even those with a particle. In better words, if there is Au in the particle, the amount of Au in the existing particles is less than the detection limitation of our XEDS measurement system in the SEM. From these observations, it can be deduced that for high In flows (low V/III) the growth mechanism changes from Au-assisted to what can be referred to as ‘semi In-assisted’ growth. For confirming the occurrence of In-seeded growth, a bare InAs substrate was placed inside the reactor when growing at low V/III ratios (see SI 2).

An explanation for the difference in the morphology of the nanowires on one sample may be related to growth

initiated by either Au particles which have accumulated an extreme amount of In (semi In-assisted), or from spontaneously formed In particles on the substrates (In-assisted). However, since the amount of Au is low and not detectable, it is difficult to differentiate if or which nanowire is In-seeded and which is semi In-seeded.

The Indium self-seeded growth is initiated at a V/III ratio somewhere between 37 and 28. As seen in the SEM images shown in figures 4(a)–(f), and the graph in figure 4(g), as long as the growth mechanism falls under Au-assisted growth, the morphology of the nanowires is similar, with a slight decrease in the nanowire length for decreasing V/III ratios. As semi In-assisted growth is initiated, the morphology undergoes a sudden change, with a significant increase in the diameter and length of the nanowires. Homogeneity in the nanowire or particle morphology is no longer observed for conditions where semi In-assisted growth dominates.

The same observation in morphology inhomogeneity is observed for the nanowires grown on the bare InAs substrate under conditions where semi In-assisted growth is observed (V/III = 28, 19, and 7.3) (see SI 2). For the two extreme cases (V/III = 19, and 7.3) the morphology and surface density of the nanowires grown on the bare substrates are similar to those grown on the substrates with initial Au particles with both surface densities. This indicates that at an extreme excess of In, the Au particles have no noticeable effect on initial nanowire nucleation, and In particles spontaneously form on the substrates independent of the presence of Au particle. If there is an Au particle present, it accumulates In to an extent that the particle predominantly contains In. For the moderate case though (V/III = 28) there is an obvious change in the morphology of the nanowires grown from the sample with the higher Au particle surface density in comparison to the bare substrate and lower surface density samples. This indicates that under these relatively moderate conditions there is an abundance of In enough to alter the growth mechanism to semi In-seeded. However, even though the In particles form on the substrate surface independent of the presence of Au seed particles, the Au seed particles have an essential role as collection centers in the initial growth steps.

The Sb incorporation in the nanowires however, stays invariant towards changes in the TMIn flow, therefore the growth mechanism (SI 3). In fact, even under conditions where various morphologies are observed on the same sample there are no significant differences observed in the Sb content of nanowires that have very different morphologies.

3.5. Correlating the vapor and solid phase compositions

For understanding how far the Sb content of the nanowires can be increased under the studied conditions, and if or how the group V flows have an effect on this, the vapor phase composition was varied in the range of $x_v = 0.2$ – 0.96 . Since each precursor has a limited variability range it was necessary to alter more than one precursor flow at a time in order to access the large range of the vapor phase composition. This made it possible to study the limits of the solid phase

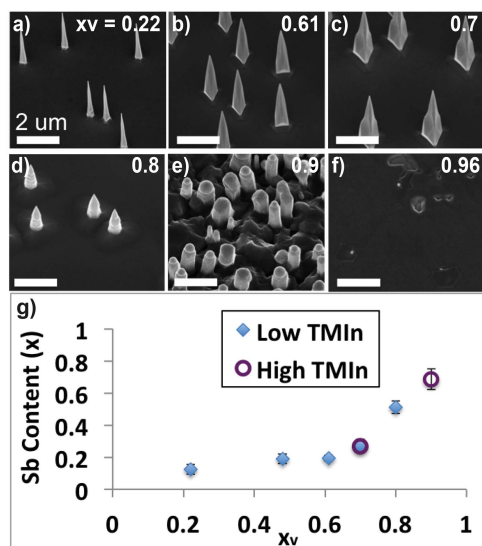


Figure 5. Nanowires grown at $T = 450^\circ\text{C}$, with a growth time of $t = 50$ min, (a)–(f) 30° tilted SEM images of nanowires with Au particles with diameters of 40 nm with a surface density of $0.1\ \mu\text{m}^{-2}$, grown with different vapor phase compositions (0.2–0.96). The set TMIn molar fraction used for growing the sample in (e) is one order of a magnitude higher than the other demonstrated samples, leading to a semi In-assisted growth mechanism. No vertical growth is observed in figure (f) where the AsH_3 molar fraction was very low (2.3×10^{-5}). (g) Solid phase Sb content of the nanowires versus the vapor phase composition. The blue data points indicate growth runs carried out with a TMIn flow around an order of a magnitude lower than that of the samples indicated by the hollow purple circles (3.6×10^{-5}). These two sets of data points fit the same trend line indicating that the Sb content of the nanowires is invariant to changes of the TMIn flow. Instead, high amounts of TMIn alters the growth mechanism to semi In-assisted, which in turn offers access to Sb compositions on the high end of the range that are not feasible by Au-seeded growth. As a result, Sb incorporation up to 0.8 grown from a vapor phase composition of 0.9 is achieved.

composition, i.e. how far the Sb in the solid phase composition could be increased within the grown nanowires. Therefore, in addition to changing the group V precursor flows, the TMIn flow was also altered when found necessary. Also, as explained in detail in the previous section, changing the TMIn flow has no detectable effect on the solid phase composition; hence changing it in this context provides an extra degree of freedom. As observed from the SEM images in figures 5(a)–(f), vertical nanowire growth is obtained for a vapor phase composition up to 0.9. At $x_v = 0.96$, no vertical nanowire growth is observed, as they fail to nucleate. This is not far from expectation since the AsH_3 molar fraction used for this run was extremely low (2.3×10^{-5}) in comparison to the runs with higher x_v . Therefore, within the investigated growth conditions, there seems to be an upper limit in how much the Sb content of the nanowires can be elevated. It

should be mentioned that for $x_v = 0.93$ very short nanowire lengths were observed for all diameters and surface densities (but transferring them to carbon tapes and/or TEM grids proved very difficult due to their small dimensions). Therefore, there is no data on their solid phase composition (SI 4).

It is worth noting that although they differ in length, diameter, and morphology, the nanowires demonstrated in panels 5(a)–(d) seem to fall in a morphological trend in comparison with the nanowires in panel 5(e): they all have a tapered morphology, and the seed particles on the nanowires are small and comparable to their initial Au particle, resembling Au-assisted growth for 5(a)–(d). This is in contrast with the nanowires demonstrated in 5(e), which are mostly taper-free with a swollen particle (if any) on the top, which implies more a semi In-assisted growth. This is because the TMIn molar fraction used in the latter was an order of magnitude higher compared to the other growth runs, promoting semi In-assisted growth. This difference in the morphology of the nanowires seems to be connected to the particle material; as mentioned, tapered growth is observed for Au seeded nanowires, while untapered nanowires are grown from semi-In particles that are also heavily overgrown. However, it can be understood that the morphology is not exclusively a factor of the seed particle, but is a consequence of the abundance of the growth rate limiting species, In. The In adatoms have a shorter diffusion length on the surface compared to the length of the nanowire, therefore under conditions that there is not an overload of In in the reactor (Au-seeded nanowires), most of the In adatoms cannot diffuse all the way to the particle, therefore lead to tapering. When abundant (semi In-seeded), In adatoms lead to an untapered morphology; there is sufficient adatoms in the seed particle to be incorporated in growth, while the adatoms diffusing from the substrate supersaturate the side facets and cause the heavy radial growth to happen. The particle composition of two typical samples grown with the Au-assisted (sample demonstrated in figure 1) and semi In-assisted (50 nm D1 sample from the same batch as demonstrated in figure 4(e)) mechanism are compared in SI 5. The particle composition of the Au-seeded nanowire is roughly Au–In (50%–50%), which is the typical post-growth composition of InAs nanowires, while the semi In-seeded nanowire does not reveal any detectable Au signal, being mainly In.

The graph in figure 5(g) demonstrates the solid phase versus the vapor phase composition where an exponential increase is observed in the Sb content of the nanowires for increasing x_v , where a value as high as $x = 0.75$ is realized for the solid phase composition. The data sets demonstrated by hollow purple circles are related to samples which are grown from a TMIn flow that is around an order of a magnitude higher compared to their counterparts demonstrated by the blue data points. Notice the data points related to the higher TMIn flows nicely follow the trend line. As observed, $x_v = 0.7$ was grown with high and low TMIn flows, which completely fall onto one another, again proving that changing only the TMIn flow has no significant effect on the solid phase composition of the nanowires within the studied range. The highest solid Sb content depicted in figure 5(g) is related

to the sample shown in 5(e); a semi In-assisted growth. Thus, it can be deduced that the semi In-assisted growth mechanism has aided nucleation and vertical growth within a window of high x_v not accessible by Au-seeded mechanism, therefore increasing the solid Sb content of the nanowires. This could be related to the dependence of the wetting properties of particles on their constituting material(s) in the presence of the surfactant Sb. It may be that a particle mainly composed of In acts very differently in the presence of high amounts of Sb compared to Au, and provides higher contact angles in comparison. This in turn leads to vertical growth of nanowires under conditions that Au seed particles are incapable of promoting nucleation. As a result, under a high vapor phase composition, the solid phase Sb-incorporation into vertical, directly nucleated nanowires can be enhanced.

4. Conclusion

We have demonstrated direct growth of $\text{InAs}_{1-x}\text{Sb}_x$ nanowires from Au seed particles on InAs (111) B substrates. We partially attribute the success in direct growth from the substrate to the very high group III flow used when growing the nanowires with higher solid phase Sb compositions. This is a very extreme growth condition compared to typical flows used for growing $\text{InAs}_{1-x}\text{Sb}_x$ nanowires. The effects of the controllable growth parameters on the dimensions and solid phase composition of the grown nanowires have been extensively studied, and by varying the vapor phase composition between $x_v = 0.2$ to 0.9 a solid phase Sb incorporation range of $x = 0.08$ to 0.75 has been covered successfully. The results of this study show that the initial seed particle density has an effect on the Sb incorporation in such a way that lower surface densities lead to a higher Sb content in the grown nanowires. We have also observed that changing initial Au seed diameter, group III flow (TMIn), and growth temperature does not have a significant effect on the Sb composition of the final nanowires. However by increasing the TMIn flow to an order of magnitude higher value, the growth mechanism is altered from Au-assisted growth to semi In-assisted growth. This in turn allows us to achieve vertical growth of $\text{InAs}_{1-x}\text{Sb}_x$ nanowires with a high solid phase Sb content that is not accessible by Au-seeded growth. It can be concluded that under the studied conditions, the seed particle material (whether a mixture of Au and In (Au-assisted growth), or mostly In (semi In-assisted growth) determines the possibility to access nucleation, hence vertical growth at high vapor phase compositions. Also, the correlation of the axial growth rate of these nanowires with the Sb incorporation has been presented.

Finally, we demonstrate that the ternary nanowires that are grown with the Au-assisted mechanism mostly demonstrate tapered structures and are self-formed core-shell structures with an Sb-poor shell. This can be related to the surfactant effect of Sb that changes the surface properties, e.g. Sb changes surface energies of the interface between the vapor and particle, and vapor and solid it covers. And since

contact angle is a function of the interfacial surface energies, it is affected to a high degree by the presence of Sb.

In addition to gaining an extensive understanding of the controllability of the material composition of $\text{InAs}_{1-x}\text{Sb}_x$, the possibility of growing ternary nanowires with material compositions containing Sb directly from the substrate, may facilitate growth of binary Sb-based nanowires such as InSb. This is when the ternary is used as a stem for the binary segment. In better words, as mentioned earlier in the paper, if conventional stems such as InAs are used, complications such as stem decomposition during As-low/free material synthesis may arise, causing vertical growing nanowires to break at the decomposed area, ultimately leading to failed synthesis or collapsed nanowires. Related to decomposition and direct nucleation issues of Sb-based nanowires such as InSb grown from Au seed particles, if an $\text{InAs}_{1-x}\text{Sb}_x$ ternary nanowire grown directly from the substrate can act as a stem for facilitating the nucleation of InSb on InAs substrates, decomposition of the stem may be avoided. In this case, the Sb present in the Sb-containing stem is expected to prevent stem decomposition during As-free growth. For utilizing the ternaries in this fashion however, it may be necessary to first gain control over the radial overgrowth, so that with a better morphology a more suitable platform for InSb growth is provided. This radial growth optimization has not been covered within the scopes of this paper, and is regarded as an independent study.

Acknowledgments

This work was supported by the Swedish Research Council (VR), the Swedish Foundation for Strategic Research (SSF), the Knut and Alice Wallenberg Foundation (KAW), and NanoLund.

References

- [1] Dayeh S A, Aplin D P R, Zhou X, Yu P K L, Yu E T and Wang D 2007 High electron mobility InAs nanowire field-effect transistors *Small* **3** 326–32
- [2] Ford A C et al 2009 Diameter-dependent electron mobility of InAs nanowires *Nano Lett.* **9** 360–5
- [3] Thelander C, Björk M T, Larsson M W, Hansen A E, Wallenberg L R and Samuelson L 2004 Electron transport in InAs nanowires and heterostructure nanowire devices *Solid State Commun.* **131** 573–9
- [4] Caroff P et al 2008 High-quality InAs/InSb nanowire heterostructures grown by metal-organic vapor-phase epitaxy *Small* **4** 878–82
- [5] Wang Y, Chi J, Banerjee K, Grützmacher D, Schäpers T and Lu J G 2011 Field effect transistor based on single crystalline InSb nanowire *J. Mater. Chem.* **21** 2459
- [6] Nilsson H A et al 2011 InSb nanowire field-effect transistors and quantum-dot devices *IEEE J. Sel. Top. Quantum Electron.* **17** 907–14
- [7] Mingo N 2004 Thermoelectric figure of merit and maximum power factor in III–V semiconductor nanowires *Appl. Phys. Lett.* **84** 2652

- [8] Svensson J, Anttu N, Vainorius N, Borg M and Wernersson L-E 2013 Diameter-dependent photocurrent in InAsSb nanowire infrared photodetectors *Nano Lett.* **13** 1380–5
- [9] Dobbelaere W, de Boeck J, Bruynseraede C, Mertens R and Borghs G 1993 InAsSb light emitting diodes and their applications to infra-red gas sensors *Electron. Lett.* **29** 890–1
- [10] Thelander C, Caroff P, Plissard S and Dick K A 2012 Electrical properties of InAs_{1-x}Sb_x and InSb nanowires grown by molecular beam epitaxy *Appl. Phys. Lett.* **100** 232105
- [11] Biefeld R M 2002 The metal-organic chemical vapor deposition and properties of III–V antimony-based semiconductor materials *Mater. Sci. Eng. R* **36** 105–42
- [12] Nilsson M, Namazi L, Lehmann S, Leijnse M, Dick K A and Thelander C 2016 Single-electron transport in InAs nanowire quantum dots formed by crystal phase engineering *Phys. Rev. B* **93** 195422
- [13] Müller E K and Richards J L 1964 Miscibility of III–V semiconductors studied by flash evaporation *J. Appl. Phys.* **35** 1233
- [14] Ishida K, Nomura T, Tokunaga H, Ohtani H and Nishizawa T 1989 Miscibility gaps in the GaPInP, GaPGeSb, InPInSn and InAsInSb systems *J. Less—Common Met.* **155** 193–206
- [15] Jou M J, Cherng Y T, Jen H R and Stringfellow G B 1988 OMVPE growth of the new semiconductor alloys GaP_{1-x}Sb_x and InP_{1-x}Sb_x *J. Cryst. Growth* **93** 62–9
- [16] Borg M, Dick K A, Eymery J and Wernersson L-E 2011 Enhanced Sb incorporation in InAsSb nanowires grown by metalorganic vapor phase epitaxy *Appl. Phys. Lett.* **98** 113104
- [17] Nebol'sin V A and Shchetinin A A Role of surface energy in the vapor–liquid–solid growth of silicon *Inorg. Mater.* **39** 899–903
- [18] Borg M and Wernersson L-E 2013 Synthesis and properties of antimonide nanowires *Nanotechnology* **24** 202001
- [19] Lugani L, Ercolani D, Beltram F and Sorba L 2011 Growth mechanism of InAs–InSb heterostructured nanowires grown by chemical beam epitaxy *J. Cryst. Growth* **323** 304–6
- [20] Ercolani D et al 2012 Growth of InAs/InAsSb heterostructured nanowires *Nanotechnology* **23** 115606
- [21] Conesa-Boj S et al 2014 Gold-free ternary III–V antimonide nanowire arrays on silicon: twin-free down to the first bilayer *Nano Lett.* **14** 326–32
- [22] Du W-N et al 2014 The self-seeded growth of InAsSb nanowires on silicon by metal-organic vapor phase epitaxy *J. Cryst. Growth* **396** 33–7
- [23] Anyebe E A and Zhuang Q 2014 Self-catalysed InAs_{1-x}Sb_x nanowires grown directly on bare Si substrates *Mater. Res. Bull.* **60** 572–5
- [24] Farrell A C, Lee W-J, Senanayake P, Haddad M A, Prikhodko S V and Huffaker D L 2015 High-quality InAsSb nanowires grown by catalyst-free selective-area metal-organic chemical vapor deposition *Nano Lett.* **15** 6614–9
- [25] Heurlin M, Anttu N, Camus C, Samuelson L and Borgström M T 2015 *In situ* characterization of nanowire dimensions and growth dynamics by optical reflectance *Nano Lett.* **15** 3597–602
- [26] Jeppsson M et al 2008 GaAs/GaSb nanowire heterostructures grown by MOVPE *J. Cryst. Growth* **310** 4115–21
- [27] Ameruddin A S, Caroff P, Tan H H, Jagadish C and Dubrovskii V G 2015 Understanding the growth and composition evolution of gold-seeded ternary InGaAs nanowires *Nanoscale* **7** 16266–72
- [28] Guo Y-N et al 2013 Phase separation induced by Au catalysts in ternary InGaAs nanowires *Nano Lett.* **13** 643–50
- [29] Mohseni P K et al 2013 In(x)Ga(1-x)As nanowire growth on graphene: van der Waals epitaxy induced phase segregation *Nano Lett.* **13** 1153–61
- [30] Fakhri A, Haddara Y M and Lapierre R R 2010 Dependence of InGaP nanowire morphology and structure on molecular beam epitaxy growth conditions *Nanotechnology* **21** 165601
- [31] Kim Y et al 2006 Influence of nanowire density on the shape and optical properties of ternary InGaAs nanowires *Nano Lett.* **6** 599–604
- [32] Persson A I, Fröberg L E, Jeppesen S, Björk M T and Samuelson L 2007 Surface diffusion effects on growth of nanowires by chemical beam epitaxy *J. Appl. Phys.* **101** 034313
- [33] Jensen L E, Björk M T, Jeppesen S, Persson A I, Ohlsson B J and Samuelson L 2004 Role of surface diffusion in chemical beam epitaxy of InAs nanowires *Nano Lett.* **4** 1961–4
- [34] Caroff P, Dick K A, Johansson J, Messing M E, Deppert K and Samuelson L 2009 Controlled polytypic and twin-plane superlattices in III–V nanowires *Nat. Nanotechnol.* **4** 50–5
- [35] Dheeraj D L et al 2008 Growth and characterization of wurtzite GaAs nanowires with defect-free zinc blende GaAsSb inserts *Nano Lett.* **8** 4459–63
- [36] Pea M et al 2013 Suppression of lateral growth in InAs/InAsSb heterostructured nanowires *J. Cryst. Growth* **366** 8–14
- [37] Stringfellow G B 1989 *Organometallic Vapor Phase Epitaxy: Theory and Practice* (Boston: Academic)
- [38] Larsen C A, Li S H and Stringfellow G B 1990 Decomposition of trimethylantimony and reactions with trimethylindium *Chem. Mater.* **3** 39–44

Supplemental information for “Direct Nucleation, Morphology and Compositional Tuning of InAs_{1-x}Sb_x Nanowires on InAs (111) B Substrates”

Luna Namazi ¹, Sepideh Gorji Ghalamestani ¹, Sebastian Lehmann ¹, Reza R. Zamani ¹, Kimberly A. Dick ^{1,2}

¹ Solid State Physics, Lund University, Box 118, S-221 00 Lund, Sweden

² Center for Analysis and Synthesis, Lund University, Box 124, S-221 00 Lund, Sweden

Table of Contents

| | |
|---|---|
| S1. Flow chart of the growth procedure of InAs _{1-x} Sb _x nanowires..... | 2 |
| S2. Comparison between the self-assisted nanowires grown on a bare InAs substrate and grown from a surface density of 0.1 and 1 μm^{-2} Au-particles | 2 |
| S3. Sb incorporation dependency on the V/III ratio with varying only the TMIn flow along with the morphology of the low surface density nanowires | 3 |
| S4. Nanowires grown at $x_v = 0.93$ (with a low TMIn flow) | 4 |
| S5. A comparison between the seed particle composition of Au-seeded and semi In-seeded nanowires..... | 5 |

S1. Schematic of the growth procedure

For growing the $\text{InAs}_{1-x}\text{Sb}_x$ nanowires, the samples containing pre-deposited aerosol Au particles were annealed under an AsH_3 flow at 550 °C for removing the native oxide. The temperature was then lowered to that of the desired growth temperature (450 °C in most cases) and nanowire growth was commenced by simultaneously introducing TMIn and TMSb into the reactor while decreasing the AsH_3 flow to lower amounts. Nanowire growth was terminated by cutting off the precursor supplied to the reactor and cooling the samples under a flow of H_2 .

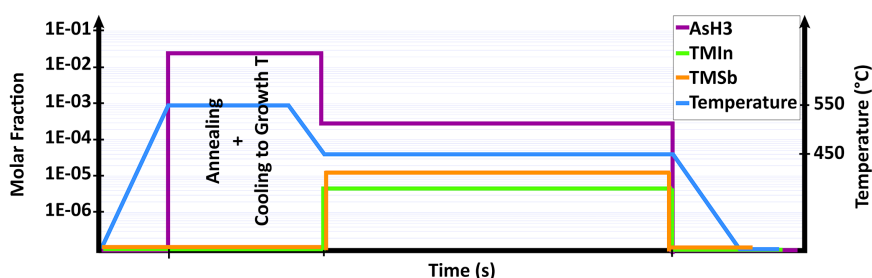


Figure S1: Schematic illustrations of temperatures, TMIn, TMSb, and AsH_3 precursor flows, and precursor switching used for the growth of $\text{InAs}_{1-x}\text{Sb}_x$ nanowires from Au seed particles versus time. The molar fraction is demonstrated with a logarithmic scale on the left y-axis, while the right y-axis shows the temperature. The time axis is not to scale with the real values used for growing the nanowires.

S2. Comparison between the self-assisted nanowires grown on a bare InAs substrate, nanowires grown from a surface density of 0.1 and 1 Au-particles

Figure S2 compares the morphology of the nanowires grown from initial Au particle surface densities of 0.1 and $1\text{ }\mu\text{m}^{-2}$ and on bare InAs substrates under conditions where semi In-assisted growth occurs ($V/\text{III} = 28, 19, 7.3$) demonstrates a similar morphology for all three samples at the two lower V/III ratios ($V/\text{III} = 19$ and 7.3). As discussed in the main text, this indicated that at very high TMIn flows the Au particles have negligible effect on nucleation, while In particles form spontaneously on the substrate independent of the presence of Au. This is in contrast to the sample with the highest V/III ratio of the three ($V/\text{III} = 28$). The nanowires grown from the sample containing initial Au-particles with a surface density of $1\text{ }\mu\text{m}^{-2}$, clearly have a different morphology. Here, the In is sufficient to alter the growth mechanism to semi In-assisted growth (deduced by the presence of nanowire growth on the bare substrate), but not as extreme as the other two conditions. Therefore, it can be concluded that Au particles in fact do have a role as collection sites of In, and In particles do not self-form on the substrate where there is moderate numbers of Au particles present.

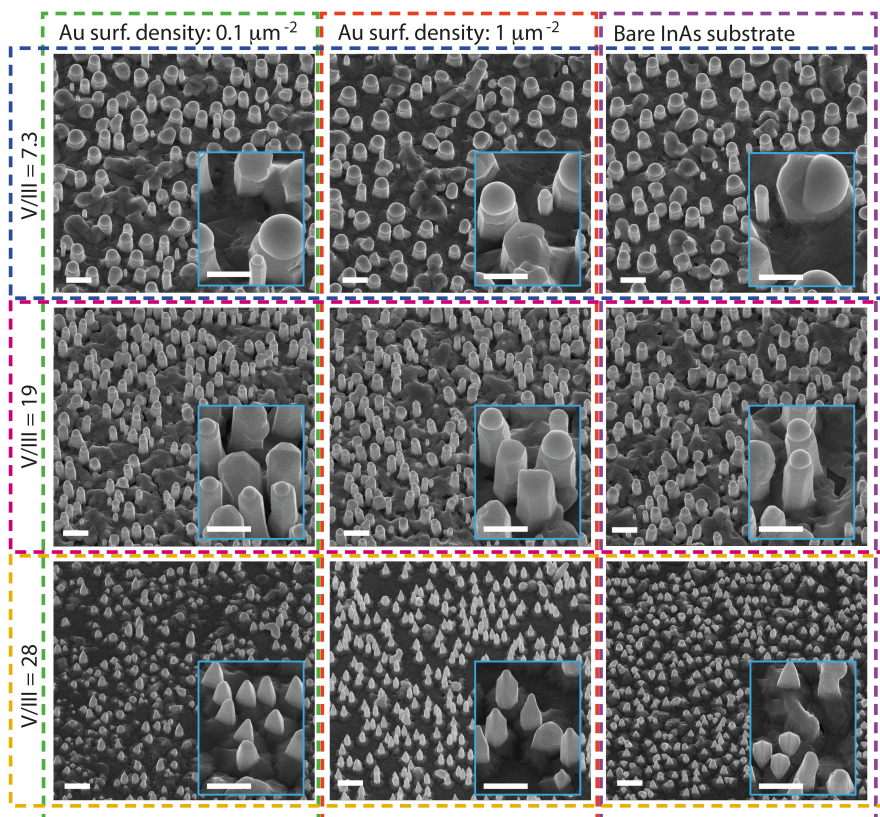


Figure S2: 30°-tilted SEM images of nanowires grown from initial Au particle surface densities of 0.1 and 1 μm^{-2} and on bare InAs substrates for the three V/III ratios where semi In-assisted growth is observed. The scale bar in all images represents 2 μm , and the scale bar in the insets represents 1 μm . The dashed lines categorize which sample belongs to which V/III value, and which initial Au particle surface density.

S3. Sb incorporation dependency on the V/III ratio with varying only the TMIn flow along with the morphology of the low surface density nanowires

Similar to the nanowires grown from samples with the higher Au particle surface density (1 μm^{-2}) under conditions where only the TMIn flow was altered, $\text{InAs}_{1-x}\text{Sb}_x$ nanowires grown from samples with the lower surface density (0.1 μm^{-2}) show a sudden change in their morphologies at TMIn flows that semi In-assisted growth mechanism dominates (figures S3a-f).

It is of utmost interest that according to the graph presented in figure S3g, the measured Sb content of the nanowires remains invariant to changes in the TMIn flow. The graph shows no distinguishable trend for the Sb content variations of either of the samples grown from high or low surface densities.

It can be observed however that as claimed in the main text of the paper, the samples grown from a lower surface density of Au particles (0.1 μm^{-2}) have a

higher Sb incorporation in comparison to their lower density counterparts ($1 \mu\text{m}^{-2}$).

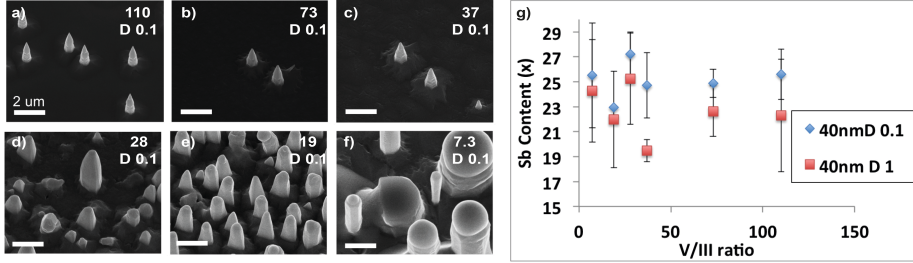


Figure 3S: Grown at a constant vapor phase composition of $x_v = 0.8$ with a growth time of $t = 50$ minutes a-g) 30° tilted SEM images of nanowires grown from particles with a diameter of 40 nm and a surface density of $0.1 \mu\text{m}^{-2}$, with V/III ratios varying between 110 - 7.3. The morphology, length and diameter of these nanowires are affected by the V/III ratio. There is an obvious change in the morphology and dimension of the nanowires grown with a higher V/III ratio than 28 (a-c), and 28 and below (d-f). g) The Sb content of the grown nanowires with both surface densities of 0.1 and $1 \mu\text{m}^{-2}$ versus V/III ratio. It is clear that changing the V/III ratio by only changing the TMIn flow does not affect the Sb incorporation into the nanowires in a cohesive way.

S4. Nanowires grown at $x_v = 0.93$ (low TMIn)

The highest vapor phase composition that resulted in vertical nanowires growth under Au-assisted growth mechanism was at $x_v = 0.93$. Unfortunately though, since these nanowires are very small and difficult to transfer to TEM grids or sticky carbon tape, XEDS measurements could not be performed on them, and hence no information on their composition is at hand.

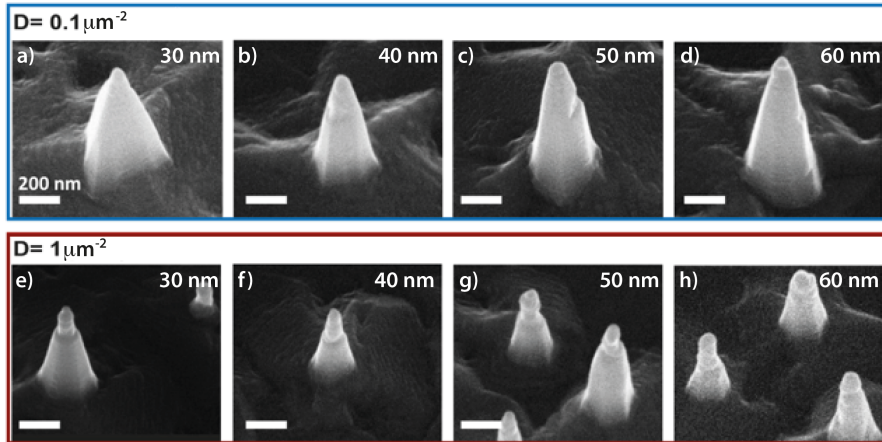


Figure S4: Nanowires grown under $x_v = 0.93$ by Au-assisted growth mechanism. From initial Au seed particles with diameters of 30, 40, 50, and 60 nm for two different surface densities of $0.1 \mu\text{m}^{-2}$ (a-d) and $1 \mu\text{m}^{-2}$ (e-h).

S5. A comparison between the seed particle composition of Au-seeded and semi In-seeded nanowires

STEM-XEDS analysis confirms that the samples with a high TMIn flow are grown with a (semi) In-seeded mechanism. Here in figure S5 the particle composition of samples grown under a V/III ratio of a) 93 and b) 19 are compared. In the table the particle compositions of the two samples are demonstrated. The compositions are for sample a) around roughly Au-In, whereas that of the sample in b) is mainly In with no meaningful signal from Au (since the detection limit is around 3 atm%). This indicates that the sample in b) is grown through the semi In-assisted mechanism in contrast to the Au-assisted growth mechanism of sample a.

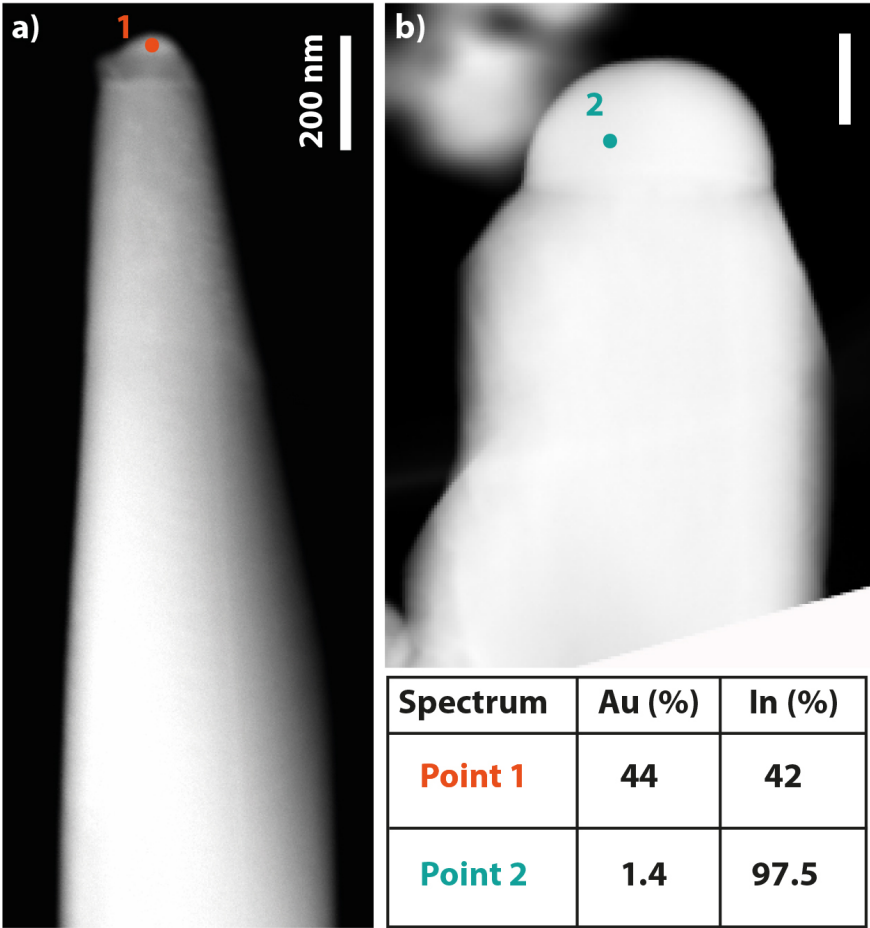


Figure S5: STEM images of nanowires grown from a 50nm D1 sample, under a V/III ratio of a) 93 and b) 19. The table on the bottom right corner of the image shows the composition of particles of both samples in atomic %. As seen, sample a) has a composition of roughly In-Au, whereas sample b) is mainly In-seeded. Note that the values of In and Au do not add up to 100% because small amounts of Sb and As were also detected.

Paper II



Cite this: *Nanoscale*, 2015, 7, 10472

Selective GaSb radial growth on crystal phase engineered InAs nanowires†

Luna Namazi,^{*a} Malin Nilsson,^a Sebastian Lehmann,^a Claes Thelander^a and Kimberly A. Dick^{*a,b}

In this work we have developed InAs nanowire templates, with designed zinc blende and wurtzite segments, for selective growth of radial GaSb heterostructures using metal organic vapor phase epitaxy. We find that the radial growth rate of GaSb is determined by the crystal phase of InAs, and that growth is suppressed on InAs segments with a pure wurtzite crystal phase. The morphology and the thickness of the grown shell can be tuned with full control by the growth conditions. We demonstrate that multiple distinct core-shell segments can be designed and realized with precise control over their length and axial position. Electrical measurements confirm that suppression of shell growth is possible on segments with wurtzite structures. This growth method enables new functionalities in structures formed by using bottom-up techniques, with complexity beyond that attainable by using top-down techniques.

Received 18th February 2015,
Accepted 4th May 2015

DOI: 10.1039/c5nr01165e

www.rsc.org/nanoscale

1. Introduction

Semiconductor nanowires are nowadays considered to be promising candidates as building blocks in future electrical and optical devices due to their tunable physical and material properties.^{1–8} Among them, heterostructure nanowires are of considerable importance, providing us with the possibility to combine the desired properties of two or more different materials with minimal strain compared to conventional layers of the same materials.⁹ These heterostructures can be grown either axially or radially based on the device requirements. Both axial^{10–12} and radial^{13–15} heterostructure growth have been extensively investigated with a high degree of control of interfaces and composition. It has also been demonstrated that radial growth can be tuned to be selective to certain nanowire facets.¹⁶ However, the unique prospect of selective radial heterostructure growth on the designed axial sections along the length of the nanowire is yet to be explored and employed in a device structure. In a number of studies it has been observed that the rate of radial growth strongly depends on the crystal phase of the nanowires,¹⁷ attributed to their different

surface energies.^{18–20} Controlling the crystal structure of different segments of the nanowire, and thereby, changing the surface energies of the segments formed along the axis would provide ideal templates for studying selective radial growth.¹⁷

In this work we demonstrate highly controlled selective radial growth in the InAs–GaSb material system, on designed InAs nanowire core templates, characterized by high resolution transmission electron microscopy (TEM) and electrical measurements. The templates are based on the findings that pure zinc blende or wurtzite structures can be formed along the length of a nanowire with high precision and control by careful tuning of the growth conditions.^{21–27} Here, the group V precursor flow has been modified to achieve the two crystal structures of the core.²⁸

The growth of GaSb–InAs and InAs–GaSb core-shell nanowires has been reported in ref. 29 and 30 by means of MOVPE and MBE, respectively. These heterostructures exhibit a broken band alignment, making such junctions interesting for various device applications, such as tunnel diodes and tunnel field effect transistors (TFETs).^{31,32} Motivated by their lower-power operation and greater scalability, TFETs are believed to be one of the most promising transistor concepts for next-generation low-power integrated circuits. For radial TFET devices, the axial extent of the radial junction is directly related to the gate length. The potential for epitaxial control of such a critical device parameter, rather than having to rely on complex etch-back processes, provides an important example of the relevance of this study.² Furthermore, InAs–GaSb heterostructures are fundamentally interesting for quantum transport studies such as electron–hole interactions, or as candidates for topolo-

^aSolid State Physics, Lund University, Box 118, S-221 00 Lund, Sweden.

E-mail: luna.namazi@fif.lth.se, kimberly.dick_thelander@fif.lth.se

^bCenter for Analysis and Synthesis, Lund University, Box 124, S-221 00 Lund, Sweden

†Electronic supplementary information (ESI) available: S1: optimization of the InAs core crystal structure, S2: the time dependence of GaSb shell growth S3. The total precursor flow influence on GaSb shell growth. See DOI: 10.1039/c5nr01165e

gical insulators.^{33–35} Epitaxial growth of well-defined core-shell segments would further allow for controlled core-shell quantum dots, where the interaction of single electrons and single holes can be studied.

It is understood that zinc blende structures possess a higher surface energy than wurtzite structures.^{28,36} Taking advantage of this information, we here intentionally suppress the radial growth on the wurtzite surfaces, while enhancing it on the zinc blende structures.¹⁷ In other words, we make use of how the low surface energies of the wurtzite side facets compared to the zinc blende side facets hinder nucleation and hence radial growth of a shell layer – GaSb in our case – under conditions where nucleation is in fact favourable on the zinc blende surfaces. The wurtzite nanowire segments have {10-10}-type side facets, predicted to have lower energy than the {110}-type facets on the corresponding zinc blende segments;³⁷ it should be emphasized that other side facets would have other energies and that selectivity may be different, perhaps even opposite, for certain other facet types. We demonstrate that the morphology and diameter of the grown GaSb shell on the crystal structure-designed InAs core nanowires vary, and can be tuned to preference by changing the direct growth parameters for the GaSb (temperature, nominal V/III ratios of the precursor flows, absolute precursor molar flow, and time). Thus, based on the interesting properties and high potential of this material system, we employ it for developing the selective radial growth concept. We also show that selective growth of shell layers on specific parts of a multiple structured core nanowire is possible.

Finally, selective InAs–GaSb core-shell and reference InAs (core-only) nanowires are evaluated with electrical measurements in top-gated devices. For InAs reference nanowires it is found that both the wurtzite and zinc blende segments have unipolar n-type transport as expected, and are depleted for negative gate voltages. For the selectively overgrown core-shell nanowires, we find that zinc blende segments show ambipolar conduction in agreement with GaSb overgrowth, whereas wurtzite segments have unipolar conduction only, evidencing a suppression of the overgrowth, and the feasibility of the template method.

2. Methods

InAs–GaSb core-shell nanowires are grown by means of metal-organic vapour phase epitaxy (MOVPE) on Au aerosol decorated InAs (111) B substrates. The utilized Au particle diameters are 30 and 40 nm at areal densities of 1 and 2 particles per μm^2 . The nanowires are grown in a standard low-pressure horizontal MOVPE reactor (Aixtron 200/4). For the InAs core trimethylindium (TMIn) and arsine (AsH_3), and for the GaSb shell trimethylgallium (TMGa) and trimethylantimony (TMSb), are used as the group III and V precursors, respectively. Hydrogen is used as the carrier gas with a total flow rate of 13 l min^{-1} , at a reactor pressure of 100 mbar. After loading the InAs samples into the reactor, the samples were annealed for

10 minutes at a temperature of 550 °C in a H_2/AsH_3 atmosphere in order to remove the native oxide from the surface of the samples. The InAs core structure was then grown at 460 °C by supplying TMIn and AsH_3 . To ensure uniform nucleation, growth was initiated with a segment grown for 3 minutes with TMIn of 3.5×10^{-6} and AsH_3 of 1.9×10^{-4} , before growing the wurtzite and zinc blende segments. This segment has mostly a wurtzite structure with frequent stacking faults. As a general guideline, regardless of the diameter of the initial Au particle, for growing the zinc blende segments higher AsH_3 flows are used, whereas for the wurtzite segments, the group V precursor flow is reduced to a small fraction of that of zinc blende.²⁸ For particles with a diameter of 40 nm the molar fractions of AsH_3 was set to 7.7×10^{-5} and 1.5×10^{-2} for the wurtzite and zinc blende segments respectively, while the TMIn precursor flow was maintained at 3.5×10^{-6} for both segments. For particles with a diameter of 30 nm the AsH_3 and TMIn molar fractions were slightly altered to 9.2×10^{-5} and 3.5×10^{-6} for wurtzite, and 1.5×10^{-2} and 1.9×10^{-5} for zinc blende, respectively. The InAs core was designed with three segments along the length, starting with a wurtzite segment, which is referred to as WZ1 throughout this paper. A zinc blende segment was grown as the second segment (ZB), followed by a second wurtzite segment referred to as WZ2. The first segment (WZ1) is used to isolate the ZB and WZ2 segments from the substrate and stem segment; in order to understand the radial growth concept we compared ZB and WZ2. Please take note that throughout this paper the wurtzite and zinc blende segments are referred to in the abbreviated form as WZ and ZB, whereas when discussing general topics related to these two crystal phases the full names are used. The growth times were varied based on the desired length of each segment, the initial particle diameter, and density. The effect of areal density on the length and morphology of the grown nanowires is demonstrated in S4 in the ESI.† Typically growth times of 6 minutes for the ZB segments resulted in a length of around 500–700 nm, and 2–5 minutes for the wurtzite segments gave a length of 400–1200 nm depending on the particle diameter and density. For more details of the InAs structure optimization see the ESI S1.†

As the next step, the GaSb shell was grown by simultaneously switching Group III and V precursors from TMIn to TMGa and AsH_3 to TMSb. The study of temperature dependence is an exception to this simultaneous switch, where the temperature was first ramped to the desired value in the constant presence of AsH_3 before switching TMGa and TMSb on. After growth all samples were cooled under a flow of H_2 .

A particular set of growth conditions for the GaSb shell are defined as the initial or reference parameters, which are referred to and compared to throughout this paper. These shell-growth conditions are then mapped out, one by one, by changing only one specific parameter while keeping the others at the constant reference values. The reference molar fractions of the TMGa and TMSb precursors are 3.4×10^{-5} and 5.4×10^{-5} , respectively, resulting in a nominal V/III ratio of 1.6. The reference GaSb shell is grown at 460 °C for 20 minutes on the pre-

optimized WZ1-ZB-WZ2 InAs core structure. The samples are then characterized by means of Scanning Electron Microscopy (SEM) (Zeiss LEO 1560) with typical acceleration voltages of 5–10 kV and high resolution TEM imaging (JEOL 3000F) with an acceleration voltage of 300 kV, combined with Scanning TEM X-ray energy dispersive spectroscopy (STEM-XEDS) for compositional investigations. For TEM characterization, the nanowires were transferred to lacey carbon-film coated copper grids by manually breaking them off from the substrate. For the TEM and XEDS analysis, 4–5 nanowires were characterized with electron beam directions parallel to the $\langle 110 \rangle$ - or $\langle 112 \rangle$ -type zone axes, respectively. For electrical characterization, source-, drain-, and gate contacts were processed on two sets of nanowires with axial WZ1-ZB-WZ2 segments: (i) InAs only, and (ii) with selective GaSb radial overgrowth (30 nm Au diameter, with a shell thickness of approximately 15 nm). The nanowires were mechanically transferred from the growth substrate to silicon substrates covered with a 110 nm thick SiO₂ layer with pre-defined gold patterns to facilitate contact design. Source and drain contacts were then processed using electron beam lithography with PMMA 950 A5 as the resist. After development of the resist O₂-plasma etching (30 s) was used to remove the resist residue, and directly before metal evaporation of 25/75 nm Ni/Au, HCl:H₂O etching (1:20) for 10 s was performed to remove the native oxide on the nanowires. After metal lift-off, the remaining resist residues were removed in a second O₂-plasma etching step (30 s). An approximately 7 nm thick HfO₂ gate dielectric layer was deposited by means of atomic layer deposition at 100 °C. Holes were opened in the oxide using focused ion beam milling to connect the top gate contacts to the pre-defined gold pads on the substrate. Finally, the top gate was processed using a similar lift-off process as for the source- and drain contacts, omitting the wet etching step prior to metallization.

3. Results

3.1 Morphology and structure of selective InAs–GaSb core–shell nanowires

The morphology of the different nanowire structures was investigated by SEM at a 30° tilt angle. Fig. 1 shows SEM images of the InAs core-only (Fig. 1a) and the InAs–GaSb core–shell structure (Fig. 1b) along with schematics of both cases as insets.

From Fig. 1a a diameter increase from the WZ to the ZB segment of the InAs core can be seen. This as well as the facet rotation from one structure to the other is a result of the overgrowth on the side facets.^{28,38} It is also clear that WZ1 has a larger diameter compared to WZ2. This occurs when the excess InAs material nucleates and overgrows on WZ1 side facets during the rest of the core growth time. This overgrowth will – as expected from the previous studies – continue the same crystal structure of the underlying nanowire, wurtzite in this case. These diameter differences and facet rotations are also schematically depicted in the insets of Fig. 1. Note also

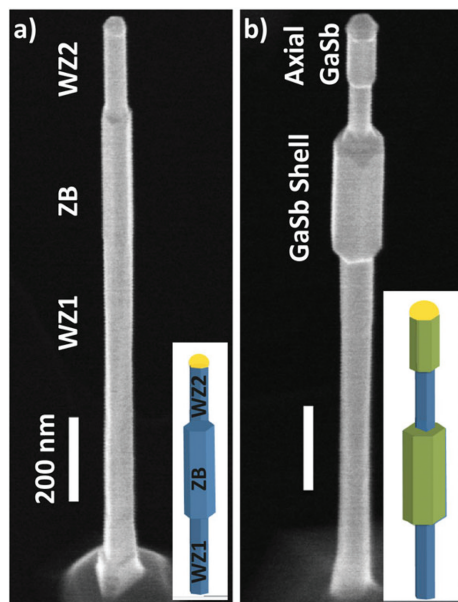


Fig. 1 30°-tilted SEM images of (a) a core InAs structure and (b) a core-shell structure with the GaSb shell only formed on the zinc blende segment. The insets are schematic demonstrations of the related nanowires, with InAs shown in blue and GaSb in green. As discussed in detail in section 3.1, under certain conditions an axial GaSb segment is also formed in addition to the shell.

that the nucleation segment at the base (which has frequent stacking defects) has the same facets as WZ1, so these cannot be distinguished. The overgrowth observed on the WZ1 and nucleation (stem) section results in more and rougher side facets, which will in turn affect radial overgrowth. For this reason, WZ2 is used for comparison with the ZB segment in order to understand the overgrowth of GaSb. As seen in Fig. 1b, the InAs–GaSb core-shell ZB segment is drastically larger in diameter compared to the WZ segment and the pure InAs core structure. From this we can tentatively conclude that the GaSb shell is preferentially formed on the ZB segment. Moreover, it is observed that an axial GaSb segment grows on the top of the second WZ segment mainly for wires with a larger diameter (40 nm) for most of the growth conditions that have been studied, and in some cases for smaller diameters (30 nm).³⁹ For more information on the GaSb material composition of this segment please see image S5 of the ESI† The thickness and length of this segment varies with the growth conditions, as discussed in the later sections.

Thereafter, the samples grown under reference parameters were characterized by high resolution TEM and XEDS analysis, which confirm the presence of a GaSb shell radially grown on

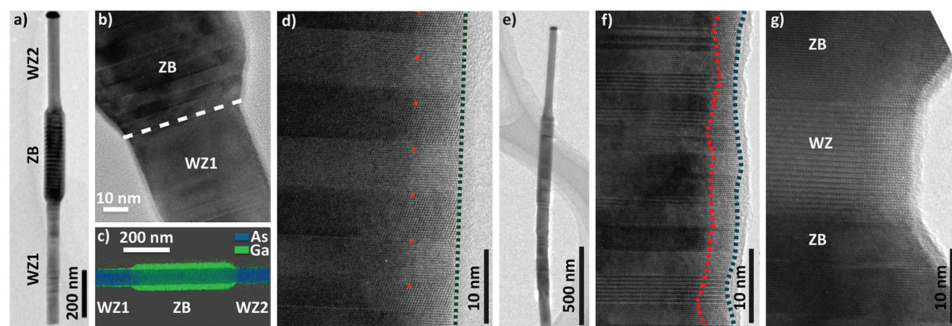


Fig. 2 (a) TEM bright field (BF) image of a core-shell nanowire grown from 40 nm Au particles at 460 °C, with a shell V/III ratio of 0.5, with a growth time equal to 20 minutes. (b) TEM BF image demonstrating the transition from the WZ1 segment of a nanowire to ZB. (c) STEM-XEDS color map of the zinc blende segment of the same wire. It is clear that the GaSb shell has grown preferentially on the zinc blende segment. (d) HRTEM image from the same wire where a smooth shell is observable on the regularly twinned zinc blende structure. The green dashed line shows the interface between the shell and the native oxide layer/carbon deposits on the nanowire, whereas the red dashed line shows the approximate position of the interface between the InAs core and the GaSb shell as determined from the contrast change in the HRTEM image. It should be noted that the exact position of the interface cannot be determined in a $\langle 110 \rangle$ direction, as the nanowires have $\{110\}$ side facets and therefore the transition represents an edge rather than a facet. (e) An overview TEM image of a nanowire grown from 30 nm Au seed particles with a faulty zinc blende segment. (f) HRTEM image from a section of the same mixed structured InAs core/GaSb shell nanowire as in (e), demonstrating the uneven shell caused by the underlying mixed core structure. The green dashed line indicates the border between the GaSb shell and the native oxide layer/carbon deposit, and the red dashed line represents the approximate position of the InAs/GaSb interface. (g) HRTEM image of a WZ inset in between two ZB structures demonstrating the high precision and control in growing crystal phase engineered nanowires. From the image it is clearly observable that the transitions between the structures on either side are clean and defect free.

the zinc blende segment. The thickness of this shell was measured to be about 8 nm, which is demonstrated as completely controllable by the set parameters of the growth conditions. Fig. 2 demonstrates high-resolution TEM with STEM-XEDS analysis for nanowires with Au aerosol particle diameters of 40 nm (Fig. 2a–d) and 30 nm (Fig. 2e and f) with an areal density of $1 \mu\text{m}^{-2}$. The XEDS map in Fig. 2c implies that a GaSb shell exists around the zinc blende segment. In Fig. 2b the transition from WZ1 to ZB is emphasized with the white dashed line. The sharp transition from one structure to the next, along with an almost equally sharp transition in shell formation, highlights the control and potential of the template method. In the high resolution TEM image shown in Fig. 2d, regularly twinned segments of the core-shell zinc blende segment can be observed. The position of the edge between the InAs core and GaSb shell, indicated by red dots, can be seen as a change in contrast accompanied by a faint line indicating slight interfacial strain. The fact that this contrast change is correlated with the change of material can be verified by EDX.

Fig. 2e and f show an overview and a high resolution TEM image, respectively, of the zinc blende segment of a nanowire from a different sample, where the intended pure ZB segment contains instead a mixture of ZB and WZ with frequent stacking defects, due to incomplete optimization of the core growth procedure. In Fig. 2f the approximate transition from InAs to GaSb is indicated by a red dashed line; note however that due

to changing facets the interface is not constant in projection and the indication is therefore approximate. Take note how the structural mixing has affected the GaSb shell growth (red and green dashed lines in Fig. 2f); unevenness is evident in the shell upon this faulty segment. Here, the surface of the shell is much rougher, with changes in the shell thickness being correlated with the underlying structure. The roughness observed in Fig. 2f can be explained by the higher radial growth rate of the zinc blende crystal phase for both InAs and GaSb, but is also exacerbated by the 30° facet rotations between consecutive ZB and WZ segments which is due to the terminating side facets of wurtzite ($\{10\bar{1}0\}$ -type), and zinc blende ($\{110\}$ -type) structures. This facet rotation results in inclined micro-facets at the interfaces between phases (see ref. 28 for details), which typically have higher surface energies than the flat ZB and WZ facets, yielding uneven surface growth when segments are short. A quick comparison of Fig. 2d and f signifies the importance of the control over the growing crystal phase along the core nanowire. This precise control is well demonstrated in Fig. 2g where a very short WZ segment is designed and grown in between two optimized ZB structures. From the HRTEM image it is clear there are no stacking defects in either transition between the two structures.

To attain a deeper understanding of the processes controlling the selectivity of the GaSb radial growth, as well as to optimize this selectivity, different series were grown in order to map out the growth conditions of the radial GaSb shell on the

zinc blende segment. From these we observe the significant effects of the temperature and GaSb V/III ratio, which are described in the following subsections. The total precursor flow did not significantly affect the growth; more information can be found in the ESI S2.† The time dependence of the shell growth is also shown in the ESI S3.† All these series were compared with the conditions of the reference shell growth described earlier. For the statistical analysis the software NanoDim⁴⁰ was used to determine the dimensions of more than 30 nanowires for each sample. The plots have been normalized to the diameter of the upper wurtzite segment (WZ2) for each sample to compensate for the Au aerosol nanoparticle diameter spread when comparing the samples. The WZ1 and ZB diameters of pure InAs core nanowires are also added as a reference for comparison.

3.2. Temperature dependence of GaSb shell growth

After growing the InAs core at 460 °C, the set temperature was investigated in a range between 420 °C–500 °C in steps of 20 °C. Several qualitative trends can be observed from the SEM images shown in Fig. 3a–e.

The nanowires consist of 4 distinct segments, corresponding to the three InAs segments and the axial GaSb segment, as shown in Fig. 1b. The axial GaSb segment clearly increases in length with increasing growth temperature, but the diameters of the various segments are nearly constant. This happens while the relative length of WZ2 decreases. This could be related to the higher decomposition rate of the InAs

nanowires at higher temperatures by the seed particle in the absence of ambient AsH₃ pressure.²⁰ At 500 °C, we speculate that the InAs segment has been completely decomposed, and as the two GaSb growth fronts merge, the initial segmented morphology of the nanowires is lost. We also speculate that for a high number of nanowires, the sudden dominance of the GaSb growth causes a change in the wetting angle of the particle, causing the nanowires to kink in a different direction than the conventional <111>-B-type growth direction.⁴¹

The diameter of each segment is plotted in Fig. 3f for temperatures up to 480 °C, together with the reference diameters for the core WZ1 and ZB segments, and the axial GaSb length is shown in Fig. 3g. The diameter of the ZB segment is nearly constant, indicating that the GaSb radial growth is nearly independent of temperature. This observation is also supported by the constant diameter of the axial GaSb segment of the wire for the studied temperature range. The WZ1 diameter is larger at lower GaSb growth temperatures, with a gradual decrease for increasing temperature, implying thin shell formations on wurtzite side facets at lower temperature ranges. Here we note, as shown in Fig. 1b, that the WZ1 diameter before GaSb shell growth is similar to or slightly smaller than the ZB diameter, so the increased thickness after shell growth at low temperatures is significant. The slight temperature dependence of the thickness for the ZB and WZ1 segments is similar, indicating that the selectivity of the shell growth between the segments cannot be efficiently tuned with temperature. It should also be noted that the stem segment used for nucleation has frequent

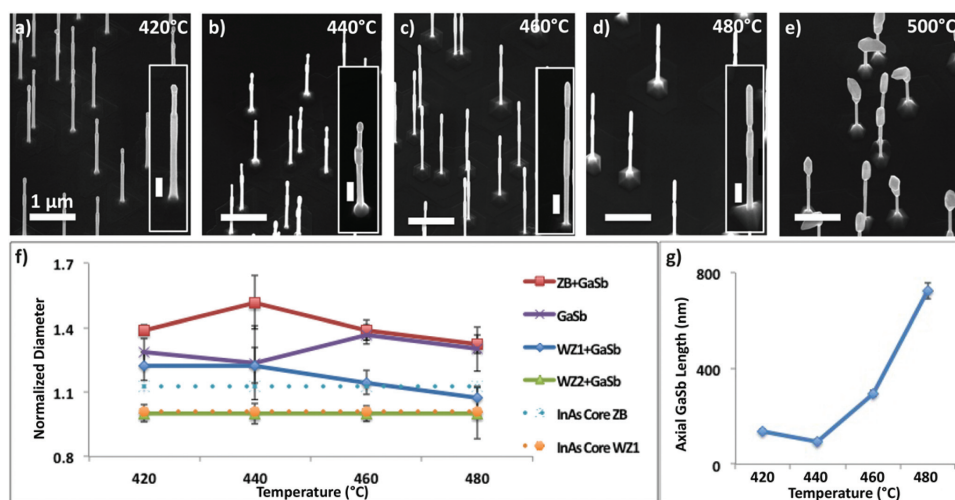


Fig. 3 Temperature series of the GaSb shell grown at: (a) 420 °C, (b) 440 °C, (c) 460 °C, (d) 480 °C, and (e) 500 °C. The V/III ratio is kept constant at 1.6. The scale bar corresponds to 1 μm. (f) Diameter of different segments versus shell growth temperature. Note that the diameters have been normalized to the diameter of WZ2. (g) Length of the axial GaSb segment at different temperatures. It is clear that the growth rate increases at higher temperatures.

stacking defects which have, in numerous other studies, been shown to act as preferential nucleation sites, enhancing radial growth (for example see ref. 39). Since the stem and WZ1 share common side facets, this will also enhance the radial overgrowth on WZ1 up to where ZB starts. The same effect is observed for radial growth of InAs (Fig. 1b), but lower temperatures also affect the overgrowth of GaSb.

3.3. Dependence of shell growth on V/III ratio of TMGa and TMSb precursors

The V/III ratio of the shell precursors was varied between 0.25 and 3.5 under the same total precursor flow as the reference run; see Fig. 4a–e. This was done by changing both the TMGa and TMSb molar fractions simultaneously to guarantee constant total precursor flow, as it is a growth variable that has a big impact on nanowire growth and crystal structure. As seen in Fig. 4f, as the V/III ratio increases from 0.5, the radial growth of GaSb on the ZB segment drastically decreases (indicated by a decreasing total diameter), while the diameter of the axial GaSb segment increases. The length of the axial GaSb segment increases as the V/III ratio of the shell increases to 1.6, and then drops to lower values again (Fig. 4g). This observation is well in line with previous studies on axial GaSb growth under different V/III ratios in the same reactor reporting a narrow axial growth window of GaSb with V/III ratios around 1.⁴² It is also consistent with previous observations of GaSb axial growth on InAs, where nucleation of the GaSb segment was reported to be very sensitive to Sb partial

pressure.³⁹ The opposing trends for the shell growth on the InAs ZB segment, and the GaSb axial and radial growth rates suggest a competition for material between the shell and the GaSb segment. The result is that at low V/III, when axial GaSb growth is suppressed, shell growth on zinc blende InAs is maximized. At the same time, the WZ1 diameter curve in Fig. 4f is constant for the different V/III ratios at a diameter very similar to the expected core diameter (the slight increase in the mid points is explained by the larger standard deviation depicted using the error bars). The low V/III ratio thus gives very good selectivity for growth of a GaSb shell on the ZB segment.

It is worth noting that for V/III ratios below 0.5 the yield of straight nanowires decreases drastically (Fig. 4a). We speculate that the kinking occurs in the presence of excessive group III (Ga) atoms in the seed particle during the shell growth, and the decomposition of the InAs core.

3.4. Multi-structured core-shell nanowires

To further demonstrate the potential and level of control that can be achieved for the GaSb shell growth on well-defined InAs zinc blende crystal structures, we show nanowires in Fig. 5 which were grown from 30 nm Au particles with three zinc blende segments separated by two very thin wurtzite segments (in addition to the base- and top segments of the nanowires). As seen in the overview SEM image in Fig. 5a we have achieved a very high yield of straight nanowires and well-defined core-shell segments with varying lengths. The length and

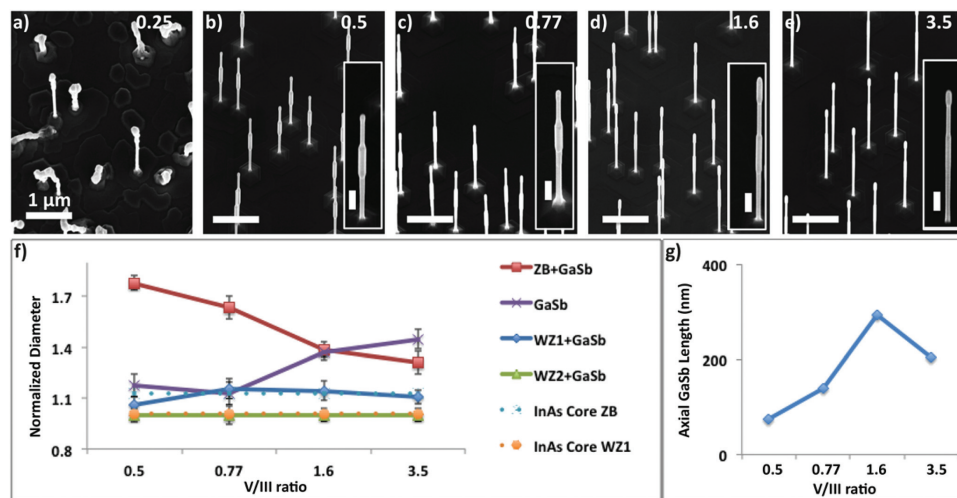


Fig. 4 V/III ratio series tested for the GaSb shell. The V/III ratio is varied between (a) 0.25, (b) 0.5, (c) 0.77, (d) 1.6, and (e) 3.5 while the growth temperature is kept constant at 460 °C. The scale bar corresponds to 1 μm. (f) Normalized diameter of different nanowire segments versus the shell V/III ratio. (g) Length of the axial GaSb segment at different V/III ratios.

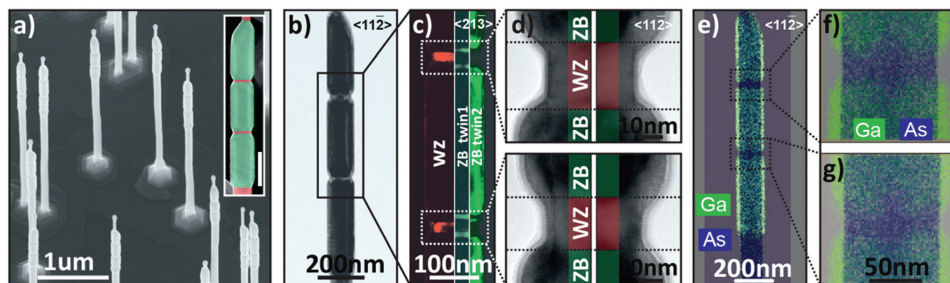


Fig. 5 (a) SEM image of InAs-GaSb core-shell nanowires grown from nominally 30 nm aerosol particles with multiple, axially stacked zinc blende and wurtzite segments. The inset displays a false colored (wurtzite – red, zinc blende – green) higher magnification side view of a representative nanowire (scale bar 200 nm). (b) TEM bright field image of a nanowire section similar to the inset given in (a) demonstrating the two WZ segments with smaller diameters. (c) Merged conventional dark field images of the wurtzite, and the two zinc blende twins given in red and green, respectively. (d) Higher magnification images of the two WZ segments color coded by overlaying the images taken along $\langle 112 \rangle$ -type and $\langle 213 \rangle$ -type directions. (e) An XEDS map of characteristic Ga (indicative of the GaSb shell) and As (indicative of the InAs core) taken for an identical nanowire as shown in (b–d), with higher magnification views of the two wurtzite segments embedded in zinc blende in (f) and (g) highlighting the selectivity of the GaSb shell growth.

positioning of these segments are precisely controlled by tailoring the crystal structure and growth time of the InAs core nanowire segments – a false colored inset is given in Fig. 5a, highlighting the different segments. Two wurtzite segments with lengths on the order of 15–20 nm are separated by three zinc blende segments of approximately 300 nm in length as shown in the TEM bright field image viewed along a $\langle 112 \rangle$ -type direction (Fig. 5b), and the dark field images acquired along a $\langle 213 \rangle$ -type direction using wurtzite and zinc blende characteristic diffraction spots (Fig. 5c). These are merged conventional dark field images of wurtzite (red) and the two 180° rotational zinc blende twins (green) which are given for the identical segment as shown in Fig. 5b. Higher magnification images of the two wurtzite segments viewed along the $\langle 112 \rangle$ -

type direction are given in Fig. 5d, with color coding for the wurtzite and zinc blende segments as revealed by overlaying the images taken along $\langle 112 \rangle$ -type and $\langle 213 \rangle$ -type directions. Here it is worth noting that the zinc blende and wurtzite characteristic bilayer stacking cannot be distinguished for the $\langle 112 \rangle$ -type viewing directions but is possible for the $\langle 213 \rangle$ -type directions perpendicular to the $\langle 111 \rangle$ -type growth direction. The subsequently smaller nanowire diameter at the position of the wurtzite segments is attributed to the selective GaSb shell growth, which almost exclusively forms on the zinc blende facets/segments, as demonstrated by the XEDS analysis in Fig. 5e–g. These images are taken along the $\langle 112 \rangle$ -type direction for an identical nanowire as shown in Fig. 5b–d. This precise control can be used in various device configurations,

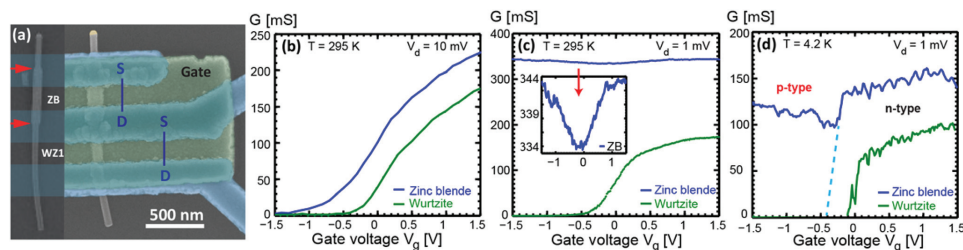


Fig. 6 (a) (left) SEM image of the nanowire prior to device fabrication, the red arrows indicate the transitions between wurtzite and zinc blende segments and the blue shadowed areas indicate where the source- and drain contacts are located. (right) False-colored SEM image of the completed device where source-/drain- and gate contacts are colored blue and green, respectively. Conductance as a function of gate voltage of ZB (blue) and WZ (green) segments in nanowires: (b) Reference InAs wire, not exposed to GaSb growth, measured at room temperature. (c) InAs wire with GaSb shell on the zinc blende segment shown in panel (a) measured at room temperature. The inset is a magnification of the data for the zinc blende segment. (d) Same nanowire as in panel (c) measured at $T = 4.2$ K.

such as interband tunnel diodes and transistors, in order to have carrier injection from the shell into the core exclusively at a desired position and length of the nanowire.

3.5. Electrical measurements

SEM images, before and after contact processing, of an InAs–GaSb core-shell nanowire used in the electrical measurements are displayed in Fig. 6a. The electrical properties of the ZB and WZ1 segments were investigated by measuring the drain current as a function of gate voltage. The bare InAs reference sample was measured at room temperature and with a drain bias of 10 mV, whereas the sample with selective GaSb overgrowth was measured at both room temperature and 4.2 K with a drain bias of 1 mV, see Fig. 6b–d. Starting with the reference sample (Fig. 6b), we note that the conductance of the ZB and WZ1 segments show similar gate voltage dependence. Going to negative gate voltages deplete the nanowire segments from charge carriers, which is expected since the nominally intrinsic InAs material with a large surface-to-volume ratio shows n-type behavior.⁴³ The current level is higher for ZB, which we attribute to a larger physical diameter and a higher charge carrier density compared with WZ. Looking next at the core-shell sample in Fig. 6a, we note that the measurements on the ZB segment (Fig. 6c) do not show the characteristics of bare InAs. Instead, the segment shows ambipolar transport characteristics, which can be attributed to an onset of hole transport in the GaSb shell at negative gate voltages, as shown in the inset of Fig. 2c. A similar ambipolarity has been observed and extensively studied in the reverse core-shell system (GaSb–InAs).⁴² By contrast, the WZ1 segment depletes at negative gate voltages, and has a conductance trace very similar to the reference segment, consistent with suppression of shell growth on wurtzite surface facets. As can be seen in Fig. 6d, the ambipolar characteristics are even more pronounced at $T = 4.2$ K. The light blue dashed line indicates the extrapolated conductance of a corresponding ZB segment without a shell of GaSb.

4. Summary

In this study we have demonstrated and investigated the selective radial growth of GaSb on chosen surfaces along the length of an InAs core nanowire. This was realized by controlled crystal phase engineering and by utilizing the higher surface energy of zinc blende structures compared to wurtzite, leading to a higher radial growth rate under optimized conditions. We have mapped out the dependence of the selective shell growth on the growth temperature, V/III ratio, total precursor flow, and growth time. From these investigations we conclude that: (i) the radial GaSb growth on the zinc blende segment is nearly independent of the growth temperature, while the undesired GaSb overgrowth on the wurtzite segment decreases with increasing temperature. (ii) Within a V/III ratio window of 0.5 to 3.5, the GaSb radial overgrowth on the zinc blende segment drastically drops with increasing V/III ratio, while no consider-

able GaSb overgrowth is observable on the wurtzite segment. Using the obtained knowledge we further demonstrate the fabrication of multiple position-controlled core-shell segments along the length of the nanowires under optimized shell growth conditions. This unique overgrowth method could be applied to any heteroepitaxial material system which exhibits different surface energies for the wurtzite and zinc blende crystal structures.

Electrical measurements show ambipolar (p- and n-) transport characteristics of the zinc blende segments in core-shell nanowires, whereas the wurtzite segments only show n-type transport, similar to bare reference InAs nanowires. These findings are consistent with selective radial growth of p-type GaSb on zinc blende InAs surface facets. Taking these findings into account, we anticipate that the template method demonstrated in this work is of considerable interest for quantum transport studies, as it allows for precise epitaxial control of core-shell quantum-dot-like structures.

Acknowledgements

This work was supported by the Swedish Research Council (VR), the Swedish Foundation for Strategic Research (SSF), the Knut and Alice Wallenberg Foundation (KAW), and the Nanometer Structure Consortium at Lund University (nmC@LU).

Notes and references

- 1 E. D. Minot, F. Kelkensberg, M. van Kouwen, J. A. van Dam, L. P. Kouwenhoven, V. Zwiller, M. T. Borgström, O. Wunnicke, M. A. Verheijen and E. P. A. M. Bakkers, Single quantum dot nanowire LEDs, *Nano Lett.*, 2007, 7(2), 367–371.
- 2 A. W. Dey, J. Svensson, M. Ek, E. Lind, C. Thelander and L.-E. Wernersson, Combining axial and radial nanowire heterostructures: radial Esaki diodes and tunnel field-effect transistors, *Nano Lett.*, 2013, 13(12), 5919–5924.
- 3 J. C. Johnson, H.-J. Choi, K. P. Knutsen, R. D. Schaller, P. Yang and R. J. Saykally, Single gallium nitride nanowire lasers, *Nat. Mater.*, 2002, 1(2), 106–110.
- 4 P. Krogstrup, H. I. Jørgensen, M. Heiss, O. Demichel, J. V. Holm, M. Aagesen, J. Nygard and A. Fontcuberta i Morral, Single-nanowire solar cells beyond the Shockley–Queisser limit, *Nat. Photonics*, 2013, 7(4), 306–310.
- 5 S. Nadj-Perge, S. M. Frolov, E. P. A. M. Bakkers and L. P. Kouwenhoven, Spin-orbit qubit in a semiconductor nanowire, *Nature*, 2010, 468(7327), 1084–1087.
- 6 B. Piccione, C.-H. Cho, L. K. van Vugt and R. Agarwal, All-optical active switching in individual semiconductor nanowires, *Nat. Nanotechnol.*, 2012, 7(10), 640–645.
- 7 K. Tomioka, M. Yoshimura and T. Fukui, A III–V nanowire channel on silicon for high-performance vertical transistors, *Nature*, 2012, 488(7410), 189–192.

- 8 R. Yan, D. Gargas and P. Yang, Nanowire photonics, *Nat. Photonics*, 2009, **3**(10), 569–576.
- 9 J. Johansson and K. A. Dick, Recent advances in semiconductor nanowire heterostructures, *CrystEngComm*, 2011, **13**(24), 7175.
- 10 P. Krogstrup, J. Yamasaki, C. B. Sørensen, E. Johnson, J. B. Wagner, R. Pennington, M. Aagesen, N. Tanaka and J. Nygård, Junctions in axial III–V heterostructure nanowires obtained via an interchange of group III elements, *Nano Lett.*, 2009, **9**(11), 3689–3693.
- 11 N. Li, T. Y. Tan and U. Gösele, Transition region width of nanowire hetero- and pn-junctions grown using vapor-liquid–solid processes, *Appl. Phys. A*, 2008, **90**(4), 591–596.
- 12 C.-Y. Wen, M. C. Reuter, J. Bruley, J. Tersoff, S. Kodambaka, E. A. Stach and F. M. Ross, Formation of compositionally abrupt axial heterojunctions in silicon-germanium nanowires, *Science*, 2009, **326**(5957), 1247–1250.
- 13 R. E. Algra, M. Hocevar, M. A. Verheijen, I. Zardo, G. G. W. Immink, W. J. P. van Enckevort, G. Abstreiter, L. P. Kouwenhoven, E. Vlieg and E. P. A. M. Bakkers, Crystal structure transfer in core/shell nanowires, *Nano Lett.*, 2011, **11**(4), 1690–1694.
- 14 L. J. Lauhon, M. S. Gudiksen, D. Wang and C. M. Lieber, Epitaxial core–shell and core-multishell nanowire heterostructures, *Nature*, 2002, **420**(6911), 57–61.
- 15 S. K. Lim, M. J. Tambe, M. M. Brewster and S. Gradecak, Controlled growth of ternary alloy nanowires using metal–organic chemical vapor deposition, *Nano Lett.*, 2008, **8**(5), 1386–1392.
- 16 T. J. Kempa, S.-K. Kim, R. W. Day, H.-G. Park, D. G. Nocera and C. M. Lieber, Facet-selective growth on nanowires yields multi-component nanostructures and photonic devices, *J. Am. Chem. Soc.*, 2013, **135**(49), 18354–18357.
- 17 T. Rieger, T. Schäpers, D. Grützmacher and M. I. Lepsa, Crystal Phase Selective Growth in GaAs/InAs Core–Shell Nanowires, *Cryst. Growth Des.*, 2014, **14**(3), 1167–1174.
- 18 J. Wallentin, M. E. Messing, E. Trygg, L. Samuelson, K. Deppert and M. T. Borgström, Growth of doped InAs_yP_{1–y} nanowires with InP shells, *J. Cryst. Growth*, 2011, **331**(1), 8–14.
- 19 S. Gorji Ghalamestani, A. M. Munshi, D. L. Dheeraj, B.-O. Fimland, H. Weman and K. A. Dick, Self-catalyzed MBE grown GaAs/GaAs(x)Sb(1–x) core–shell nanowires in ZB and WZ crystal structures, *Nanotechnology*, 2013, **24**(40), 405601.
- 20 S. Gorji Ghalamestani, M. Heurlin, L.-E. Wernersson, S. Lehmann and K. A. Dick, Growth of InAs/InP core–shell nanowires with various pure crystal structures, *Nanotechnology*, 2012, **23**(28), 285601.
- 21 K. A. Dick, J. Bolinsson, M. E. Messing, S. Lehmann, J. Johansson and P. Caroff, Parameter space mapping of InAs nanowire crystal structure, *J. Vac. Sci. Technol. B*, 2011, **29**(4), 04D103.
- 22 P. Caroff, K. A. Dick, J. Johansson, M. E. Messing, K. Deppert and L. Samuelson, Controlled polytypic and twin-plane superlattices in iii–v nanowires, *Nat. Nanotechnol.*, 2009, **4**(1), 50–55.
- 23 J. Bolinsson, P. Caroff, B. Mandl and K. A. Dick, Wurtzite–zincblende superlattices in InAs nanowires using a supply interruption method, *Nanotechnology*, 2011, **22**(26), 265606.
- 24 R. E. Algra, M. A. Verheijen, M. T. Borgström, L.-F. Feiner, G. Immink, W. J. P. van Enckevort, E. Vlieg and E. P. A. M. Bakkers, Twinning superlattices in indium phosphide nanowires, *Nature*, 2008, **456**(7220), 369–372.
- 25 P. Caroff, J. Bolinsson and J. Johansson, Crystal Phases in III–V Nanowires: From Random Toward Engineered Polytypism, *IEEE J. Sel. Top. Quantum Electron.*, 2011, **17**(4), 829–846.
- 26 H. J. Joyce, J. Wong-Leung, Q. Gao, H. H. Tan and C. Jagadish, Phase perfection in zinc Blende and Wurtzite III–V nanowires using basic growth parameters, *Nano Lett.*, 2010, **10**(3), 908–915.
- 27 H. Huang, X. Ren, X. Ye, J. Guo, Q. Wang, X. Zhang, S. Cai and Y. Huang, Control of the crystal structure of InAs nanowires by tuning contributions of adatom diffusion, *Nanotechnology*, 2010, **21**(47), 475602.
- 28 S. Lehmann, J. Wallentin, D. Jacobsson, K. Deppert and K. A. Dick, A general approach for sharp crystal phase switching in InAs, GaAs, InP, and GaP nanowires using only group V flow, *Nano Lett.*, 2013, **13**(9), 4099–4105.
- 29 B. Ganjipour, M. Ek, B. Mattias Borg, K. A. Dick, M.-E. Pistol, L.-E. Wernersson and C. Thelander, Carrier control and transport modulation in GaSb/InAsSb core/shell nanowires, *Appl. Phys. Lett.*, 2012, **101**(10), 103501.
- 30 T. Rieger, D. Grützmacher and M. I. Lepsa, Misfit dislocation free InAs/GaSb core–shell nanowires grown by molecular beam epitaxy, *Nanoscale*, 2014, **7**, 356–364.
- 31 A. W. Dey, B. M. Borg, B. Ganjipour, M. Ek, K. A. Dick, E. Lind, C. Thelander and L.-E. Wernersson, High-Current GaSb/InAs(Sb) Nanowire Tunnel Field-Effect Transistors, *IEEE Electron Device Lett.*, 2013, **34**(2), 211–213.
- 32 B. M. Borg, K. A. Dick, B. Ganjipour, M.-E. Pistol, L.-E. Wernersson and C. Thelander, InAs/GaSb heterostructure nanowires for tunnel field-effect transistors, *Nano Lett.*, 2010, **10**(10), 4080–4085.
- 33 I. Knez, R.-R. Du and G. Sullivan, Evidence for Helical Edge Modes in Inverted InAs/GaSb Quantum Wells, *Phys. Rev. Lett.*, 2011, **107**(13), 136603.
- 34 C. Liu, T. Hughes, X.-L. Qi, K. Wang and S.-C. Zhang, Quantum Spin Hall Effect in Inverted Type-II Semiconductors, *Phys. Rev. Lett.*, 2008, **100**(23), 236601.
- 35 B. Ganjipour, M. Leijnse, L. Samuelson, H. Q. Xu and C. Thelander, Transport studies of electron-hole and spin-orbit interaction in GaSb/InAsSb core–shell nanowire quantum dots, *Phys. Rev. B: Condens. Matter*, 2015, **91**(16), 161301.
- 36 V. Pankoke, P. Kratzer and S. Sakong, Calculation of the diameter-dependent polytypism in GaAs nanowires from an atomic motif expansion of the formation energy, *Phys. Rev. B: Condens. Matter*, 2011, **84**(7), 075455.

- 37 N. V. Sibirev, M. A. Timofeeva, A. D. Bol'shakov, M. V. Nazarenko and V. G. Dubrovskii, Surface energy and crystal structure of nanowhiskers of III-V semiconductor compounds, *Phys. Solid State*, 2010, **52**(5), 1531.
- 38 T. Xu, K. A. Dick, S. Plissard, T. H. Nguyen, Y. Makoudi, M. Berthe, J.-P. Nys, X. Wallart, B. Grandidier and P. Caroff, Faceting, composition and crystal phase evolution in III-V antimonide nanowire heterostructures revealed by combining microscopy techniques, *Nanotechnology*, 2012, **23**(9), 095702.
- 39 M. Ek, B. M. Borg, J. Johansson and K. A. Dick, Diameter limitation in growth of III-Sb-containing nanowire heterostructures, *ACS Nano*, 2013, **7**(4), 3668–3675.
- 40 NanoDim Software, <http://www.nanodim.net>.
- 41 B. M. Borg and L.-E. Wernersson, Synthesis and properties of antimonide nanowires, *Nanotechnology*, 2013, **24**(20), 202001.
- 42 M. Jeppsson, K. A. Dick, J. B. Wagner, P. Caroff, K. Deppert, L. Samuelson and L.-E. Wernersson, GaAs/GaSb nanowire heterostructures grown by MOVPE, *J. Cryst. Growth*, 2008, **310**(18), 4115–4121.
- 43 C. Thelander, M. T. Björk, M. W. Larsson, A. E. Hansen, L. R. Wallenberg and L. Samuelson, Electron transport in InAs nanowires and heterostructure nanowire devices, *Solid State Commun.*, 2004, **131**(9–10), 573–579.

Supplemental information for “Selective GaSb Radial Growth on Crystal Phase Engineered InAs Nanowires”

Luna Namazi¹, Malin Nilsson¹, Sebastian Lehmann¹, Claes Thelander¹, Kimberly A. Dick^{1,2}

¹ Solid State Physics, Lund University, Box 118, S-221 00 Lund, Sweden

² Center for Analysis and Synthesis, Lund University, Box 124, S-221 00 Lund, Sweden

Table of Contents

| | |
|--|---|
| <i>S1. Optimization of InAs core crystal structure for different diameters</i> | 2 |
| S2. Time dependence of GaSb shell growth | 4 |
| S3. Time dependence of GaSb shell growth | 5 |
| S4. Seed particle density effect | 7 |
| S5. Material composition of the axial GaSb segment | 8 |
| S6. Elemental maps of Sb and In on the multiple segmented nanowires | 9 |

S1. Optimization of InAs core crystal structure for different diameters

For different seed particle diameters specific growth timings with different flows and pressures of the precursors were used in order to obtain the optimized InAs core structure. After loading the InAs samples inside the reactor, the temperature was raised to 550 °C for 7 minutes to anneal the sample and remove any oxide on the surface of the substrate. An AsH₃ flow ranging from 7.69×10^{-5} to 1.54×10^{-2} was present in the reactor, starting from the annealing step, until the InAs core growth was completed in order to avoid InAs from decomposing at high temperatures. After the annealing step the temperature was ramped down to 460 °C. For Au particles with 40 nm diameter, the InAs nanowire growth was commenced by providing a TMIn flow equal to (3.48×10^{-6}) while the AsH₃ flow was switched to (1.92×10^{-2}) to nucleate the growth from the seed particle. The first wurtzite segment (WZ1) was then grown for 5 minutes at a lower AsH₃ flow of 9.23×10^{-5} , while keeping the TMIn flow constant. For growing the zinc blende segment a significantly higher V/III ratio is required. Therefore, a higher AsH₃ flow (1.54×10^{-2}) was provided into the reactor for a set time depending on the desired length of the zinc blende segment (5 minutes in figure S1). Then after, the AsH₃ flow was switched to the set values for wurtzite growth (9.23×10^{-5}) and the second wurtzite segment was grown for 2 minutes.

Since tuning the crystal phase becomes more sensitive to growth conditions as the diameter of the Au seed particle gets smaller, in order to optimize the crystal structure for Au particles with 30nm diameters, different TMIn flows for the different structures were used in contrary to the constant TMIn flow utilized for both WZ and ZB segments for diameter of 40nm. Also, pausing steps were introduced in between consecutive segments of the InAs core structure. This was done to allow time to purge away excess material from the reactor, while switching the AsH₃ flows. During these short pausing steps TMIn was switched off, and the samples remained under an AsH₃ flow. The TMIn flow used for the wurtzite segments was slightly higher (3.48×10^{-6}) compared to that used for growing the zinc blende segment (1.93×10^{-6}). The pausing time used between wurtzite and zinc blende was 45s, whereas it was set to 3s when switching from zinc blende to wurtzite. For attaining a better understanding, figure S1 depicts the sequence of flows and pausing steps of the growth of an InAs core with a WZ-ZB-WZ structure. Growth times for the different segments for 30 nm samples that were similar to those of 40 nm, lead to longer segments as expected e.g. for 5 minutes of ZB growth 450 nm versus 300 nm, and for 5 minutes of WZ2 growth time 550 nm versus 400 nm for nanowires with particle diameters of 30 nm and 40 nm respectively. The lengths of different segments were tailored to desire by adjusting the growth times based on the diameter and areal particle density.

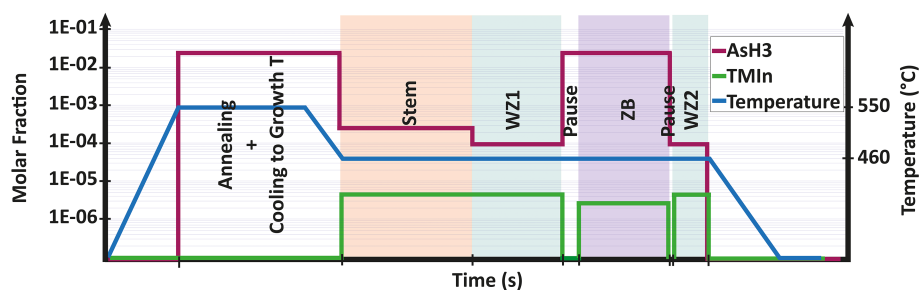


Figure S1: Schematics for set temperatures, precursor flows, and precursor switching as used for growing an InAs core structure from Au seed particles of 30nm versus time. The molar fraction is demonstrated with a logarithmic scale on the left y-axis, while the right y-axis shows the temperature. The time axis is to scale with the real values used for growing the nanowires.

S2. Time dependence of GaSb shell growth

Starting from the reference shell growth time (20 minutes), 3 additional growth times, 10, 40, and 60 minutes were investigated. From the 30° tilted SEM images (S2a-d) and the analysis given in S2e it can be seen that neither the shell thickness around the ZB segment, nor the diameter of the axial GaSb do not considerably change as time increases (S2e). The offset from the trend of the data point related to 40 minutes can be explained by the Au aerosol nanoparticle variability and the diameter spread caused by this artefact. On the other hand, the axial growth rate increases with time (S2f). Therefore, it can be concluded that at these growth conditions, longer shell growth times do not necessarily lead to thicker shells on the ZB segments since the material is all consumed by the axial growth of the axial GaSb segment.

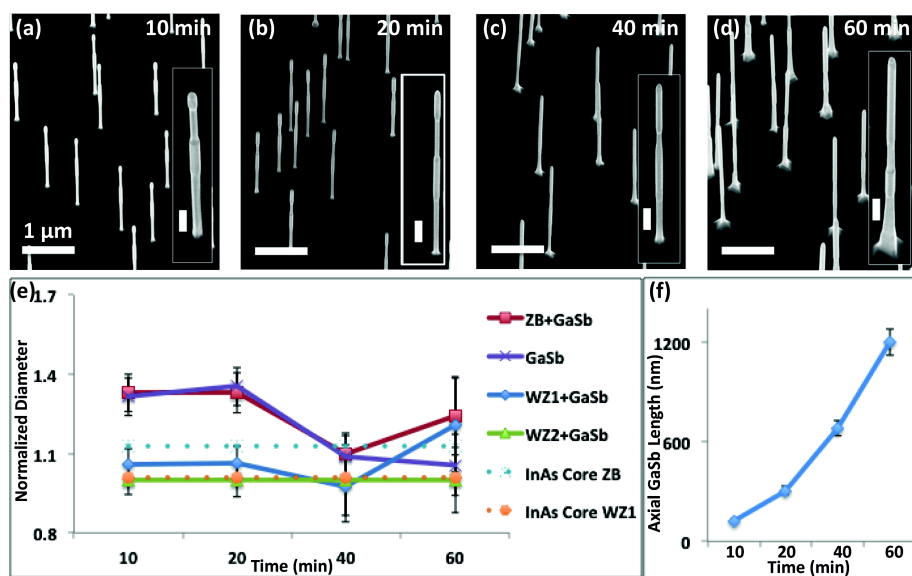


Figure S2: 30°-tilted SEM images of the GaSb shell growth time series of a) 10, b) 20, c) 40, and d) 60 minutes. The scale bar corresponds to 1 μ m. Insets in a-d show a higher magnification image of a representative nanowire highlighting the different axial segments. The measured diameter of the various nanowire segments is given in (e), normalized to the WZ core diameter, and for the different shell growth times. Please note that for WZ1 the error bars on 40 and 60 minutes of shell growth time are relatively large, showing a large variation in nanowire diameter caused by the spread in the aerosol particle diameter or due to unstable growth conditions. Taking this into consideration, the diameter of the WZ1 segment can be considered constant; independent from the GaSb shell growth time.

S3. Total precursor flow influence on GaSb shell growth

A series of different total precursor flows was also carried out under a constant nominal V/III ratio of 1.6. Starting from the reference recipe's total precursor flow of 8.87×10^{-5} (the sum of the molar fractions of the group III and V precursors), two additional flows were studied, namely 4.44×10^{-5} and 17.0×10^{-5} . As seen in image S3, at the lower total flow the GaSb shell on the zinc blende segment is asymmetric, growing on only one of the side facets of the ZB. The SEM image in figure S3a and b indicates that the nanowires are bent probably due to the strain between the InAs core and the GaSb shell caused by the asymmetric shell growth. From this figure it is also observable that the distribution of this one facet-growth selectivity is statistically equal for all three facets. Therefore the measurements done on the diameter of the zinc blende are not reliable as they do not represent a values corresponding to a uniform shell layer thickness around the zinc blende. One can relate this to a kinetic process when nucleation is initiated on one facet leading to the preference of growth continuation on that facet only. We speculate that this is due to a very low nucleation rate of the GaSb layer. Once nucleation occurs on one side facet, continuation of growth on that side facet is more favoured than nucleation on other facets, leading to the formation of these asymmetrical shells.

Other than that, the two experiments with higher total flows (figures S3c, and d) show uniform shell (thickness) formation. It is clear from the graph in figure S3e that the diameter of the axial GaSb segment and the zinc blende diameter have opposite trends, meeting in the mid point. In other words, relating this to the increment observed in figure S3f in the length of the axial GaSb segment, it can be stated that as the amount of precursors in the reactor increases the axial GaSb segment growth becomes dominant related to the competition between the radial shell growth on the zinc blende segment and the axial GaSb growth. At the medium total precursor flow the radial growth rates of both the ZB segment and the axial GaSb are more or less equal to each other.

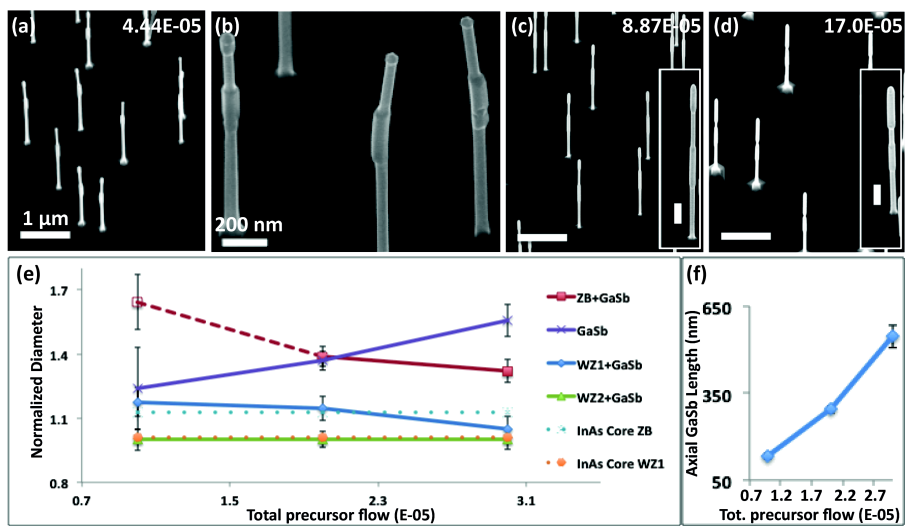


Figure S3: Total flows of a) 4.44×10^{-5} , c) 8.87×10^{-5} , and d) 17.0×10^{-5} of the GaSb shell precursors. In a) asymmetric shells are observed on the zinc blende segments of the nanowires. The three-fold asymmetrical shell formation is clearly observable from the zoomed in image displayed in (b). d) The normalized diameter of the different segments of the core-shell nanowires for different shell growth times. e) demonstrates a linear increment in the length of the axial GaSb segment for increasing total flows which is explained by the presence for more material in the reactor during growth.

S4. Seed particle density effect

The areal density of the deposited Au seed particles has a big influence on the length and morphology of the grown nanowires.

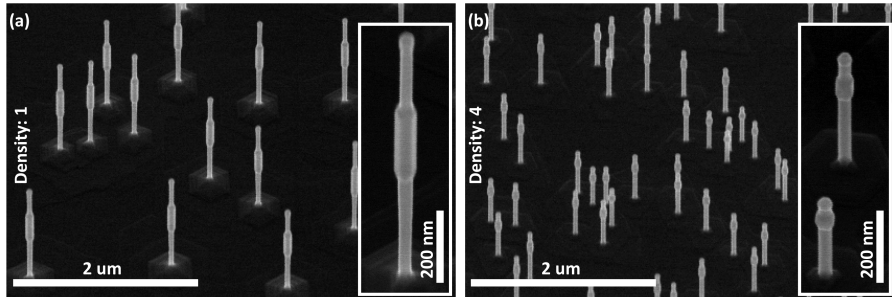


Figure S4: SEM images of core/shell InAs GaSb nanowires grown from Au seed particles with a diameter of 40 nm and an areal density of (a) 1 particle/ μm^2 , and (b) 4 particle/ μm^2 grown under the exact same conditions. Due to competition for material the nanowires with a higher surface density have a lower growth rate, leading to shorter length of the different segments. Also, at higher densities a nanowire to nanowire variation is observed, which is again related to material competition at the growth sites.

S5. Material composition of the axial GaSb segment

Under certain shell growth conditions an axial GaSb segment grows above the WZ2 segment. In figure S5 the XEDS map analysis confirms that this segment is pure GaSb and is not an InAs segment related to the core structure.

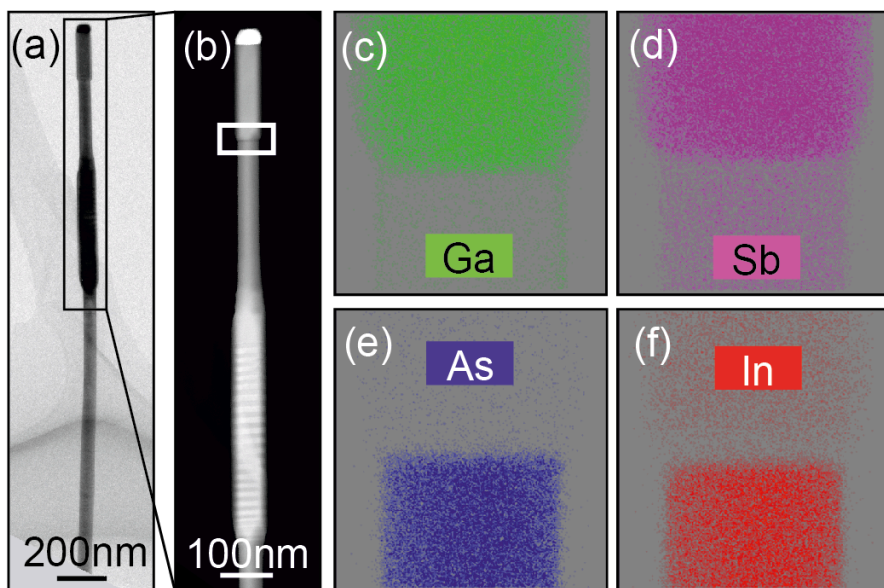


Figure S5: a) TEM overview of a core-shell InAs-GaSb nanowire where the black box indicates where the higher magnification dark field image in (b) is corresponding to. The transition between the WZ2 segment and the top axial GaSb segment is represented by the white box in (b). c-f) XEDS elemental maps acquired from the area indicated by the white box in b). These maps confirm that the top segment is pure GaSb with no traces of the core InAs.

S6. Elemental maps of Sb and In on the multiple segmented nanowires

A full elemental map of all the elements of the core and shell are given here. However, it is worth noting that due to the overlap between the Sb L_{α} line and the In L_{β} line, distinguishing In and Sb, is not as straight forward. Therefore, it ruling out the In trace from the shell and the Sb trace from the core is not completely feasible. In addition, the GaSb shell entirely surrounds the InAs core on the ZB segments. This leads to uncertainty in determining the existence of interdiffusion based on the XEDS technique.

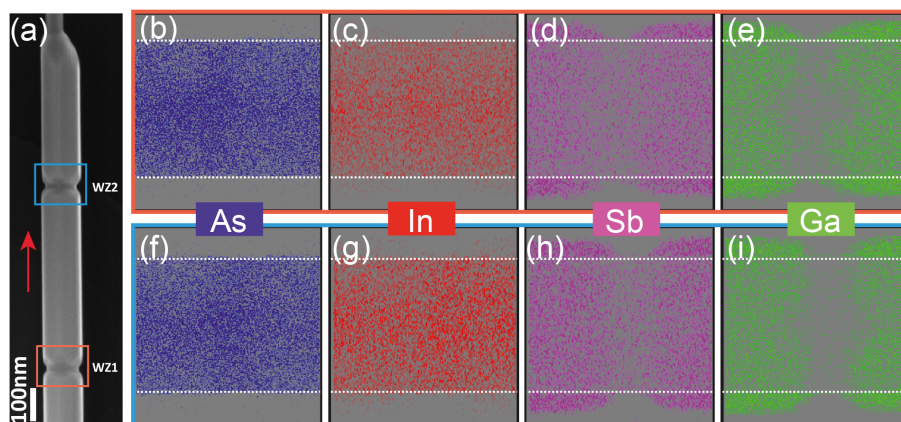


Figure S6: a) SEM image of a multiple segmented InAs/GaSb core/ shell nanowire. The red arrow shows the growth direction. The colored boxes correspond to the XEDS maps of all the composing material of both the core (In and As) and the shell (Ga and Sb) shown in figures S6 b-i.

Paper III



Realization of wurtzite GaSb using InAs nanowire templates

Luna Namazi,^{*,†} Louise Gren,^{†,‡} Malin Nilsson,[†] Magnus Garbrecht,[¶] Claes Thelander,[†] Reza R. Zamani,^{*,†} and Kimberly A. Dick^{†,§}

Solid State Physics, Lund University, Box 118, Lund 22100, Sweden, Ergonomics and Aerosol Technology, Lund University, Box 118, Lund 22100, Sweden, Thin Film Physics Division, IFM, Linköping University, Linköping 58183, Sweden, and Centre for Analysis and Synthesis, Lund University, Box 124, Lund 22100, Sweden

E-mail: luna.namazi@ftf.lth.se; reza.zamani@ftf.lth.se, reza.r.zamani@gmail.com

Abstract

The crystal structure of a material has a large impact on the electronic and material properties such as band alignment, band gap energy, and surface energies. Au-seeded III–V nanowires are a promising technology for exploring these effects, since for most III–V materials they readily grow in either wurtzite or zinc blende crystal structure. In III–Sb nanowires however, wurtzite crystal structure growth has proven difficult. Therefore, other methods must be developed to achieve wurtzite antimonides. For GaSb, theoretical predictions of the band structure diverge significantly, but the absence of wurtzite GaSb material has prevented any experimental verification of the

^{*}To whom correspondence should be addressed

[†]Solid State Physics, Lund University

[‡]Ergonomics and Aerosol Technology, Lund University

[¶]Thin Film Physics Division, IFM, Linköping University

[§]Centre for Synthesis and Analysis, Lund University

properties. Having access to this material is a critical step towards clearing the uncertainty in the electronic properties, improving the theoretical band structure models and potentially opening doors towards application of this new material. In this work we demonstrate the use of InAs wurtzite nanowires as templates to realize GaSb wurtzite shell layers with varying thicknesses. We study the properties of the axial and radial heterointerfaces at the atomic scale by means of aberration-corrected scanning transmission electron microscopy, revealing their sharpness and structural quality. The transport characterizations point towards a positive offset in the valence band edge of wurtzite compared to zinc blende.

Keywords

wurtzite GaSb, GaSb - InAs, III-V nanowire, heterointerface, aberration-corrected STEM

1. Introduction

III-V semiconducting nanowires, specifically those with heterostructure configurations, are drawing attention due to their unique properties promising for electronic and optoelectronic applications such as transistors,¹⁻⁴ solar cells⁵⁻⁷ and photodetectors.⁸⁻¹⁰ The InAs-GaSb heterostructure system is particularly suitable for various tunneling-based device applications such as tunneling field effect transistors (TFETs) and diodes due to the broken band gap alignment it exhibits.¹¹ This material combination has been previously investigated in detail in the axial and radial configurations.¹¹⁻¹⁵

Most III-V nanowires grow both in the zinc blende and metastable wurtzite crystal structure.¹⁶⁻²¹ It has been demonstrated that the crystal structure of the nanowires can be precisely controlled for different materials such as InAs.²²⁻²⁴ One method is to use a high V/III ratio of the precursors for growth of zinc blende, while using a much lower value for the

wurtzite structure.²⁵ Having control over the crystal structure is important since it strongly affects the physical properties of the material.^{26–28} For instance it has been previously shown that the conduction and valence bands of wurtzite and zinc blende crystal structures of the same material can be offset when compared to one another.^{16,29–31} In addition, the band gap size differs for some materials such as InAs and GaAs, with some theory and experiments indicating a larger gap for wurtzite.^{16,28,32,33} The potential to precisely switch between crystal phases during nanowire growth allows for the formation of well-defined crystal phase quantum dots³⁴ with interfaces that are atomically sharp and effectively strain-free. Finally, the surface properties are very different, with wurtzite nanowire side facets typically having lower surface energies compared to the corresponding zinc blende facets. This property has been exploited in the development of selective radial heterostructures [35][36].^{35,36}

For GaSb, the effect of crystal structure on material properties is still unknown. Wurtzite GaSb material has not yet been demonstrated experimentally, and so there are no experimental measurements of its properties. Moreover, theoretical investigations of its band structure have predicted very different results. Most investigations predict a much smaller band gap for wurtzite GaSb than for zinc blende, with a positive valence band offset.^{30,37–39} This would lead to a type-I band alignment between wurtzite and zinc blende GaSb, a configuration that may be unique among III–V crystal phase heterostructures. The much smaller band gap would also have implications for other properties such as the hole mobility. However, other works predict instead a slightly larger band gap for wurtzite GaSb³¹ with a positive valence band offset, leading to a type-II alignment similar to other III–Vs such as InAs. Experimental investigations of the properties of wurtzite GaSb are therefore critically needed in order to verify and improve theoretical predictions, and potentially exploit the properties of this material. The synthesis of well-controlled wurtzite GaSb material is an essential first step.

Moreover, in various applications of heterostructure nanowires, such as TFETs, the exact nature of the heterointerfaces have a considerable impact on the functionality as they affect

the band alignment.^{40–44} Depending on how the secondary material is accommodated on the initial, the coherence between the crystal structures of the two may be influenced, giving rise to potential misfit dislocations or strain in the vicinity of the heterointerface.⁴⁵ Such aspects can significantly affect the physical properties of the heterostructures.^{46,47} Additionally, any intermixing of the two compounds or inter-diffusion of elements, even at the atomic scale, can have a large impact on the properties of the heterostructures and hence the performance of any device based on them⁴⁸ Therefore, it is of high importance to study the interfaces at the atomic scale.

However, compared to other III–V nanowires, in which wurtzite structure is comparatively much easier to form, Sb–based nanowires are challenging to grow in the wurtzite crystal phase. This can be attributed to the low ionicity of III–Sb materials in general, together with the surfactant effect of Sb and its effects on the surface energetics of the system.⁴⁹ As a result, wurtzite antimonides, and in particular wurtzite GaSb, and their physical and material properties have remained an unexplored area of research. Therefore, development of alternative methods to synthesize wurtzite GaSb is very important.

We here report on successful growth of wurtzite GaSb using wurtzite InAs nanowires as templates for radial (shell) growth. GaSb shell thickness up to 30–40 nm is demonstrated, which is controllable with growth time. We discuss the shell formation mechanism along with shell uniformity in detail, and show that the wurtzite material grows by step flow along the side facets. We also demonstrate high-resolution scanning transmission electron microscopy (STEM) studies at the atomic scale on both the radial and axial heterointerfaces of the nanowires and discuss differences between their composition and sharpness. In the radial direction, we find heterointerfaces to be nearly sharp, with only one bilayer of ternary material marking the boundary, while in the axial direction, a gradual change in composition over a few bilayers is revealed. Finally, we investigate the electrical characteristics of the wurtzite core-shell InAs–GaSb nanowires, and observe ambipolar behavior at liquid helium temperature (4.2 K), indicative of parallel electron and hole channels. In addition, we observe

significantly higher hole conductance in the wurtzite InAs-GaSb core-shell in comparison to the zinc blende axial GaSb segment. This is an indication of a positive offset in the valence band edge of wurtzite compared to zinc blende in agreement with theoretical predictions.

2. Results and Discussion

2.1. General overview of the material systems

We will first discuss the wurtzite GaSb shell grown for 40 minutes under a set of conditions stated in the methods section that, for convenience, we will refer to as reference GaSb shell conditions throughout the rest of the text. In Figure 1 we demonstrate schematic representations (left), and cross sections (inset), along with overview (center) and magnified (right) scanning electron microscopy (SEM) images of wurtzite InAs core (figure 1a), wurtzite InAs-GaSb core-shell (CS) reference (figure 1b), and wurtzite InAs-GaSb-InAs core-shell-shell (CSS) (figure 1c) nanowires. It is observed that the reference InAs core nanowires (figure 1a) are taper-free. Following the GaSb growth (figure 1b), the nanowires exhibit two distinct segments, where the bottom segment is thicker and slightly longer than the reference InAs, and is tapered. This is presumed to be a core-shell InAs-GaSb segment, where the morphology indicates that the GaSb growth is tapered, which is evidence of a diffusion limited shell growth mechanism. We will discuss this tapering further in the paper, under section 2; shell growth mechanism. Above this segment, there is a thicker section following a clear diameter step, which is attributed to an unintentionally grown axial GaSb segment. Figure 1c shows schematic, overview and magnified images of nanowires with a thin InAs outer shell (2–5 nm) surrounding the GaSb shell. This InAs-GaSb-InAs core-shell-shell configuration is designed and synthesized for electrical characterization purposes, which will be discussed further in the paper (section 2.4; electrical characterization). From figure 1c it is clear that the overall morphology of these nanowires is similar to the CS sample (figure 1b).

The transmission electron microscopy (TEM) images in figure 2a-c confirm the wurtzite crystal structure of the InAs/GaSb segment. The TEM analysis confirms that the shell has a complete epitaxial relation with the core, and despite the 1% difference between the unit cell parameters of wurtzite InAs and GaSb, no misfit dislocations are observed over the entire length of any of the investigated core-shell segments. The high-resolution TEM (HRTEM) image along with the power spectrum (fast Fourier transform, FFT) in figure 2b (upper inset), also reveals the zinc blende crystal structure of the axial GaSb segment. This is expected, since, as mentioned earlier in the introduction, antimonide nanowires grow in the zinc blende crystal phase at typical growth conditions. Also, from figure 2b it is clear that the crystal structure transition at the axial heterointerface between the wurtzite core/shell segment and the zinc blende axial segment is sharp. Figures 2d and e show high-angle annular dark-field (HAADF)-STEM images together with the X-ray energy dispersive spectroscopy (XEDS) compositional maps of the core-shell and core-shell-shell nanowires, respectively. The map of the core-shell nanowire (figure 2d) is obtained at high magnification in order to show the sharpness of the heterointerface, which will be discussed in section 2.3. The presence of Ga and Sb signals in the core region is due to the 3D geometry of the core-shell structure where the shell covers the entire core. As expected from a sharp transition, In and As signals, in contrast, do not emerge from the shell region. The XEDS maps in figure 2e demonstrate the presence of a thin InAs shell in the core-shell-shell nanowire.

2.2. GaSb shell growth mechanism

The optimized growth conditions for the wurtzite InAs-GaSb core-shell nanowires mentioned in the introduction were based on previous studies of InAs-GaSb core-shell heterostructures with zinc blende crystal structure grown in the same reactor.³⁵ The growth parameters of the GaSb shell such as temperature, V/III ratio and total precursor flow have been changed and the effects have been studied in order to achieve the desired wurtzite shell growth. When compared to the optimum conditions for zinc blende GaSb shell growth on InAs, the wurtzite

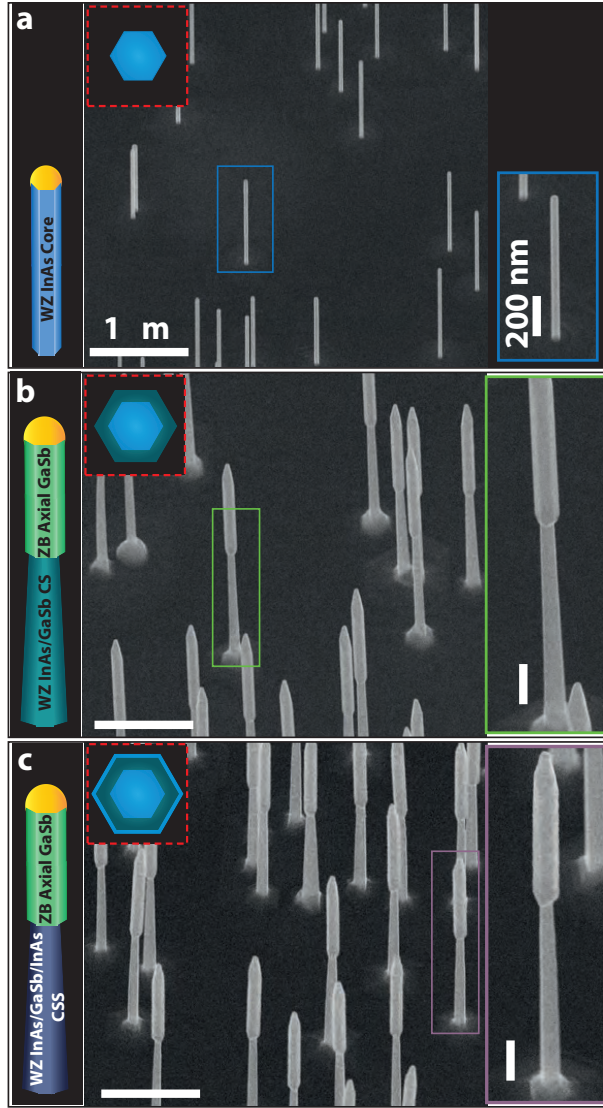


Figure 1: Schematic overview, SEM overview and magnified images along with radial cross-section representations of (a) InAs wurzite core, (b) wurtzite InAs-GaSb core-shell (CS), and (c) wurtzite InAs-GaSb-InAs core-shell-shell (CSS) nanowires. An axial GaSb segment grows unintentionally for the CS (b) and CSS (c) nanowires.

conditions are higher in temperature (470 °C instead of 460 °C), and an order of magnitude higher in total precursor flow (6.44×10^{-4} compared to 8.61×10^{-5}), while the V/III ratio is

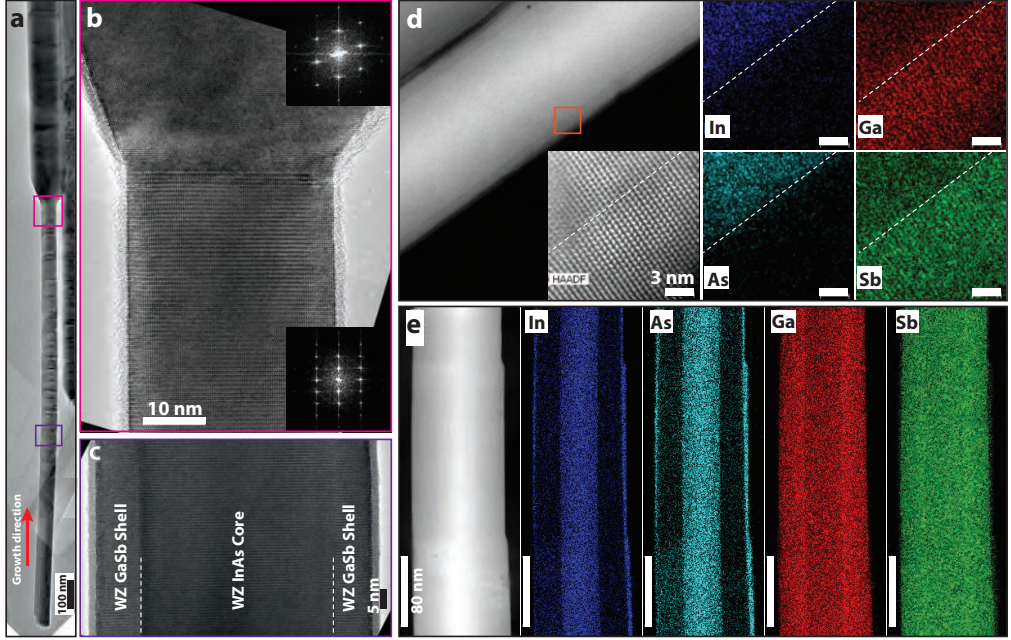


Figure 2: (a) Low-magnification TEM micrograph of a wurtzite InAs-GaSb core-shell nanowire followed by a zinc blende GaSb segment; (b) HRTEM image of the axial heterointerface between the wurtzite core-shell segment and zinc blende GaSb one, associated with power spectra (FFT); (c) HRTEM image indicating the radial heterointerface between the wurtzite InAs core and the wurtzite GaSb shell; (d) HAADF-STEM micrograph of a core-shell nanowire associated with XEDS compositional maps; (e) HAADF-STEM micrograph of a core-shell-shell nanowire associated with XEDS compositional maps.

similar (0.50 vs. 0.48). It is interesting that the optimum V/III ratio is the same for wurtzite and zinc blende radial growth, even though it is a key parameter for selecting between wurtzite and zinc blend in axial growth.²⁵ Both total flow and temperature significantly affect the amount of material available during growth, hence increasing the vapor supersaturation of the system. At higher temperatures, not only is the cracking of the precursors more efficient, but the diffusion lengths of the adatoms are also higher. It is known that in general wurtzite nanowire surfaces have lower energy compared to zinc blende nanowire surfaces.^{25,50} Therefore, it can be argued that at higher vapor phase supersaturations, the nucleation barrier for wurtzite growth of GaSb is overcome, and thick layers of shell material

can be grown.

Figure 3 demonstrates HAADF-STEM along with HRTEM images of the core-shell nanowire from which the shell morphology can be understood. From the HAADF-STEM image shown in figure 3a, it is apparent that the tapering of the shell occurs in steps. When taking a closer look at these steps (shown in figure 3b) it is observed that most of the steps coincide with the presence of stacking faults (indicated by black arrows). The step morphology suggests that stacking faults act as a small barrier for shell growth. It is worth noting, that such morphology is an indication that the wurtzite shell growth occurs by step flow along the nanowires. Intuitively the barrier-like behavior of stacking faults might seem in opposition to what would be expected from radial shell growth on stacking defects. First of all, they would act as kinks, and therefore as preferential nucleation sites, expected to increase radial growth of the shell. Secondly, defects in a wurtzite structure are layers with a zinc blende structure. Since zinc blende side facets have higher surface energy compared to wurtzite, it would be expected that, existing zinc blende insertions would enhance shell growth. However, we explain the hindering effect of stacking defects as follows: The shell grows bottom-upward along the side facets ($[000\bar{1}]$ direction) as opposed to outward growth in the $\langle 1\bar{1}00 \rangle$ direction (normal to the side facets). When the growing shell meets a stacking fault that is perpendicular to the growth direction, the energy barrier it needs to overcome is sufficiently large so that the existence of the stacking fault briefly blocks the step-flow growth. This leads to the stepwise tapered morphology of the wurtzite shell. This description is illustrated in the schematic axial cross-section shown in figure 3c.

It is also evident that the wurtzite shell growth on the InAs segment is primarily induced from the base and not from the top axial GaSb segment, in which case an inverted tapering would be expected.

Interestingly, as indicated by the green arrows in figure 3b, not every defect induces a stepping event in the shell growth, and also more importantly, the stepping is sometimes observed on defect-free segments of the nanowire. Therefore, it could be hypothesized that

the step-like tapering is also a consequence of diffusion-limited growth of the shell layer. At very high material supply (present case), the migration length of the adatoms decreases, as the nucleation probability increases. As a result, the time between each nucleation event becomes relatively short, hence nucleation of next atomic layer will occur long before the completion of the underlying progressing layer ($\{1\bar{1}00\}$ planes on the side facet).

It is also worth noting that the shell stepping is not always observed on both sides (figure 3d). We attribute this to the direction of the wurtzite twin boundary and surface polarity (surface polarity is determined by the terminating atomic layer at the surface which can be either group III (A-polar) or group V (B-polar)). All six side facets of the wurtzite structure from $\{1\bar{1}00\}$ plane family are non-polar; the same number of group III and group V atoms are present at the terminating surface. In contrast, each twin boundary creates a single-bilayer-thick segment of zinc blende with six semi-polar edges of $\{112\}$ planes (semi-polarity denotes both elements are present at the surface, however with different contribution). Three of these semi-polar facets are A-polar (more contribution from group III element than group V at the surface) and the other three are B-polar, leading to a three-fold symmetry. Therefore, the emergence of the step is caused by one polarity and not the other. Atomic-resolution HAADF-STEM images reveal that the InAs outer shell grows in a similar step-like mode, which will be discussed later in section 2.3; Heterointerfaces.

Another interesting phenomenon related to the formation of wurtzite GaSb shells, is that the shell forms with either 3- or 6- fold symmetry. The two possibilities can be observed in figure 4. Figures 4a-c show an InAs nanowire with an asymmetric GaSb shell. In contrast, a symmetric GaSb shell is shown in figure 4d-f. The cross section of the nanowires with a non-uniform shell is an asymmetric hexagon (as shown in the insets in figure 4b and e), which is indeed confirmed by the intensity profiles taken along the radial direction (in HAADF-STEM (Z-contrast) images) depicted in the insets of figures 4c and f. From this it can be understood that three out of six side facets of the nanowires with a non-uniform shell have a higher growth rate, hence tend to grow faster and fill out. Wurtzite $\{1\bar{1}00\}$ side facets are

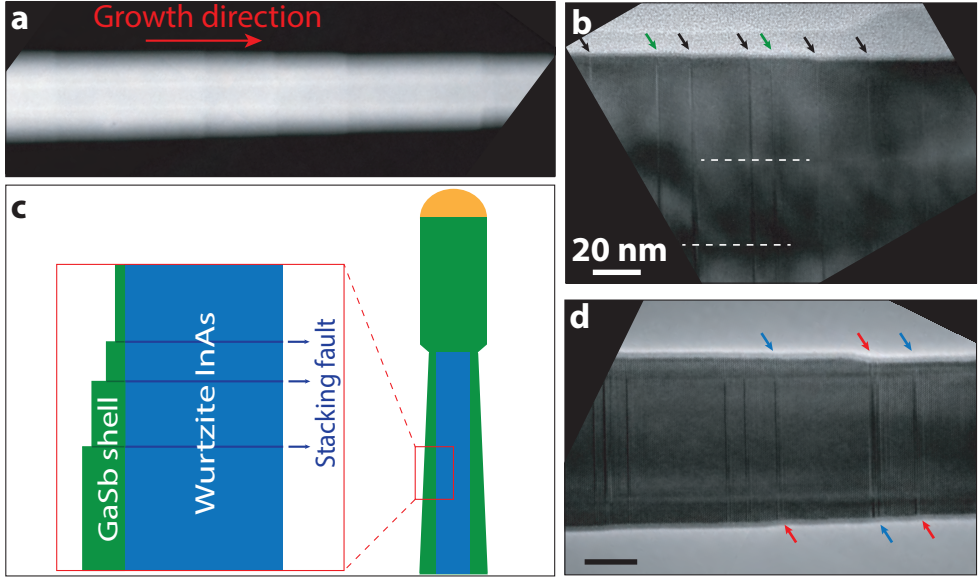


Figure 3: HAADF-STEM image of a wurtzite InAs-GaSb core-shell nanowire showing the lateral steps, (b) HRTEM image showing the correlation between lateral steps and twin defects. Black arrows indicate the steps that are associated with twin defects. Green arrows indicate the defects that have not caused steps. (c) Schematic illustration of correlation between the twin defects and lateral steps. (d) HRTEM image showing one-sided steps

non-polar, meaning that the surface energy of all six side facets in wurtzite structures are equal, and consequently must have equal growth rates. Thus, it is unexpected to observe 3-fold symmetry for wurtzite. We attempt to explain this through the possibility that the forming micro facets are polar in some directions. As mentioned above, the twin boundaries create atomic-bilayer-thick zinc blende segments with semi-polar facets. Statistically, it occurs that twin defects in some nanowires emerge more in one direction than the other, and hence favor the shell growth in a three-fold-symmetry fashion. The polar stacking faults significantly affect shell morphology; therefore they could conceivably also be responsible for its overall symmetry.

We performed a study on the shell growth time to get a better understanding of the stepwise shell tapering, and also to investigate whether the step-like features will fill out

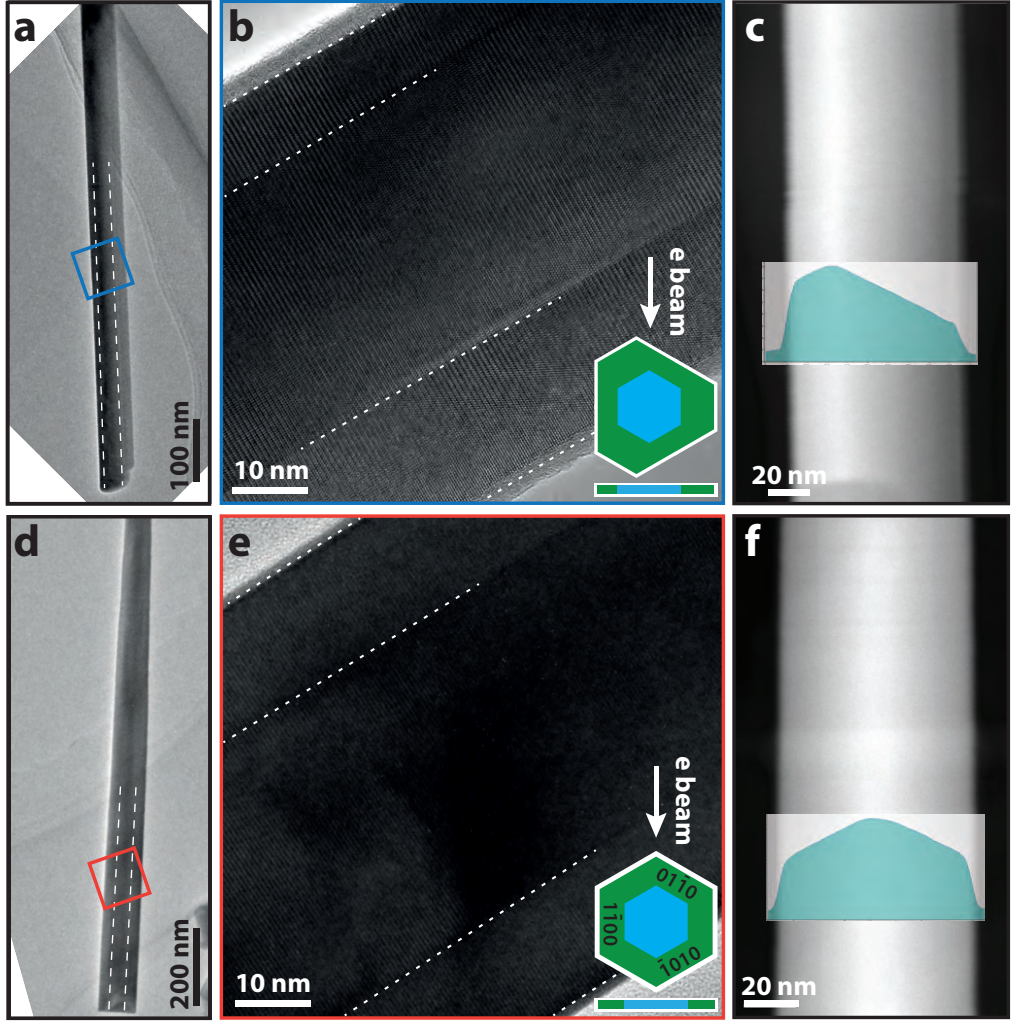


Figure 4: (a and d) Low-magnification TEM, (b and e) HRTEM, and (c and f) HAADF-STEM images of InAs-GaSb core-shell nanowires with (a through c) asymmetric and (d through f) symmetric shells. (b and e) insets schematically show the cross-section of the nanowires. (c and f) insets show the intensity profiles proving the symmetry/asymmetry of the GaSb shell.

given sufficient time. As demonstrated in figure 5, samples with shorter (15 minutes) and longer (50 minutes) GaSb shell growth times were grown for comparison with the reference (40 minutes) nanowires.

XEDS analysis confirms that the shell does not extend all the way to the top of the wurtzite segment (along the entire core) for the 15-minute shell growth time, while for both 40 and 50 minutes of shell growth time, the entire length of the wurtzite InAs core nanowires are covered with a GaSb shell (see Figure SI 1). This confirms the hypothesis that the main shell growth mechanism in these nanowires is adatom diffusion from the substrate. From measurements performed on the SEM images at the full-width half maximum of the core-shell segment of the nanowires, the shell thickness is larger for the 50 minutes sample compared to the reference (roughly 9 nm thicker on average), which is expected; longer growth times usually lead to thicker shell growth, unless a self-limiting process is involved.^{51,52} However, as observed in figure 5c the nanowires with 50 minutes of shell growth are also tapered (similar to the reference nanowires shown in figure 5b), indicating that longer growth times do not necessarily lead to uniform shell thicknesses. Furthermore, following the red arrows in figure 5c it is clear that some of the step-like features are more pronounced for the long growth time compared to the reference sample. This again can be explained through the blockage or delay of the growing shell at stacking faults.

In addition, for the thin shell (15 minutes), we observe a down-growing shell at the uppermost part of the InAs core connected to the axial GaSb segment. This is demonstrated in figure 6. This shell is apparently induced by the axial GaSb segment. As shown in the XEDS line scan and the HRTEM image of the topmost insets of figures 6a and b respectively, this shell can only be seen on one side of the nanowire. Apparently, it is related to the three-fold symmetry of the zinc blende axial GaSb segment. As shown in the low-magnification TEM micrographs and schematic in figure 6b, the lower side facets of the axial segment are constituted of three $\{111\}$ and three $\{100\}$ facets. The down-grown shell is connected to the $\{100\}$ facets; since they have a higher energy they induce nucleation and grow faster than their $\{111\}$ counterparts. Moreover, it is observed that the bottom shell (the green and blue parts of figure 6b) has the same thickness on both sides. We suggest that the two shell growth fronts merge when given enough time, leading to a full coverage of the wurtzite

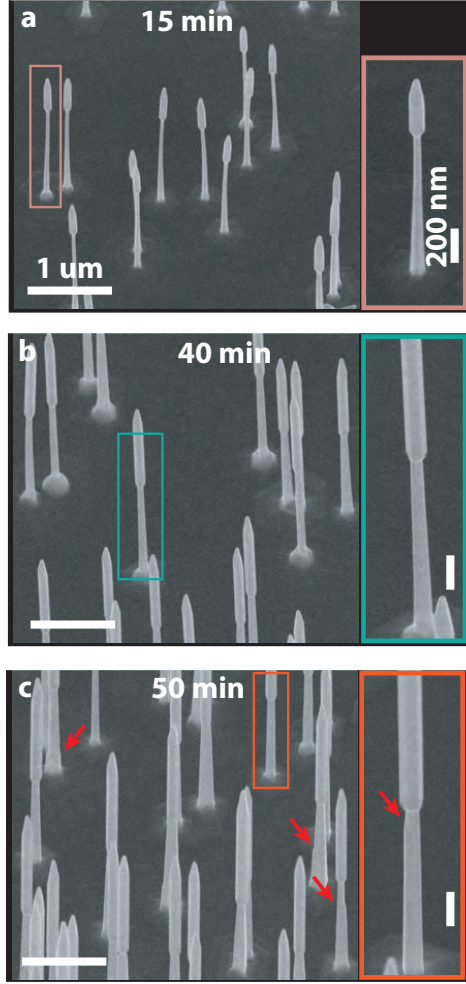


Figure 5: InAs-GaSb core-shell nanowires, with shell growth time of (a) 15 minutes, (b) 40 minutes (reference nanowires), and (c) 50 minutes. The tapered morphology is common in all samples. For the 50 minutes the tapering appears to be less significant compared to 40 minutes, however some of the stepping are more pronounced (marked with red arrows).

GaSb shell on the InAs core as seen for the 40 and 50 minute shell cases. It is also observed that the down-grown shell is stopped at the first twin defect.

To investigate whether the 3-fold symmetry of the fully covering shell is a consequence of the 3-fold symmetry of the down-growing shell on the top, in figures 4a-c we depict three

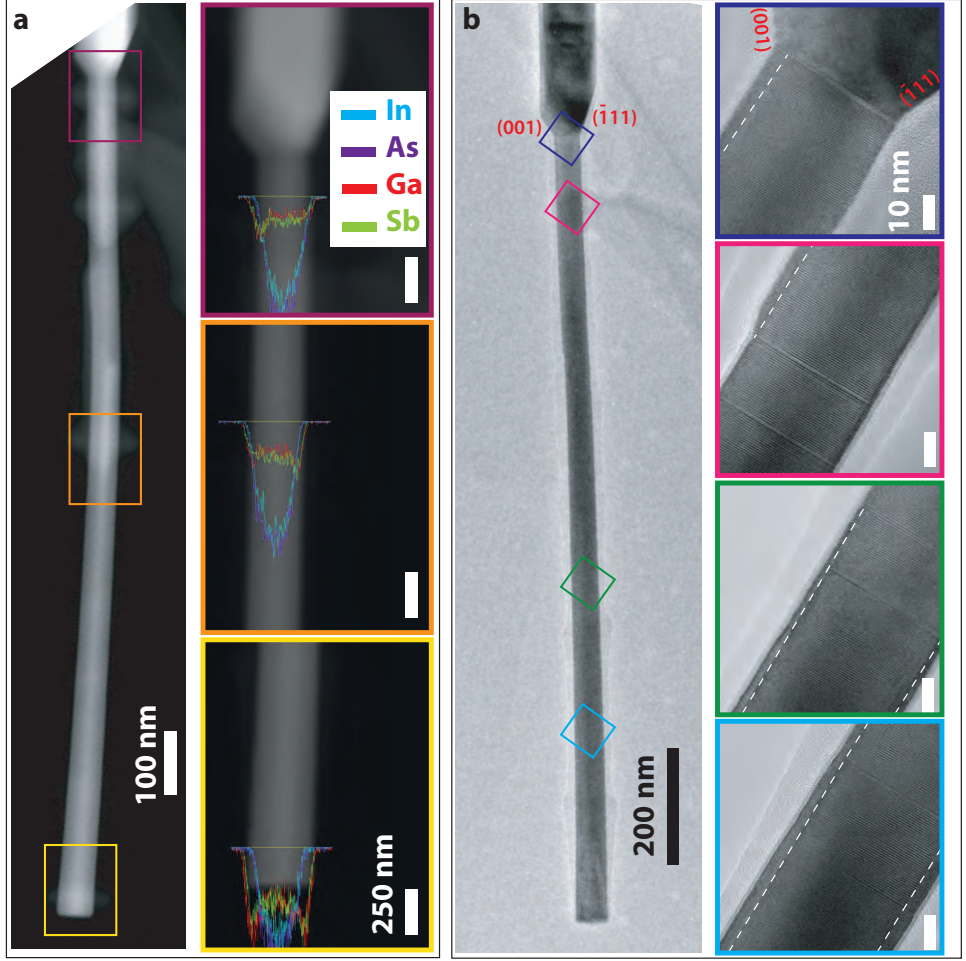


Figure 6: (a) HAADF-STEM images with XEDS line scans showing the presence of a relatively thick GaSb shell at the bottom of the nanowire (yellow), which becomes thinner gradually till it disappears (orange), and reappears on one side right below the zinc blende GaSb axial segment (purple); (b) TEM/HRTEM images on the same nanowires also show the InAs shell non-uniformity.

different cases of shell thickness uniformity. In each of these cases we have closely studied the relation between the thicknesses of the shell on the two projected sides of the nanowire with the downward facets of the axial GaSb segment. Figure 4a demonstrates a nanowire with a more-or-less equal shell thickness on both sides, indicating 6-fold symmetry. In figure

4b the thicker side of the nanowire image corresponds in fact with the (001) facet of the axial segment. In figure 4c however, it can be observed that the thicker side of the GaSb shell is reversed in relation to the side facets of the axial segment, and corresponds to the (111) facet instead. Therefore, the unevenness of the down-growing shell can be ruled out as a possible explanation for the occurrence of the 3-fold symmetry on fully covered nanowires (nanowires with longer shell growth times).

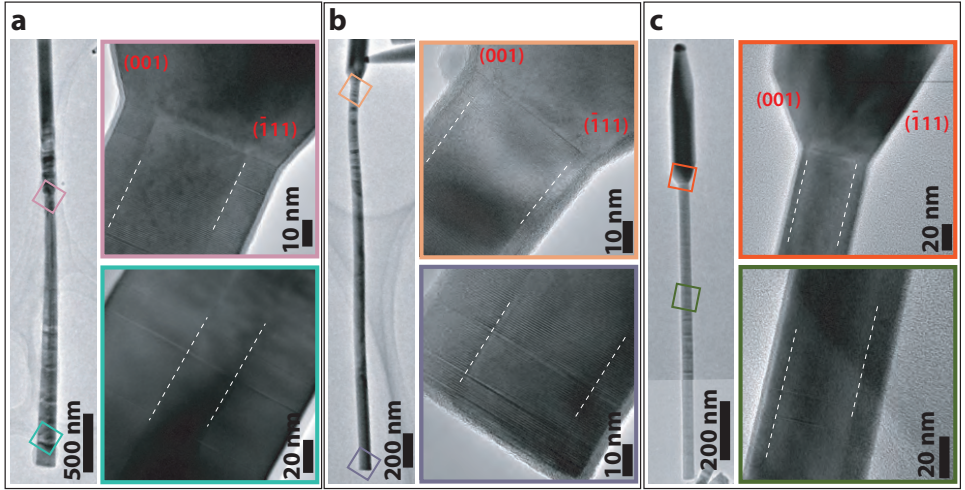


Figure 7: Overview and high resolution TEM images of core/shell nanowires with (a) uniform shell thicknesses on both sides, (b) thicker shell on side correlated to the (001) downward facet of axial GaSb, and (c) thicker shell on side in correlation with (-111) downward facet of axial segment. From these examples it is clear that the commonly observed non-uniformity of shell thickness is not related to down-growth from axial GaSb segment.

2.3. Heterointerfaces

As mentioned briefly in the introduction, the heterointerface quality is of importance in device performance, and also of interest in studies investigating various quantum phenomena.^{53–55} Therefore, in the following we thoroughly investigate the material composition and crystal quality of the heterointerfaces in our wurtzite InAs-GaSb(-InAs) core-shell(-shell)

nanowires, namely the radial interfaces between wurtzite InAs core and GaSb shell, and between the GaSb shell and the outer InAs shell. For comparison the axial interface between the wurtzite InAs-GaSb core-shell and the axial zinc blende GaSb segment is also investigated.

Figure 8 shows HAADF-STEM micrographs of the radial segment of a wurtzite InAs-GaSb core-shell nanowire. The lateral facets are from the $\{1\bar{1}00\}$ plane family, therefore, the heterointerfaces are along the suitable zone axis (i.e. $\langle 1\bar{1}00 \rangle$, the direction from which the dumbbell units can be visualized and wurtzite and zinc blende can be distinguished). This is an advantage for wurtzite nanowires, since the heterointerfaces can be visualized more clearly as already shown in the schematic in figure 4e. Note that the overall atomic numbers of the two materials, InAs and GaSb, are exactly the same. Therefore, in low-magnification images where the other effects do not play a significant role, for instance in figure 4f, the contrast shown in the intensity profile is related to the thickness (since thickness contrast is the predominant mechanism), and hence reveals the occurrence of $\{1\bar{1}00\}$ lateral facets.

Figure 8c shows the atomic-resolution HAADF-STEM micrograph at the interface of the core-shell segment as indicated in the schematic. The growth direction is upwards, the right side is the InAs core and the left side is the GaSb shell. The dumbbell units reveal a B-polarity in the growth direction, which as expected is inherited from the $\{111\}$ B substrates. In the InAs core, the heavier element (In) is at the bottom in each dumbbell unit, appearing brighter in the HAADF-STEM micrographs, (intensity profile in figure 8d)-blue). On the other hand, as indicated in the intensity profile in figure 8d-green, in the GaSb shell the heavier element (Sb) appears at the top of the dumbbell units, which again shows the B-polarity. At the heterointerface, as indicated in the intensity profile in figure 8d-purple, both group III and group V elements appear relatively dark, which indicates the presence of the two lighter elements: Ga and As. However, in the intensity profiles the lower atom, which is supposed to be Ga, appears slightly brighter than the other atom, supposedly As. This is not expected as Ga is slightly lighter than As.⁵⁶ The first hypothesis can be occurrence of A-

polarity at the heterointerface where Ga appears on top in the dumbbell units. This does not seem feasible, as for such a phenomenon, two consecutive inversion domain boundaries (IDBs) must occur, which is not energetically favorable. The second hypothesis, which is much more plausible, is the emergence of a ternary alloy at the heterointerface. From the intensity profile in figure 8d-purple we can speculate that the group III element is a mix of Ga and In, causing a slightly higher intensity in HAADF-STEM micrographs than the group V element, As. Therefore, the chemical composition of the dark line at the heterointerface appears to be $\text{In}_x\text{Ga}_{1-x}\text{As}$, a ternary. The linearly simulated HAADF-STEM image also confirms this composition (figure 8c-yellow inset). In the 3D atomic model (figure 8c - bottom-right inset), which is used for STEM image simulation, an atomic bilayer of $\text{In}_x\text{Ga}_{1-x}\text{As}$ is considered at the radial heterointerface.

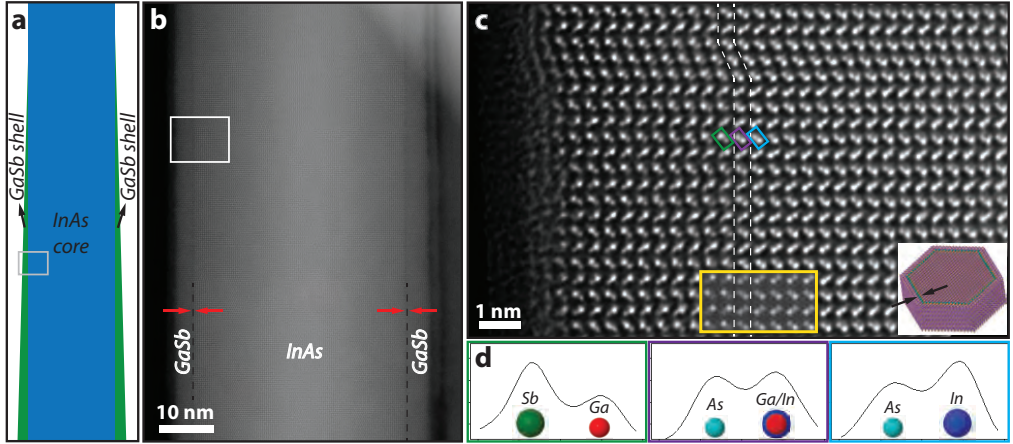


Figure 8: HAADF-STEM analysis of wurtzite InAs-GaSb core-shell nanowires, (a) schematic and (b) HAADF-STEM micrograph showing the overview of the material and the dark line at the heterointerfaces, (c) atomic-resolution HAADF-STEM micrograph showing the composition of the core (blue), shell (green), and the heterointerface (purple), indicating one atomic bilayer of a ternary InGaAs material, (d) corresponding intensity profiles. The yellow inset in (c) is a simulated HAADF-STEM image obtained from the 3D atomic model (bottom-right inset).

We have also studied the heterointerfaces in the radial InAs-GaSb-InAs core-shell-shell nanowire systems, as shown in figure 9. As can be seen in figure 9b both InAs-GaSb and

GaSb-InAs heterointerfaces appear as slightly darker lines. Also, it is observable that for the InAs outer shell A-polarity induces lateral steps, while B-polarity does not. This might indicate that A-polar lateral facets have a lower surface energy, which hinders the radial growth. In contrast, B-polarity does not have the same effect, since the steps do not occur at the presence of these facet types.

Figure 9c shows an atomically resolved HAADF-STEM micrograph of the heterointerface between the GaSb inner shell and InAs outer shell. Similar to the previous case, B-polarity of both materials is explicitly revealed. Moreover, the single atomic bilayer at the interface seems to be the same ternary $\text{In}_x\text{Ga}_{1-x}\text{As}$ material, since the heterointerface appears darker than the two shell materials, and the group III element appears brighter. In addition, the transition from the inner to the outer shell is abrupt, apart from the one atomic bilayer of the ternary material. Another notable point is the presence of one twin boundary seen in figure 9c, which causes a step in the lateral facet in the right side of the nanowire, as mentioned. No corresponding step is present on the left side, as seen in figure 9b. Considering this defect as two atomic bilayers of a zinc blende structure, its lateral surface will be polar. In this case, A-surface-polarity can be seen in this side in figure 9c, which makes the other side B-polar. Therefore, it can be speculated that the A-polarity induces steps in the side facets of InAs shell while it is not observed in B-polarity.

So far we have shown the sharpness of the radial interfaces. In contrast to the radial heterointerfaces, the axial heterointerface between wurtzite InAs and zinc blende GaSb is not sharp, and in fact an intermixing of the two materials occur as shown in figure 10. In the low-magnification HAADF-STEM micrographs (figure 10a) we observe a dark region directly on top of the heterointerface in the nominally zinc blende GaSb region. It is shown more clearly in figure 10b and c. This lower brightness in the zinc blende GaSb region, as it is clearly not related to thickness change, indicates the presence of a lighter element, As, substituting a heavier one, Sb. This is corroborated by XEDS results as shown in figure 10d. White dashed lines in the HAADF-STEM images and XEDS elemental maps (figure

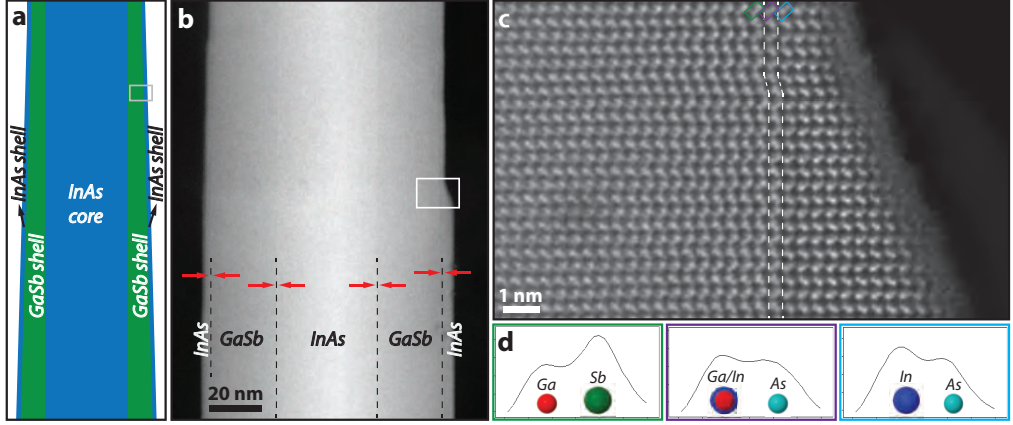


Figure 9: HAADF-STEM analysis of wurtzite InAs-GaSb-InAs core-shell-shell nanowires, (a) schematic, and (b) HAADF-STEM micrograph showing the overview of the material and the dark lines at the heterointerfaces, (c) atomic-resolution HAADF-STEM micrograph showing the composition of the GaSb inner shell (green), InAs outer shell (blue), and the heterointerface (purple), indicating one atomic bilayer of a ternary InGaAs material, (d) corresponding intensity profiles.

10b-d) indicate the axial heterointerface as determined by the wurtzite-to-zinc-blende crystal structure change, occurring at the In-Ga switch during growth. It is clear that an As signal is still detected up to 5-6 nm after the heterointerface in the GaSb region, whereas the Sb signal is weaker in the same region. Therefore, a ternary $\text{GaAs}_x\text{Sb}_{1-x}$ material occurs at the interfacial region.

We have shown the emergence of sharp radial heterointerfaces, on the one hand, with an abrupt transition of InAs to GaSb and GaSb to InAs, except for one atomic bilayer of $\text{In}_x\text{Ga}_{1-x}\text{As}$ ternary material. On the other hand, for axial heterointerfaces, we observe a smooth transition with a relatively large interfacial region where As is intermixed with GaSb. This leads to the ternary $\text{GaAs}_x\text{Sb}_{1-x}$ material in which As content decreases gradually. The difference in the axial and radial interfaces is related to the different growth mechanisms and the different pathways materials have for contributing to growth. The axial growth occurs via vapor-liquid-solid (VLS) mechanism, in contrast to the shell growth conducted by vapor-solid (VS) mechanism. We attribute the occurrence of a gradual transition at

the axial heterointerface to the reservoir effect of the Au seed particle,⁵⁷ which we did not try to mitigate since it was not the focus of this study. The solubility of Sb in Au, while relatively low, is considerably higher than As. It thus takes some time for Sb to build up in the particle when the Sb precursor is introduced into the reactor. Consequently, the short ternary segment grows during this time. By contrast, there is no liquid phase involved in the VS mechanism, and adatoms incorporated in shell growth undergo a different pathway compared to the axial segment.

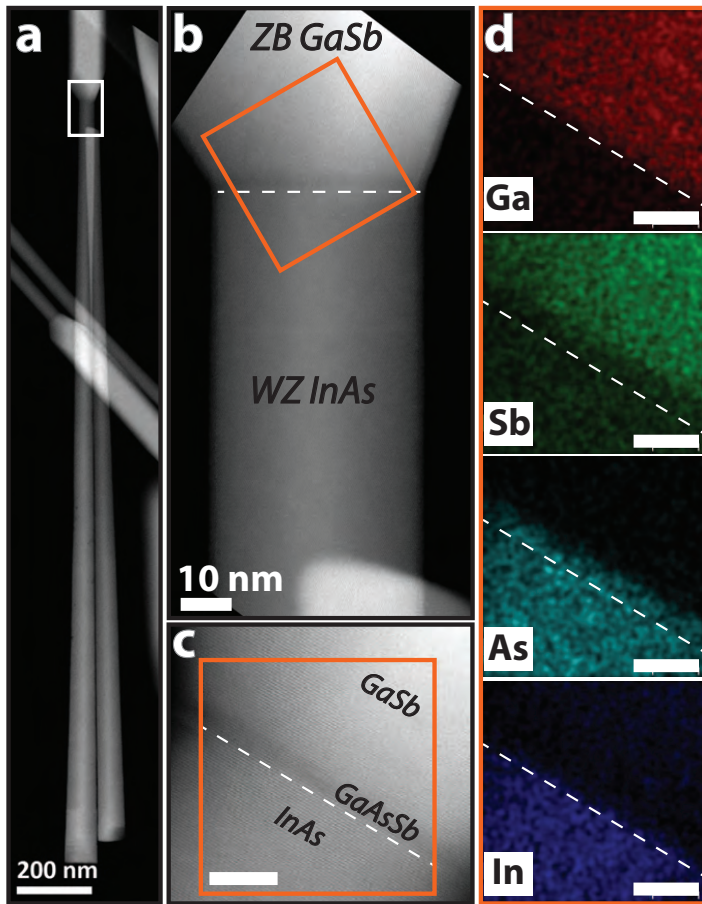


Figure 10: Axial heterointerface between wurtzite InAs and zinc blende GaSb, (a) low-mag HAADF-STEM micrograph, (b) HAADF-STEM micrograph of the axial heterointerface, (c) XEDS elemental maps.

2.4. Electrical characterization

Nominally undoped GaSb material is always found to be p-type regardless of growth technique, explained by acceptor levels from Ga vacancies, and Ga in Sb sites.⁵⁸ InAs, on the other hand, typically shows *n*-type conductivity. Here, a major contribution comes from a surface state-related band-bending, leading to a strong accumulation layer of electrons at the InAs surface, which is particularly important in nanoscale materials with large surface-to-volume ratios. In a heterostructure consisting of a parallel GaSb/InAs channel, one therefore expects ambipolar transport properties, with a substantial contribution from both electron and holes to the measured source-drain current, dependent on the relative size of the channels. By using such a parallel heterojunction in a field-effect transistor configuration, the relative contributions of the two carrier types would be tunable with an applied gate voltage, V_G , with a hole (electron) concentration that increases at negative (positive) V_G .⁵⁹

Contrary to typical *p-n* junctions, the GaSb-InAs *p-n* junction does not form a depletion region at the heterointerface. The broken band gap alignment instead leads to an accumulation of electrons (InAs) and holes (GaSb) near the interface, and a very low junction resistance. A layer of InAs can for this reason be used to improve the contacts to GaSb.⁶⁰ In addition to an increased carrier concentration, it has also been found that surrounding a GaSb *p*-channel with a very thin, depleted InAs layer protects the GaSb from surface oxidation and reduces surface scattering.⁶⁰⁻⁶³

In our analysis of the electrical properties, we start by investigating the zinc blende material found in the top section of the nanowires, which will act as reference when assessing the properties of the wurtzite GaSb shells located in the bottom segments. A set of four contacts (Ni/Au) were made to each nanowire such that a comparison of the electrical properties was possible, where the wurtzite and zinc blende contact separations are identical. A fifth contact, connected to the degenerately doped Si below a 110 nm insulating SiO₂ surface layer, was used as an electrostatic gate to modulate the band energies relative to source and drain.

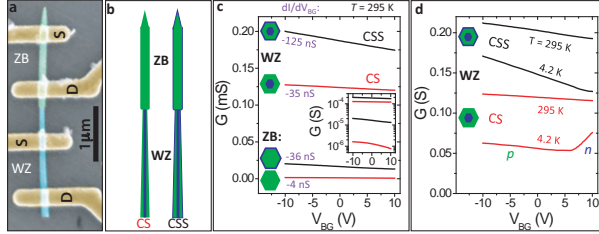


Figure 11: (a) Falsely colored SEM image of a contacted InAs/GaSb CS nanowire, where blue represents the CS segment, green the axial zinc blende GaSb segment, and yellow is used for the Au source-drain contacts, and the Au seed particle on top of the nanowire. (b) Schematic representations of the CS and CSS nanowires, intended as legends for panels (c) and (d). (c) Conductance (G) as a function of back gate V_{BG} performed at $T = 295$ K for wurtzite and zinc blende segments of the CS and CSS nanowires. The inset demonstrates the same measurements at a logarithmic scale. (d) Conductance (G) as a function of back gate V_{BG} for devices without (CS) and with (CSS) outer InAs shell recorded at $T = 295$ K and 4.2 K.

The two lower curves in Figure 11c are obtained from zinc blende GaSb segments with, and without, a thin InAs shell. From the log scale in the inset, it is clear that a more positive V_{BG} effectively reduces the overall nanowire carrier concentration, which agrees with the expected p -type character of GaSb. We note that the 2-probe resistivity drops an order of magnitude by the addition of a thin InAs shell, from $1000 \text{ m}\Omega\text{cm}$ to $90 \text{ m}\Omega\text{cm}$. This is also in good agreement with previous reports,^{62,63} where a compound effect of reduced contact resistance, increased carrier concentration and improved mobility were reported for zinc blende GaSb nanowires with thin InAs shells.

Comparing the zinc blende material with the wurtzite, we find a very dramatic difference

in the source-drain current levels, which increases 1–2 orders of magnitude for the wurtzite material despite a considerably reduced effective GaSb cross-sectional area. However, in order to draw any conclusions from this data, it is important to identify and isolate the contribution from hole (p) transport in the GaSb shell, from the parasitic electron (n) transport in the InAs core. Such a separation of the two components is facilitated by a reduction in the thermal energy of the carriers in the conduction and valence bands. Figure 11d shows the 2-terminal conductance of the wurtzite base segments for a core-shell (red) and a CSS (black) nanowire at $T = 295$ K and $T = 4.2$ K. For the core-shell nanowire, a clear ambipolarity is observed at 4.2 K, with dominant electron contribution at $V_{BG} > 7$ V. For the core-shell-shell nanowire, we find that the outer InAs shell has considerably increased the hole concentration, almost fully obscuring the corresponding n-branch, however, a weak upturn is visible for the most positive $V_{BG} = 10$ V.

By extrapolating the InAs core contribution to the transport in the core-shell nanowire, and assuming it has a similar contribution in the core-shell-shell nanowire, it is clear that hole transport should be dominant in these structures at negative V_{BG} . It then also follows that the dramatic increase in source-drain current in the wurtzite material is in fact a result of a significant increase in the hole (p) conductance.

What is then the origin of the high conductance? A higher hole concentration in the wurtzite GaSb shell could be explained by the presence of the InAs core, leading to a local upwards band-bending in the GaSb at the interface, and hole accumulation. However, it is unclear why the band-bending effect from a core heterojunction would be considerably greater than that from a surface junction.

Another important contribution to the high hole-conductance likely comes from differences in the relative alignment of the valence band-edge energies of the wurtzite and zinc blende GaSb. Theory predicts that the wurtzite GaSb valence band edge is 95–110 meV higher in energy compared to zinc blende.^{31,38} The much higher hole concentrations found here for the wurtzite material are in agreement with such a relative band alignment. We note

that this is also in agreement with findings for zinc blende/wurtzite InAs, where a similar positive staggered alignment is predicated in most theoretical works,^{30,31} and where electron concentrations are typically found to be higher in the zinc blende.^{29,32}

Finally, we note that adding a thin InAs shell to the wurtzite GaSb provides even higher source-drain current levels (Figure 11c) and improves the p -type transconductance (dI/dV_{BG}) by a factor of 3.6. From these results we expect that access to wurtzite GaSb channels, and passivation of the GaSb surface, will provide a significant boost in the hole-conductance in III-V complementary (p /textitn) transistor channels, to better match the conductance of the corresponding electron channel.^{61,64}

3. Conclusion

In summary, we demonstrate radial growth of GaSb in the wurtzite crystal structure for the first time. On InAs wurtzite template nanowires we have grown shell layers of GaSb with different growth times (core-shell structures), and GaSb + thin InAs shell (core-shell-shell structure). We discuss wurtzite shell formation in detail, giving insight to the step-flow wurtzite shell growth mechanism, step formation in the growth direction, and shell homogeneity. We also investigate the sharpness and material composition of the radial interface (between InAs core and GaSb shell in core-shell nanowires, and GaSb shell and InAs outer shell in core-shell-shell nanowires), along with the axial heterointerface between the wurtzite core-shell segments and the unintentionally grown axial zinc blende GaSb segment, by means of atomic-resolution HAADF-STEM imaging. Our results suggest the presence of one atomic bilayer of GaInAs ternary material at the radial heterointerfaces, and a few nanometers of GaAsSb ternary material at the axial heterointerface between the wurtzite InAs and zinc blende GaSb.

Electrical characterization of the core-shell and core-shell-shell nanowires reveals ambipolar behavior at liquid helium temperature, revealing p -type characteristic of wurtzite GaSb.

In addition, electrical measurement comparisons performed on the axial zinc blende GaSb and radial wurtzite GaSb shell, are in agreement with a positive offset in the valence band edge alignment of wurtzite versus zinc blende through significantly higher hole concentrations in wurtzite.

In order to gain a more comprehensive understanding of the wurtzite GaSb properties, it will next be necessary to devise methods for isolating the wurtzite GaSb from the InAs core template. By this, disentangling the effects of the heterointerface from intrinsic wurtzite properties will become feasible in future electrical and optical measurements.

4. Methods

Wurtzite InAs-GaSb core-shell nanowires were grown by means of metal-organic vapor phase epitaxy (MOVPE) on InAs (111) B substrates from predeposited Aerosol Au seed particles. The utilized Au particle diameters were 30 and 40 nm with an areal density of $1 \mu m^{-2}$. The nanowires were grown in a standard low-pressure horizontal MOVPE reactor (Aixtron 200/4). For the InAs core Trimethylindium (TMIn) and Arsine (AsH_3), and for the GaSb shell Trimethylgallium (TMGa) and Trimethylantimony (TMSb), were used as the group III and V precursors, respectively. Hydrogen was used as the carrier gas with a total flow rate of 13 l/min, at a reactor pressure of 100 mbar. After loading the InAs samples inside the reactor, the samples were annealed for 7 minutes at a temperature of 550 °C in an H_2/AsH_3 atmosphere in order to remove the native oxide from the surface of the samples. The temperature was then reduced to the wurtzite InAs core growth temperature of 460 °C. The temperature reduction was done under a constant supply of AsH_3 in order to prevent substrate decomposition at high temperatures. InAs core growth was commenced by supplying TMIn with a molar fraction of 3.5×10^{-6} and adjusting the AsH_3 flow to 7.7×10^{-5} . To ensure uniform nucleation, before growing the wurtzite core, growth was initiated with a segment grown for 3 minutes with a slightly higher AsH_3 flow of 1.9×10^{-4} . This segment

has similar side facets to wurtzite (mostly wurtzite structure with frequent stacking faults). After 12 minutes of InAs wurtzite core growth, the TMIn flow was terminated and the reactor temperature was changed to that of the GaSb shell growth (470 °C) under a supply of AsH₃. Upon reaching the desired temperature, in order to purge the excessive AsH₃, the AsH₃ supply was cut off, and the samples were kept in a H₂ atmosphere for 30 seconds. In order to grow the GaSb shell on the wurtzite InAs nanowires, TMGa and TMSb were introduced simultaneously into the reactor with precursor molar fractions of 4.34×10^{-4} and 2.1×10^{-4} respectively, adding to a total precursor flow of 6.44×10^{-4} . These parameters lead to a V/III ratio of 0.48. After growth, the samples were cooled down under a flow of H₂. In addition, for reasons later addressed in the paper, a thin outer InAs shell was grown for one sample. The outer shell of these core-shell-shell (CSS) InAs-GaSb-InAs nanowires was grown at 470 °C by shutting the TMGa and TMSb precursors and opening the TMIn and AsH₃ simultaneously. The precursor flows used for the outer shell are equal to values used for the core growth (3.5×10^{-6} and 1.9×10^{-4} respectively), and the outer shell growth time is set to 3 minutes.

The grown samples were investigated by means of scanning electron microscopy (SEM). These micrographs reveal an existing axial GaSb segment grown above the core-shell segment. High-resolution transmission electron microscopy (HRTEM) along with X-ray energy dispersive spectroscopy (XEDS) reveals long segments of defect-free GaSb wurtzite shells with controllable thicknesses up to 30 nm. TEM experiments were performed on a JEOL 3000F, equipped with a field emission gun (FEG) operating at 300 kV. Atomic resolution high-angle annular dark-field (HAADF)-STEM was performed by means of a double aberration-corrected (second generation probe and image *mathrmC_s*-correctors), monochromated high-brightness FEG-TEM (FEI Titan³ 60-300) with ultrafast dual electron energy loss spectrometers and Super-X XEDS detector system for ultra-high count rates, and spatial resolution higher than 70 pm in STEM mode at 300 kV. TEM samples were prepared by breaking the nanowires off from the substrate, and mechanically transferring them onto

Lacey-carbon Cu grids.

Rhodium software package was used for creating 3D atomic models.⁶⁵ The prepared models were used for linear STEM image simulations. STEM image filtering (deconvolution) and simulation were performed by means of the STEM_CELL software tool. This tool uses a modified version of Kirkland "multislice" approach for simulating STEM images. By the deconvolution process we remove the probe contribution from the experimental images by numerical methods, which separate the probe contribution from the object function peaked on each atomic position. The process is followed by a reconstruction step.^{66,67}

In order to investigate the electrical characteristics, nanowires both with and without the outer InAs shell were transferred to measurement substrate where metal contacts were fabricated in a similar manner as described in reference.¹³ Here, the substrate is used as a global back gate and the distance between source and drain contacts are 800 nm.

Acknowledgement

This work was supported by the Swedish Research Council (VR), the Swedish Foundation for Strategic Research (SSF), the Knut and Alice Wallenberg Foundation (KAW), and NanoLund. The Knut and Alice Wallenberg (KAW) Foundation is also acknowledged for the Electron Microscope Laboratory in Linköping.

References

- (1) Tomioka, K.; Yoshimura, M.; Fukui, T. *Nature* **2012**, *488*, 189–192.
- (2) Egard, M.; Johansson, S.; Johansson, A.-C.; Persson, K.-M.; Dey, A. W.; Borg, B. M.; Thelander, C.; Wernersson, L.-E.; Lind, E. *Nano Letters* **2010**, *10*, 809–812.
- (3) Zhang, C.; Li, X. *IEEE Transactions on Electron Devices* **2016**, *63*, 223–234.
- (4) Tomioka, K.; Fukui, T. *Journal of Physics D: Applied Physics* **2014**, *47*, 394001.
- (5) Kempa, T. J.; Tian, B.; Kim, D. R.; Hu, J.; Zheng, X.; Lieber, C. M. *Nano Letters* **2008**, *8*, 3456–3460.
- (6) Tian, B.; Lieber, C. M. *Pure and Applied Chemistry* **2011**, *83*.
- (7) Borgstrm, M. T.; Wallentin, J.; Heurlin, M.; Flt, S.; Wickert, P.; Leene, J.; Magnusson, M. H.; Deppert, K.; Samuelson, L. *IEEE Journal of Selected Topics in Quantum Electronics* **2011**, *17*, 1050–1061.
- (8) Lackner, D.; Pitts, O. J.; Martine, M.; Cherng, Y. T.; Mooney, P. M.; Thewalt, M. L. W.; Plis, E.; Watkins, S. P. InAsSb and InPSb materials for mid infrared photodetectors. 2010 22nd International Conference on Indium Phosphide and Related Materials (IPRM). 2010.
- (9) Soci, C.; Zhang, A.; Bao, X.-Y.; Kim, H.; Lo, Y.; Wang, D. *Journal of Nanoscience and Nanotechnology* **2010**, *10*, 1430–1449.
- (10) Gudiksen, M. S.; Lauhon, L. J.; Wang, J.; Smith, D. C.; Lieber, C. M. *Nature* **2002**, *415*, 617–620.
- (11) Borg, B. M.; Dick, K. A.; Ganjipour, B.; Pistol, M.-E.; Wernersson, L.-E.; Thelander, C. *Nano Letters* **2010**, *10*, 4080–4085.
- (12) Rieger, T.; Grützmacher, D.; Lepsa, M. I. *Nanoscale* **2015**, *7*, 356–364.

- (13) Nilsson, M.; Namazi, L.; Lehmann, S.; Leijnse, M.; Dick, K. A.; Thelander, C. *Physical Review B* **2016**, *94*.
- (14) Kishore, V. V. R.; Partoens, B.; Peeters, F. M. *Physical Review B* **2012**, *86*.
- (15) Zamani, R. R.; Hage, F. S.; Lehmann, S.; Ramasse, Q. M.; Dick, K. A. *Nano Letters* **2018**, doi: 10.1021/acs.nanolett.7b03929.
- (16) Spirkoska, D. et al. *Phys. Rev. B* **2009**, *80*, 245325.
- (17) Glas, F.; Harmand, J.-C.; Patriarche, G. *Physical Review Letters* **2007**, *99*.
- (18) Zardo, I.; Conesa-Boj, S.; Peiro, F.; Morante, J. R.; Arbiol, J.; Uccelli, E.; Abstreiter, G.; i Morral, A. F. *Physical Review B* **2009**, *80*.
- (19) Heiss, M.; Conesa-Boj, S.; Ren, J.; Tseng, H.-H.; Gali, A.; Rudolph, A.; Uccelli, E.; Peiró, F.; Morante, J. R.; Schuh, D.; Reiger, E.; Kaxiras, E.; Arbiol, J.; i Morral, A. F. *Physical Review B* **2011**, *83*.
- (20) Krogstrup, P.; Jørgensen, H. I.; Johnson, E.; Madsen, M. H.; Sørensen, C. B.; i Morral, A. F.; Aagesen, M.; Nygård, J.; Glas, F. *Journal of Physics D: Applied Physics* **2013**, *46*, 313001.
- (21) Mishra, A.; Titova, L. V.; Hoang, T. B.; Jackson, H. E.; Smith, L. M.; Yarrison-Rice, J. M.; Kim, Y.; Joyce, H. J.; Gao, Q.; Tan, H. H.; Jagadish, C. *Applied Physics Letters* **2007**, *91*, 263104.
- (22) Dick, K. A.; Bolinsson, J.; Messing, M. E.; Lehmann, S.; Johansson, J.; Caroff, P. *Journal of Vacuum Science & Technology B, Nanotechnology and Microelectronics: Materials, Processing, Measurement, and Phenomena* **2011**, *29*, 04D103.
- (23) Joyce, H. J.; Wong-Leung, J.; Gao, Q.; Tan, H. H.; Jagadish, C. *Nano Letters* **2010**, *10*, 908–915.

- (24) Huang, H.; Ren, X.; Ye, X.; Guo, J.; Wang, Q.; Zhang, X.; Cai, S.; Huang, Y. *Nanotechnology* **2010**, *21*, 475602.
- (25) Lehmann, S.; Wallentin, J.; Jacobsson, D.; Deppert, K.; Dick, K. A. *Nano Letters* **2013**, *13*, 4099–4105.
- (26) Bechstedt, F.; Belabbes, A. *Journal of Physics: Condensed Matter* **2013**, *25*, 273201.
- (27) Kriegner, D.; Panse, C.; Mandl, B.; Dick, K. A.; Keplinger, M.; Persson, J. M.; Caroff, P.; Ercolani, D.; Sorba, L.; Bechstedt, F.; Stangl, J.; Bauer, G. *Nano Lett.* **2011**, *11*, 1483–1489.
- (28) Zanolli, Z.; Fuchs, F.; Furthmüller, J.; von Barth, U.; Bechstedt, F. *Physical Review B* **2007**, *75*.
- (29) Chen, I.-J.; Lehmann, S.; Nilsson, M.; Kivisaari, P.; Linke, H.; Dick, K. A.; Thelander, C. *Nano Letters* **2017**, *17*, 902–908.
- (30) Murayama, M.; Nakayama, T. *Physical Review B* **1994**, *49*, 4710–4724.
- (31) Belabbes, A.; Panse, C.; Furthmüller, J.; Bechstedt, F. *Physical Review B* **2012**, *86*.
- (32) Nilsson, M.; Namazi, L.; Lehmann, S.; Leijnse, M.; Dick, K. A.; Thelander, C. *Physical Review B* **2016**, *93*.
- (33) Ketterer, B.; Heiss, M.; Uccelli, E.; Arbiol, J.; Fontcuberta i Morral, A. *ACS Nano* **2011**, *5*, 7585–7592.
- (34) Nilsson, M.; Chen, I.-J.; Lehmann, S.; Maulerova, V.; Dick, K. A.; Thelander, C. *Nano Letters* **2017**, *17*, 7847–7852.
- (35) Namazi, L.; Nilsson, M.; Lehmann, S.; Thelander, C.; Dick, K. A. *Nanoscale* **2015**, *7*, 10472–10481.

- (36) Rieger, T.; Schpers, T.; Grtzmacher, D.; Lepsa, M. I. *Crystal Growth & Design* **2014**, *14*, 1167–1174.
- (37) Yeh, C.-Y.; Wei, S.-H.; Zunger, A. *Physical Review B* **1994**, *50*, 2715–2718.
- (38) De, A.; Pryor, C. E. *Physical Review B* **2010**, *81*.
- (39) Gmitra, M.; Fabian, J. *Physical Review B* **2016**, *94*.
- (40) Siol, S.; Hellmann, J. C.; Tilley, S. D.; Graetzel, M.; Morasch, J.; Deuermeier, J.; Jaegermann, W.; Klein, A. *ACS Applied Materials & Interfaces* **2016**, *8*, 21824–21831.
- (41) Hjort, M.; Lehmann, S.; Knutsson, J.; Timm, R.; Jacobsson, D.; Lundgren, E.; Dick, K.; Mikkelsen, A. *Nano Letters* **2013**, *13*, 4492–4498.
- (42) Huang, B.-C.; Chiu, Y.-P.; Huang, P.-C.; Wang, W.-C.; Tra, V. T.; Yang, J.-C.; He, Q.; Lin, J.-Y.; Chang, C.-S.; Chu, Y.-H. *Physical Review Letters* **2012**, *109*.
- (43) Dillen, D. C.; Kim, K.; Liu, E.-S.; Tutuc, E. *Nature Nanotechnology* **2014**, *9*, 116–120.
- (44) Knutsson, J. V.; Lehmann, S.; Hjort, M.; Lundgren, E.; Dick, K. A.; Timm, R.; Mikkelsen, A. *ACS Nano* **2017**, *11*, 10519–10528.
- (45) de la Mata, M.; Magén, C.; Caroff, P.; Arbiol, J. *Nano Letters* **2014**, *14*, 6614–6620.
- (46) Yahyaoui, M.; Sellami, K.; Radhia, S. B.; Boujdaria, K.; Chamarro, M.; Eble, B.; Testelin, C.; Lemaître, A. *Semiconductor Science and Technology* **2014**, *29*, 075013.
- (47) Musolino, M.; Tahraoui, A.; Geelhaar, L.; Sacconi, F.; Panetta, F.; Santi, C. D.; Meneghini, M.; Zanoni, E. *Physical Review Applied* **2017**, *7*.
- (48) Oksenberg, E.; Martí-Sánchez, S.; Popovitz-Biro, R.; Arbiol, J.; Joselevich, E. *ACS Nano* **2017**, *11*, 6155–6166.

- (49) Caroff, P.; Bolinsson, J.; Johansson, J. *IEEE Journal of Selected Topics in Quantum Electronics* **2011**, *17*, 829–846.
- (50) Pankoke, V.; Kratzer, P.; Sakong, S. *Physical Review B* **2011**, *84*.
- (51) Wang, X.-L.; Ogura, M.; Matsuhata, H. *Journal of Crystal Growth* **1998**, *195*, 586–590.
- (52) Hu, H.; Niu, X.; Liu, F. *Nano Letters* **2016**, *16*, 3919–3924.
- (53) Watanabe, I.; Shinohara, K.; Kitada, T.; Shimomura, S.; Endoh, A.; Yamashita, Y.; Mimura, T.; Hiyamizu, S.; Matsui, T. *Japanese Journal of Applied Physics* **2007**, *46*, 2325–2329.
- (54) Goldman, R. S. *Journal of Physics D: Applied Physics* **2004**, *37*, R163–R178.
- (55) Kümmell, T.; Hutten, U.; Heyer, F.; Derr, K.; Neubieser, R.-M.; Quitsch, W.; Bacher, G. *Physical Review B* **2017**, *95*.
- (56) de la Mata, M.; Magén, C.; Gazquez, J.; Utama, M. I. B.; Heiss, M.; Lopatin, S.; Furtmayr, F.; Fernández-Rojas, C. J.; Peng, B.; Morante, J. R.; Rurali, R.; Eickhoff, M.; Fontcuberta i Morral, A.; Xiong, Q.; Arbiol, J. *Nano Lett.* **2012**, *12*, 2579–2586.
- (57) Ek, M.; Borg, B. M.; Dey, A. W.; Ganjipour, B.; Thelander, C.; Wernersson, L.-E.; Dick, K. A. *Crystal Growth & Design* **2011**, *11*, 4588–4593.
- (58) Dutta, P. S.; Bhat, H. L.; Kumar, V. *Journal of Applied Physics* **1997**, *81*, 5821–5870.
- (59) Yang, M. J.; Wang, F.-C.; Yang, C. H.; Bennett, B. R.; Do, T. Q. *Applied Physics Letters* **1996**, *69*, 85–87.
- (60) Takei, K.; Madsen, M.; Fang, H.; Kapadia, R.; Chuang, S.; Kim, H. S.; Liu, C.-H.; Plis, E.; Nah, J.; Krishna, S.; Chueh, Y.-L.; Guo, J.; Javey, A. *Nano Letters* **2012**, *12*, 2060–2066.

- (61) Nah, J.; Fang, H.; Wang, C.; Takei, K.; Lee, M. H.; Plis, E.; Krishna, S.; Javey, A. *Nano Letters* **2012**, *12*, 3592–3595.
- (62) Ganjipour, B.; Ek, M.; Borg, B. M.; Dick, K. A.; Pistol, M.-E.; Wernersson, L.-E.; Thelander, C. *Applied Physics Letters* **2012**, *101*, 103501.
- (63) Ganjipour, B.; Sepehri, S.; Dey, A. W.; Tizno, O.; Borg, B. M.; Dick, K. A.; Samuelson, L.; Wernersson, L.-E.; Thelander, C. *Nanotechnology* **2014**, *25*, 425201.
- (64) Dey, A. W.; Svensson, J.; Borg, B. M.; Ek, M.; Wernersson, L.-E. *Nano Letters* **2012**, *12*, 5593–5597.
- (65) Bernal, S.; Botana, F. J.; Calvino, J. J.; López-Cartes, C.; Pérez-Omil, J. A.; Rodríguez-Izquierdo, J. M. *Ultramicroscopy* **1998**, *72*, 135–164.
- (66) Grillo, V.; Rossi, F. *Ultramicroscopy* **2013**, *125*, 112–129.
- (67) Grillo, V.; Rotunno, E. *Ultramicroscopy* **2013**, *125*, 97–111.

Supplemental information for “Realization and characterization of wurtzite GaSb; heterointerfaces and electrical properties”

Luna Namazi^{1*}, Louise Gren^{1,2}, Malin Nilsson¹, Magnus Garbrecht³, Claes Thelander¹, Reza R. Zamani^{1*}, and Kimberly A. Dick^{1,4}

¹ *Solid State Physics, Lund University, Box 118, S-221 00 Lund, Sweden*

² *Ergonomics and Aerosol Technology, Lund University, Box 118, S-221 00, Lund, Sweden*

³ *Thin Film Physics Division, IFM, Linköping University, S-581 83 Linköping, Sweden*

⁴ *Centre for Analysis and Synthesis, Lund University, Box 124, S-221 00 Lund, Sweden*

Corresponding authors' email: Luna.Namazi@ftf.lth.se, Reza.R.Zamani@gmail.com

Table of Contents

S1. GaSb wurtzite shell coverage at different shell growth times2

SI 1: GaSb wurtzite shell coverage at different shell growth times

As seen from the XEDS line scan in figure 1a, the shell does not extend all the way to the top of the wurtzite segment (along the entire core) for the 15-minute shell growth time. This confirms the statement made in the paper that, the main shell growth mechanism in these nanowires is adatom diffusion from the substrate. From figures 1b and 1c it is observed that for 40 and 50 minutes of shell growth time, the entire length of the wurtzite InAs core nanowires are covered with a GaSb shell.

Note that the slight curve in the acquired spectra of figure 1b and c (more observable from the In and As spectra) are due to nanowire bending, and not related to changes in material composition along the length of the nanowires.

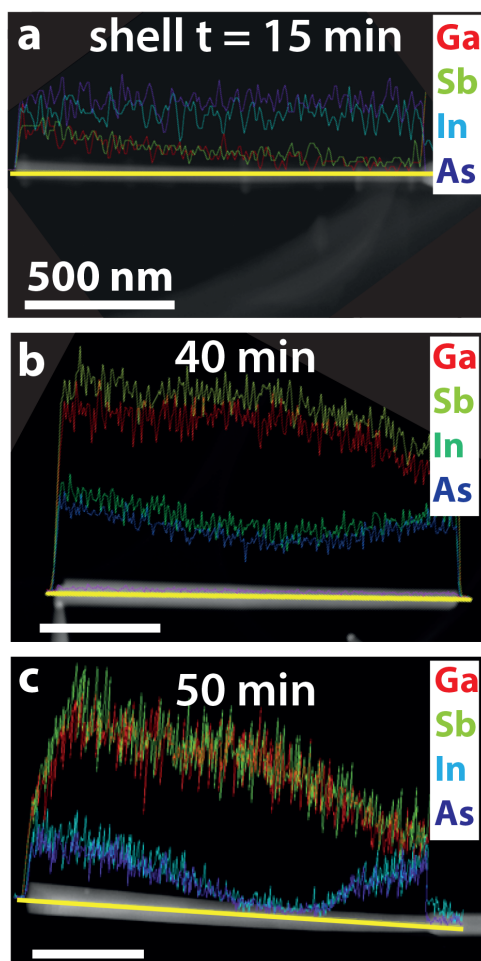


Figure 1. XEDS line scans of InAs-GaSb wurtzite nanowires with shell growth times of a) 15 minutes, b) 40 minutes, and c) 50 minutes. 15 minutes of shell growth is not sufficient for complete shell coverage on the InAs core.

Paper IV



Sb Incorporation in Wurtzite and Zinc Blende $\text{InAs}_{1-x}\text{Sb}_x$ Branches on InAs Template Nanowires

Magnus Dahl, Luna Namazi,* Reza R. Zamani, and Kimberly A. Dick*

The physical properties of material largely depend on their crystal structure. Nanowire growth is an important method for attaining metastable crystal structures in III–V semiconductors, giving access to advantageous electronic and surface properties. Antimonides are an exception, as growing metastable wurtzite structure has proven to be challenging. As a result, the properties of these materials remain unknown. One promising means of accessing wurtzite antimonides is to use a wurtzite template to facilitate their growth. Here, a template technique using branched nanowire growth for realizing wurtzite antimonide material is demonstrated. On wurtzite InAs trunks, $\text{InAs}_{1-x}\text{Sb}_x$ branch nanowires at different Sb vapor phase compositions are grown. For comparison, branches on zinc blende nanowire trunks are also grown under identical conditions. Studying the crystal structure and the material composition of the grown branches at different x , shows that the Sb incorporation is higher in zinc blende than in wurtzite. Branches grown on wurtzite trunks are usually correlated with stacking defects in the trunk, leading to the emergence of a zinc blende segment of higher Sb content growing parallel to the wurtzite structure within a branch. However, the average amount of Sb incorporated within the branch is determined by the vapor phase composition.

energy—by tuning their material composition. Among them $\text{InAs}_{1-x}\text{Sb}_x$ nanowire, a ternary compound of InAs and InSb, combines the material benefits of both these binaries^[12–16] into the useful nanowire configuration. $\text{InAs}_{1-x}\text{Sb}_x$ is promising for future optical applications such as Infrared photodetectors^[17,18] and gas sensors.^[19] Also, at a composition of $x = 0.63$, $\text{InAs}_{1-x}\text{Sb}_x$ offers the narrowest possible band gap among all III–V materials (100 meV).^[20] Due to a small electron effective mass, this material system is also interesting for fundamental electron transport studies.^[21,22]

In addition, branched nanowire structures from InAs, InSb, and $\text{InAs}_{1-x}\text{Sb}_x$ material systems are suitable templates for studying phenomena such as Majorana fermions^[23,24] due to their high carrier mobilities and large g factors. As mentioned, $\text{InAs}_{1-x}\text{Sb}_x$ is a good candidate for IR detection. Having access to branched nanowires of these materials will increase the surface area interacting with the surrounding environment. This

will ultimately lead to more absorption, hence a better detection ability.^[25–27]

Moreover, the physical and material properties a material system exhibits are largely dependent on its crystal structure.^[28–31] Most III–V nanowires grow both in the zinc blende and metastable wurtzite crystal structure.^[32,33] It has been demonstrated that the nanowire crystal structure can be precisely controlled for different materials such as InAs.^[34] This control allows access to crystal phase engineered multi-heterostructures and crystal structure quantum dots of the same material.^[22] Also, the different surface properties that wurtzite and zinc blende have lead to different radial growth.^[35] Antimonide based nanowires, however, are an exception, as it has been proven challenging to grow them in the wurtzite crystal structure. This can be largely attributed to the surfactant effects of Sb and the general trend of lower ionicity of III–Sb compounds.^[36] Therefore, the properties of antimonide nanowires in the wurtzite crystal structure remain unknown, and the latter mentioned multistuctures are yet to be realized in antimonides. Furthermore, although controlled growth of short wurtzite segments of III–Sb binary nanowires has been demonstrated,^[37] there have been no reports on Sb-rich wurtzite ternary segments. Indeed, for $\text{InAs}_{1-x}\text{Sb}_x$ nanowires it has been demonstrated that adding a small amount of Sb to InAs

1. Introduction

III–V nanowires have proven to be excellent platforms for studying the fundamental physics of semiconductors^[1–3] as well as potential candidates for future electronic and optical devices.^[1,4–9] III–Sb nanowires are promising candidates in both areas as they have the lowest charge carrier effective masses hence highest carrier mobilities among III–V materials^[10] and the narrowest band gap energy.^[11] Ternary compound III–V nanowires are interesting due to the possibility of modulating their physical and material properties—such as their band gap

M. Dahl, L. Namazi, Dr. R. R. Zamani, Prof. K. A. Dick
Solid State Physics
Lund University
Box 118 S-221 00, Lund, Sweden
E-mail: luna.namazi@ffl.lth.se; kimberly.dick_thelander@ffl.lth.se
Prof. K. A. Dick
Centre for Analysis and Synthesis
Lund University
Box 124 S-221 00, Lund, Sweden

 The ORCID identification number(s) for the author(s) of this article can be found under <https://doi.org/10.1002/sml.201703785>.

DOI: 10.1002/sml.201703785

changes the crystal structure to zinc blende.^[38–41] Major questions remain on why and how Sb causes the structure to be zinc blende, at what Sb composition this occurs, whether this critical composition depends on growth conditions, and what relative roles kinetics and thermodynamics play. It is interesting to add that, crystal structure tuning is also of interest and can be challenging in II–VI materials.^[50] Specifically wurtzite II–Te materials, similar to III–Sbs are considered relatively difficult to attain.^[51–53]

Since growing III–Sb nanowires in wurtzite is extremely challenging, we need to explore other techniques for exploiting the polytypic behavior of nanowires in order to form wurtzite antimonide material. One promising option is to use III–V nanowires as a template that can “lock” the crystal structure of the newly growing antimonide material to that of the underlying structure. Radial growth of III–Sb shell layers is one method for obtaining the required “locking” mechanism. As it is an extension of the already existing side facet, the growing layer must maintain the underlying structure in order to keep its epitaxial relation to the core.^[42,54] This has been studied in^[20] where wurtzite InAs acts as a template for wurtzite ternary InAs_{1–x}Sb_x. A notable disadvantage of this method is that the Sb composition will ultimately be limited by strain, making high Sb compositions inaccessible. This method also gives only limited access to the specific advantages of 1D nanowire geometry discussed above.

An alternative approach for attaining 1D wurtzite antimonide material is to grow branches from secondary Au seed particles deposited on the sidewalls of wurtzite template nanowires.^[55] Through this approach we can achieve localized growth through the vapor–liquid–solid (VLS) growth mechanism while forcing the new forming material to maintain the crystal structure of the part of the nanowire underneath the secondary particle. This will lead to the extension of the side facet (regardless of the crystal structure it has) into a 1D structure at a localized position as shown schematically in **Figure 1a**. Unlike in the axial close-packed direction, in the orthogonal branch direction, the crystallographic planes of wurtzite side facet ({1100}) and zinc blende ({112}) do not match, providing a barrier to formation of zinc blende in branches. Moreover, by this method one can overcome the strain-induced limitation of radial growth, as axial nanowires are efficient in strain relaxation in the radial direction due to their small diameter.^[43,44]

We here demonstrate successful utilization of branch growth approach for accessing wurtzite InAs_{1–x}Sb_x, and explore the conditions for wurtzite formation. InAs_{1–x}Sb_x branches are grown by metal organic vapor phase epitaxy (MOVPE) using secondary Au-seed particles deposited on already-grown wurtzite and zinc blende InAs nanowires. We find that the epitaxially grown branch will partially transfer the underlying crystal structure of the InAs trunk, while simultaneously grown axial segments exhibit zinc blende structure. This confirms the hypothesis that the branch growth approach offers access to growth directions in which zinc blende is at least partially suppressed. Furthermore, we show that wurtzite branches most often correlate with occasional stacking defects in the trunk structure. This stacking defect propagates into the branch and is responsible for the formation of a zinc blende segment within the branch, growing parallel to the wurtzite structure. By compositional analysis, we

find that when wurtzite and zinc blende segments coexist in the branches, the wurtzite segment demonstrates considerably lower Sb content than the zinc blende segment. However, their average value is similar to that of branches grown from zinc blende nanowires under identical conditions. This indicates that overall Sb content is determined by growth conditions, but incorporation of Sb into wurtzite is suppressed.

2. Results and Discussion

2.1. General Description of Branched Nanowires

In this section we will give an overview of the trunk nanowires pre- and postbranch growth.

In **Figure 1b,c** schematic illustrations, along with overview and magnified images of the zinc blende and wurtzite trunks, are given respectively. As seen in the schematics, for both trunk types, a short wurtzite stem was grown prior to the main segment. This was done to improve the crystal quality of subsequent growth by decoupling it from the substrate. For growing the InAs zinc blende trunks (**Figure 1b**), a wurtzite segment (WZ in schematics of **Figure 1b**) was first grown to improve the crystal quality of the zinc blende segment.

InAs_{1–x}Sb_x branches were grown on InAs zinc blende and wurtzite trunk nanowires seeded with secondary Au aerosol particles. The InAs_{1–x}Sb_x branches (see **Figure 1d**) were grown simultaneously on both wurtzite and zinc blende trunks for each set of growth parameters. The Sb vapor phase composition (x_v), is defined as the ratio of the TMSb flow to the total group V precursor pressure in the vapor.

To study how varying the Sb vapor phase composition (x_v) affects the incorporation of Sb in the InAs_{1–x}Sb_x branches, and to obtain an insight into potential differences between branches adopting zinc blende and wurtzite crystal structures, the Sb vapor phase composition was varied, under constant group III flow. For clarity, in **Figure 1d** both wurtzite and zinc blende nanowires are schematically demonstrated post branch growth. Throughout the paper, we will refer to different segments of these nanowires as demonstrated in **Figure 1d** with the following description.

In zinc blende nanowires: Bottom segment is referred to as the wurtzite segment grown for optimizing the zinc blende conditions. Top segment is used to describe the actual zinc blende segment of the trunk and possible axial InAs(Sb) segment grown during branch growth (described in more detail in Section 2.3.1).

In wurtzite nanowires: Bottom segment describes the actual wurtzite segment of trunk. Top segment refers to an axially grown segment of InAs(Sb) above the original wurtzite trunk segment during branch growth.

In the following sections we will demonstrate the effects of Sb vapor phase composition (x_v), and attempt to explain the observations made on the crystal structure and material composition of the branches, and nanowire trunks. Depending on the trunk crystal structure of the trunk–branch nanowires, we will refer to them as wurtzite, or zinc blende nanowires (as in **Figure 1d**). When referring to individual segments in the nanowires, we will use the abbreviated form, WZ (wurtzite) and ZB (zinc blende).

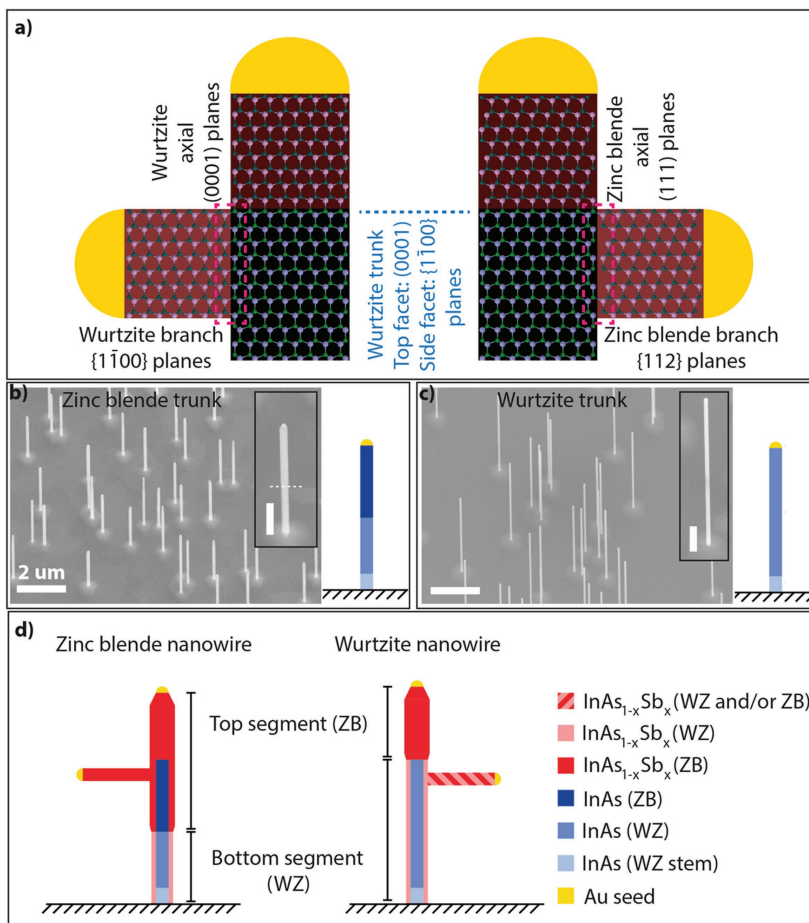


Figure 1. a) Schematic illustration of wurtzite trunk with wurtzite (left-hand side) and zinc blende (right-hand side) axial and branch growths. From the right-hand side image, it is seen that from every six planes of the growing zinc blende branch, one and only one matches with that of the underlying wurtzite side facet (marked with pink dashed box). This is in contrast with the wurtzite branches (left-hand side). Overview and magnified SEM images of reference b) zinc blende and c) wurtzite trunk nanowires, along with schematic illustrations of the different segments of each trunk type. Light blue representing the stem segment in both nanowires, intermediate blue representing the wurtzite segment (decoupling segment of the zinc blende and main segment of the wurtzite nanowires), and dark blue representing the zinc blende segment of the zinc blende nanowires. d) Schematic illustrations of the zinc blende and wurtzite branched nanowires demonstrating their different segments. During branch growth, axial InAs_{1-x}Sb_x segments grow on the trunk with a zinc blende crystal structure.

2.2. Morphological Aspects

The Sb vapor composition was varied in six steps from 0.15 to 0.89. The Group III precursor—Trimethyl indium (TMIn)—flow was kept at constant value for all grown samples. For obtaining the interval $x_v = 0.15$ –0.55, the Trimethyl antimony (TMSb) flow was increased, while to achieve the two higher Sb x_v

the Arsine (AsH₃) flow was reduced (please see Supporting Information Section S1 for detailed information on the precursor flows). In Figure 2, overview and magnified scanning electron microscopy (SEM) images of zinc blende (Figure 2a–f) and wurtzite (Figure 2g–l) branched nanowires grown at different Sb vapor phase compositions are depicted. With a matching average particle density of secondary and initial Au

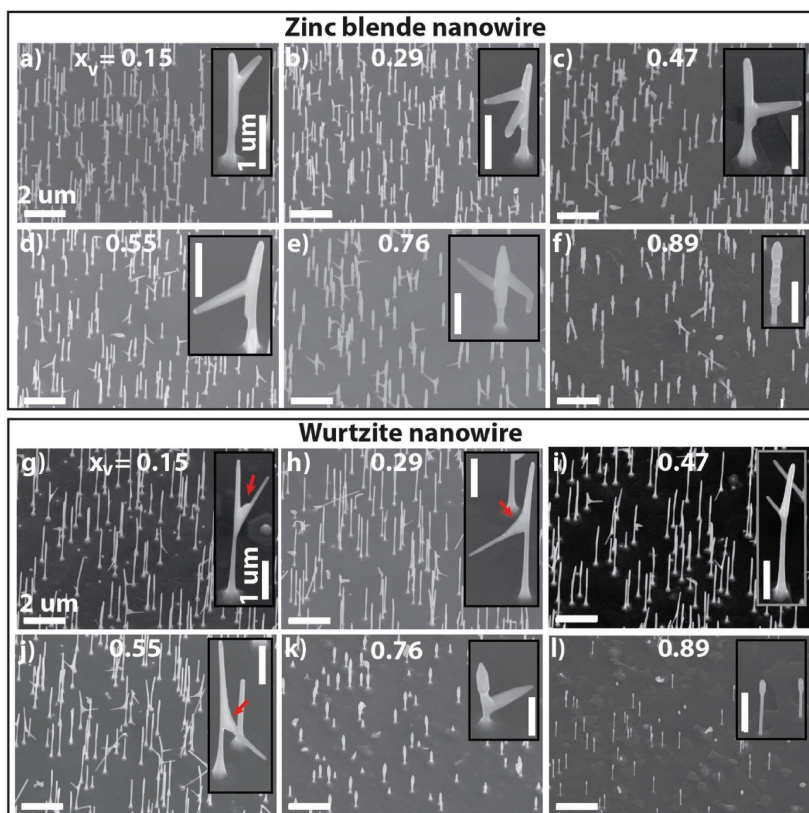


Figure 2. Overview and magnified SEM images of a–f) zinc blende and g–l) wurtzite branched nanowires grown from 30 nm Au initial and secondary particles, under vapor phase Sb compositions ranging from 0.15 to 0.89. For each x_v value, the zinc blende and wurtzite branched nanowires were grown simultaneously together inside the reactor. The red arrows in inset images of (g), (h), and (j) indicate the flag-like structure the branches initially form before continuing into a 1D structure.

seed particles ($1 \mu\text{m}^{-2}$), it is expected that on average there will be one branching event per nanowire. It is understandable however; that a fraction of the nanowire trunks will not receive any secondary particles, while a number of them might receive more than one particle (inset of Figure 2b,e). The branches, specifically for the wurtzite nanowires, tend to form a flag-like structure at the base of the branches (marked with red arrows in insets of Figure 2g,h,j for instance), filling in the sharp kink site between the branch and the trunk.^[45] Filling up this preferential nucleation site at the first stages of branch growth seems to be energetically more favorable than for the wurtzite branch to grow solely in a 1D structure in the $\langle 1\text{--}100 \rangle$ direction.

It is clear from the images that the wurtzite nanowires tend to show noticeably fewer branching events compared to their counterpart, zinc blende nanowires. We will provide an explanation for this further in the paper (Section 2.3.2). The presence

of a top segment on the wurtzite nanowires is attributed to axial growth of (presumably ZB) $\text{InAs}_{1-x}\text{Sb}_x$ during branch growth. This is understood through comparisons between the bottom segment length of the wurtzite nanowires and the reference nanowires (see Supporting Information Section S2).

Looking at the zinc blende nanowires, we observe that at $x_v = 0.76$ the nanowires are noticeably thicker. At the highest point; $x_v = 0.89$, for both nanowire types, the thicknesses of the nanowires are very inhomogeneous, and the overall length is visibly lower. The density of the trunks—specifically for the wurtzite nanowires—has also dropped compared to the other samples in the series and reference samples. This is a clear sign of decomposition as the AsH_3 flow is almost negligible at this data point. There are also very few branches present at this vapor phase composition. This may indicate that there is a limit to how far one can push the Sb vapor phase composition

for growing branches, and pure InSb branches on InAs trunks may be very challenging to obtain.

2.3. Branch Crystal Structure and Trunk Composition

Discussions on the branch crystal structure and composition (discussed in detail in Section 2.4) are closely linked to one another; therefore, at times in these two sections, we will go back and forth in the order of presented material. Also, it is of importance to study the trunk composition and crystal structure post branch growth. Comparing the composition of the trunk to the branch could provide an understanding of Sb incorporation in VS growth compared to VLS, which in turn would enlighten how composition is related to crystal structure, and thus VLS, rather than just the growth environment.

2.3.1. Zinc Blende Structure

Figure 3 demonstrates overview and high-resolution transmission electron microscopy (HRTEM) images of the crystal structure of a typical branched nanowire grown from zinc blende nanowire trunks. These images reveal that the bottom fraction of the ZB segment belonging to the original trunk nanowire before branch growth has a twinned crystal structure. This is in contrast with the later growing axial ZB segment during branch growth, as the latter is found to be pure zinc blende. (For a clearer understanding of the segments mentioned here, we refer the reader to Figure 1d, zinc blende nanowire, top segment.) Both in the scanning TEM (STEM) image of Figure 3b and the graph in Figure 3c, two dashed lines, green and purple, are drawn, which represent the interface between the WZ stem and the twin-plane ZB, and that of the twin plane segment and pure ZB segment, respectively.

By performing energy-dispersive X-ray spectroscopy (EDX) analysis in the axial and radial directions of the trunk of these nanowires, differences in the material composition of the pure and twinned ZB segments of the trunk are revealed. This is demonstrated in Figure 3b,c, where the red squares represent point analysis on the center, and the blue triangles on the edge of the nanowire. From the graph in Figure 3c, it is clear that along the entire length of the trunk, up to where the twin plane ZB ends, the edges of the nanowire have considerably higher Sb compositions compared to the center. This suggests radial growth of an Sb-rich shell during branch growth. Past the purple line (pure ZB segment) the Sb composition increases significantly in the center of the wire and also slightly at the edges compared to the twin planed segment, and there is no evident difference between data obtained from the center and the edges. This confirms that, the pure ZB segment is axially grown during branch growth. It is also notable that the axial growth incorporates slightly more Sb than radial growth. Similar behavior has also been observed previously in.^[46]

The correlation between compositional and crystal structure indicates that the region above the twin plane is grown axially, with a more homogeneous distribution of Sb. This homogeneity is also realized in the branch composition deducible from

the elemental line scan given in the inset of Figure 3b. We will discuss the branch composition in more detail in Section 2.4.

The overview and inset images of Figure 3a reveal that the branch crystal structure is zinc blende with twin planes. The twin planes are observed to run along the length of the branch (in contrast to twins in the trunk which are normal to the growth direction, as is usual for nanowires). It can also be seen that these twins correlate with twins in the trunk, and in fact the branch transfers the twinned structure from the trunk into its crystal structure.

The zinc blende branch grows along $\langle 111 \rangle$ direction. However, the upfront facet of the branch in contact with the seed particle is not perpendicular to this direction. As can be seen in the Figure 3a inset in orange, the surface below the seed is not flat. It makes an angle of almost $\pm 70^\circ$ with the branch growth direction, which corresponds to $\{111\}$ plane families. Note that it changes from $+70^\circ$ to -70° and vice versa when it encounters a twin boundary. In this specific nanowire, the branch seems to have slightly changed its growth direction toward the tip. We note that, since the crystal structure remains the same, and there are no defects visible, this is just related to the bending of the branch on the TEM grid. During the TEM study, moving from one end of the branch to the other, it was observed that the structure was moving away from the zone axis, and it was necessary to reorientate the nanowire by tilting the sample stage. We also note that this bending of the tip was not a general feature observed for all zinc blende nanowires. Another important point is that some of the twin boundaries, especially at the lower part of the branch, are stopped during the branch growth and the structure of the branch shows an eventual tendency to become pure zinc blende as it approaches the tip.

2.3.2. Wurtzite Structure

Figure 4 demonstrates a typical branched nanowire grown from a wurtzite trunk. From careful analysis of several similar branched wurtzite nanowires it is understood that these branches predominantly exist in the vicinity of and are correlated to a stacking fault in the trunk (a short zinc blende segment in an otherwise wurtzite structure). This finding is demonstrated in the overview and magnified TEM images of Figure 4a,b, respectively. The branch originates in the vicinity of a single stacking defect in the trunk marked by the red dot in Figure 4a. Interestingly, the branch crystal structure is half wurtzite-half zinc blende (falsely colored red for wurtzite and blue for zinc blende in Figure 4b), unlike that of the trunk. Evidently, the stacking fault not only does propagate into the branch, it also induces a zinc blende structure coexisting parallel to the wurtzite structure within the branch.

Since nearly every observed branch had originated from a stacking fault, which is surprising given the relatively low density of stacking defects in the trunk nanowires, and the random distribution of the secondary Au particles, it could be speculated that Au particles on wurtzite InAs are able to migrate on the trunk sidewalls until a favorable nucleation site is reached.^[47–49] It appears that the existence of the zinc blende defect not only enables branch growth with a partially zinc blende crystal structure, but also facilitates growth of the

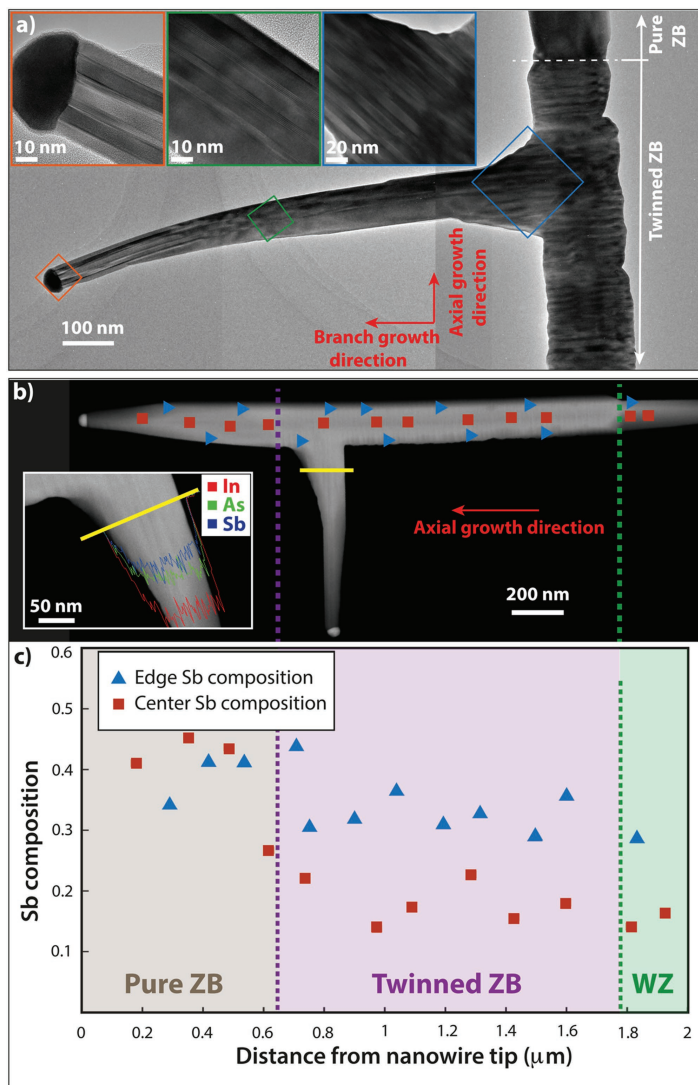


Figure 3. a) Overview and HRTEM images of a zinc blende branched nanowire grown under $x_{\text{V}} = 0.55$. Along its entire length, the branch has a twin planed zinc blende crystal structure transferred from the twin plane structure of the underlying trunk. b) STEM HAADF image of the nanowire where the transitions between WZ/twinned ZB and twinned/pure ZB are marked with green and purple dashed lines, respectively. The inset demonstrates an XEDS line scan of the branch along the [111] direction, revealing $\text{InAs}_{1-x}\text{Sb}_x$ material composition. The blue triangles and the red squares specify the positions from which the compositional data along the edge and center of the trunk shown in (c) has been obtained. The difference in composition of the edge and core corresponds perfectly with where the crystal structure changes from twinned to pure zinc blende, which indicates that the pure zinc blende segment of the trunk is grown during branch growth.

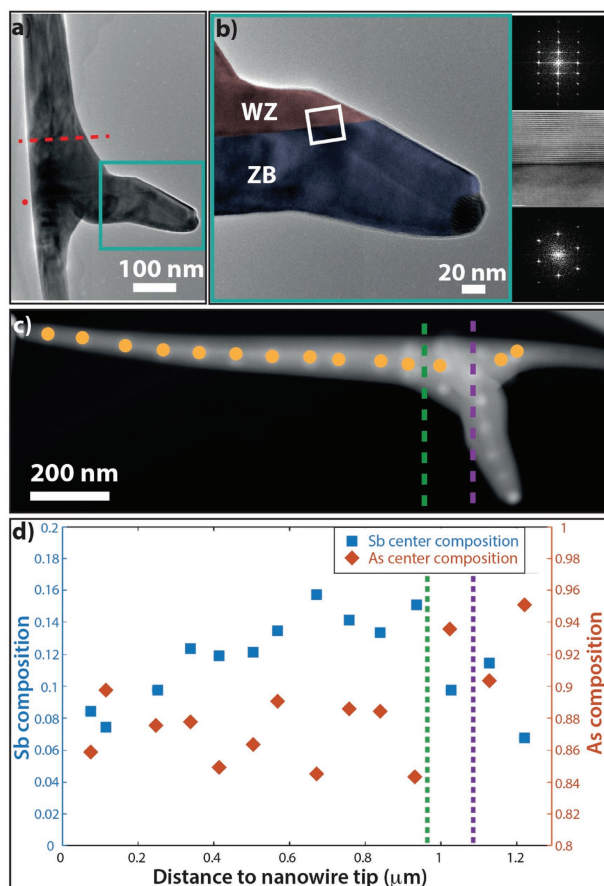


Figure 4. a) Overview TEM image of a wurtzite branched nanowire grown under $x_v = 0.55$. The red dot indicates the stacking defect position, while the red dashed line marks the interface between WZ and ZB segments on the trunk. b) False colored HRTEM image of the branch clearly depicting the parallel existence of both wurtzite and zinc blende crystal structures within the branch. The insets show the diffraction patterns of the WZ (top) and ZB (bottom) segments of the branch along with an HRTEM image of the interface (middle) marked with a white box. c) HAADF-STEM image of the nanowire. The yellow dots identify the positions along the center of the trunk from which the compositional analysis has been obtained and plotted in panel (d). The purple and green dashed lines represent the branch position and the WZ/ZB interface on the trunk, respectively. d) Sb (left axis) and As (right axis) composition of the trunk center. Correlating the measurements with the position of the branch and WZ/ZB interface, it is understood that the axial segment grown during branch growth has a higher Sb composition compared to the $\text{InAs}_{1-x}\text{Sb}_x$ shell layer grown on the original trunk segment.

wurtzite structure within the branch, alongside the zinc blende structure. This tendency is consistent with previous literature showing the utterly low preference of Sb structures to grow in the wurtzite crystal phase.^[36] What is even more interesting is

the gradual elimination of the WZ segment within the branch as the particle gradually moves completely over the ZB segment. Zinc blende has a higher surface energy, and by moving the particle to the ZB segment, the total energy of the system is reduced. In fact, we see that initially the structure of the lower part of the branch (where the ZB segment eventually forms) is wurtzite, and gradually changes to zinc blende. Since this change is in the $(1-100)$ direction it occurs not via stacking faults, but grain boundaries with a much higher energy cost. It can be speculated that forming wurtzite antimonides is so energetically unfavorable, that the energy cost of this unlikely crystallographic change is lower than forming wurtzite antimonide. Therefore, Sb “pushes” the system from wurtzite to zinc blende instead to compensate for this unfavorable situation.

This is a general trend for branches grown from wurtzite trunks, as the same behavior can be observed in the TEM image of another wurtzite branched nanowire provided in Figure 5. The branch growth direction is $\langle 1-100 \rangle$ for wurtzite which is parallel to the $\langle 112 \rangle$ for zinc blende. Apparently, when wurtzite is terminated, the zinc blende growth direction changes from $\langle 112 \rangle$ to $\langle 111 \rangle$, which is not perpendicular to the zone axis. It is deduced from the facts that, first, the branch droplet interface with the branch is not perpendicular to the zone axis, and second, the tip of the branch becomes out of focus in the TEM images while the trunk is in focus.

The red dashed line in Figure 4a marks where the top segment of the trunk starts (For a clearer understanding we refer the reader to Figure 1d, wurtzite nanowire, top segment). This segment has a zinc blende crystal structure, and grows axially during branch growth from the original seed particle. Figure 4c,d show the solid phase composition of the nanowire trunk in the central position along the axial direction. The yellow dots on the high-angle annular dark-field (HAADF)-STEM image depict the exact locations from which the compositional data has been obtained and plotted in Figure 4d. The purple and green lines in both images mark the branch, and wurtzite-zinc blende interface positions in the trunk and the branch, respectively. Both As and Sb compositions are demonstrated in the graph in Figure 4d,

from which it is clear that: a) even on the right side of the green line (the WZ segment) significant amounts of Sb can be detected. This is evidence of a radially grown $\text{InAs}_{1-x}\text{Sb}_x$ shell on the InAs wurtzite trunk during branch growth; and

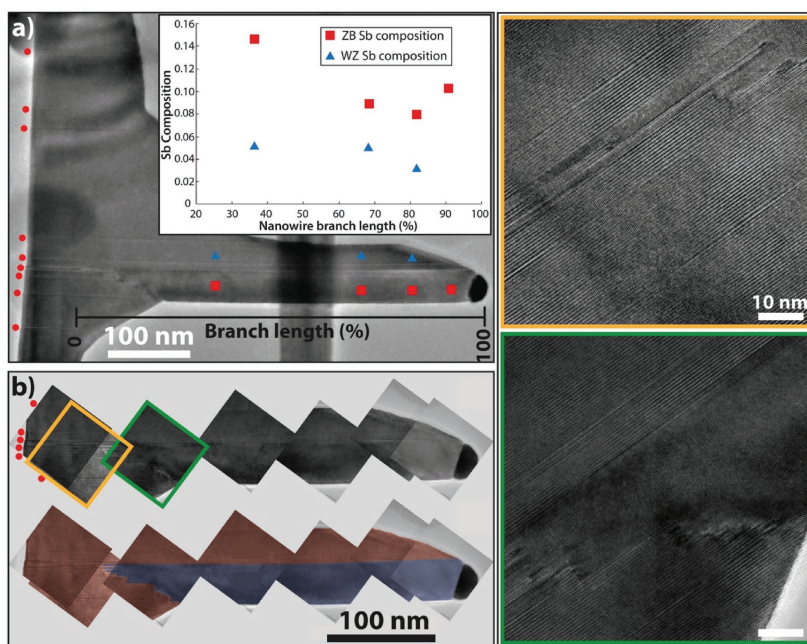


Figure 5. a) Overview TEM image of a wurtzite nanowire branch grown under $x_v = 0.55$ (same sample as Table 1, 0.55, wurtzite). The red circles beside the trunk mark the present stacking defects of the trunk in the vicinity of the branch. The blue triangles and red squares identify the locations from which the compositional data from the WZ and ZB segments of the branch are acquired, respectively. The compositional data are presented in the inset graph, showing a higher Sb incorporation in ZB, the average Sb incorporated in WZ, and ZB fall on 0.11 for all data pairs. b) HRTEM image of the branch along with a false colored version clearly specifying the WZ and ZB segments. Panels (c) and (d) are HRTEM images of the transition region marked in panel (b) depicting the sudden formation of ZB at the cost of WZ discontinuation.

b) the axially grown ZB segment is $\text{InAs}_{1-x}\text{Sb}_x$, with a higher solid phase Sb composition of that of the shell layer on the wurtzite segment. This is deducible from the sudden significant increase in the Sb composition to the left side of the green line (ZB).

2.4. Branch Composition

In the following we will focus on the branch composition for both wurtzite and zinc blende nanowires, and discuss how changing the Sb vapor phase composition ultimately affects the Sb incorporation in the different crystal structures. In Table 1,

we present the branch composition from wurtzite and zinc blende nanowires with three different Sb vapor phase compositions; $x_v = 0.29, 0.55$, and 0.76 . Data from $x_v = 0.15$ are not included, since already at 0.29 the detectable Sb signal is very low for zinc blende nanowires, and below the detection limit of our EDX system for the wurtzite. The highest ($x_v = 0.89$) data point is also left out since the numbers of branches were very few for both types of nanowires, while decomposition of the trunk was very significant. The mid-point ($x_v = 0.47$) is eliminated to keep the discussion short, as it is close to 0.55 and will presumably have similar values.

For 0.55 and 0.76 , the Sb composition of the wurtzite and zinc blende part of the branch are given as separate values.

Table 1. Sb branch composition (x) from wurtzite and zinc blende nanowires with Sb vapor phase compositions of $x_v = 0.29, 0.55$, and 0.76 . Where parallel WZ and ZB segments exist within a branch, their Sb compositions are given separately.

| x_v | 0.29 | 0.55 | 0.76 |
|-------------|-----------------|---|--|
| Nanowire | | | |
| Zinc blende | 0.08 ± 0.02 | 0.11 ± 0.03 | 0.33 ± 0.06 |
| Wurtzite | Undetectable Sb | WZ: 0.06 ± 0.02 ZB: 0.16 ± 0.06 | WZ: 0.23 ± 0.03 ZB: 0.47 ± 0.007 |

From the table it is clear that as a general trend, the zinc blende crystal structure tends to have a higher Sb incorporation. This trend also holds for the WZ and ZB segments of the same branches for the wurtzite nanowires. This strongly suggests that Sb incorporation into the wurtzite crystal structure is less favorable compared to zinc blende even under constant growth conditions.

More interesting is the Sb incorporation measured for the WZ and ZB parts of the branch on wurtzite nanowires for 0.55 and 0.76; the average value of the Sb incorporation of the two parallel segments under given x_z (0.11 and 0.35 respectively) is similar to that of the zinc blende nanowire grown under the same condition (0.11 and 0.33 respectively), indicating that total Sb incorporated in the branch is determined by the x_z . More importantly, this also implies there is a hard limit to the amount of Sb that can be incorporated into wurtzite crystal structures at given vapor phase compositions. In other words, the excess amount of Sb in wurtzite (being 0.05 and 0.12, respectively) is expelled to the zinc blende section, and is incorporated there instead.

Figure 5 shows another example of a branch growing from a wurtzite nanowire. The preceding discussions on the correlation of the branch to a stacking defect, the eventual appearance of a zinc blende segment in the branch, and the gradual elimination of wurtzite structure discussed previously are again visible from the overview and high-resolution TEM images of Figure 5a,b, and Figure 5c,d, respectively. The inset graph in Figure 5a depicts the Sb incorporation of the branch WZ and ZB sections at identical positions of the branch growth direction. For all data points, the Sb incorporation in ZB is higher than that of WZ. Worth noting is the last data point related to the tip of the branch. At this position, the wurtzite structure has already been eliminated, and only the zinc blende structure remains. The Sb composition at this position reveals a value of 0.11, which again is equal to the average value of wurtzite and zinc blende when they existed parallel in the branch, and also the branches grown on zinc blende trunks simultaneously under the same vapor phase composition. The red dots in Figure 5a,b point to stacking defects, and again it is clear that the branch has originated from a defective region. The false-colored HRTEM image of 5b reveals that few layers by few layers, originating from twin defects, the wurtzite structure is abruptly stopped along forming layers, and the zinc blende structure—initially carried into the branch as a defect—grows into a full segment of the branch. Figure 5c demonstrates magnified images of the transition region. Not only do the existing defects propagate into the branch, new defective regions emerge as they bring the wurtzite structure to a sudden halt. Again, the observation here indicates that the energy barrier to form the defects (ZB segment in the branch) is presumably lower than the barrier to form the wurtzite structure with the full/average Sb composition. From Figure 5c,d it is observed that the wurtzite crystal structure is gradually converted to zinc blende.

2.5. Origin of Zinc Blende Formation in Branches on Wurtzite Nanowires

In order to explain the unlikely formation of the parallel ZB segments in wurtzite nanowires, we can suggest two possibilities.

First, it may be that during the VLS branch growth twin defects induce this wurtzite to zinc blende conversion from the 0001 layers in the vicinity by changing the stacking from ABABAB to ABCABC. Alternatively, the change may be caused by the seed particle once the branch is grown, and the zinc blende stacking is induced from the particle back toward the trunk. Both can be due to the presence of Sb in the system. Possibly, the particle eventually moves to the zinc blende segment since it is energetically more favorable, and therefore the wurtzite segment disappears after some time.

In the following we demonstrate a pure wurtzite branch grown on wurtzite nanowires. As mentioned throughout the paper, the branches growing from wurtzite trunks usually grow from a stacking defect, and carry the zinc blende structure into the branch. Therefore, a pure wurtzite branch grown from a defect-free segment of the trunk is rather an exception and a rare observation. Figure 6a demonstrates a TEM overview image with HRTEM insets from different positions along the wurtzite branch. The branch is grown under an Sb vapor phase composition of 0.76 (same sample as the right side lower most box in Table 1). The interesting fact is that, as observed in the yellow and green inset boxes, two defect lines run through the entire length of the wurtzite branch (marked with white dashed lines). Following these lines to the trunk however (purple inset box), it can be seen that the defect lines disappear halfway into the trunk. This is an indication that, the defects are induced from the branch into the trunk, rather than being a structural defect of the trunk. This observation raises the speculation that, the defects seen in all other wurtzite nanowire branches may have actually been caused by the branch itself, propagating into the trunk, rather than the branch originating at a defect. Assuming this speculation correct, it can be further hypothesized that the ZB segment originates from segregation of a metastable wurtzite $\text{InAs}_{1-x}\text{Sb}_x$.

Figure 6b,c demonstrate HAADF-STEM images of the branch and point EDX measurements of the center and both sides (marked on the STEM image) of the branch, respectively. The average solid phase Sb composition on both edges and center are similar, with an average value of 0.36. The edges show more or less constant Sb compositions as depicted in the graph, while in the center the Sb composition decreases as we approach the tip of the branch. This indicates a core/shell structure of the branch, where the Sb composition of the core decreases, as the branch grows longer. It must be noted though, that due to the tapered structure of the branch, the thickness of the branch shell varies from bottom to top. Therefore, a higher Sb composition measured at the bottom of the branch center could also be related to a thicker shell at that position. The top-most point of the blue triangles is an outlier compared to the rather constant Sb composition of the edges. This indicates that a shell layer has not yet been formed on the downward edge of the branch, while shell formation is much faster on the upward side (topmost green triangle has the same constant Sb composition). We can attribute this to a higher preference in nucleation in the top corner formed between the trunk and the branch compared to the bottom corner. This is readily obvious from the rounded feature of the top corner resulted from faster VS growth, versus the sharp edge of the bottom corner. This can be attributed to the difference in polarity of these two

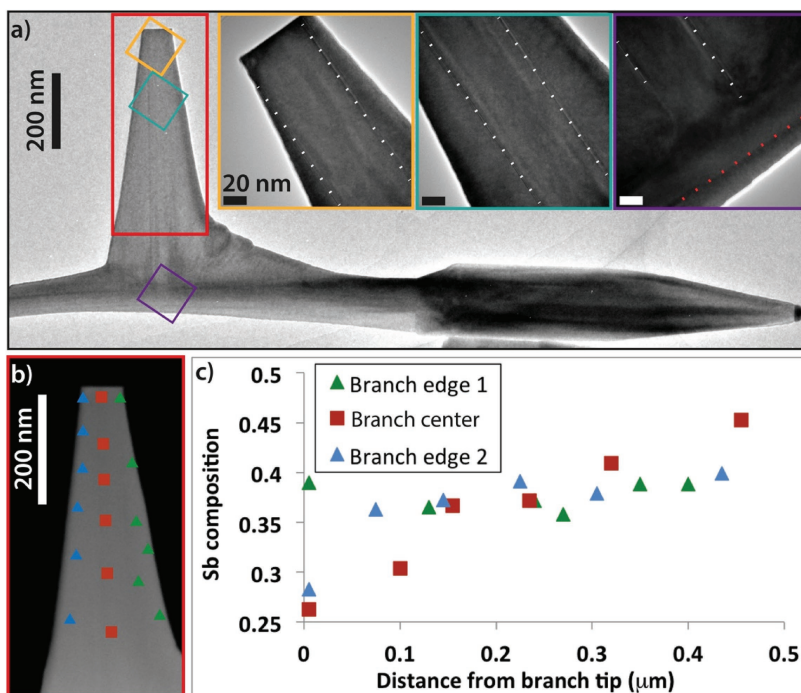


Figure 6. a) Overview TEM image of a pure wurtzite branch growing from a wurtzite trunk under $x_v = 0.76$. Please note that the Au seed particle on the branch tip is missing; most likely broken off during transfer to the TEM grid. The insets show HRTEM images of the specified parts of the branch. The white dashed lines in the inset mark the two defect lines running through the branch from tip (yellow inset), disappearing somewhere in the trunk (purple inset). The red dashed line in the purple inset defines the core-shell interface of the trunk (the shell grown radially during branch growth). b) STEM-HAADF image of the branch with red squares, blue and green triangles identifying the positions from which compositional data have been acquired. c) Sb composition of the center, downward and upward edges along the branch. The edges show a constant Sb composition (except of the topmost data point of the downward edge), while the center composition decreases from base to top. This reveals a core-shell structure of the pure wurtzite branch.

pockets: the top pocket has the same polarity as the substrate, which has a higher surface energy in comparison to the opposite polarity (bottom pocket). Please note, the higher nucleation preference on one side of the branch is the cause of the flag-like structures discussed earlier in Figure 1. Interestingly, if the positions of the defect lines in the yellow inset of Figure 6a are compared, one can clearly see that the defect line on the downward edge does not run all the way to the top, but slightly later than the other defect line. Comparing this to the EDX data acquired from the edges, and the not-yet existing shell of the downward edge at the tip, it can be understood that these defect lines actually mark the interface of the branch core-shell structure.

Comparing the average value of the center composition of the pure wurtzite branch with that of the wurtzite nanowire from the same sample, but with parallel WZ and ZB segments (wurtzite, x_v 0.76 in Table 1), and zinc blende nanowires grown under exact conditions (zinc blende, x_v 0.76 in Table 1), we surprisingly see that the pure wurtzite branch has a very close Sb incorporation

compared to the zinc blende nanowire, and the average value of the WZ and ZB segments of the wurtzite nanowire (0.36 vs 0.33 and 0.35, respectively). However, if we relate the varying Sb composition of the center, to the branch shell thickness, we can take the value of the topmost point of the branch as the Sb incorporation of the VLS grown part of the branch (0.26). In this case, we can observe a close similarity of this value to that of the WZ branch segment of the wurtzite nanowire grown under the same conditions (right side lower most box in Table 1, WZ segment). From the latter observations it can be deduced that, in the pure wurtzite case, the extra Sb gets incorporated into radial growth, instead of forming a ZB segment.

3. Conclusion

In this work we demonstrate a novel approach for achieving Sb-rich ternary nanowires with wurtzite crystal structure. We

utilize the existing nanowire branching technique from secondary Au seed particles to provide a suitable wurtzite template for growing wurtzite $\text{InAs}_{1-x}\text{Sb}_x$ branches on wurtzite InAs trunk nanowires. We study the effects of Sb vapor phase composition on the Sb incorporation and crystal structure of branches grown simultaneously on wurtzite and zinc blende InAs trunk nanowires.

We show that, for the wurtzite nanowires, the branching event typically occurs in relation with an occasional stacking defect in the trunk structure, which then not only propagates into the branch, but also gives rise to the sudden appearance of a zinc blende segment not present in the trunk. This zinc blende segment grows parallel to the wurtzite segment within the branch and eventually the wurtzite segment is eliminated. The Sb incorporation into the wurtzite segments of these branches is significantly lower, while their parallel zinc blende segment has a higher Sb incorporation when compared to zinc blende branches grown from zinc blende trunk nanowires. However, the average Sb composition value of these segments is very close to that of the zinc blende nanowire branches grown on zinc blende trunks. Similarly, in a rare example of a pure wurtzite branch grown on a nondefective area of a wurtzite nanowire, the average composition is similar. In this case we argue that the branch forms a core-shell structure, with the Sb incorporation of the radial shell being higher than the core, and the core having a composition similar to the wurtzite segment in branches with coexisting zinc blende segments.

From the two latter discussions we draw the conclusion that there exists a hard limit to how much Sb can be incorporated within wurtzite at given growth conditions. Sb that is supplied in excess of this limit is incorporated into a coexisting zinc blende segment, or within a radially grown shell.

4. Experimental Section

Growing Wurtzite and Zinc Blende $\text{InAs}_{1-x}\text{Sb}_x$ Nanowire Branches: The trunks for the InAs - $\text{InAs}_{1-x}\text{Sb}_x$ (trunk-branch) nanowires were grown from size-selected 30 and 40 nm diameter gold particles on separate InAs (111) B substrates. Aerosol seed particles were used, with an average particle density of $1 \mu\text{m}^{-2}$. To grow the branches, aerosol gold particles of the same diameter and density as the ones used for the trunk growth were deposited, i.e., trunks grown from 40 nm gold particles received a secondary deposition of 40 nm Au particles. All nanowire growth was conducted using MOVPE with vertical flow in an Aixtron 3" \times 2" close-coupled showerhead reactor. TMIn, and AsH_3 and TMSb were used as group III and V precursors, respectively. H_2 was used as the carrier gas with a flow of 8 L min^{-1} and a pressure of 100 mbar. The samples were annealed prior to both trunk and branch growth at 540°C for 420 s under an AsH_3/H_2 atmosphere with an AsH_3 molar fraction of 2.5×10^{-3} to prevent desorption of the substrate/trunk nanowire.

Both wurtzite and zinc blende trunks were grown at 465°C , and the different crystal structures were achieved by only changing the group V flow. For both trunk types, a short wurtzite stem was grown prior to the main segment. This was done to improve the crystal quality of subsequent growth by decoupling it from the substrate. As the length of the stem approaches the diffusion length of the precursors, the growth conditions stabilize. The stems were grown at similar conditions for both trunk types at 465°C for 240 s under a flow of TMIn and AsH_3 with respective molar fractions of 1.8×10^{-6} and 1.2×10^{-4} , yielding a V/III ratio of 67.

In order to grow the InAs wurtzite trunk, the AsH_3 molar fraction was altered to 3.8×10^{-5} , while keeping the temperature and TMIn flow at the same values used for stem growth. The growth time was set to 20 min.

For growing the InAs zinc blende trunks, however, a wurtzite segment was grown for 15 min prior to the zinc blende segment. This was done to improve the crystal quality of the zinc blende segment. Consequently, the zinc blende trunks were then grown for 15 min by changing the AsH_3 molar fraction to 1.6×10^{-2} .

All the $\text{InAs}_{1-x}\text{Sb}_x$ branches were grown at a similar temperature of 450°C for 20 min. Branch growth was terminated by shutting down the TMIn and TMSb flows simultaneously and cooling the samples down under an H_2/AsH_3 atmosphere.

To study how varying the Sb vapor phase composition (x_s) affects the incorporation of Sb in the $\text{InAs}_{1-x}\text{Sb}_x$ branches, and to obtain an insight to potential differences between branches adopting zinc blende and wurtzite crystal structures, the Sb vapor phase composition was varied, while keeping the TMIn flow constant.

For studying the effect of varying Sb vapor phase composition, $\text{InAs}_{1-x}\text{Sb}_x$ branches were grown under a TMIn flow of 2.5×10^{-6} for all the studied x_s . In order to achieve the studied range of x_s (0.15–0.89), initially the AsH_3 molar fraction was kept constant at 2.5×10^{-4} , while the TMSb molar fraction was varied between 4.5×10^{-5} and 3.1×10^{-4} . This covered an Sb vapor phase ratio between 0.15 and 0.55. It is noted that, since the other flows were kept at constant values throughout the study, the V/III ratio and the total flow of precursors increase with increased TMSb flow. With the setup used, however, it was not possible to further increase the TMSb flow, so to achieve x_s of 0.76 and 0.89, the AsH_3 flow was reduced to 1×10^{-4} and 3.8×10^{-5} , respectively. Again note that this leads to a decrease of the total flow and V/III ratio.

Post trunk and branch growth, the morphology and crystal structure of the nanowires were studied using SEM in a Hitachi SU8010 cold field emission SEM, with an acceleration voltage of 15 kV and with a 30° tilt of the samples. The dimensions of the nanowires were measured using ImageJ from the obtained SEM images.

The crystal structure and the composition of the branched nanowires were analyzed using HRTEM conducted in a JEOL 3000F TEM equipped with a field-emission gun using an acceleration voltage of 300 kV. The images from the compositional analysis were recorded in the same microscope in HAADF-STEM mode with a HAADF detector. Compositional analysis was performed using an Oxford Instruments EDX detector, and material composition was measured in atomic percentage (at%). The percentage was normalized to 50% In and converted to Sb solid phase composition (x). For specimen preparation for TEM analysis, the nanowires were manually broken off the substrates and transferred to holey carbon copper grids. 3D atomic models were created by using Rhodius software tool.^[56]

Supporting Information

Supporting Information is available from the Wiley Online Library or from the author.

Acknowledgements

M.D. and L.N. contributed equally to this work. This work was supported by the Swedish Research Council (VR), the Swedish Foundation for Strategic Research (SSF), the Knut and Alice Wallenberg Foundation (KAW), and NanoLund.

Conflict of Interest

The authors declare no conflict of interest.

Keywords

antimonide, Au seeded, branched nanowires, InAsSb, wurtzite

Received: October 31, 2017

Revised: December 7, 2017

Published online:

- [1] S. Nadj-Perge, S. M. Frolov, E. P. A. M. Bakkers, L. P. Kouwenhoven, *Nature* **2010**, 468, 1084.
- [2] V. Mourik, K. Zuo, S. M. Frolov, S. R. Plissard, E. P. A. M. Bakkers, L. P. Kouwenhoven, *Science* **2012**, 336, 1003.
- [3] M. Nilsson, L. Namazi, S. Lehmann, M. Leijnse, K. A. Dick, C. Thelander, *Phys. Rev. B* **2016**, 94, 115313.
- [4] H. J. Joyce, Q. Gao, H. Hoe Tan, C. Jagadish, Y. Kim, J. Zou, L. M. Smith, H. E. Jackson, J. M. Yarrison-Rice, P. Parkinson, M. B. Johnston, *Prog. Quantum Electron.* **2011**, 35, 23.
- [5] A. W. Dey, J. Svensson, M. Ek, E. Lind, C. Thelander, L.-E. Wernersson, *Nano Lett.* **2013**, 13, 5919.
- [6] J. C. Johnson, H.-J. Choi, K. P. Knutsen, R. D. Schaller, P. Yang, R. J. Saykally, *Nat. Mater.* **2002**, 1, 106.
- [7] P. Krogstrup, H. I. Jørgensen, M. Heiss, O. Demichel, J. V. Holm, M. Aagesen, J. Nygard, A. Fontcuberta, I. Morral, *Nat. Photonics* **2013**, 7, 306.
- [8] K. Tomioka, M. Yoshimura, T. Fukui, *Nature* **2012**, 488, 189.
- [9] R. Yan, D. Gargas, P. Yang, *Nat. Photonics* **2009**, 3, 569.
- [10] J. A. del Alamo, *Nature* **2011**, 479, 317.
- [11] S. Sakai, Y. Ueta, Y. Terauchi, *Jpn. J. Appl. Phys.* **1993**, 32, 4413.
- [12] S. A. Dayeh, D. P. R. Aplin, X. Zhou, P. K. L. Yu, E. T. Yu, D. Wang, *Small* **2007**, 3, 326.
- [13] A. C. Ford, J. C. Ho, Y.-L. Chueh, Y.-C. Tseng, Z. Fan, J. Guo, J. Bokor, A. Javey, *Nano Lett.* **2009**, 9, 360.
- [14] C. Thelander, M. T. Björk, M. W. Larsson, A. E. Hansen, L. R. Wallenberg, L. Samuelson, *Solid State Commun.* **2004**, 131, 573.
- [15] P. Caroff, J. B. Wagner, K. A. Dick, H. a Nilsson, M. Jeppsson, K. Deppert, L. Samuelson, L. R. Wallenberg, L.-E. Wernersson, *Small* **2008**, 4, 878.
- [16] Y. Wang, J. Chi, K. Banerjee, D. Grützmacher, T. Schäpers, J. G. Lu, *J. Mater. Chem.* **2011**, 21, 2459.
- [17] H. H. Wiedner, A. R. Clawson, *Thin Solid Films* **1973**, 15, 217.
- [18] J. Svensson, N. Anttu, N. Vainorius, B. M. Borg, L.-E. Wernersson, *Nano Lett.* **2013**, 13, 1380.
- [19] W. Dobbelaere, J. de Boeck, C. Bruynsraede, R. Mertens, G. Borghs, *Electron. Lett.* **1993**, 29, 890.
- [20] C. Thelander, P. Caroff, S. Plissard, K. A. Dick, *Appl. Phys. Lett.* **2012**, 100, 232105.
- [21] R. M. Biefeld, *Mater. Sci. Eng., R* **2002**, 36, 105.
- [22] M. Nilsson, L. Namazi, S. Lehmann, M. Leijnse, K. A. Dick, C. Thelander, *Phys. Rev. B* **2016**, 93, 195422.
- [23] H. J. Suominen, M. Kjaergaard, A. R. Hamilton, J. Shabani, C. J. Palmström, C. M. Marcus, F. Nichele, *Phys. Rev. Lett.* **2017**, 119, 176805.
- [24] S. R. Plissard, I. van Weperen, D. Car, M. A. Verheijen, G. W. G. Immink, J. Kammhuber, L. J. Cornelissen, D. B. Szombati, A. Geresdi, S. M. Frolov, L. P. Kouwenhoven, E. P. A. M. Bakkers, *Nat. Nanotechnol.* **2013**, 8, 859.
- [25] D. Li, X. Yan, C. Lin, S. Huang, Z. R. Tian, B. He, Q. Yang, B. Yu, X. He, J. Li, J. Wang, H. Zhan, S. Li, J. Kang, *Nanoscale Res. Lett.* **2017**, 12, 10.
- [26] M. J. Bierman, S. Jin, *Energy Environ. Sci.* **2009**, 2, 1050.
- [27] K. A. Dick, S. Kodambaka, M. C. Reuter, K. Deppert, L. Samuelson, W. Seifert, L. R. Wallenberg, F. M. Ross, *Nano Lett.* **2007**, 7, 1817.
- [28] F. Bechstedt, A. Belabbes, *J. Phys.: Condens. Matter* **2013**, 25, 273201.
- [29] D. Kriegner, C. Panse, B. Mandl, K. A. Dick, M. Keplinger, J. M. Persson, P. Caroff, D. Ercolani, L. Sorba, F. Bechstedt, J. Stangl, G. Bauer, *Nano Lett.* **2011**, 11, 1483.
- [30] Z. Zanoli, F. Fuchs, J. Furthmüller, U. von Barth, F. Bechstedt, *Phys. Rev. B* **2007**, 75, 245121.
- [31] M. Hjort, S. Lehmann, J. Knutsson, A. A. Zakharov, Y. A. Du, S. Sakong, R. Timm, G. Nylund, E. Lundgren, P. Kratzer, K. A. Dick, A. Mikkelsen, *ACS Nano* **2014**, 8, 12346.
- [32] H. J. Joyce, J. Wong-Leung, Q. Gao, H. H. Tan, C. Jagadish, *Nano Lett.* **2010**, 10, 908.
- [33] P. Caroff, K. A. Dick, J. Johansson, M. E. Messing, K. Deppert, L. Samuelson, *Nat. Nanotechnol.* **2009**, 4, 50.
- [34] S. Lehmann, J. Wallentin, D. Jacobsson, K. Deppert, K. A. Dick, *Nano Lett.* **2013**, 13, 4099.
- [35] L. Namazi, M. Nilsson, S. Lehmann, C. Thelander, K. A. Dick, *Nanoscale* **2015**, 7, 10472.
- [36] P. Caroff, J. Bolinsson, J. Johansson, *IEEE J. Sel. Top. Quantum Electron.* **2011**, 17, 829.
- [37] S. Gorji Ghalamestani, S. Lehmann, K. A. Dick, *Nanoscale* **2016**, 8, 2778.
- [38] T. Xu, K. A. Dick, S. Plissard, T. H. Nguyen, Y. Makoudi, M. Berthe, J.-P. Nys, X. Wallart, B. Grandidier, P. Caroff, *Nanotechnology* **2012**, 23, 095702.
- [39] Q. D. Zhuang, E. A. Anyebe, R. Chen, H. Liu, A. M. Sanchez, M. K. Rajpalke, T. D. Veal, Z. M. Wang, Y. Z. Huang, H. D. Sun, *Nano Lett.* **2015**, 15, 1109.
- [40] M. J. L. Sourribes, I. Isakov, M. Panfilova, H. Liu, P. A. Warburton, *Nano Lett.* **2014**, 14, 1643.
- [41] H. Potts, M. Friedl, F. Amaduzzi, K. Tang, G. Tütüncüoğlu, F. Matteini, E. Alarcon Lladó, P. C. McIntyre, A. Fontcuberta, I. Morral, *Nano Lett.* **2016**, 16, 637.
- [42] S. G. Ghalamestani, A. M. Munshi, D. L. Dheeraj, B.-O. Fimland, H. Weman, K. A. Dick, *Nanotechnology* **2013**, 24, 405601.
- [43] L. C. Chuang, M. Moewe, C. Chase, N. P. Kobayashi, C. Chang-Hasnain, S. Crankshaw, *Appl. Phys. Lett.* **2007**, 90, 043115.
- [44] F. Glas, *Phys. Rev. B* **2006**, 74, 121302.
- [45] A. Kelrich, O. Soria, Y. Calahorra, Y. Kauffmann, R. Gladstone, S. Cohen, M. Orenstein, D. Ritter, *Nano Lett.* **2016**, 16, 2837.
- [46] L. Namazi, S. G. Ghalamestani, S. Lehmann, R. R. Zamani, K. A. Dick, *Nanotechnology* **2017**, 28, 165601.
- [47] M. U. Tornberg, K. A. Dick, S. Lehmann, *J. Phys. Chem. C* **2017**, 121, 21678.
- [48] M. Paladugu, J. Zou, G. J. Auchterlonie, Y. N. Guo, Y. Kim, H. J. Joyce, Q. Gao, H. H. Tan, C. Jagadish, *Appl. Phys. Lett.* **2007**, 91, 133115.
- [49] M. Paladugu, J. Zou, Y.-N. Guo, X. Zhang, H. J. Joyce, Q. Gao, H. Hoe Tan, C. Jagadish, Y. Kim, *J. Appl. Phys.* **2009**, 105, 073503.
- [50] T. Ito, *Jpn. J. Appl. Phys.* **1998**, 37, L1217.
- [51] S. Neretina, R. A. Hughes, J. F. Britten, N. V. Sochinskii, J. S. Preston, P. Mascher, *Nanotechnology* **2007**, 18, 275301.
- [52] M. S. Song, S. Bin Choi, Y. Kim, *Nano Lett.* **2017**, 17, 4365.
- [53] P. Boieriu, R. Sporken, Y. Xin, N. D. Browning, S. Sivananthan, *J. Electron. Mater.* **2000**, 29, 718.
- [54] H. I. T. Hauge, M. A. Verheijen, S. Conesa-Boj, T. Etzelstorfer, M. Watzinger, D. Kriegner, I. Zardo, C. Fasolato, F. Capitani, P. Postorino, S. Kölling, A. Li, S. Assali, J. Stangl, E. P. A. M. Bakkers, *Nano Lett.* **2015**, 15, 5855.
- [55] H. Potts, N. P. Morgan, G. Tütüncüoğlu, M. Friedl, A. F. I. Morral, *Nanotechnology* **2017**, 28, 054001.
- [56] S. Bernal, F. J. Botana, J. J. Calvino, C. López-Cartes, J. A. Pérez-Omil, *Ultramicroscopy* **1998**, 72, 135.



Supporting Information

for *Small*, DOI: 10.1002/sml.201703785

Sb Incorporation in Wurtzite and Zinc Blende $\text{InAs}_{1-x}\text{Sb}_x$
Branches on InAs Template Nanowires

Magnus Dahl, Luna Namazi, Reza R. Zamani, and Kimberly A. Dick**

Supporting Information

Supplemental information for “Sb incorporation in Wurtzite and Zinc blende InAs1-xSbx Branches on InAs Template Nanowires”

Magnus Dahl, Luna Namazi, Reza R. Zamani, and Kimberly A. Dick**

SI 1. Growth parameters at given Sb vapor phase compositions

Precursor flows, along with the V/III ratio at given vapor phase compositions. The group III floe (TMIn) was kept constant for all x_v . To increase the x_v , for the first four data points the AsH₃ flow was kept at constant value, while the TMSb flow was the only varying growth parameter. This leads to an increasing total precursor flow and V/III ratio profile (this trend is better seen in the graphs of figure SI 2, Group V precursor flow). 3.1×10^{-4} was the highest accessible TMSb flow with our set up. Therefore, in order to obtain higher x_v , the AsH₃ flow was reduced, while keeping the TMSb constant at the maximum value. This Results in a decrease in the total precursor flow, and the V/III ratio.

Table SI 1. Growth parameters at studied Sb vapor phase compositions (x_v)

| x_v | TMIn | AsH ₃ | TMSb | Total flow | V/III |
|-------------|----------------------|----------------------|----------------------|----------------------|-------|
| 0.15 | 2.5×10^{-6} | 2.5×10^{-4} | 4.5×10^{-5} | 3.0×10^{-4} | 116.3 |
| 0.29 | 2.5×10^{-6} | 2.5×10^{-4} | 1.0×10^{-4} | 3.5×10^{-4} | 139.6 |
| 0.47 | 2.5×10^{-6} | 2.5×10^{-4} | 2.2×10^{-4} | 4.7×10^{-4} | 186.7 |
| 0.55 | 2.5×10^{-6} | 2.5×10^{-4} | 3.1×10^{-4} | 5.6×10^{-4} | 221.9 |
| 0.76 | 2.5×10^{-6} | 1×10^{-4} | 3.1×10^{-4} | 4.1×10^{-4} | 162.6 |
| 0.89 | 2.5×10^{-6} | 3.8×10^{-5} | 3.1×10^{-4} | 3.5×10^{-4} | 137.9 |

SI 2. Average total length of zinc blende (ZB) and wurtzite (WZ) nanowires

The average length of the nanowire trunks of both zinc blende (Figure SI 2a) and wurtzite (SI 2b) nanowires were measured before (reference in graph), and after branch growth. The length of nanowires with and without branching events are also

measured and demonstrated separately in these graphs. As observed for almost all cases the average length of the nanowires after branch growth is longer than the nanowire trunks previous the branch growth. This implies that an axial segment grows from the initial Au particle on top of the original trunk during branch growth. At $x_v = 0.76$ and 0.89 of wurtzite nanowires however, it is observed that the average length of the reference trunks are longer than the nanowires after branch growth (with and without any branching events). This indicates that, under these conditions (very high Sb flows, and low As flow) decomposition of the original trunk occurs. From this plot we can also see that at $x_v = 0.89$ there is no data point for branched nanowire with branches. It is speculated that, under this extreme condition, formation of wurtzite branches with high Sb compositions was not favorable.

In both Figure SI 2a and b, the group V precursor flow is also shown. This demonstrates the total flow precursor profile discussed in SI 1.

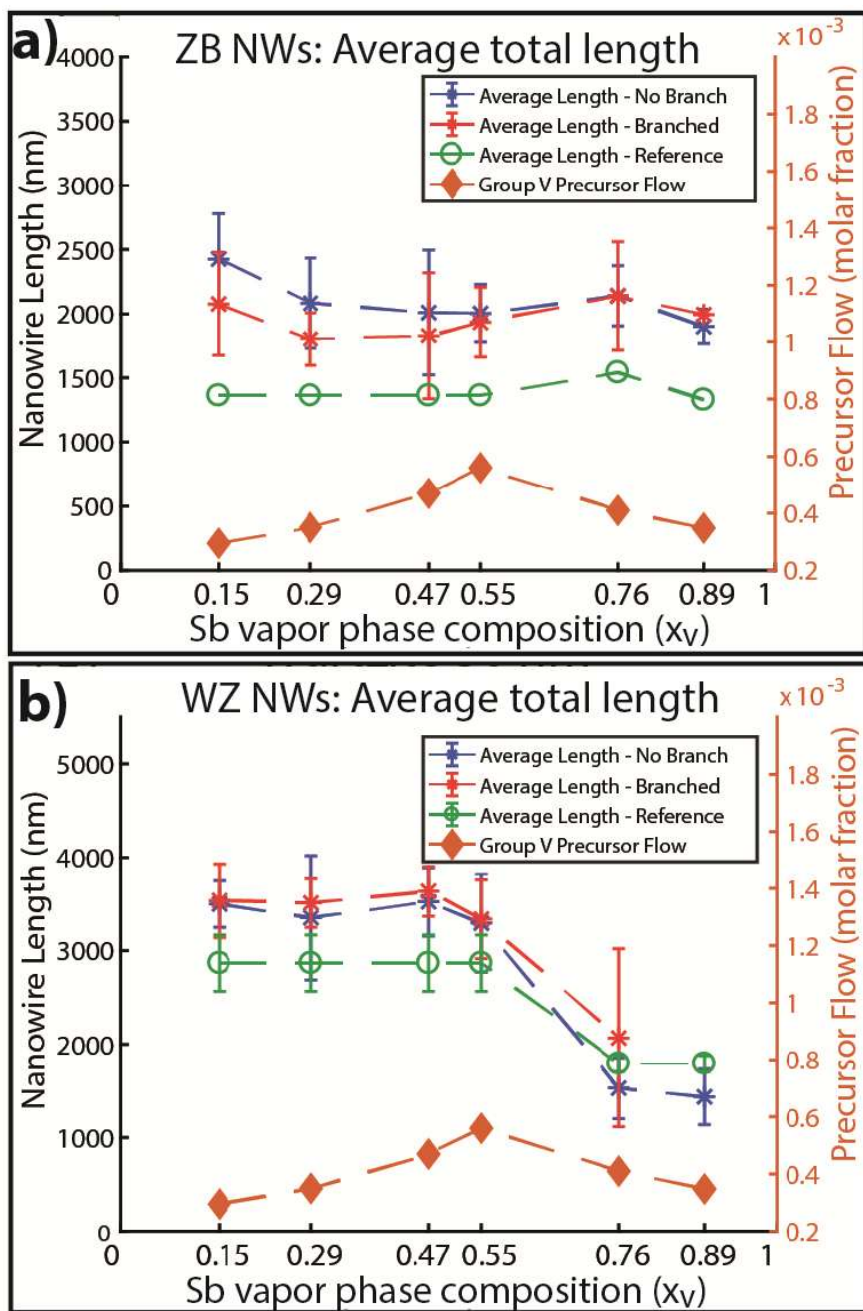


Figure SI 2. Measured average total length of a) zinc blende and b) wurtzite nanowire trunks before and after branch growth.

